THERMOCHEMICAL ENERGY STORAGE FOR CABIN HEATING APPLICATION IN HYBRID ELECTRIC VEHICLES

Report submitted in partial fulfillment of the requirements for the course

MASTER OF TECHNOLOGY

In

MECHANICAL ENGINEERING

By

AKSHAY BHIMRAO CHATE

Under the guidance of

Prof. PRADIP DUTTA

DEPARTMENT OF MECHANICAL ENGINEERING

INDIAN INSTITUTE OF SCIENCE

BANGALORE, 560012

JUNE 2019

DECLARATION

I, AKSHAY BHIMRAO CHATE, with SR No. 05-07-00-10-42-17-1-14533 hereby declare that the work presented in the present thesis titled THERMOCHEMICAL ENERGY STORAGE FOR CABIN HEATING APPLICATION IN HYBRID ELECTRIC VEHICLES in the partial fulfillment of the requirements for the award of the degree of MASTER OF TECHNOLOGY and submitted in the DISCIPLINE OF MECHNICAL ENGINEERING, INDIAN INSTITUTE OF SCIENCE, BANGALORE, is an authentic record of my own work carried out during the time period from September 2018 to June 2019 under the supervision of Prof. PRADIP DUTTA.

Date: Signature of the student

This is to certify that the above statement made by the candidate is correct to the best of my/our knowledge.

Date: Signature of Thesis Supervisor #1

Date: Signature of Invigilator #1

Date: Signature of Invigilator #2

ACKNOWLEDGEMENTS

First and foremost, I would like to thank my advisor Prof. Pradip Dutta, for giving me opportunity to work on this topic. His insightful advice, encouragement, guidance, critics, and valuable suggestions throughout the course of my project work have been really helpful. I would also like to thank Prof. S. S. Murthy, who has been providing his continuous support throughout the highs and lows of this project. His immense knowledge in thermal energy storage field has been really helpful to validate the correctness of simulation results performed in the present work. I am also grateful to have received support from Dr. Rakesh Sharma, especially with proper presentation and documentation of the work. Also, his practical knowledge has been very helpful for in-depth understanding of the present study.

Secondly, I would like to thank all my fellow lab mates for their support. At the start of project, I was novice to the simulation software used. Ashwin and Sayuj have always been there for me in any sort of difficulty regarding the simulations or in general. I would also like to express my gratitude to Madhuri for bearing with me and providing important insights on wider range of topics. I am also grateful to all my batch mates and other friends in IISc. It has been a wonderful experience. Also, I would like to thank academic staff of Mechanical Engineering Department, especially Somavathi and Chinnamma madam, who have always helped me with academics related matters.

Last but not least, I am forever indebted to my parents and family members for all their hard work and unconditional love.

The list of acknowledgements is almost never ending. So, I take this opportunity to express my sincere and heartfelt gratitude to all those who have helped me directly or indirectly towards the successful completion of this thesis.

ABSTRACT

Due to depleting fossil fuels and increase in air pollution from the exhaust gas (EG) of internal combustion (IC) engine vehicles, electric vehicles are gaining popularity all over the world. But due to scarcity of required infrastructure and higher costs, electric vehicles are yet to become a lucrative option to replace IC engine vehicles. Under these circumstances, hybrid electric vehicles (HEVs) are being looked as a suitable option. In colder countries, average ambient temperature values are low (10 to 20 ˚C) for most part of the year. For such colder conditions, cabin heating becomes essential part of passenger comfort. Currently, electric heaters are widely used for cabin heating application in most of the vehicles. These heaters are driven by IC engine or electric battery. Thus, present study explores possibility of employing suitable energy storage system for cabin heating application in HEVs. Proposed system is expected to store thermal energy from EG and to release the stored energy for cabin heating during intermittent shutdown of IC engine in HEVs. After detailed study of different methods to store thermal energy, it is found that thermochemical energy storage (TES) method provides higher energy storage density. Thus, TES method is selected to develop thermal energy storage system in HEVs. The components required in TES system are Energy Storage Bed (ESB) and Gas Storage Bed (GSB). Solid reactant is kept in ESB in which gas is allowed to interact with solid. The bonding of gas with solid is characterized by exothermic reaction, whereas dissociation is endothermic. Gas released or supplied during chemical reaction is stored in GSB.

Initially, hydration/dehydration of K_2CO_3 was chosen to develop TES system. However due to lack of experimental study and kinetic expressions, the focus is shifted on other materials. After thorough literature study, hydration/dehydration of $CaO/Ca(OH)_2$ is selected for the proposed TES system.

In the present study, the analysis is focused mainly on ESB. A simplified 2-D model is created to perform parametric studies of hydration and dehydration reaction that occur in ESB.

Hydration reaction is studied first. The effects of varying the water vapour supply pressure, initial ESB temperature, heat transfer fluid (HTF) mass flow rate, ESB permeability and time of reaction are examined during hydration. Based on the simulation results, it is observed that rate of reaction increases with increase in water vapour supply pressure. The effect of initial ESB temperature on hydration reaction is negligible. At higher mass flow rates, HTF receives higher amount of energy released by ESB, but the rise in HTF average outlet temperature drops. High energy output is observed for low porosity values of ESB and large average particle size. It is observed that the conversion of reactant into product reaches 83.75 % in 1200 s beyond which the rate of conversion becomes very low. On the basis of 2-D simulation results of hydration, initial operating conditions are revised. 2-D simulations as per revised operating conditions are also performed.

The simulation study of 3-D model for the hydration reaction is performed for three different case studies. It is observed that more conversion is observed in 3-D model as compared to 2-D model due to the edge effect. Also, HTF average outlet temperature is lower in 3-D model due to energy loss from HTF to steel frame duct. The efficiency of heat transfer from ESB to HTF significantly increases from 78.66 % when there are no fins to 82.65 % by addition of fins in ESB domain. Whereas, the addition of fins in both ESB and HTF domains results in increase in rate of reaction thereby reduction in reaction completion time. With fins

added in both ESB and HTF domains, reaction completion time is reduced by 39.13 % in comparison to fins in ESB domain only.

For dehydration reaction, the effects of varying the water vapour outlet pressure, EG inlet temperature, EG mass flow rate, ESB permeability and time of reaction are studied. It is observed that the rate of dehydration reaction increases with lower values of water vapour outlet pressure. The reaction rate is negligible at EG inlet temperatures below 623 K. High extent of conversion is noticed at high EG inlet temperature. No significant impact of EG mass flow rate is observed on dehydration reaction performance. The energy storage is observed to be higher for low porosity values of ESB and larger average particle size. The conversion of 48.39 % is observed till 1200 s after which the rate conversion becomes very low.

The simulation study of a complete dehydration-hydration cycle is also performed for a single cycle in 2-D model. The complete dehydration-hydration cycle involves preheating of ESB, dehydration reaction, sensible cooling of ESB and hydration reaction in sequence. Chemical reaction efficiency and overall cycle efficiency is observed to be 55.94 % and 64.28%, respectively.

The present study is performed in the collaboration with Faurecia Emissions Control Technologies India Pvt. Ltd. For brief period at the start of project, DLR University from Germany was also involved with Faurecia team.

TABLE OF CONTENTS

LIST OF FIGURES

LIST OF TABLES

NOMENCLATURE

P	Pressure (Pa)
T	Temperature (K)
P_{eq}	Equilibrium pressure (Pa)
T_{eq}	Equilibrium temperature (K)
ΔH	Enthalpy of reaction (kJ mol^{-1})
$\dot{r}$	Interface velocity (m s^{-1})
$\bar{\dot{r}}$	Dehydration rate (mol m^{-3} s^{-1})
ρ	Density (kg m^{-3})
M	Molecular mass (kg $kmol^{-1}$)
k''_0	Rate constant (m $K^{1/2}$ s^{-1})
r_0	Initial radius of particle (m)
E_a	Activation energy (J)
k	Boltzmann constant (J K^{-1})
γ	Constant (K^3)
φ	Bed porosity
X	Extent of reaction
k_0	Unknown to be determined by curve fitting (s^{-1})
w	Width of the EG flow channel
h	Height of the EG flow channel
D_h	Hydraulic diameter (m)
V	Mean flow velocity (m s^{-1})
ν	Kinematic viscosity of EG
Re	Reynold's number
L	Turbulence length scale (m)
I	Turbulence intensity
k'	Turbulence kinetic energy (m^{-2} s^{-2})
ε	Dissipation rate (m^{-2} s^{-3})
K	ESB permeability (m^2)

Subscript

s	solid
g	gas
eq	equilibrium
sat	saturation

ACRONYMS

HEV	Hybrid Electric Vehicle
IC	Internal Combustion
EG	Exhaust Gas
HTF	Heat Transfer Fluid
TES	Thermochemical Energy Storage
SHS	Sensible Heat Storage
LHS	Latent Heat Storage
THS	Thermochemical Heat Storage
ESB	Energy Storage Bed
GSB	Gas Storage Bed
0-D	Zero dimensional
2-D	Two dimensional
3-D	Three dimensional
UDF	User Defined Functions
FEM	Finite Element Method
RANS	Reynolds-Averaged Navier-Stokes
dia	Average particle diameter
p_in	Water vapour supply pressure
T_ini	Initial ESB temperature
mfr	Mass flow rate
p_out	Water vapour outlet pressure

CHAPTER 1

INTRODUCTION

1.1 Introduction and working principle of Hybrid Electric Vehicles (HEVs)

Due to depleting fossil fuels and increase in air pollution from the exhaust gas (EG) of Internal Combustion (IC) engine vehicles, electric vehicles are gaining popularity all over the world. But due to scarcity of required infrastructure and higher costs, electric vehicles are yet to become a lucrative option to replace IC engine vehicles. Under these circumstances, hybrid electric vehicles (HEVs) are being looked as a suitable option. The working principle of HEVs is based on two working steps as mentioned below:

Step 1: IC engine is ON – In HEVs, IC engine is the principle source of power. When it is ON it provides required torque to drive the vehicle. At the same it charges on board electric batteries with the help of generator.

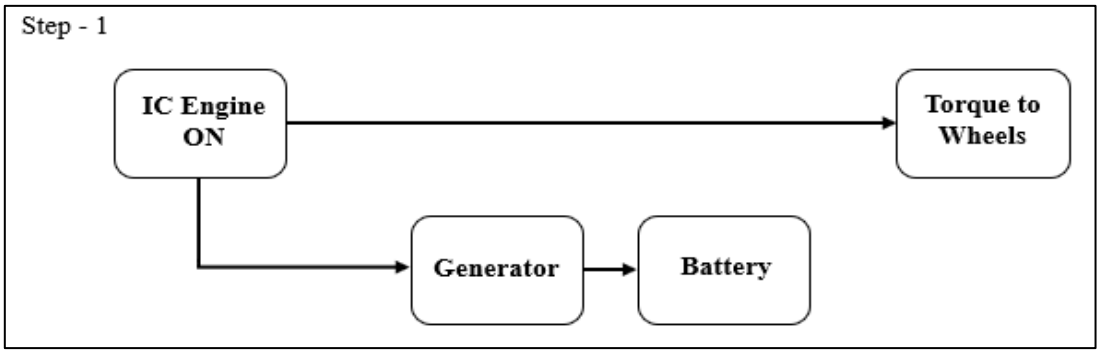

Fig. 1.1: Working principle of HEVs – Step 1

Step 2: IC engine is OFF – After charging batteries, IC engine is shut off. Then HEV is driven by electric motor which are operated with the help of electric batteries. When voltage across batteries drop below a certain threshold value, IC engine is re-started and the step 1 is repeated again.

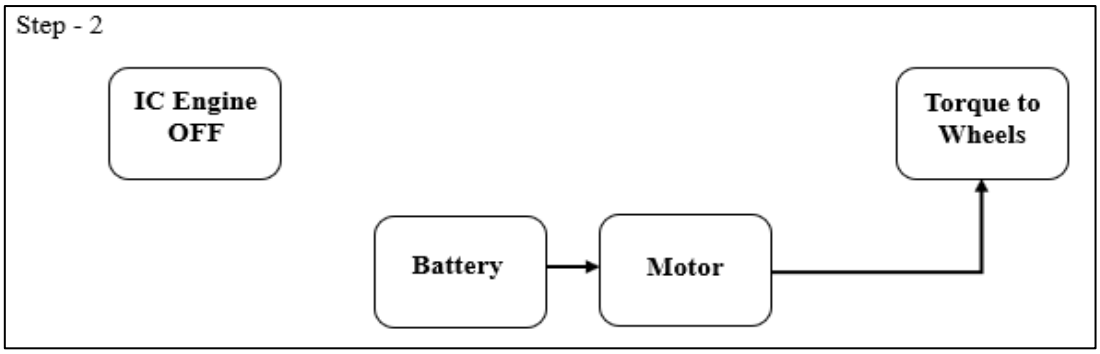

Fig. 1.2: Working principle of HEVs – Step 2

1.2 Existing arrangements for cabin heating in HEVs

The present assembly for cabin heating in HEVs work in two steps as below:

Step 1: IC engine is ON – EG from IC engine is passed through heat exchanger as shown in Fig. 1.3. In the heat exchanger, EG rejects heat to Heat Transfer Fluid (HTF) which is further used for cabin heating.

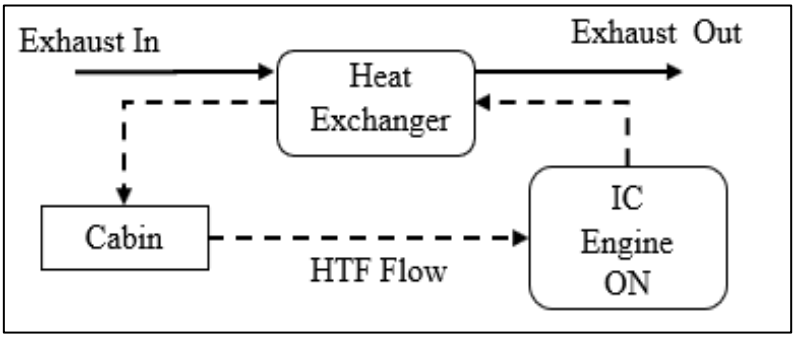

Fig. 1.3: Existing cabin heating arrangement – Step 1

Step 2: IC engine is OFF – In this case, electric heater driven by batteries is used to heat the HTF as shown in Fig. 1.4.

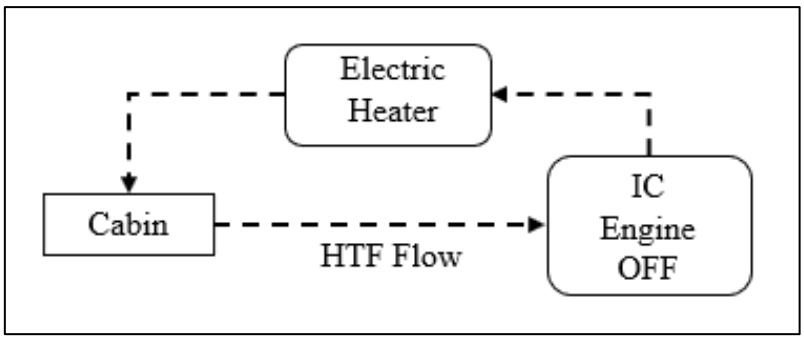

Fig. 1.4: Existing cabin heating arrangement – Step 2

1.3 Motivation of the present study

In colder countries, average ambient temperature values are low (10 to 20 ˚C) for most part of the year. For such colder conditions, cabin heating becomes essential part of passenger comfort. Currently, electric heaters are widely used for cabin heating application in most of the vehicles. These heaters are driven by IC Engine or electric battery. Thus, present study explores possibility of employing suitable energy storage system for cabin heating application in HEVs. Proposed system is expected to store thermal energy from exhaust gas and to release the stored energy for cabin heating during intermittent shutdown of IC engine in HEVs. The advantages of TES in HEVs are:

1. Thermal energy carried by EG is stored in TES system which can be used for cabin heating application.

2. This results in reduction in energy requirement from IC engine or battery for cabin heating application.

3. Increase in overall efficiency of HEV which leads to saving in fuel or energy and reduction in EG emissions from HEVs.

1.4 Overview of different thermal energy storage systems

Detailed study of different methods of thermal energy storage are studied for proposed application. There are three main types of thermal energy storage systems available:

1. Sensible heat storage (SHS) – SHS works on the principle of storing or extracting heat in the form temperature change of higher specific heat materials (without undergoing phase change). Suitable materials for this type of storage are rocks, bricks, soil, etc. But SHS are not suitable for long term heat storage. Weight and volume requirement per unit of energy storage is higher.

2. Latent heat storage (LHS) – Large values of latent heat during phase change are utilized in this case. Energy can be stored or extracted at almost constant temperature. Paraffin wax and water are common examples. Limited number of suitable materials and very small leeway on operating parameters during the phase change are some of the limitations of LHS.

3. Thermochemical heat storage (THS) – THS stores or extracts heat based on the principle of either adsorption process or chemical reactions. This type of systems can be used for long term heat storage. Weight or volume requirement per unit of energy stored is comparatively lesser. Performance of THS system can be controlled easily by controlling different operating parameters. THS materials have approximately 8–10 times higher storage density over SHS, and two times higher over LHS materials when compared for like storage volume basis [1]. Variation in heat storage densities of different materials is shown in Fig. 1.5. It also shows that materials used for THS give higher storage densities as compared to materials used in SHS and LHS. Hence THS or thermochemical energy storage (TES) method is the most suitable option for an application such as thermal energy storage in HEVs.

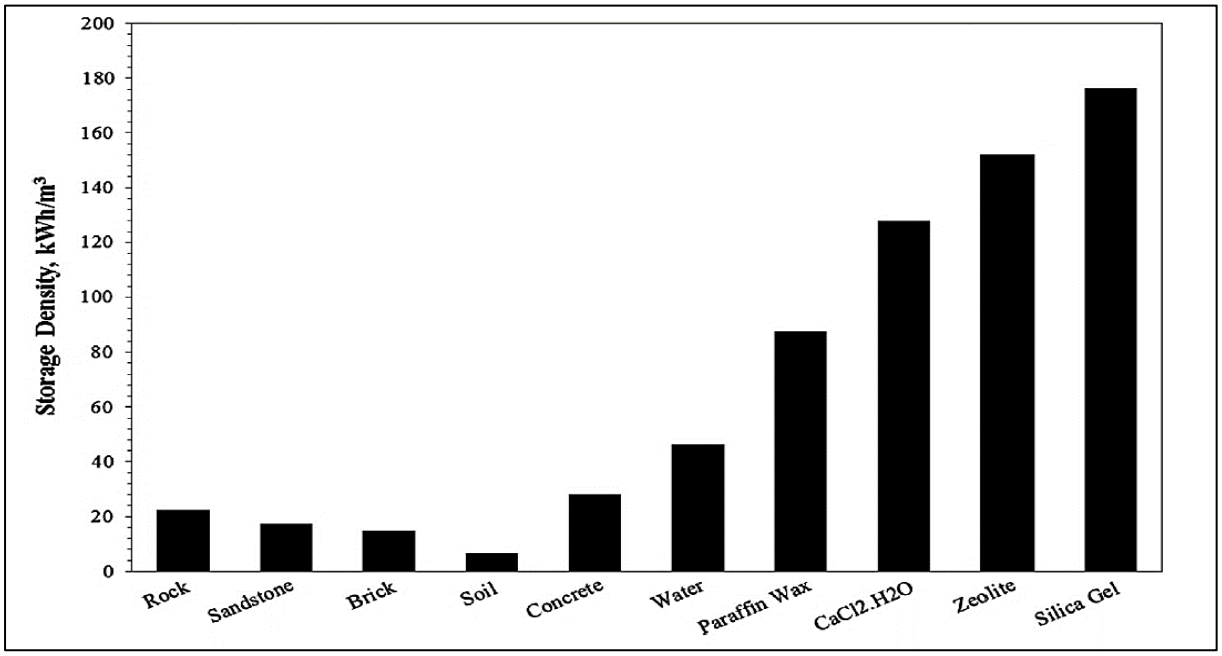

Fig. 1.5: Comparison of heat storage densities of different materials [1]

1.5 Objective of the present study

After deciding to use thermochemical energy storage (TES) system for proposed energy storage objective of the present study is finalized.

Objective of the present study is to design and optimize a feasible TES system, which is to be used as an alternate energy source for cabin heating application during intermittent shutdown of IC engine in HEVs within the provided operating conditions.

The present study is performed in the collaboration with Faurecia Emissions Control Technologies India Pvt. Ltd. For brief period at the start of project, DLR University from Germany was also involved with Faurecia team.

1.6 Modifications in current arrangement for cabin heating while employing TES system

At the start of project, upon recommendation of DLR university Faurecia team has suggested hydration and dehydration of Potassium Carbonate ($K_2CO_3.1.5H_2O$ and K_2CO_3) as one of the suitable material for TES system. Dehydration occurs when $K_2CO_3.1.5H_2O$ is heated with the help of EG, which is an endothermic reaction. The generated water vapour is required to be condensed and stored in another container. When the stored thermal energy is required to be retrieved for cabin heating, water vapour is generated which is allowed to interact with the anhydrous K_2CO_3. Hydration of K_2CO_3 occurs which is an exothermic reaction and results in the release of heat. The heat released is carried away by HTF for cabin heating application.

Thus, additional components required in TES system are:

1. Energy Storage Bed (ESB) which consist of the reactant K_2CO_3 where the hydration and dehydration take place.

2. A separate container for storage of water where condensation and evaporation of water vapour occur. It is termed as Gas Storage Bed (GSB).

3. Connection between ESB and GSB to facilitate transfer of water vapour along with control system.

The operating modes of HEV cycle with TES system are shown in Table 1.1.

Table 1.1. Different operating modes of TES in HEV

IC Engine Status	Terminology used for process	Energy storage/ release	Process in ESB	Process in GSB
ON	Charging of ESB	Energy storage	Endothermic reaction	Condensation of water vapour coming from ESB
ON	Discharging of ESB	Energy release (Start-off)	Exothermic reaction	Start of water vapour formation in GSB
OFF	Discharging of ESB	Energy release	Exothermic reaction	Continuous water vapour formation due to pressure gradient between ESB and GSB

The different operating modes of TES in HEV are further explained with the help of schematic diagrams as shown,

1. Energy storage mode – In this mode, the dehydration of ESB takes place by consuming the heat of EG. Water vapour is released from ESB as per the reaction shown in Eqn. 1.1:

   $K_2CO_3.1.5H_2O_{(s)} \Leftrightarrow K_2CO_{3\,(s)} + 1.5H_2O_{(g)}$, $\Delta H = 65.8$ kJ mol^{-1}, [2] (1.1)

   Released water vapour is condensed in GSB. During this mode, a fraction of heat from EG is used to heat HTF in heat exchanger as shown in Fig. 1.6 which is used for cabin heating.

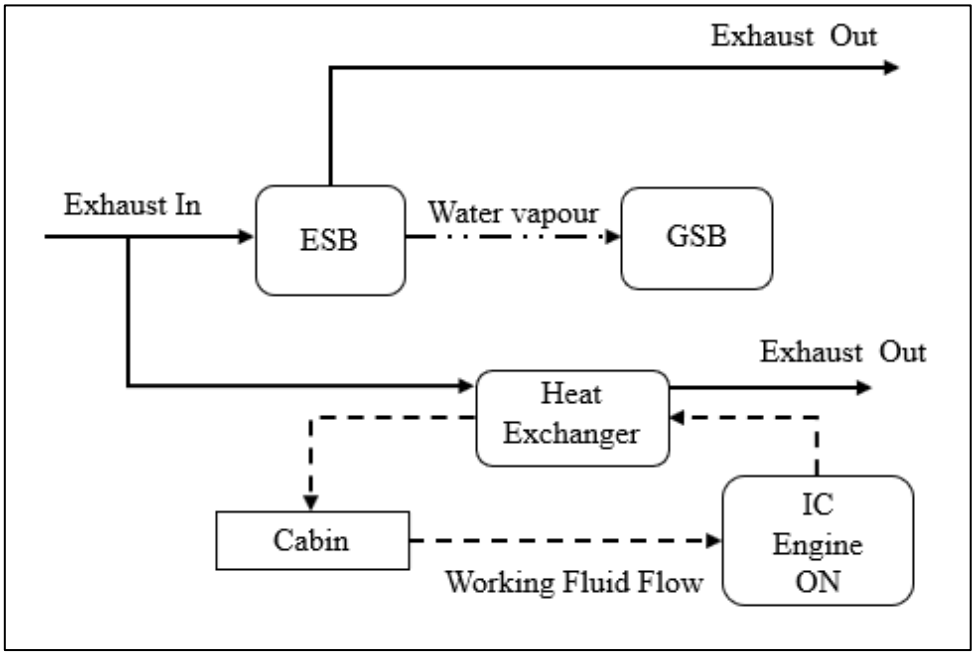

Fig. 1.6: Schematic diagram of TES system in energy storage mode

2. Energy release mode (Start-off) – To start hydration reaction, before shutting off IC engine, heat from EG is supplied to GSB to generate water vapour as shown in Fig. 1.7. The pressure of generated water vapour should be higher than pressure of ESB (ESB pressure is equal to equilibrium pressure corresponding to its temperature). Due to the pressure difference between GSB and ESB, water vapour enters ESB and exothermic hydration reaction starts as shown by Eqn. 1.2:

   $K_2CO_{3\,(s)} + 1.5H_2O_{(g)} \Leftrightarrow K_2CO_3.1.5H_2O_{(s)}$, $\Delta H = -65.8$ kJ mol^{-1}, [2] (1.2)

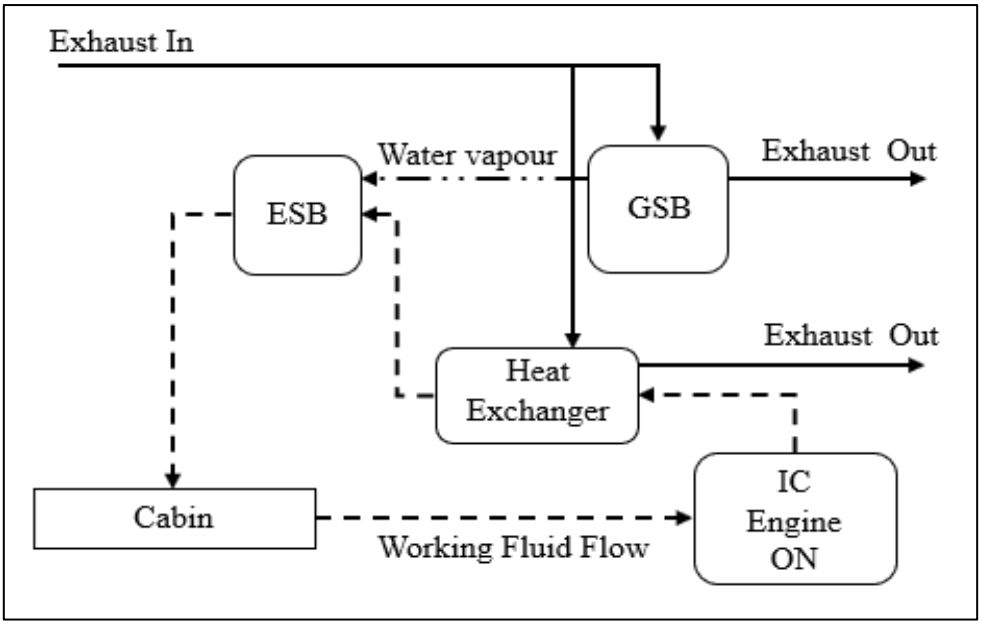

Fig. 1.7: Schematic diagram of TES system in energy release mode (Start-off)

3. Energy release mode – Once hydration reaction starts, ESB temperature increases and accordingly its equilibrium pressure also increases. GSB is to be designed in such a way that water vapour supply pressure must be always higher than equilibrium pressure of ESB. Provided this condition is satisfied then there will be continuous energy release from ESB as long as there is enough amount of reactant available in ESB. Exothermic reaction given by Eqn. 1.2 is the energy source in this mode.

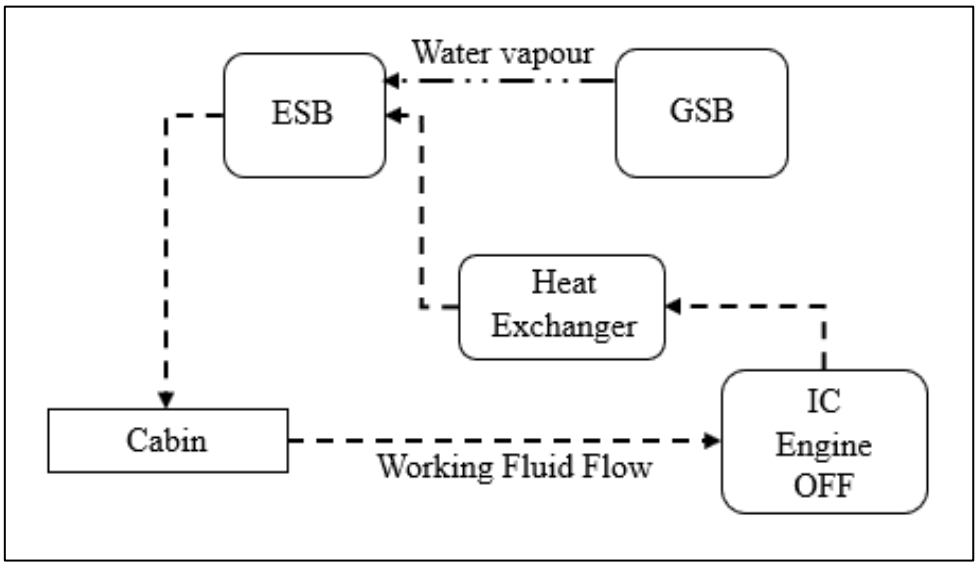

Fig. 1.8: Schematic diagram of TES system in energy release mode

In this way, proposed TES system can be used for cabin heating application even when IC engine is shut-off. After understanding the basic operational modes of TES system, detailed literature review for TES material has been carried out and explained in Chapter 2.

CHAPTER 2

LITERATURE REVIEW

Upon recommendation of DLR University, Faurecia team has suggested dehydration and hydration of Potassium Carbonate (K_2CO_3) as one of the suitable material for TES system based on operating conditions. Thus, literature study for Potassium Carbonate as potential TES material has been carried out.

2.1 Study of reaction kinetics of K_2CO_3 hydration and dehydration reactions

After thorough investigation for reaction kinetics of K_2CO_3 hydration and dehydration reactions, it is observed that limited amount of work has been done for K_2CO_3 hydration and dehydration reaction. With the available literature following observations are made.

2.1.1 Rate expressions for dehydration reaction from interface velocity relation

For dehydration reaction, interface velocity relation is used to deduce rate expression. Dehydration reaction is given as

$$K_2CO_3.1.5H_2O \Leftrightarrow K_2CO_3 + 1.5H_2O,\ \Delta H = 65.8\ kJ\ mol^{-1}\ [3] \quad (2.1)$$

It is required to find the relation between equilibrium pressure and temperature i.e. van't Hoff plot to deduce rate of reaction. The van't Hoff plot is constructed in Fig. 2.1 using the set of values for equilibrium pressures and temperatures given in Stanish and Perlmutter [3]

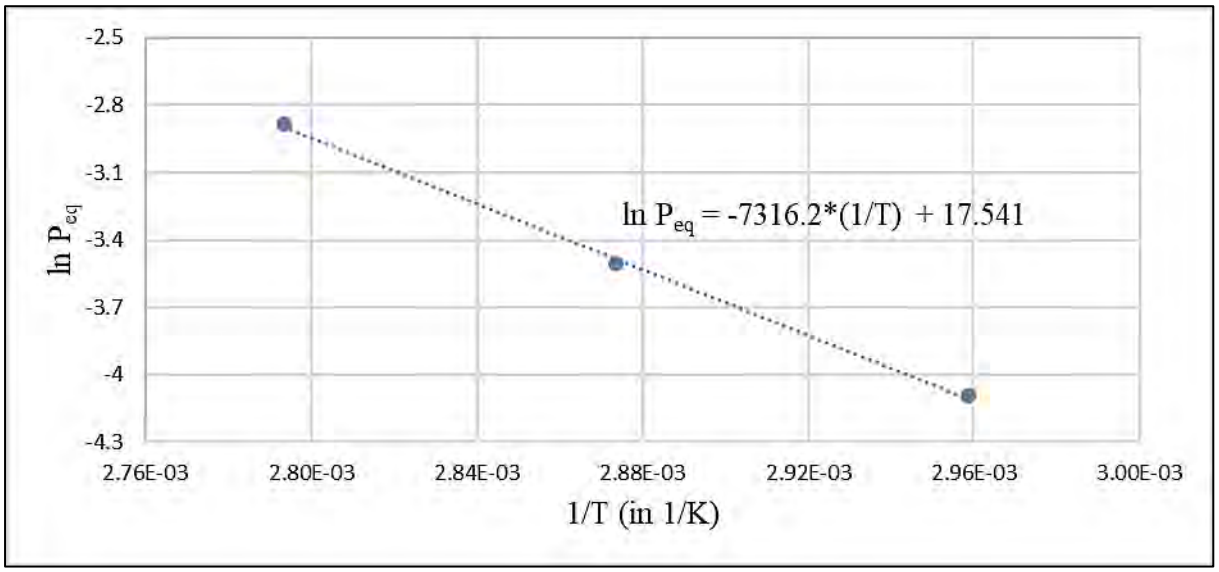

Fig. 2.1: Van't Hoff plot for dehydration reaction of $K_2CO_3.1.5H_2O$

The van't Hoff equation is given as,

$$\ln\left(P_{eq}\right) = -\frac{\Delta h}{RT} + \frac{\Delta s}{R} \quad (2.2)$$

Equation of line of best fit as shown in Fig. 2.1 is given by Eqn. 2.3

$$\ln\left(P_{eq}\right) = -\frac{7316.2}{T} + 17.541 \quad (2.3)$$

On comparing coefficients of Eqn. 2.2 and 2.3, ΔH value is calculated as 60.827 kJ mol^{-1}.

Table 2.1 represents the calculated and literature values of reaction enthalpy. It is observed that the calculated and reported values of reaction enthalpy are approximately close which validates the relation between equilibrium pressure and temperature given by Eqn. 2.3.

Table 2.1 Comparison of enthalpy of reaction for dehydration reaction of $K_2CO_3.1.5H_2O$

	Stanish and Perlmutter [3]	Sogutoglu et al. [2]	Calculated	As provided by Faurecia team
Δh (kJ mol^{-1})	63.0	65.8	60.8	70.2

The equation of reaction rate for dehydration reaction is deduced from interface velocity [3]. Assumptions for the interface velocity derivation are applicable for this derivation also and are as follows:

1. The dehydration of $K_2CO_3 1.5H_2O$ is assumed to take place according to shrinking core gas – solid reaction model.
2. The relative pressure (P/P_{eq}) is smaller than 0.35 during analysis as the reaction rate becomes extremely low at $P/P_{eq} > 0.35$.
3. For the assumed particle size range (30-40 μm and 150 μm), heat transfer resistance within the particle and diffusional resistances within the product layer are negligible.

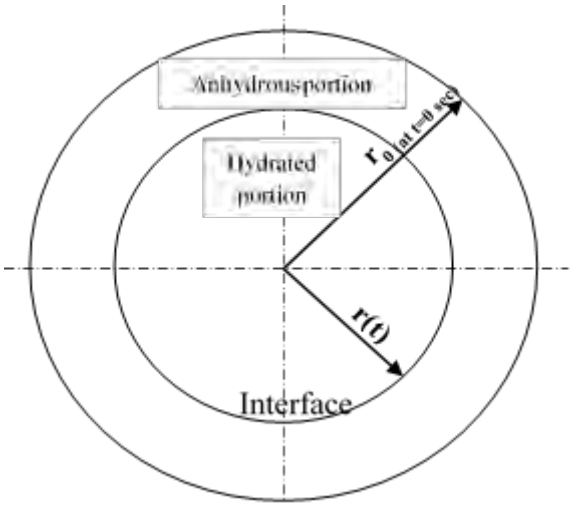

Fig. 2.2: Schematic of single bed particle ($K_2CO_3.1.5H_2O$) undergoing dehydration reaction [4]

Fig. 2.2 shows schematic of single bed particle (K2CO3.1.5H2O) undergoing dehydration reaction. Initial radius of particle is r_0 and as dehydration reaction proceeds its radius reduces as a function of time. Dehydration reaction interface velocity is given by

$$\dot{r} = -k''_0 T^{-1/2} * \exp\left(\frac{-E_a}{kT}\right) * \exp\left(\frac{-\gamma}{T^3 * \ln\left(\frac{P}{P_{eq}}\right)^2}\right) \quad (2.4)$$

where the interface velocity is function of pressure and temperature and can be written as

$$\dot{r} = -f(P, T) \quad (2.5)$$

$$\therefore \frac{dr}{dt} = -f(P, T) \quad (2.6)$$

$$\therefore \frac{1}{r_0} * \frac{dr}{dt} = -\frac{f(p,T)}{r_0} \quad (2.7)$$

From Fig. 2.2, the initial volume of a single spherical particle of $K_2CO_3.1.5H_2O$ in bed is

$$V_0 = \frac{4}{3} * \pi * {r_0}^3 \quad (2.8)$$

The volume of particle after dehydration in time t is

$$V = \frac{4}{3} * \pi * r^3 \quad (2.9)$$

∴ The volume of anhydrous K_2CO_3 particle (product) is

$$V_0 - V = \frac{4}{3} * \pi * \{(r_0)^3 - (r)^3\} \quad (2.10)$$

The extent of reaction is defined as

$$X \text{ (in terms of volume)} = \frac{\text{Volume of product}}{\text{Initial volume of the reactant}}$$

∴ Volume of product is given by

$$V_0 - V = X * \frac{4}{3} * \pi * {r_0}^3 \quad (2.11)$$

From equations (2.10) and (2.11) the relation between radius of particle before and after conversion (dehydration) is obtained as

$$1 - \left(\frac{r}{r_0}\right)^3 = X \quad (2.12)$$

$$\therefore \left(\frac{r}{r_0}\right) = (1 - X)^{1/3} \quad (2.13)$$

The rate of change of volume ($m^3 s^{-1}$) is given as,

$$\frac{dV}{dt} = 4\pi * r(t)^2 * \frac{dr}{dt} \quad (2.14)$$

Equation (2.14) can be modified as,

$$\frac{1}{V_0} * \frac{dV}{dt} = \frac{4\pi * r(t)^2}{\frac{4}{3} * \pi * {r_0}^3} * \frac{dr}{dt} \tag{2.15}$$

$$\therefore \frac{d}{dt}\left(\frac{V}{V_0}\right) = 3 * \left(\frac{r(t)}{r_0}\right)^2 * \left(\frac{1}{r_0} * \frac{dr}{dt}\right) \tag{2.16}$$

From Eqns. 2.11 and 2.16

$$\frac{d}{dt}(1 - X) = 3 * \left(\frac{r(t)}{r_0}\right)^2 * \left(\frac{1}{r_0} * \frac{dr}{dt}\right) \tag{2.17}$$

Using Eqns. 2.7 and 2.13, Eqn. 2.17 is reduced to

$$-\frac{dX}{dt} = 3 * (1 - X)^{2/3} * \left(-\frac{f(P,T)}{r_0}\right) \tag{2.18}$$

From Eqns. 2.4 and 2.5,

$$\frac{dX}{dt} = 3 * (1 - X)^{2/3} * \left(\frac{{k"}_0 T^{-1/2}}{r_0} * \exp\left(\frac{-E_a}{kT}\right) * \exp\left(\frac{-\gamma}{T^3 * \ln\left(\frac{P}{P_{eq}}\right)^2}\right)\right) \tag{2.19}$$

Rate of dehydration reaction (mol m^{-3} s^{-1}) can be expressed as $\frac{dX}{dt} * \frac{(1-\varphi)*\rho}{M}$

$$\dot{\bar{r}} = \frac{3*(1-\varphi)*\rho*(1-X)^{2/3}}{M} * \left(\frac{{k"}_0 T^{-1/2}}{r_0} * \exp\left(\frac{-E_a}{kT}\right) * \exp\left(\frac{-\gamma}{T^3 * \ln\left(\frac{P}{P_{eq}}\right)^2}\right)\right) \tag{2.20}$$

Table 2.2 shows the value of different constants used in Eqn. 2.20.

Table 2.2 Values of constants used in Eqn. 2.20 [4]

Symbol	Value
$k"_0$	6.65 x 10^{8} m $K^{1/2}$ s^{-1}
r_0	Max 305 μm
E_a	1.54 x 10^{-19} J
k	1.381 x 10^{-23} J K^{-1}
γ	2.40 x 10^{8} K^3

As there is no literature available regarding the hydration reaction, such derivation cannot be done for hydration reaction. After performing preliminary simulations with the rate expression obtained from Eqn. 2.20, it is observed that the denominator term of $T^3 * \ln\left(\frac{P}{P_{eq}}\right)^2$ shows large increase for small rise in T. Due to this rapid increase in denominator, corresponding exponential term decays very fast. Thus, rate of reaction drops to very low

values within short interval of time. This was not in accordance with experimental results observed by team of DLR University. Thus, these rate expressions are not used further.

2.1.2 Rate of reaction for hydration reaction from curve fitting

Using experimental data given in Stanish and Perlmutter [6] for hydration reaction, rate expressions are derived using curve fitting. Experimental data is available in the form of rate of reaction vs time (X vs t) plot at four discrete temperature values of 305.5, 312, 319.5 and 327 K. For each temperature value, curves are available for different values of water vapour supply pressure. Objective of curve fitting is to find suitable rate of reaction expression with minimum deviation from actual experimental curves. Expression for rate of reaction is assumed as,

$$\frac{dX}{dt} = k_0 * \exp\left(\frac{-E_a}{R*T}\right) \times \left(\frac{P}{P_{eq}} - 1\right) \times (1 - X) \quad (2.21)$$

Where P_{eq} is in bar and given by Eqn. 2.3, T is in K and k_0 and E_a are unknowns. At constant T and P, Eqn. 2.21 can be written as,

$$\frac{dX}{dt} = z * (1 - X) \quad (2.23)$$

Where z is a constant which is given by Eqn. 2.24

$$z = k_0 * \exp\left(\frac{-E_a}{R*T}\right) \times \left(\frac{p}{P_{eq}} - 1\right) \quad (2.24)$$

On integrating Eqn. (2.23),

$$-\ln(1 - X) = zt + c \quad (2.25)$$

At t = 0 s, X = 0, so c = 0,

$$\therefore X = 1 - e^{-zt} \quad (2.26)$$

Eqn. 2.26 is fitted with actual data points from experimental data to obtain desired rate of reaction expressions.

Table 2.3. Cumulative error for different z values in curve fitting

z expression	Cumulative error
$z = k_0 * \exp\left(\frac{-E_a}{R*T}\right) * \left(\frac{P}{P_{eq}} - 1\right)$	10.06
$z = k_0 * \exp\left(\frac{-E_a}{R*T}\right) * \log\left(\frac{P}{P_{eq}}\right)$	21.59
$z = k_0 * \exp\left(\frac{-E_a}{R*T}\right) * \log\left(\frac{P}{P_{eq}}\right)^a$	13.54
$z = k_0 * \exp\left(\frac{-E_a}{R*T}\right) * \left(\left(\frac{P}{P_{eq}}\right)^b - 1\right)$	11.54
$z = k_0 * \exp\left(\frac{-E_a}{R*T}\right) * \left(\frac{P}{P_{eq}} - 1\right)^a$	5.24
$z = k_0 * \exp\left(\frac{-E_a}{R*T}\right) * \left(\left(\frac{P}{P_{eq}}\right)^b - 1\right)^a$	4.70

In practice, rate of reaction becomes zero when reactor bed pressure becomes equal to water vapour partial pressure or extent of reaction reaches value of 1, i.e. 100 % conversion of

reactant into product. Only few expressions of z satisfy these two conditions and these expressions are given in Table 2.3. Deviation of assumed expression from actual values is termed as cumulative error. By changing z values, different profiles are tried for curved fitting. Table 2.3 gives cumulative error for different z values. From Table 2.3, rate expression is chosen based on minimum cumulative error and is given by Eqn. 2.27

$$\frac{dX}{dt} = k_0 \times \exp\left(\frac{-E_a}{R*T}\right) \times \left(\left(\frac{P}{P_{eq}}\right)^b - 1\right)^a \times (1 - X) \qquad (2.27)$$

where, $k_0 = 2.99 \times 10^9\ s^{-1}$,

$E_a = 7.05 \times 10^4\ J\ mol^{-1}\ K^{-1}$,

a = 2.188,

b = 0.399.

Figs. 2.3 to 2.10 show variation of fitted curve using Eqn. 2.27 and actual experimental curve. Figs. 2.3 to 2.6 show variation of experimental curve with fitted curve using Eqn. 2.27 at temperature of 305.5 K and different water vapour supply pressure values. It is observed that experimental and fitted curves are in good agreement with each other for overall time of reaction.

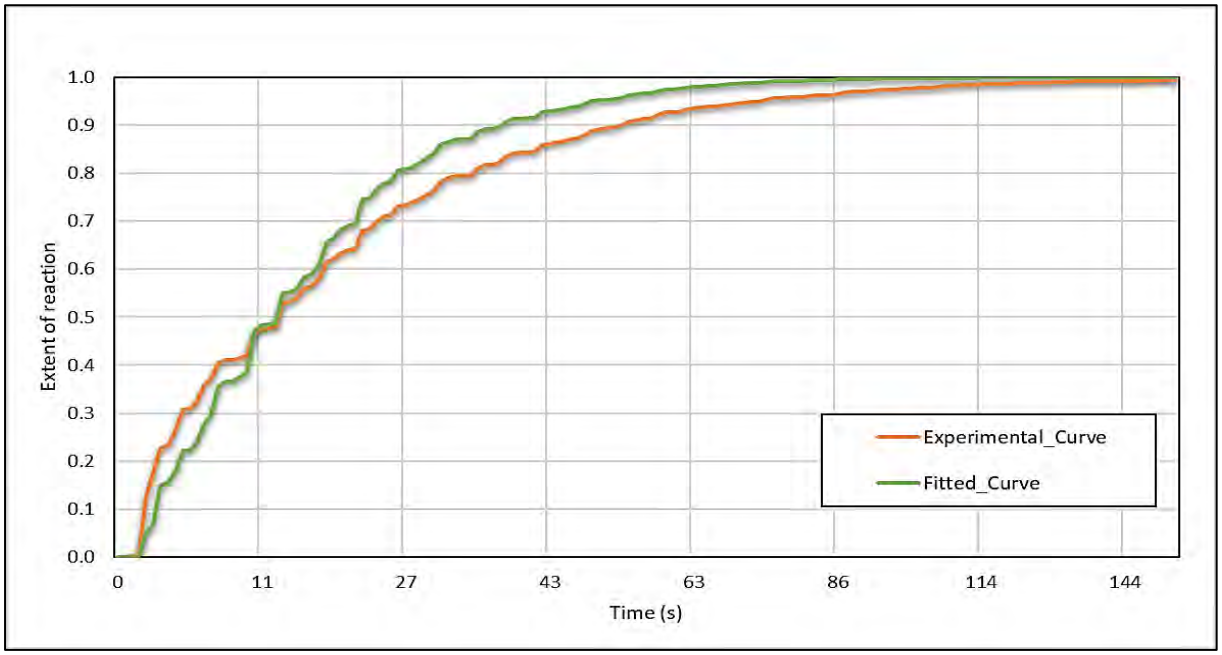

Fig. 2.3: Curve fitting results for initial temperature of 305.5 K and water vapour supply pressure of 1.6 kPa

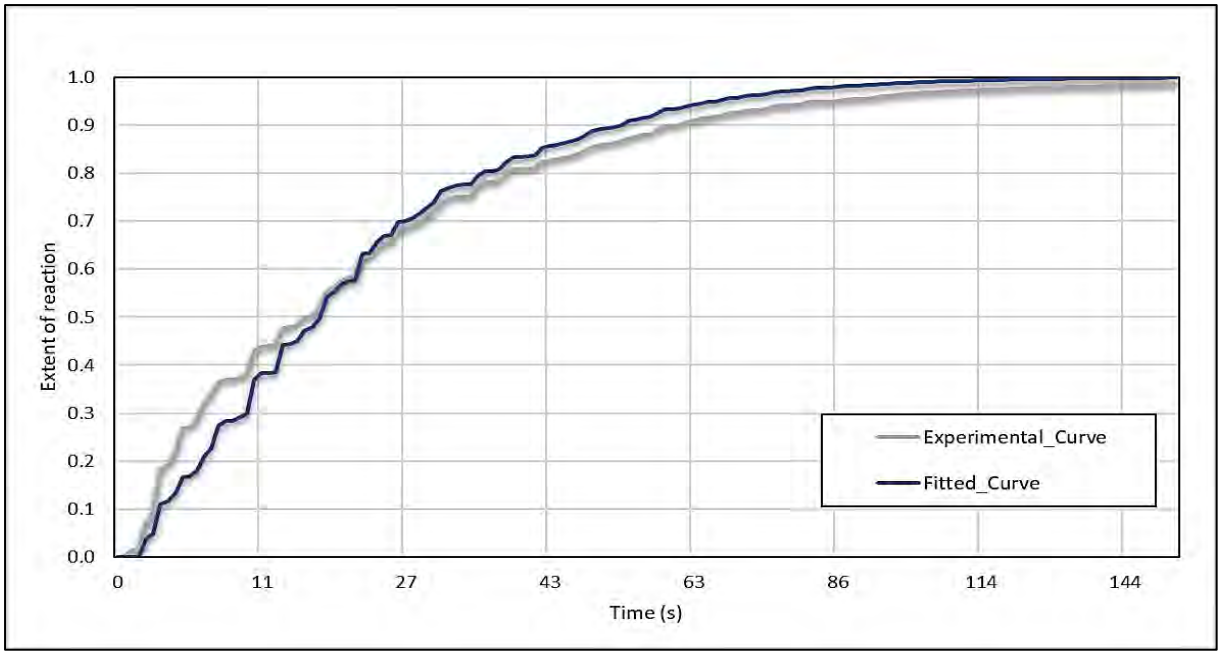

Fig. 2.4: Curve fitting results for initial temperature of 305.5 K and water vapour supply pressure of 1.3 kPa

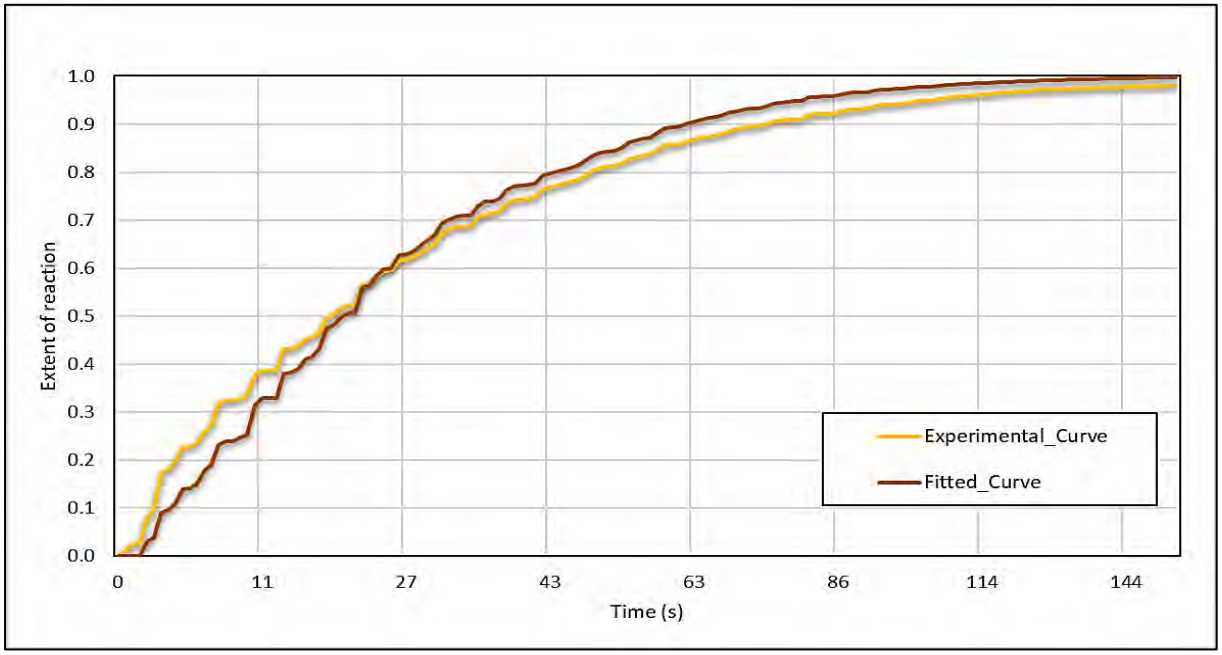

Fig. 2.5: Curve fitting results for initial temperature of 305.5 K and water vapour supply pressure of 1.15 kPa

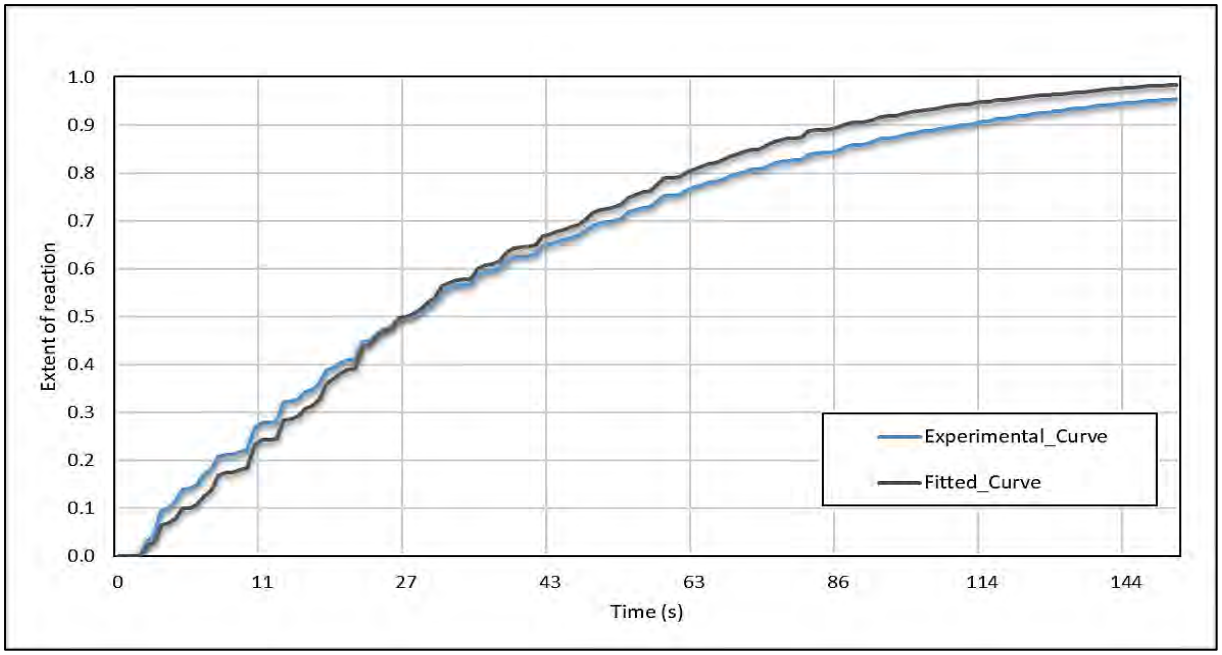

Fig. 2.6: Curve fitting results for initial temperature of 305.5 K and water vapour supply pressure of 0.93 kPa

Figs. 2.7 to 2.10 show variation of experimental curve with fitted curve using Eqn. 2.27 at temperature of 327 K and different water vapour supply pressure values. It is observed that there is no significant deviation in experimental and fitted curves.

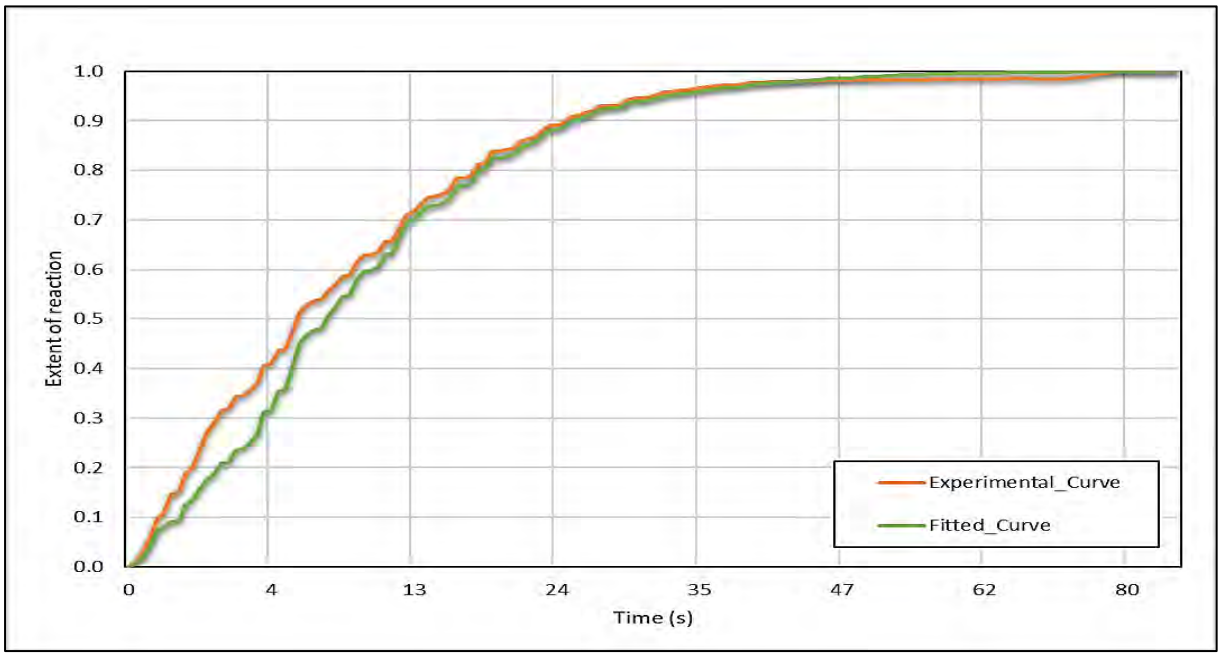

Fig. 2.7: Curve fitting results for initial temperature of 327 K and water vapour supply pressure of 3.3 kPa

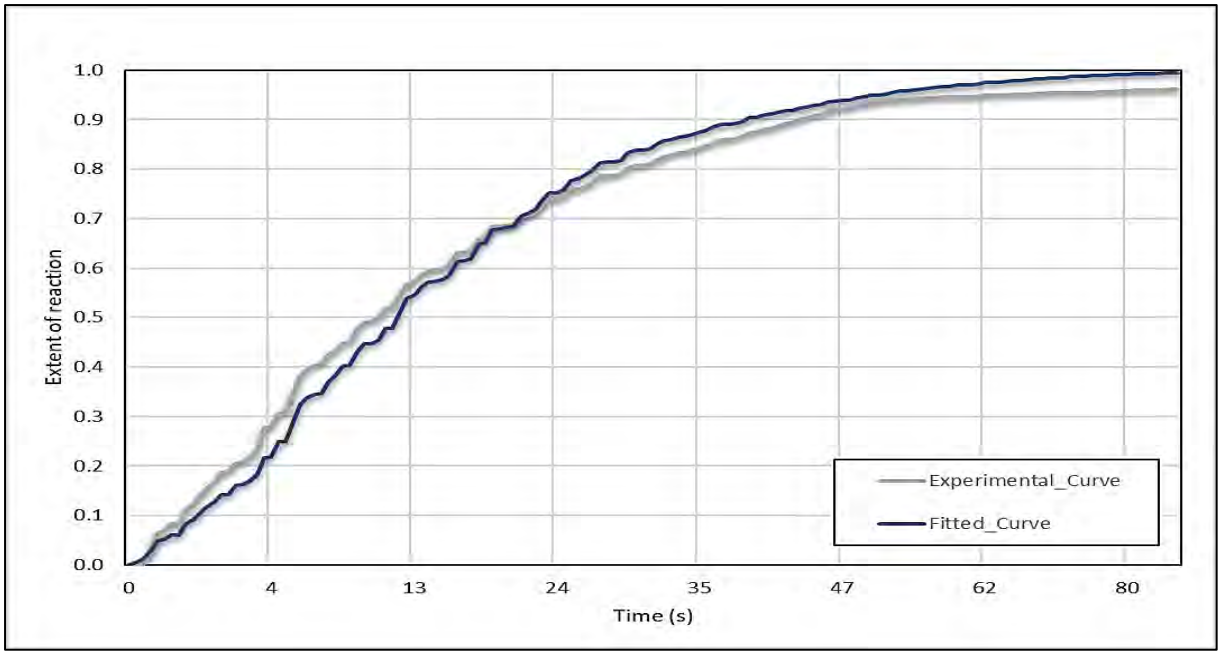

Fig. 2.8: Curve fitting results for initial temperature of 327 K and water vapour supply pressure of 2.7 kPa

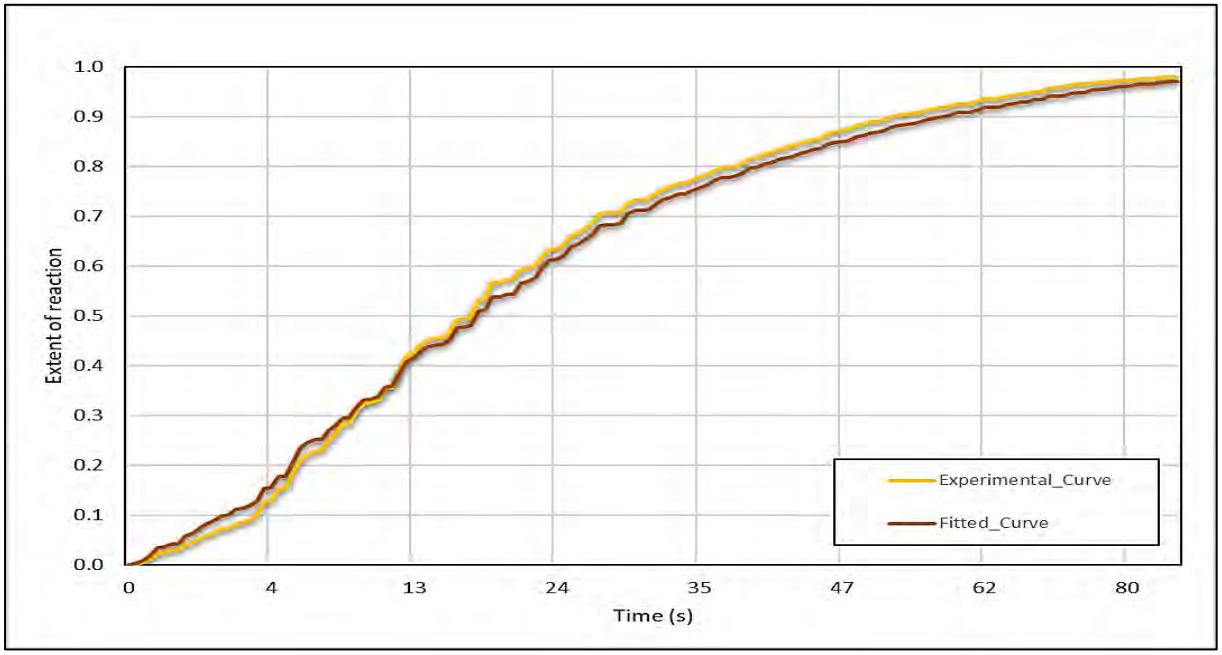

Fig. 2.9: Curve fitting results for initial temperature of 327 K and water vapour supply pressure of 2.3 kPa

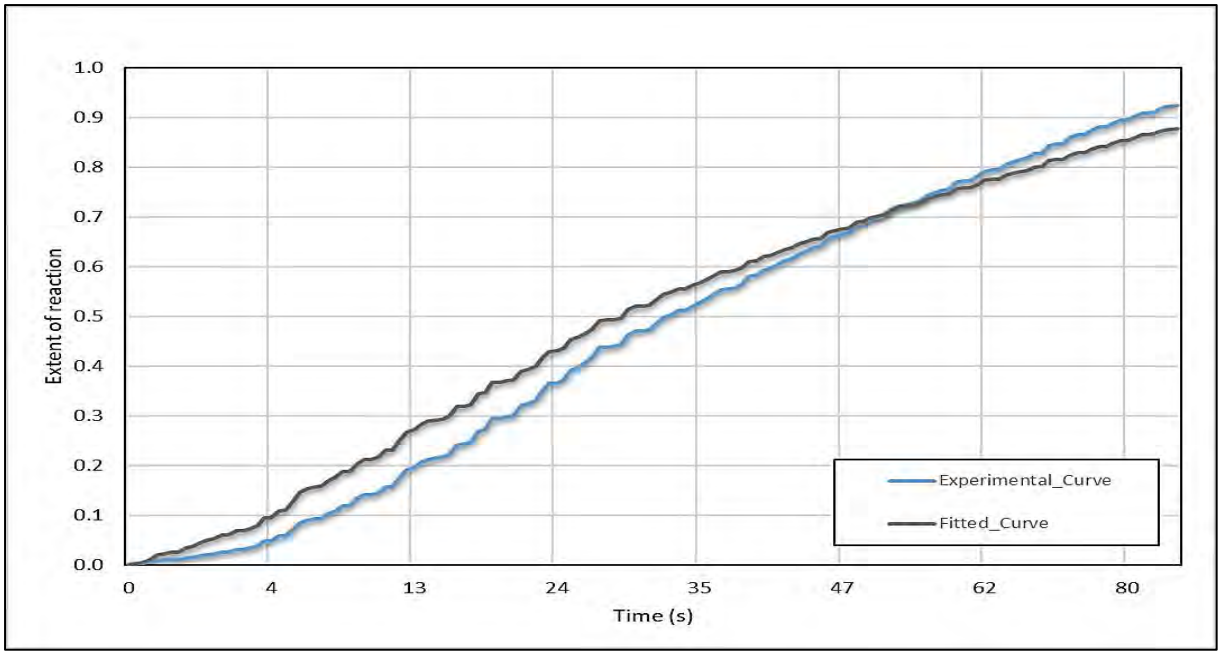

Fig. 2.10: Curve fitting results for initial temperature of 327 K and water vapour supply pressure of 1.9 kPa

But for dehydration reaction, similar experimental data are not available in literature. So, it has been decided with collaborative team to carry outstudy for other suitable TES materials. Thus, detailed literature survey of various TES materials is performed.

2.2 Literature review for suitable TES materials

For cabin heating application in HEVs, selected TES material should also satisfy following mentioned criteria:

1. The material should have high energy storage density.
2. Desirable operating temperatures and pressures.
3. Easy to handle, non-poisonous and compatible to other components.
4. It must be abundantly available with ease and eco-friendly.
5. It should have low cost for given amount of thermal energy stored.
6. The material should be thermally stable during subsequent cycling processes.

According to the kind of interaction between gas and solid, the working pairs are grouped in the category of sorption processes and chemical reactions as shown in Fig. 2.11. In sorption process, the gas is adsorbed by the solid, whereas gas-solid pair reacts chemically in chemical reactions. In comparison to the sorption working pair, the gas-solid pair undergoes chemical reactions are favourable for the storage of thermal energy due to their high enthalpy of reaction. Besides, there are certain drawbacks of gas-solid sorption pairs which are mentioned as follows:

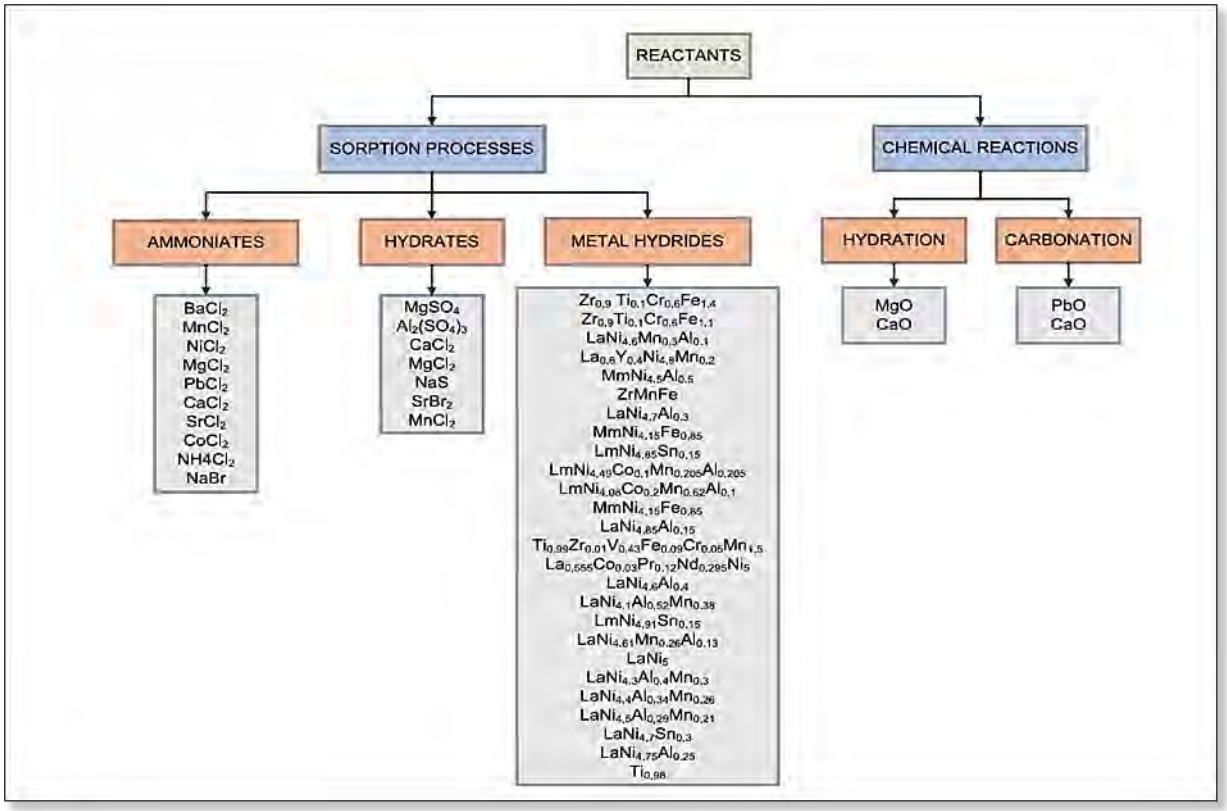

Fig. 2.11: Overview of available reaction materials [7]

1. Use of ammonia is quite risky due to its toxicity and corrosiveness.

2. Metal hydrides are reactive in nature, expensive and narrowly available.

3. A gel-like layered material is observed in hydrates due to its hygroscopic nature which hampers further adsorption.

Among the chemical reaction working pairs, extremely high temperature and pressures (1100 K and 101 kPa for $CaCO_3$) are required for carbonation reaction which are not suitable for application purpose. Thus, the favourable gas-solid pair for the storage of thermal energy is observed as water and metal oxide as the water does not pose any problem of risk, toxicity, compatibility and availability. Also, metal oxides are economical and easily available. These oxides operate at relatively lower temperature and pressure as compared to carbonation reaction (778 K and 95.6 kPa for $Ca(OH)_2$). It is further required to select the suitable hydroxides based on their thermodynamic properties for the storage of thermal energy. After studying different metal oxides, two materials namely $Mg(OH)_2$ and $Ca(OH)_2$ are the promising candidates which are further analyzed.

2.2.1 Comparison between $Mg(OH)_2$ and $Ca(OH)_2$ for TES material

A comparison between $Mg(OH)_2$ and $Ca(OH)_2$ has been made based on their thermodynamic and hydration/dehydration properties taken from the literature. Table 2.4 shows the comparison based on different parameters.

Table 2.4 Comparison between $Ca(OH)_2$ and $Mg(OH)_2$

	$Ca(OH)_2$	**$Mg(OH)_2$**	**Literature**
T_{eq} at 1 bar [K]	752 (479 ˚C)	531 (258 ˚C)	[2.7]
Enthalpy of reaction (ΔH) [kJ mol^{-1}]	109.2	81.2	[2.7]
Energy Density	615 kWh m^{-3}	465 kWh m^{-3}	[2.8]
Cyclic Repeatability	Average capacity of 95% (study up to 211 cycles)	Capacity degrades from 95% to 60% after 40 cycles (study up to 500 cycles)	[2.9]
Material cost	Lower	Higher	[2.10]

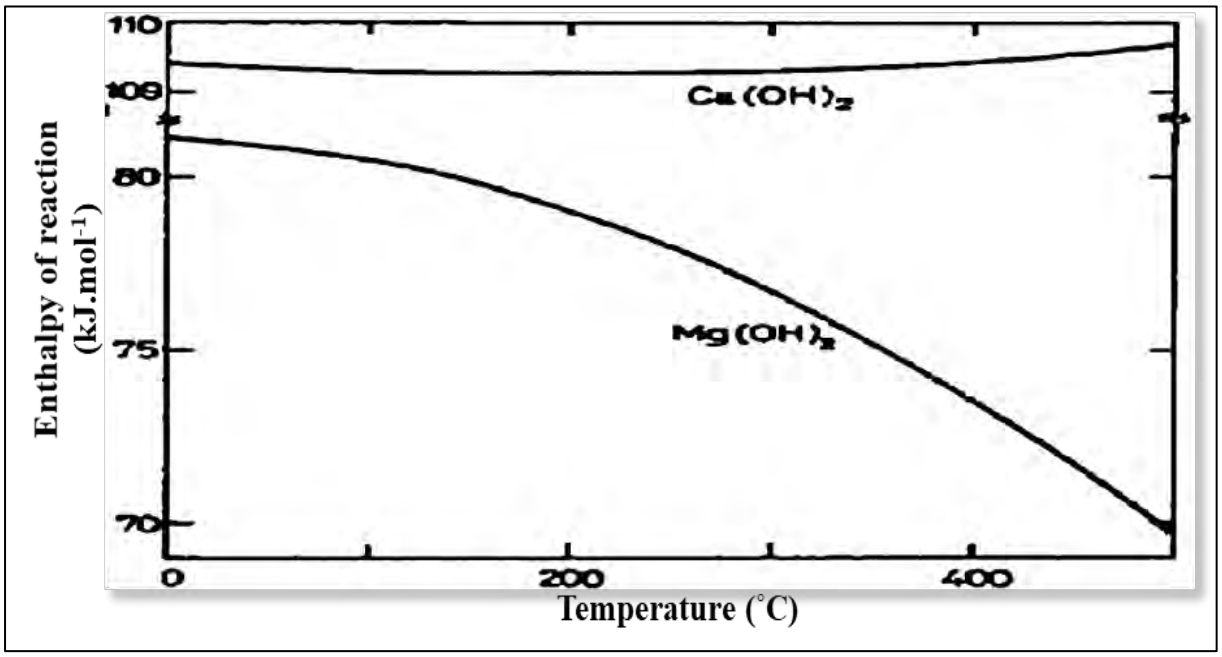

Fig. 2.12: Enthalpy of reaction of $Ca(OH)_2$ and $Mg(OH)_2$ with respect to temperature [11]

Besides, it is observed that the enthalpy of reaction of $Ca(OH)_2$ remains nearly constant with increase in temperature, whereas that of $Mg(OH)_2$ degrades with temperature as represented in Fig. 2.12.

Therefore, it is observed that $Ca(OH)_2$ is the suitable material for storage of thermal energy. A detailed study for dehydration/hydration reactions of $Ca(OH)_2$/CaO is carried out in subsequent section for the performance simulation of thermal energy storage system.

2.3 Selection of kinetic expressions and properties of dehydration/hydration of $Ca(OH)_2$/CaO

2.3.1 Selection of kinetic expressions

The various kinetic expressions for the hydration/dehydration of CaO/$Ca(OH)_2$ used in the literature are studied. As observed from the study of hydration/dehydration of CaO/$Ca(OH)_2$ that both hydration and dehydration are affected by the temperature of reactive bed, pressure of bed and steam partial pressure and by the extent of hydration/dehydration. So, the reaction rate depends upon the temperature, pressure and extent of conversion. Among several

previous works, it is observed that the kinetic expressions given by Schaube et al. [12] and Criado et al. [13] include the effects of temperature, pressure and conversion. But the expressions given by Criado et al. [13] are validated at 450 ℃ for hydration and 500 ℃ where the steam partial pressure ranges up to 100 kPa. Whereas, the kinetic expressions in the work of Schaube et al. [12] has been fitted well with the experimental results in the temperature range of 300–530 ℃ for dehydration and in the temperature range 252- 452 ℃ for hydration where the H_2O partial pressure ranges from 0 to 95.6 kPa.

So, the expressions given by Schaube et al. [12] will be used to carry out simulations.

The pressure-temperature equilibrium equation for hydration/dehydration of $CaO/Ca(OH)_2$ is

$$\ln\frac{P_{eq}}{10^5} = -\frac{12845}{T_{eq}} + 16.508 \tag{2.28}$$

Dehydration reaction rate equations:

$$Ca(OH)_{2\,(s)} \Leftrightarrow CaO_{\,(s)} + H_2O_{\,(g)},\ \Delta H = 109.2\ kJ\ mol^{-1} \tag{2.29}$$

For $X < 0.2$ the dehydration kinetics can be expressed by:

$$\frac{dX}{dt} = (1.9425 \times 10^{12}) \times \exp\left(-\frac{187.88\times10^3}{RT}\right) \times \left(1 - \frac{P}{P_{eq}}\right)^3 \times (1 - X) \tag{2.30}$$

For $X > 0.2$ the dehydration kinetics can be expressed by:

$$\frac{dX}{dt} = (8.9588 \times 10^{9}) \times \exp\left(-\frac{162.62\times10^3}{RT}\right) \times \left(1 - \frac{P}{P_{eq}}\right)^3 \times 2(1 - X)^{0.5} \tag{2.31}$$

Hydration reaction rate equations:

$$CaO_{\,(s)} + H_2O_{\,(g)} \Leftrightarrow Ca(OH)_{2\,(s)},\ \Delta H = -109.2\ kJ.mol^{-1} \tag{2.32}$$

For $T_{eq} - T \geq 50$ K the hydration kinetics is:

$$\frac{dX}{dt} = 13945 \times \exp\left(-\frac{89.486\times10^3}{RT}\right) \times \left(\frac{P}{P_{eq}} - 1\right)^{0.83} \times 3\,(1 - X)[-\ln(1 - X)]^{0.666} \tag{2.33}$$

for $T_{eq} - T < 50$ K:

$$\frac{dX}{dt} = 1.004 \times 10^{-34} \times \exp\left(\frac{53.332\times10^3}{T}\right) \times \left(\frac{P}{10^5}\right)^6 \times (1 - X),\ P > P_{eq} \tag{2.34}$$

where P, P_{eq} are in bar and T is in K.

2.3.2 Thermophysical properties of CaO and $Ca(OH)_2$

The thermophysical properties of CaO and $Ca(OH)_2$ are shown in Table 2.5 as adopted by Shao et al. [14].

Table 2.5 Thermophysical properties of $Ca(OH)_2$ and CaO [14]

Thermophysical property	**$Ca(OH)_2$**	**CaO**
Specific heat capacity	1530 J kg^{-1} K^{-1}	934 J kg^{-1} K^{-1}
Density	2200 kg m^{-3}	1656 kg m^{-3}
Thermal conductivity	0.4 W m^{-1} K^{-1}	0.4 W m^{-1} K^{-1}
Molecular weight	74 kg $kmol^{-1}$	56 kg k mol^{-1}

Water vapour properties are taken from COMSOL Multiphysics 5.4 standard material library.

CHAPTER 3

PROBLEM MODELLING

3.1 Problem solving approach

1. It is decided to start with component level analysis i.e. analysis of ESB at first then that of GSB and finally whole system level analysis is to be performed. Present study mainly focuses on analysis of ESB.

2. Since rate expressions and operating conditions are different for hydration and dehydration reaction, the study of hydration and dehydration is to be done separately. Once the influence of different operating parameters is studied, then hydration and dehydration reactions are to be studied in a single cycle.

3. A simplified 2-D model is setup to study the hydration reaction. Effects of varying different operating parameters on hydration reaction are studied. The results of 2-D hydration simulation are to be discussed and the operating parameters are to be optimized. Similar approach is to be followed to study dehydration reaction.

4. Setup of 3-D model for hydration and dehydration reaction. Simulations of 3-D model are to be done using the optimized operating conditions.

3.2 Selection of simulation software

For the present study, simulation is to be carried out in COMSOL Multiphysics 5.4 due to following advantages

1. User friendly interface.

2. Easy interlinking of different complex physical phenomena.

3. No need to write separate user defined functions (UDFs) as opposed to Fluent.

4. Since it uses FEM (Finite Element Method) based solver, computation time is significantly reduced.

5. Flexibility of importing various types of geometry files.

3.3 Selection of appropriate simulation modules for the involved physics

Table 3.1. Selection of different simulation modules

Physics involved	Related operating variables	Suitable COMSOL module
Chemical reaction	Rate of reaction, rate of different species consumption or generation, etc.	Chemistry module, Transport of diluted species in porous media module
Water vapour flow through porous medium	Velocity field variables for water vapour flow	Darcy's Law module
Heat transfer from/to ESB	Temperature field variables	Heat transfer in porous media (for both ESB and HTF) module
HTF flow through a duct in hydration reaction	Velocity and temperature field for HTF flow	Laminar flow module
EG flow through a duct in dehydration reaction	Velocity and temperature field for EG flow	Turbulent (k-ε) flow module

3.4 Detailed study of selected simulation modules

1. **Chemistry module** - This module is used for generating set of variables to be used for modelling chemical species and reaction systems. Chemistry module is 0-D module. The variables are generated from species and reaction properties and are divided in two categories:
   1.1 Rate expressions and heat sources for use in mass and heat balances
   1.2 Material property variables (like density, thermal conductivity, specific heat capacity, etc.) for use in transport equations

   Rate expressions and required thermo-physical properties are taken from section 2.3. For water vapour consumption/generation, mass sink/source term is created in the same module. Enthalpy of reaction is given as separate variable in this module. The enthalpy of reaction variable is used to calculate values of heat source/sink terms in energy balance equations.

2. **Transport of diluted species in porous media module** - This interface is dedicated to modeling transport in porous media, including immobile and mobile phases, where the chemical species may be subjected to diffusion, convection, migration, dispersion, adsorption, and volatilization in porous media. This module is used to establish the connection between Chemistry module and relevant domains.

3. **Darcy's Law module** - Darcy's law describes fluid movement through interstices in a fully saturated porous medium that is mainly driven by a pressure gradient. It can be used to model low-velocity flows or media where the permeability and porosity are very small, and for which the pressure gradient is the major driving force and the flow is mostly influenced by the frictional resistance within the pores. Thus, this module is used to simulate fluid flow through ESB.

4. **Heat transfer in porous media module** - This module is used to model heat transfer by conduction, convection and radiation in porous media. This model is valid only when temperatures in porous matrix and fluid are in equilibrium i.e. in case of local thermal equilibrium. Heat source/sink term is related to enthalpy of reaction. Same module can also be used to study heat transfer in single phase fluid flow and heat transfer in solid phase due to conduction. Thus, the same module is used to study heat transfer in ESB which is modelled as porous medium as well as to study heat transfer from ESB to HTF/from EG to ESB, respectively. Also, heat transfer through solid phase, i.e. in steel domain, is studied in the same module.

5. **Laminar flow module** - This module is used to compute the velocity and pressure fields for the flow of a single-phase fluid in the laminar flow regime. A flow remains laminar as long as the Reynolds number is below a certain critical value (2300 for fluid flow through duct). Since, HTF flow through its channel is laminar this module is selected for modelling HTF flow.

6. **Turbulent flow, k-ε module** - This module is used for simulating single-phase flows at high Reynolds numbers (higher than 2300 for fluid flow through duct). The physics interface is suitable for incompressible flows, weak compressible flows, and compressible flows at low Mach numbers (typically less than 0.3). The equations solved by the Turbulent Flow, k-ε module are the Reynolds-averaged Navier-Stokes (RANS) equations for conservation of momentum and the continuity equation for conservation of mass. Turbulence effects are modelled using the standard two-equation k-ε model with realizability constraints. The flow near walls is modelled using wall functions. It is observed that EG flow through its channel is turbulent, hence this module is selected for modelling EG flow.

3.5 Interlinking of different simulations modules

Table 3.2. Interlinking of different simulations modules

Field variable	Generated by	Linked to
Temperature field	Heat transfer in porous media module	All other modules involved
ESB pressure and water vapour velocity field	Darcy's Law module	Heat transfer in porous media module
Rate of reaction, rate of different species consumption or generation	Chemistry module	Transport of diluted species in porous media module
Rate of water vapour consumption or generation	Chemistry module	Darcy's Law module (as mass sink or source term)
Rate of heat absorption or generation due to chemical reaction	Chemistry module	Heat transfer in porous media module (as heat sink or source term)
HTF pressure and velocity field	Laminar flow module	Heat transfer in porous media module (to solve for heat transfer between ESB and HTF)
EG pressure and velocity field	Turbulent flow (k-ε) module	Heat transfer in porous media module (to solve for heat transfer between ESB and EG)

Simulation model is setup using different modules as explained in section 3.3 and 3.4. Also, selected modules are interlinked with each other as shown in Table 3.2. All modules necessarily satisfy mass and energy balance. These equations are solved simultaneously in COMSOL software with suitable solver settings. COMSOL provides suitable meshing options in predefined format, but manual meshing can also be done. For present study, extremely fine mesh size is used in 2-D simulations. This is the most refined mesh size offered in COMSOL with maximum element size of 1 mm. But for 3-D simulations, fine mesh size is used with maximum element size of 19.1 mm. Mesh selection in 3-D simulations is restricted due to system configuration on which simulations are performed. COMSOL also provides option of adaptive time steps instead of fixed time steps for simulation. In adaptive time steps, larger step size is taken for calculation to reduce the error. But in fixed time steps, solver takes equal time steps irrespective of error value. Thus, adaptive time steps give the result in short time. So, for present study adaptive time steps are used.

3.6 Operating conditions and thermophysical properties of HTF, EG and steel frame

Operating conditions for simulations as provided by Faurecia team are mentioned in Table 3.3.

Table 3.3. Operating conditions for simulations

Ambient temperature	-20 to 40 ˚C (253 K TO 313 K)
Energy to be stored in ESB	1.5 MJ
Time available for reaction	Hydration – 10 minutes, Dehydration – To be decided accordingly
Water vapour outlet/supply pressure	To be decided accordingly
Bed particle size and distribution	Initial assumption of 60% bed porosity, 2 sizes, 30-40μm & 150μm
Maximum chemical mass	< 3 kg
Maximum chemical volume	< 1.5 litre
Heat transfer fluid (HTF) temperature range	65 to 120 ˚C (338 K TO 393 K)
Heat transfer fluid (HTF) mass flow rate range	5-40 ltr min^{-1}
Exhaust gas temperature range	350 to 800 ˚C (623 K to 1073 K)
Exhaust gas mass flow rate range	100-350 kg hr^{-1}

Also, thermophysical properties of HTF, EG and steel frame which separates HTF and EG are required to perform simulations. The relevant thermophysical properties are obtained from Faurecia team which are mentioned in Table 3.4.

Table 3.4 Thermophysical properties of HTF, EG and steel

Thermophysical property	**HTF**	**EG**	**Steel (SS 1.4828)**
Specific heat capacity	3593 J kg^{-1} K^{-1}	1122 J kg^{-1} K^{-1}	500 J kg^{-1} K^{-1}
Density	1027 kg m^{-3}	0.393 kg m^{-3}	7900 kg m^{-3}
Thermal conductivity	0.4 W m^{-1} K^{-1}	0.062 W m^{-1} K^{-1}	17 W m^{-1} K^{-1}
Dynamic viscosity	1 x 10^{-3} Pa s	3.83 x 10^{-5} Pa s	N/A
Ration of specific heats (C_p/C_v)	1	1.344	N/A

3.7 Preliminary calculations

Before starting simulations, preliminary calculations are performed to understand the mass and volume requirement of ESB material for TES system.

For hydration reaction, from Eqn. 2.32,

$$CaO_{(s)} + H_2O_{(g)} \Leftrightarrow Ca(OH)_{2(s)},\ \Delta H = -109.2\ kJ\ mol^{-1}$$

Assuming full conversion, mass of CaO required for 1.5 MJ output is 0.769 kg.

Solid density of CaO is taken as 1656 kg m^{-3}.

So, the volume occupied by CaO is obtained as 4.645 x 10^{-4} m^3.

For the porosity of 60% of Energy Storage Bed (ESB), volume occupied by water vapour is 6.968 x 10^{-4} m^3 and thus, total volume of ESB is estimated as 11.613 x 10^{-4} m^3.

For the desired average power output and HTF flow rate of 1.875 kW and 5 ltr min^{-1}, respectively, the estimated rise in temperature of HTF is observed as 6.093 K.

For dehydration reaction, from Eqn. 2.29,

$$Ca(OH)_{2\,(s)} \Leftrightarrow CaO_{\,(s)} + H_2O_{\,(g)}\,,\ \Delta H = 109.2\ kJ\ mol^{-1}$$

Assuming full conversion, mass of $Ca(OH)_2$ required for 1.5 MJ storage is 1.016 kg.

Solid density of $Ca(OH)_2$ is taken as 2200 kg m^{-3}.

So, the volume occupied by $Ca(OH)_2$ is obtained as 4.618 x 10^{-4} m^3.

For the porosity of 60% of Energy Storage Bed (ESB), volume occupied by water vapour is 6.927 x 10^{-4} m^3 and thus, total volume of ESB is estimated as 11.545 x 10^{-4} m^3.

Since both hydration and dehydration occur in the same reactor chamber, the total volume of ESB required is taken as 11.613 x 10^{-4} m^3 by considering the maximum of two values obtained for hydration and dehydration.

But, the volume of ESB as provided in the design without considering fin volume is 3.741 x 10^{-4} m^3.

So, it is observed that the design volume of ESB is not sufficient to store 1.5 MJ of thermal energy with $CaO/Ca(OH)_2$. But it is decided to start the simulations with the shared ESB design. Operating conditions are revised accordingly and mentioned in subsequent sections.

CHAPTER 4

HYDRATION REACTION SIMULATIONS

As per the approach for solving the problem (explained in section 3.1), it is decided to study hydration and dehydration reaction separately in the initial stage. In this chapter, hydration reaction is studied. To start the simulations, first simplified 2-D model is setup. Effect of variation of different operating parameters on hydration reaction performance is studied by performing different parametric studies on the 2-D model. Based on discussions of 2-D parametric studies' results, operating parameters are revised which are given in subsequent sections. As per revised operating conditions, 3-D model simulations are also performed.

4.1 Assumptions for simulations of hydration reaction

1. ESB is modelled as porous medium with uniform distribution of material.
2. As hydration reaction proceeds with time, CaO gets converted into $Ca(OH)_2$. Hence solid phase of ESB is combination of CaO and $Ca(OH)_2$ depending on extent of reaction. Thus, all the required thermophysical properties of solid phase of ESB are assumed as a linear function of extent of reaction.
   For example,
   density of solid phase of ESB = X*density of $Ca(OH)_2$ + (1-X)*density of CaO
   where X is extent of reaction.
3. Average particle diameter of ESB particles and ESB porosity remains constant throughout the reaction.
4. At the start of simulation, it is assumed that only CaO and water vapour is present in ESB.
5. Water vapour is uniformly distributed throughout the ESB domain for whole reaction time.
6. At the start, ESB pressure is assumed to be equal to water vapour supply pressure. Time required for ESB pressure (which will be equal to equilibrium pressure for corresponding ESB temperature) to reach water vapour supply pressure is neglected.
7. At the start, ESB is considered to be at uniform temperature. Also, local thermal equilibrium is assumed between solid and vapour phase of ESB.
8. Water vapour supply pressure remains constant throughout the reaction.
9. The inlet temperature of HTF is constant throughout the reaction.
10. Except for water vapour inlet boundary/surface and HTF inlet and outlet boundaries/surfaces (depending on 2-D/3-D case), all other exterior boundaries are insulated.
11. For hydration reaction, initial temperature of ESB and HTF is assumed to be same.
12. Different parameters shown in plots are calculated as average values by taking integrals at appropriate locations.
    For example, in 2-D simulations, ESB average tempreture is calculated by taking surface integral of entire ESB domain. HTF average outlet temperature is calculated by taking line integral at the HTF outlet.

13. ESB particle agglomeration and degradation in material properties are not taken into account in the present study.

4.2 2-D simulations

To understand effect of different operating parameters on hydration reaction, simplified 2-D model is created and different parametric studies are performed.

4.2.1 2-D model: Geometry and operating conditions

Based on the prototype of design model of flat ESB, a simplified 2-D model is created as shown in Fig. 4.1. Energy Storage Bed (ESB) domain is modelled as porous medium. Water vapour enters ESB through boundary at the bottom. ESB domain is separated from Heat Transfer Fluid (HTF) domain by steel plate. Dimensions of 2-D model are taken from design of flat ESB and are given in Table 4.1.

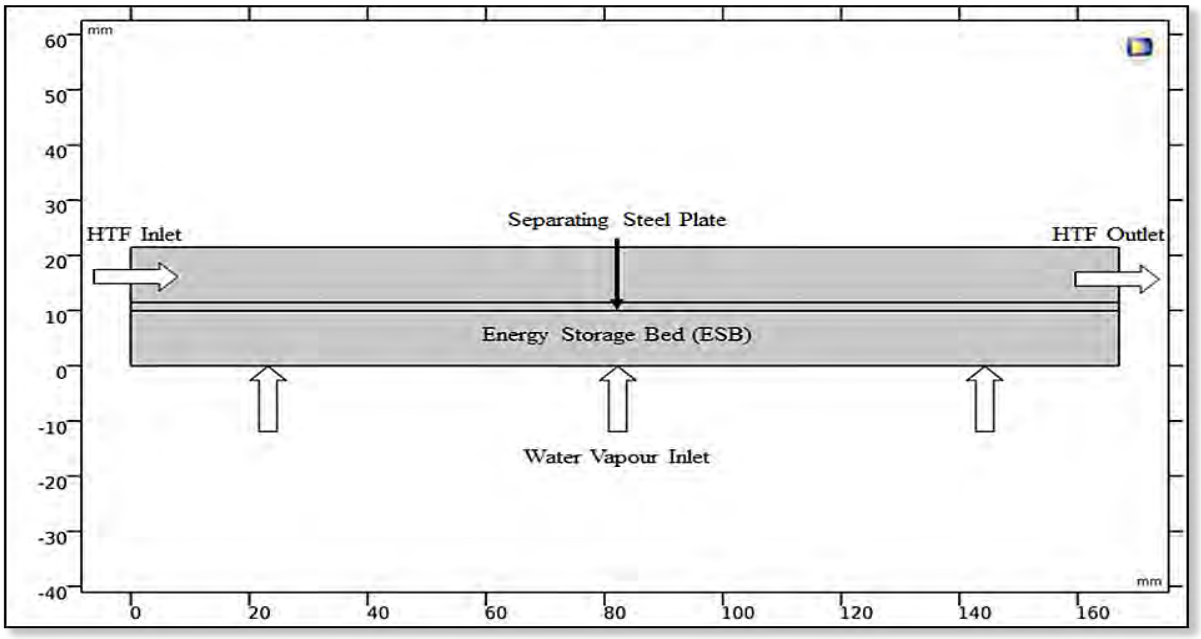

Fig. 4.1: Simplified 2-D model of ESB

Table 4.1. Dimension of 2-D model of ESB

Length of ESB domain	167 mm
Height of ESB domain	10 mm
Height of Steel Plate	1.5 mm
Height of HTF domain	10 mm

Table 4.2 gives different operating conditions for 2-D simulations provided by Faurecia team.

Table 4.2. Operating conditions for simulation

Initial temperature of ESB	Minimum 338 K (65 ˚C)
Water vapour supply pressure	To be decided accordingly
HTF inlet temperature	Minimum 338 K (65 ˚C)
HTF flow rate	5 to 40 ltr min^{-1}
ESB porosity	40 to 60 %
ESB average particle diameter	30 μm and 150 μm
Hydration reaction time	10 minutes

4.2.2 Results and discussions

To understand the effect of each of the parameter given in Table 4.2 on overall hydration reaction performance, parametric study of each parameter is carried out. Other operating conditions are kept constant while studying the effect of varying a parameter. Results of these parametric studies are presented in subsequent sections.

4.2.2.1 Variation in water vapour supply pressure

In hydration reaction, the water vapor is generated by heating the liquid water stored in GSB and is supplied to ESB. Water vapour supply pressure is equal to the saturation pressure corresponding to temperature of water in GSB. Temperature values as shown in Table 4.3 are selected for simulation.

Table 4.3. Water vapour supply pressure values for simulation

Temperature of water vapour in GSB (˚C)	Temperature of water vapour in GSB (K)	Corresponding saturation pressure (kPa)
25	298	3.14
35	308	5.58
45	318	9.52
60	333	19.81
80	353	47.13
100	373	100.88
120	393	197.73

The other operating conditions are considered constant and shown in Table 4.4.

Table 4.4. Other operating conditions for simulation

Initial temperature of ESB	338 K (65 ˚C)
HTF inlet temperature	338 K (65 ˚C)
HTF flow rate	10 ltr min^{-1}
ESB porosity	60 %
ESB average particle diameter	30 μm
Hydration reaction time	800 s

Based on above operating conditions simulations are performed and following results are obtained.

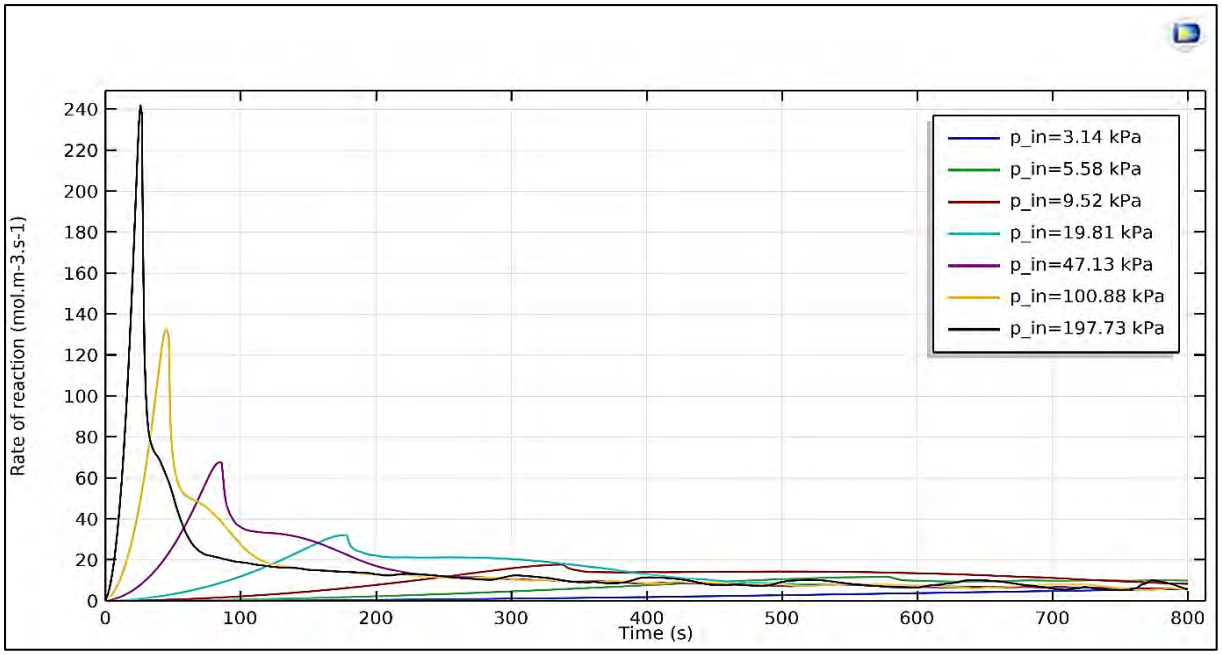

Fig. 4.2: Average rate of reaction variation

At the start of the hydration reaction, free reactive sites of reactant, i.e. CaO, are available in large quantity which results in higher rate of reaction and consequently higher consumption of water vapour. At the later stage of hydration, the reaction rate slows down due to scarcity of active sites of reactant, as shown in Figs. 4.2 and 4.3.

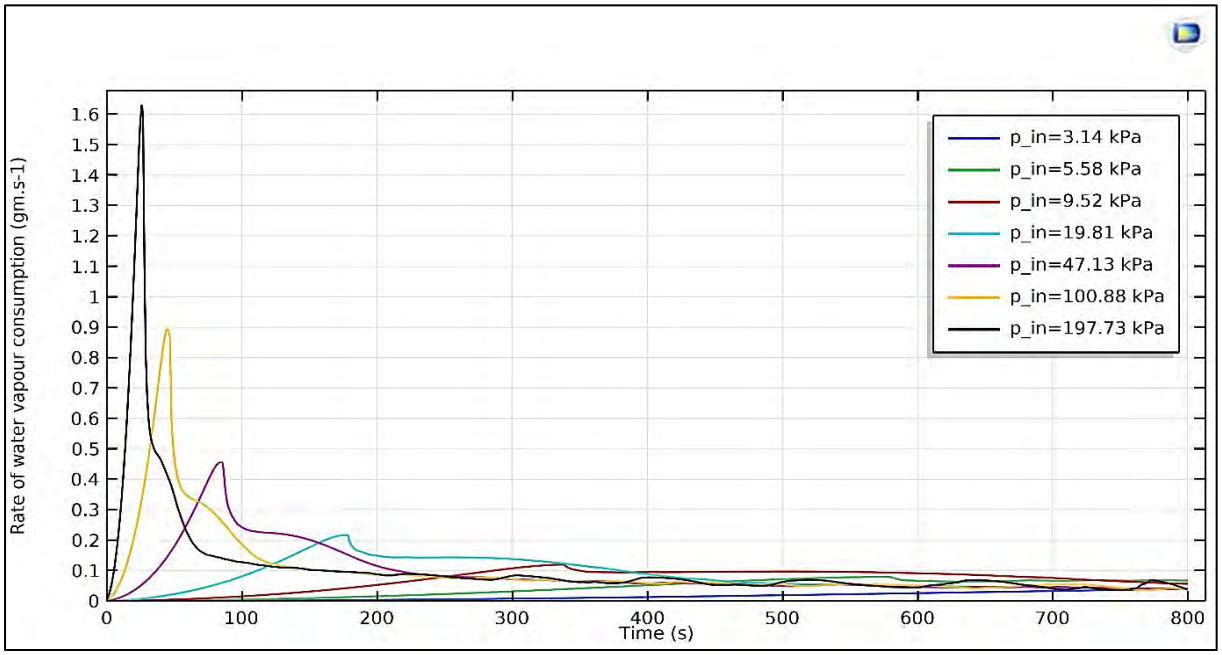

Fig. 4.3: Average rate of water vapour consumption variation

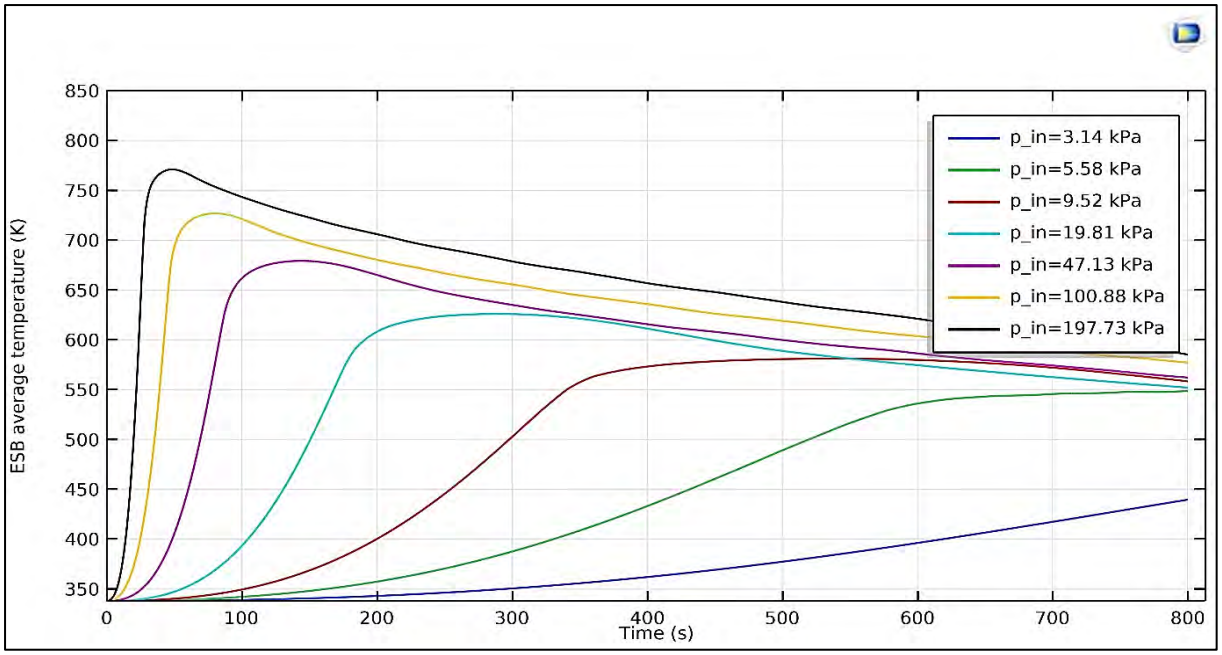

Fig. 4.4: ESB average temperature variation

ESB average temperature increases rapidly at the start of hydration as reaction rates are higher. But as reaction rate slows down, corresponding change in ESB average temperature is lower due to low thermal conductivity as shown in Fig. 4.4. From Figs. 4.4 and 4.5, it is observed that higher the water vapour supply pressure (p_in), higher is the rise in ESB average temperature and HTF average outlet temperature.

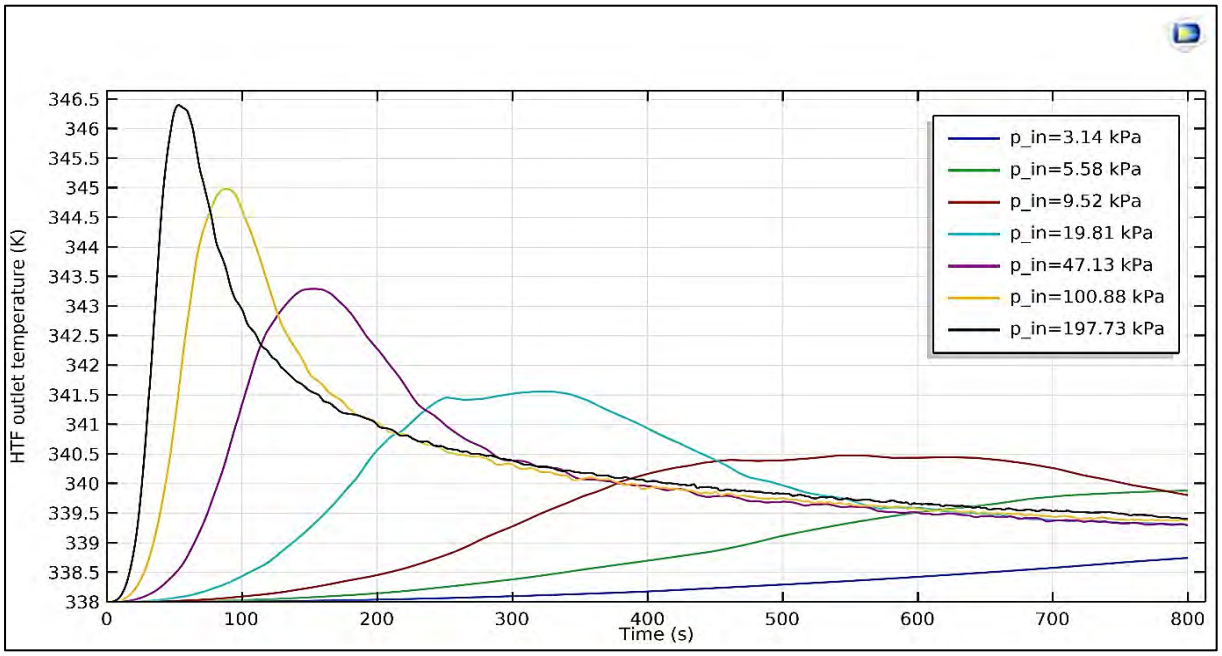

Fig. 4.5: HTF average outlet temperature variation

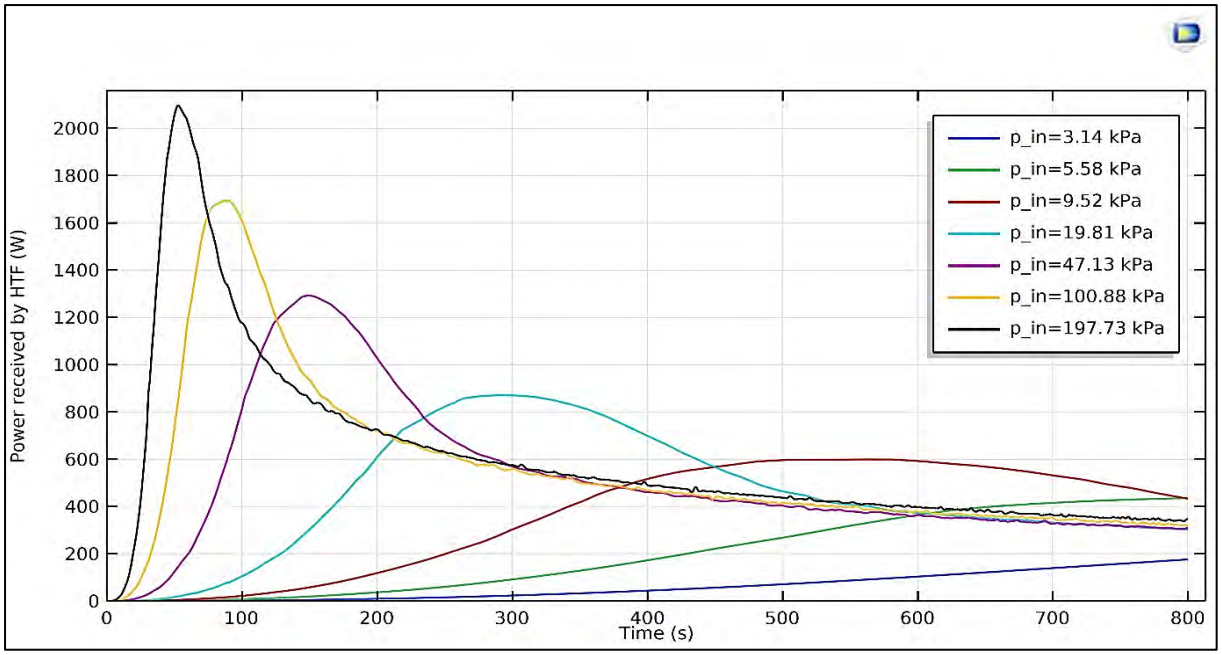

Fig. 4.6: Average power received by HTF variation

According to Fig. 4.6 and Table 4.5, the energy received by HTF is higher for higher supply pressure values. So, it is desirable to have supply pressure as high as possible. Table 4.5

Table 4.5. Effect of water vapour supply pressure on energy received by HTF

Temperature of water vapour in GSB (˚C)	Saturation Pressure (kPa)	Total energy received by HTF (kJ) (Target = 500 kJ)	Total energy for sensible heating (kJ)	Total energy output from ESB (kJ)	Efficiency of energy transfer from ESB to HTF (%)
25	3.14	47.84	27.35	75.19	63.62
35	5.58	139.73	71.47	211.20	66.16
45	9.52	254.89	86.80	341.69	74.59
60	19.81	307.42	90.73	398.15	77.21
80	47.13	339.34	103.11	442.45	76.69
100	100.88	365.70	117.95	483.65	75.61
120	197.73	393.32	128.48	521.80	75.38

Table 4.6. Effect of water vapour supply pressure on HTF average outlet temperature

Temperature of water vapour in GSB (˚C)	Saturation Pressure (kPa)	HTF average outlet temperature (K) after 800 sec	HTF temperature rise (K) after 800 sec	HTF average temperature rise (K) (Target = 3.052 K)
25	3.14	338.75	0.75	0.25
35	5.58	339.88	1.88	0.82
45	9.52	339.81	1.81	1.51
60	19.81	339.30	1.30	1.88
80	47.13	339.29	1.29	2.14
100	100.88	339.38	1.38	2.34
120	197.73	339.40	1.40	2.51

Table 4.7. Effect of water vapour supply pressure on average reaction rate and average water vapour consumption rate

Temperature of water vapour in GSB (˚C)	Saturation Pressure (kPa)	Average rate of reaction (mol m^{-3} s^{-1})	Average rate of water vapour consumption (g s^{-1})
25	3.14	2.30	0.015
35	5.58	6.46	0.044
45	9.52	10.46	0.070
60	19.81	12.18	0.082
80	47.13	13.54	0.091
100	100.88	14.80	0.100
120	197.73	15.97	0.108

From Table 4.7 it is observed that as the water vapour supply pressure increases (p_in), average rate of reaction increases and consequently, energy received by HTF also increases. But the efficiency of energy transfer from ESB to HTF increases initially with maximum value around 60 – 80 ˚C and then gradually decreases as observed in Table 4.5. So, water vapour supply pressure of 47.13 kPa (saturation pressure corresponding to 80 ˚C) is finally selected for further simulations.

4.2.2.2 Variation in initial ESB temperature

To check the effect of initial ESB temperature, the three values are chosen according to the HTF temperature range as mentioned in the Table 3.3. The study is carried out by increasing the initial ESB temperature (T_ini) keeping HTF inlet temperature at constant value of 338 K.

Table 4.8. Initial ESB temperature values for simulation

Initial ESB temperature (˚C)	Initial ESB temperature (K)
65	338
85	358
105	378

The other operating conditions are considered constant and shown in Table 4.9.

Table 4.9. Other operating conditions for simulation

Water vapour supply pressure	9.52 kPa
HTF inlet temperature	338 K (65 ˚C)
HTF flow rate	10 ltr min^{-1}
ESB porosity	60 %
ESB average particle diameter	30 μm
Hydration reaction time	800 s

Based on above operating conditions simulations are performed and following results are obtained.

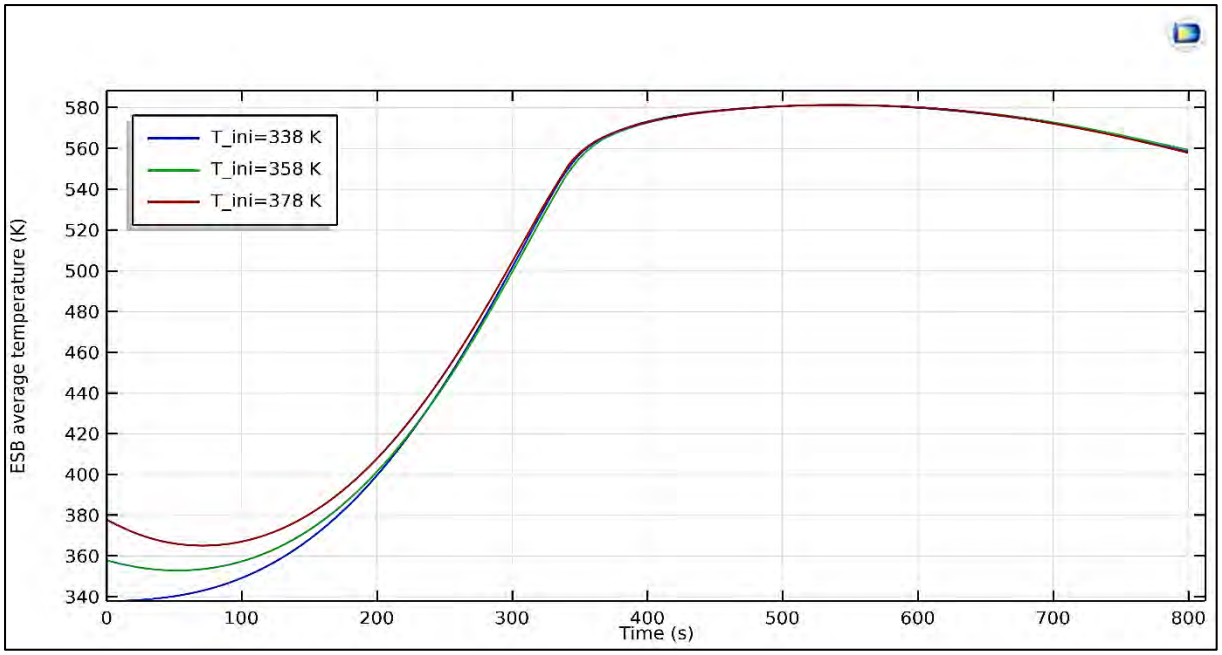

Fig. 4.7: ESB average temperature variation

The effect of different initial temperature of ESB on the ESB average temperature during hydration is shown in Figs. 4.7. It is observed that there is no significant impact of changing initial ESB temperature in ESB average temperature variation.

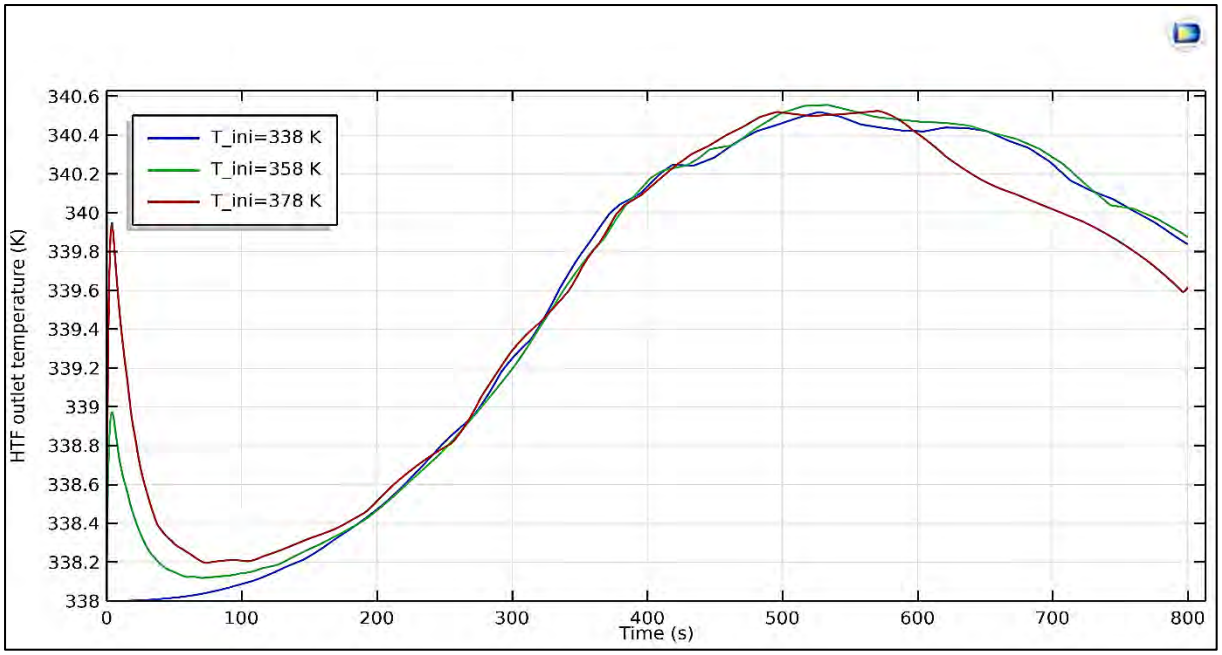

Fig. 4.8: HTF average outlet temperature variation

Table 4.10. Effect of initial ESB temperature variation on HTF average outlet temperature

Initial ESB temperature (K)	HTF average outlet temperature (K) after 800 sec	HTF average temperature rise (K) after 800 sec	HTF average temperature rise (K) (Target = 3.052 K)
338	339.84	1.84	1.93
358	339.88	1.88	1.97
378	339.62	1.62	1.96

The effect of different initial temperature of ESB on the HTF outlet average temperature during hydration is shown in Figs. 4.8. In this case also, it is observed that there is no significant impact of changing initial ESB temperature in HTF outlet average temperature variation.

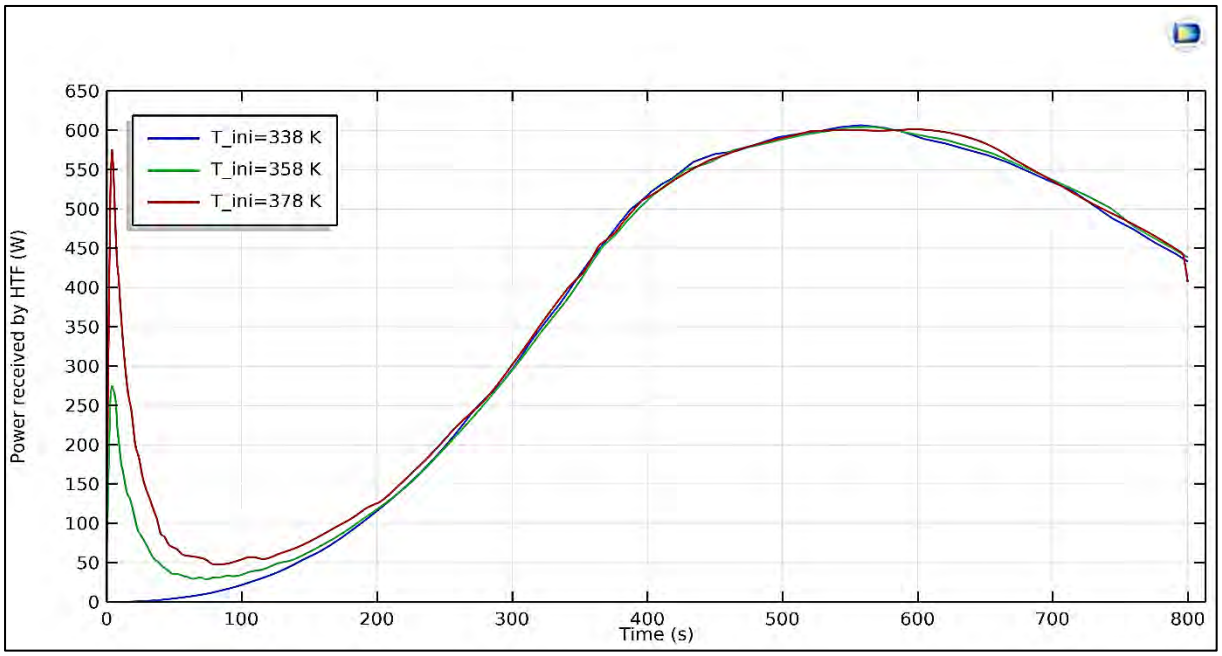

Fig. 4.9: Average power received by HTF variation

Table 4.11. Effect of initial ESB temperature variation on energy received by HTF

Initial ESB temperature (K)	Total energy received by HTF (kJ) (Target = 500 kJ)	Total energy for sensible heating (kJ)	Total energy output from ESB (kJ)	Efficiency of energy transfer from ESB to HTF (%)
338	254.52	86.74	341.26	74.58
358	260.44	78.55	338.99	76.83
378	268.39	69.56	337.95	79.42

But for the overall range of initial ESB temperature considered, it is observed that there is no significant impact of increasing the initial ESB temperature on overall reaction performance as shown in Table 4.10 and 4.11.

4.2.2.3 Variation in HTF mass flow rate

The different values of mass flow rate are chosen according to the mass flow range mentioned in the Table 3.3.

Table 4.12. HTF mass flow rate values for simulation

Volume flow rate (ltr min^{-1})	Mass flow rate (kg s^{-1})
1.25	0.0214
2.5	0.0428
5	0.0856
10	0.171
15	0.257

The other operating conditions are considered constant and shown in Table 4.13

Table 4.13. Other operating conditions for simulation

Initial ESB temperature (K)	338 K (65 ˚C)
Water vapour supply pressure	9.52 kPa
HTF inlet temperature	338 K (65 ˚C)
ESB porosity	60 %
ESB average particle diameter	30 μm
Hydration reaction time	800 s

Based on above operating conditions simulations are performed and following results are obtained.

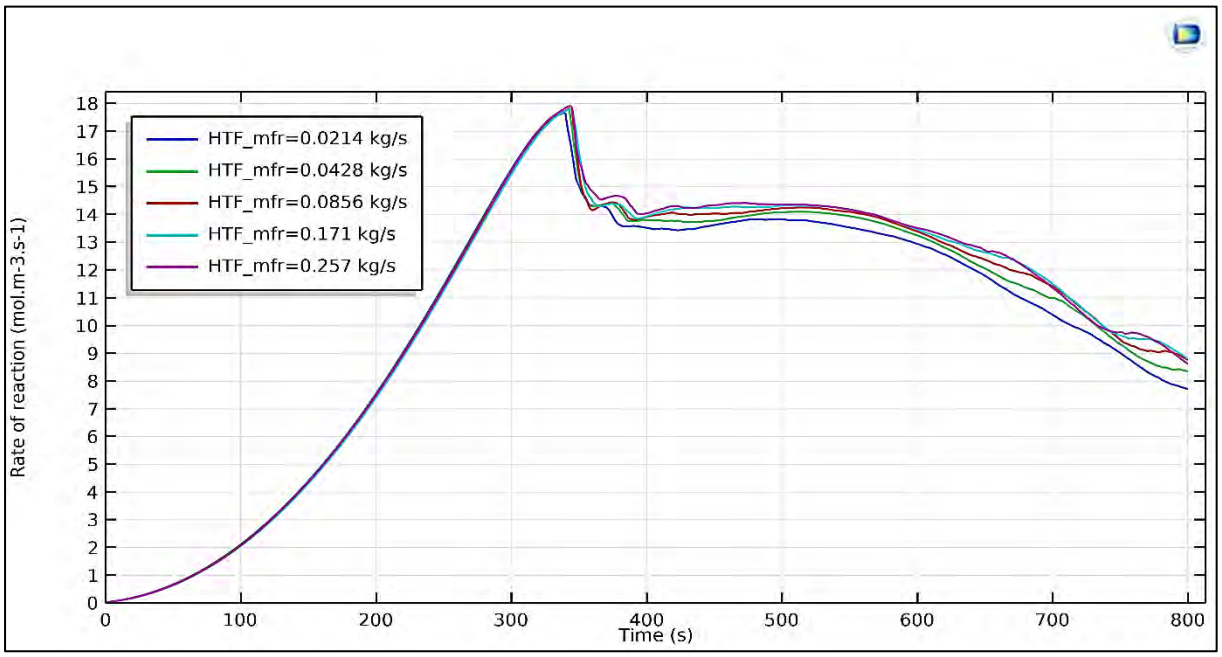

Fig. 4.10: Average rate of reaction variation

From Fig. 4.10 it is observed that there is no significant variation in average rate of reaction with respect to increase mass flow rate. Consequently, there is no significant variation in ESB average temperature as shown in Fig. 4.11.

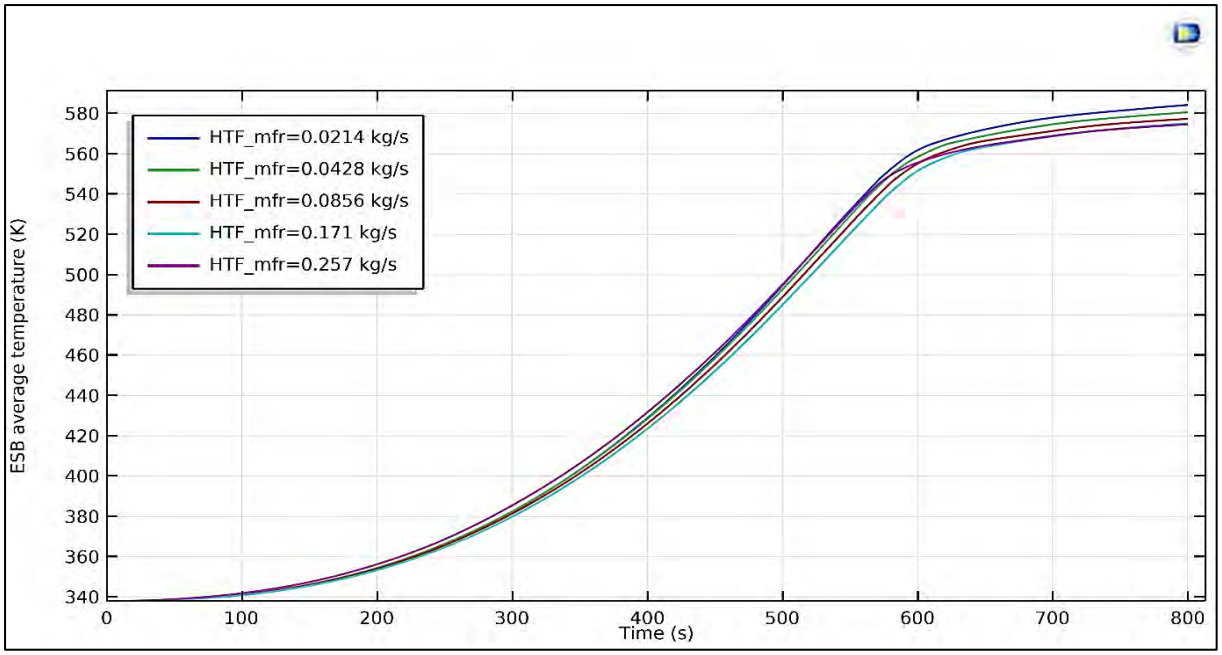

Fig. 4.11: ESB average temperature variation

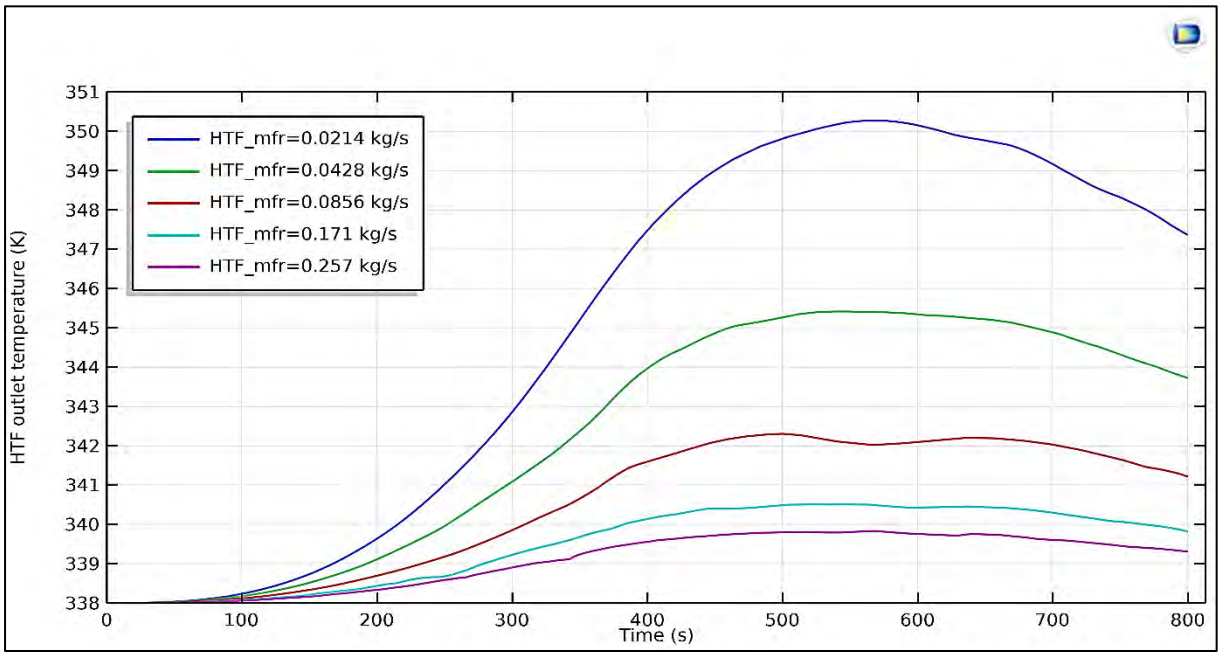

Fig. 4.12: HTF average outlet temperature variation

As mean flow velocity increases, available contact time between ESB and HTF decreases. Hence, the change in HTF average outlet temperature decreases as shown in Fig. 4.12. Table 4.14 also shows similar trend in HTF average outlet temperature.

Table 4.14. Effect of HTF mass flow rate variation on HTF average outlet temperature

Mass flow rate (kg s^{-1})	HTF average outlet temperature (K) after 800 sec	HTF temperature rise (K) after 800 sec	Average HTF temperature rise (K) (Target = 3.052 K)
0.0214	347.36	9.36	7.02
0.0428	343.72	5.72	4.34
0.0856	341.22	3.22	2.53
0.171	339.82	1.82	1.50
0.257	339.31	0.31	1.09

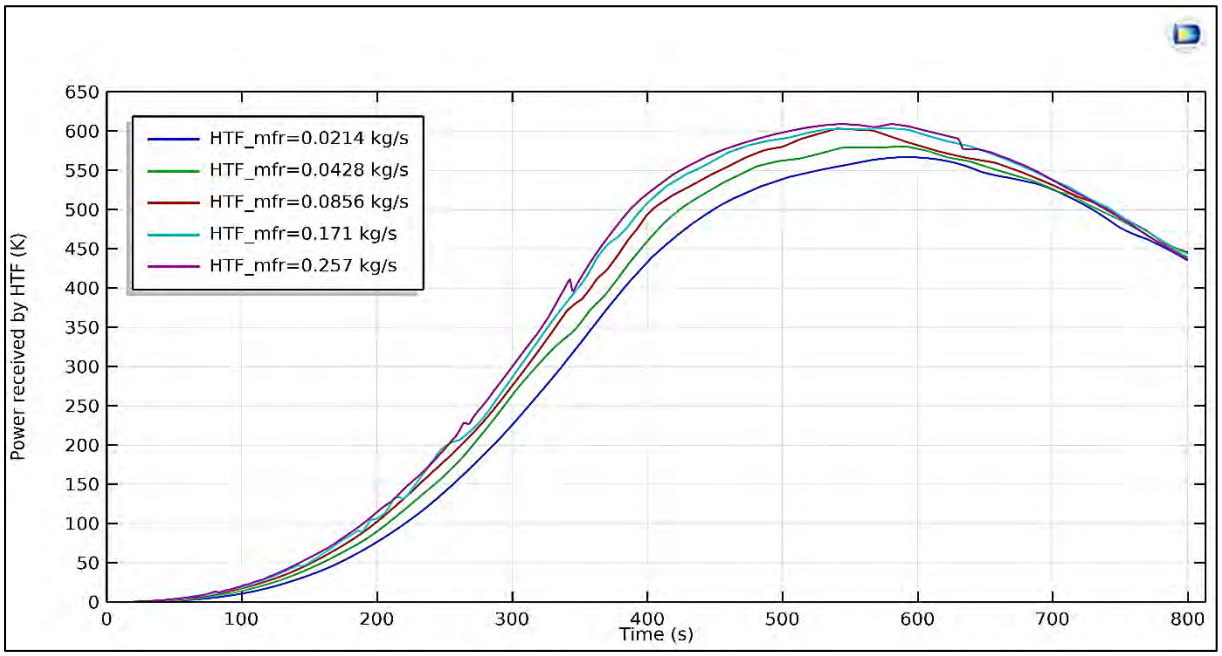

Fig. 4.13: Average power received by HTF variation

Fig. 4.13 shows variation of average power received by HTF variation. It is observed that for higher value of HTF mass flow rate, average power received by HTF is slightly higher.

Table 4.15. Effect of HTF mass flow rate variation on energy received by HTF

Mass flow rate (kg s^{-1})	Total energy received by HTF (kJ) (Target = 500 kJ)	Total energy for sensible heating (kJ)	Total energy output from ESB (kJ)	Efficiency of energy transfer from ESB to HTF (%)
0.0214	0.0214	237.38	89.75	327.13
0.0428	0.0428	244.18	89.07	333.25
0.0856	0.0856	249.07	88.26	337.33
0.171	0.171	251.74	87.44	339.18
0.257	0.257	254.03	86.89	340.92

Since flow is incompressible, with increase in the HTF mass flow rate (HTF_mfr), mean flow velocity increases. This gives higher value of heat transfer coefficients between ESB and HTF. Thus, total energy received by HTF slightly increases as shown in Table 4.15. So, it is

required to choose the optimum value of HTF mass flow rate to attain the highest possible temperature rise and maximum energy carried away by HTF.

Due to design constraints, HTF mass flow rate is fixed at 10 ltr min^{-1} for further simulations.

4.2.2.4 Variation in ESB permeability

Based on the operating conditions provided in Table 3.3, the particle size of ESB material is selected as 30 and 150 μm. The porosity values of ESB are chosen as 40% and 60% . Based on these parameters, ESB permeability values are calculated using Eqn 4.1 as shown in Table 4.16. The permeability of ESB is calculated by using Ergen's formula, where d is average particle diameter and φ is ESB porosity.

$$K = \frac{d^2 \varphi^3}{150(1-\varphi)^2} \quad (4.1)$$

Table 4.16. ESB permeability values for simulation

ESB porosity	ESB average particle diameter (μm)	ESB permeability (m^2)
0.4	30	1.07×10^{-12}
0.4	150	2.67×10^{-11}
0.6	30	8.1×10^{-12}
0.6	150	2.02×10^{-10}

The other operating conditions are considered constant and shown in Table 4.17.

Table 4.17. Other boundary conditions for simulation

Initial ESB temperature (K)	338 K (65 ˚C)
Water vapour supply pressure	9.52 kPa
HTF inlet temperature	338 K (65 ˚C)
Hydration reaction time	800 s
HTF flow rate	10 ltr min^{-1}

Based on above operating conditions simulations are performed and following results are obtained.

Permeability is defined as ease with which fluid (water vapour) can flow through porous medium (ESB). From Eqn. 4.1 it is observed that as ESB porosity or ESB average particle diameter is increased, ESB permeability would increase. As ESB permeability increases, resistance to water vapour flow through ESB domain decreases which results in higher reaction rate and consequently higher temperature rise.

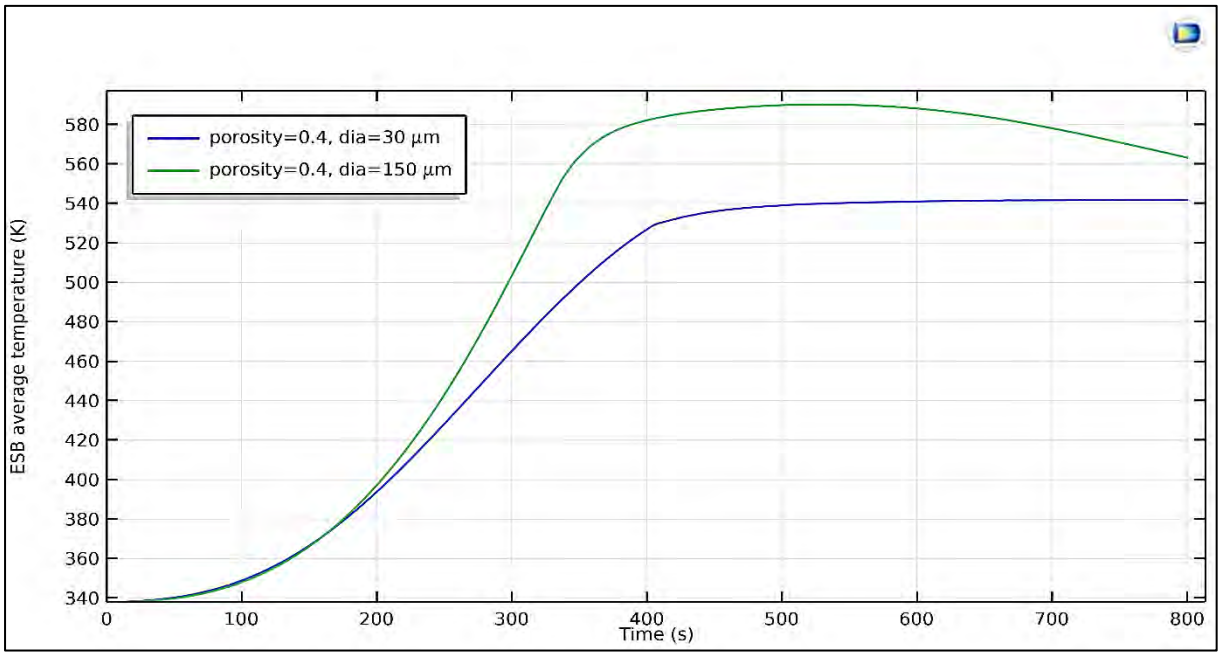

Fig. 4.14: ESB average temperature variation for different particle sizes with porosity of 0.4

For 40% porosity of ESB, there is significant variation in ESB average temperature for different particle sizes as observed in Fig. 4.14. But for 60% porosity of ESB, the variation in ESB average temperature is low as shown in Fig. 4.15.

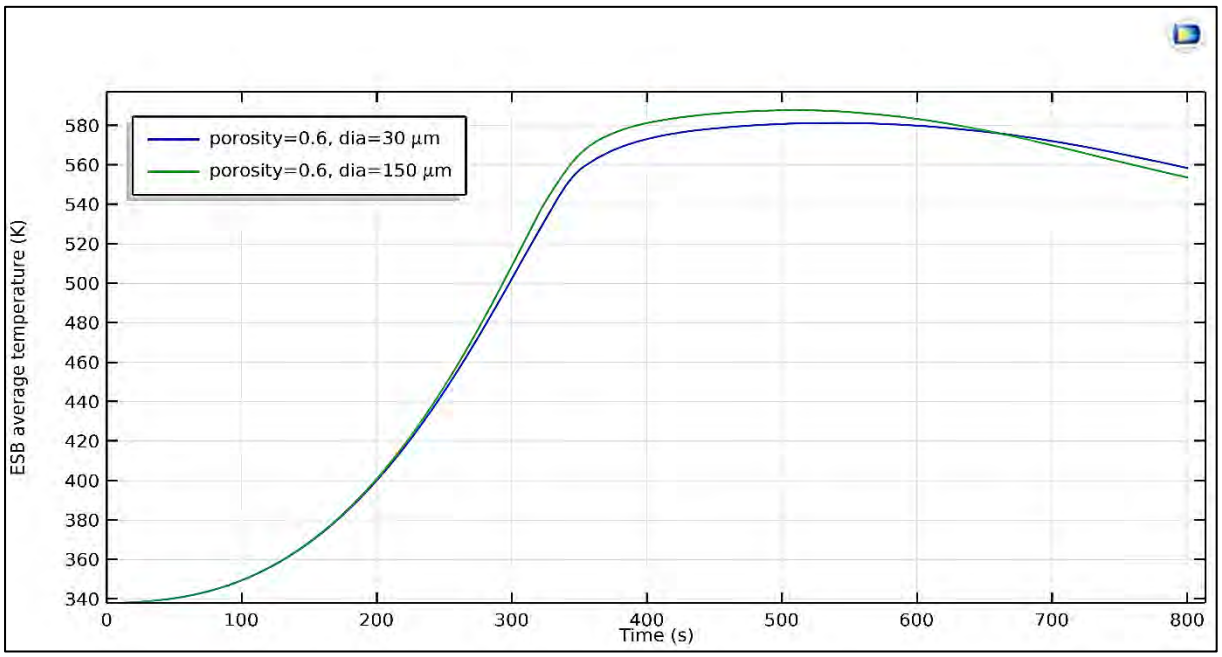

Fig. 4.15: ESB average temperature variation for different particle sizes with porosity of 0.6

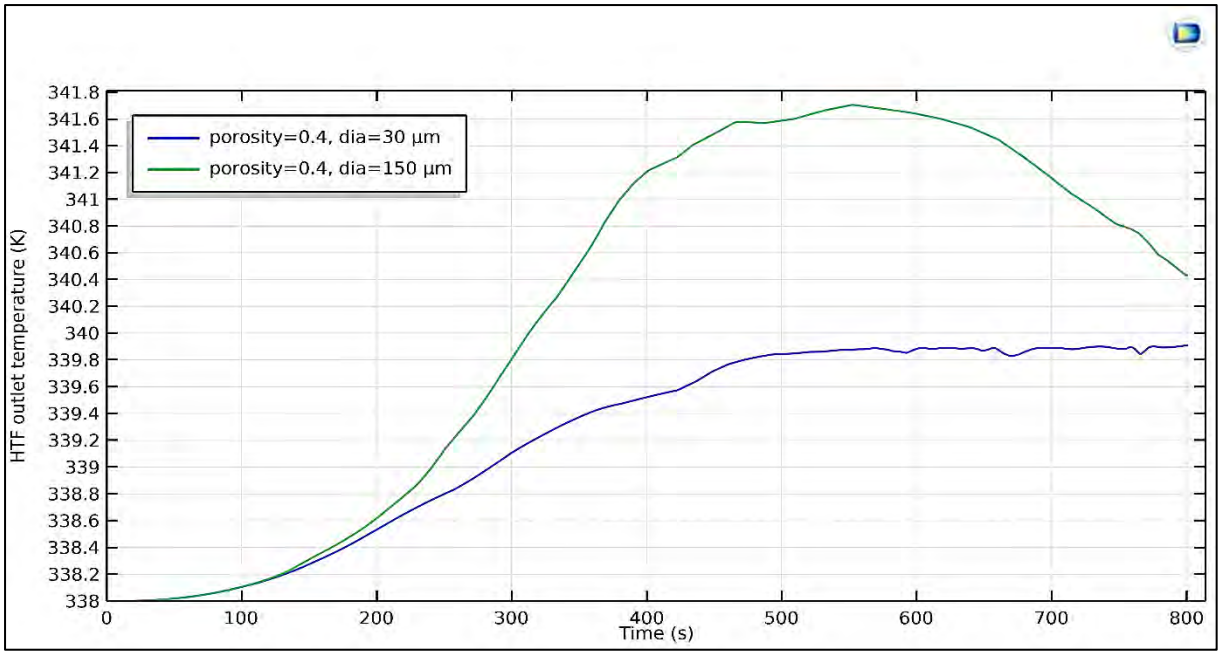

Fig. 4.16: HTF average outlet temperature variation for different particle sizes with porosity of 0.4

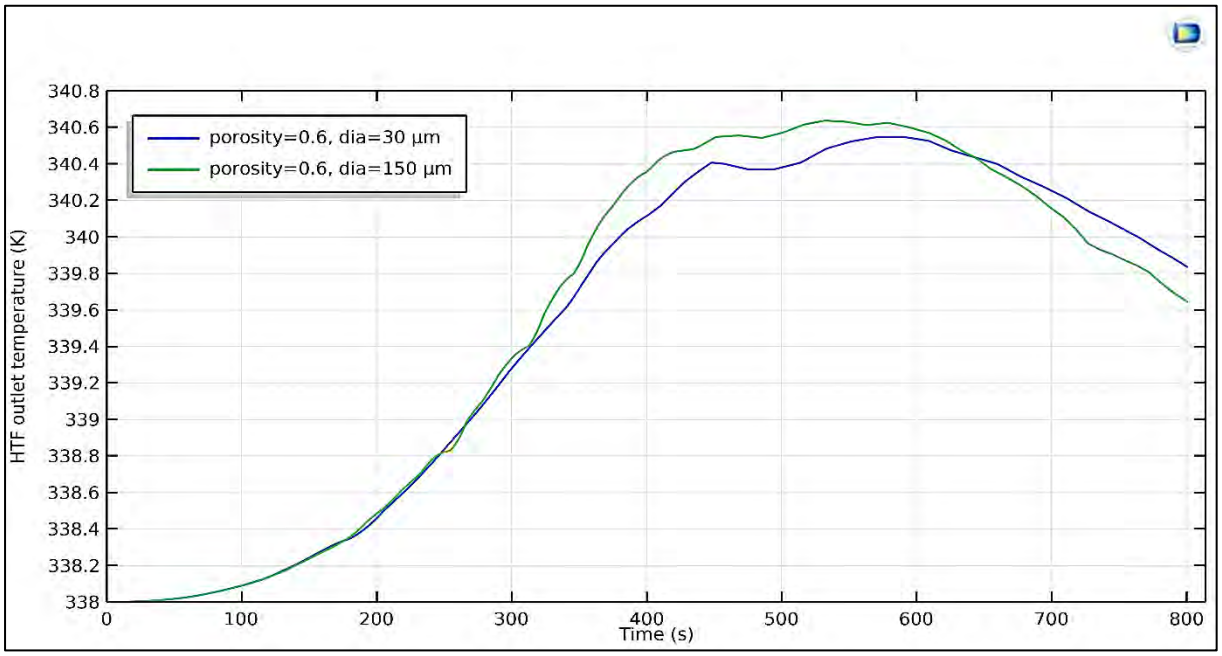

Fig. 4.17: HTF average outlet temperature variation for different particle sizes with porosity of 0.6

Similar variation is observed in case of HTF average outlet temperature as shown in Figs. 4.16 and 4.17. From obtained results, it can also be concluded that larger particle size gives higher temperature rise for the same value of porosity.

Table 4.18. Effect of ESB permeability variation on HTF average outlet temperature

ESB porosity	Average particle diameter (μm)	Initial mass of CaO in ESB (kg)	HTF average outlet temperature (K) after 800 sec	HTF average temperature rise (K) after 800 sec	HTF average temperature rise (K) (Target = 3.052 K)
0.4	30	0.384	339.91	1.91	1.66
0.4	150	0.384	340.43	2.43	2.62
0.6	30	0.256	339.83	1.83	1.94
0.6	150	0.256	339.64	1.64	1.98

Table 4.19. Effect of ESB permeability variation on energy received by HTF

ESB porosity	Average particle diameter (μm)	Initial mass of CaO in ESB (kg)	Total energy received by HTF (kJ) (Target = 500 kJ)	Total energy for sensible heating (kJ)	Total energy output from ESB (kJ)	Efficiency of energy transfer from ESB to HTF (%)
0.4	30	0.384	196.76	108.48	305.24	64.46
0.4	150	0.384	363.92	129.88	493.80	73.70
0.6	30	0.256	255.35	86.80	342.15	74.63
0.6	150	0.256	261.73	84.66	346.39	75.56

Tables 4.18 and 4.19 show the effect of HTF mass flow rate variation on HTF average outlet temperature and energy received by HTF, respectively. As porosity of ESB decreases, initial mass of CaO (reactant) increases, hence it results in higher energy output from ESB. Thus, it is decided to take 0.4 as porosity of ESB and 150 μm as average particle diameter for further simulations.

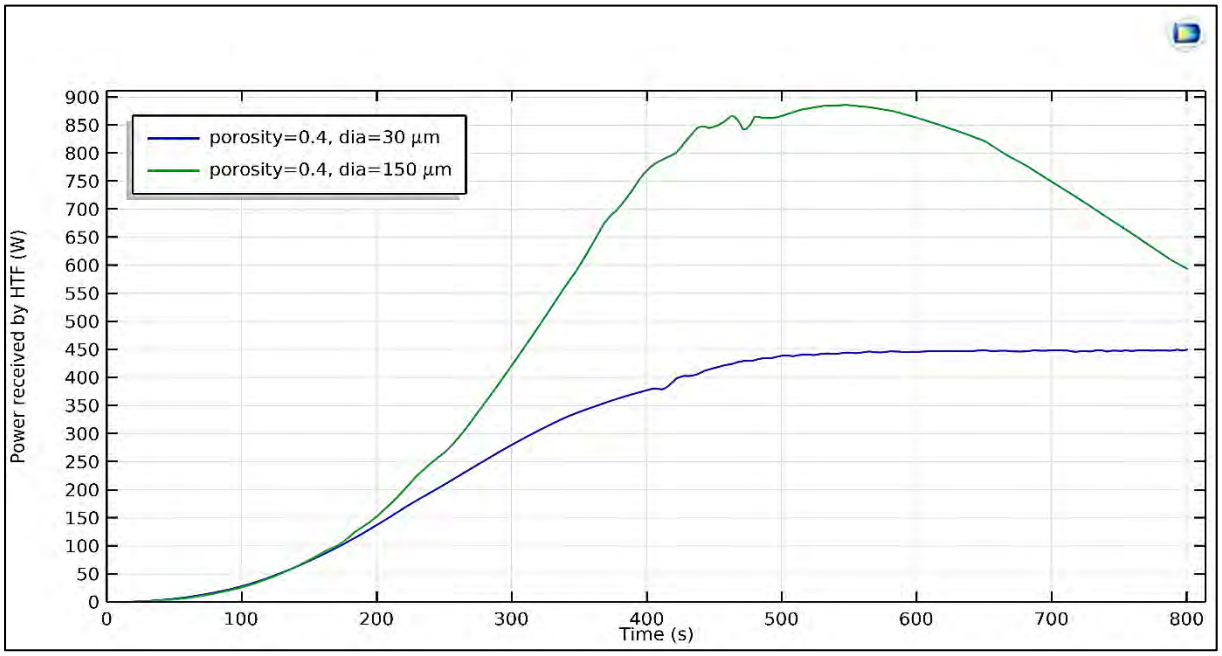

Fig. 4.18: Average power received by HTF variation for different particle sizes with porosity of 0.4

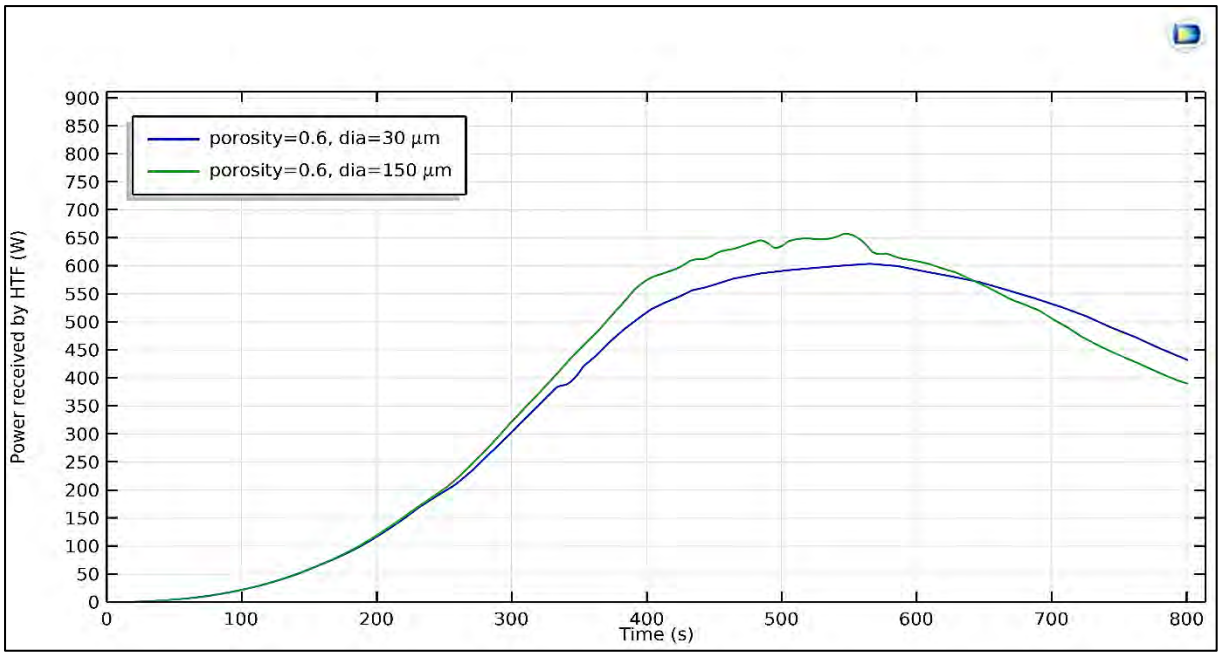

Fig. 4.19: Average power received by HTF variation for different particle sizes with porosity of 0.6

Figs. 4.18 and 4.19 show average power received by HTF variation for different particle sizes with porosity of 0.4 and 0.6, respectively. These plots also show similar trend as that of ESB average temperature and HTF average outlet temperature,

For the various values of particle size, only the change in permeability value is considered. The effect of particle size variation in the rate expressions for hydration is not accounted. But in actual practice, as the porosity and resistance to vapour flow through ESB change with particle size. Thus, a separate study is to be carried out to examine the effect of particle size variation on performance of ESB.

4.2.2.5 Variation in time of hydration reaction

For the previous simulations, time of reaction was taken to be 800 s. But it is observed that the hydration reaction is incomplete in 800 s. Table 4.20 shows operating conditions used for simulation. So, time of reaction is increased, and following results are obtained.

Table 4.20. Operating conditions for time of hydration reaction simulation

Initial temperature of ESB	338 K (65 ˚C)
Water vapour supply pressure	9.52 kPa
HTF inlet temperature	338 K
HTF flow rate	10 ltr/min
ESB porosity	60 %
ESB average particle diameter	30 µm
Hydration reaction time	1200 s

Figs. 4.20 and 4.21 show the variation in extent of reaction after 800 and 1200 s, respectively. From Table 4.21, it is observed that at the end of 800s, 60.38 % of reactant (CaO) is converted to product ($Ca(OH)_2$). This value increases to 83.75 % by the end of 1200 s. Thus, with increase in time of hydration, more amount of reactant is getting converted into product and consequently more energy is released by ESB.

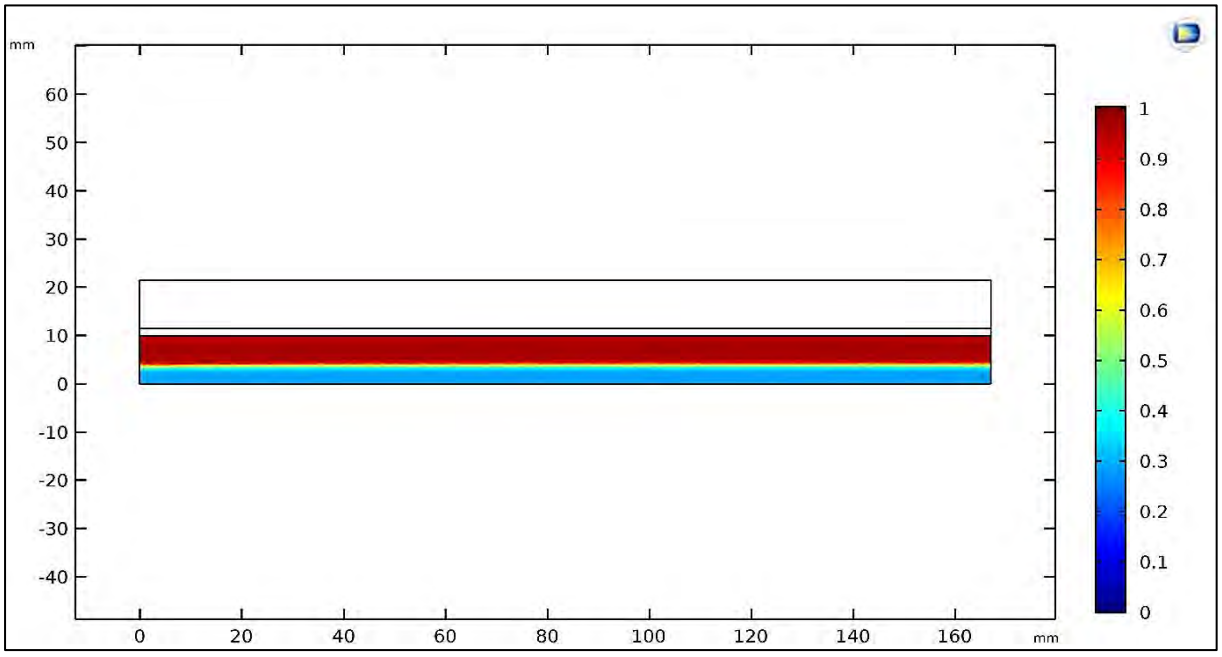

Fig. 4.20: Extent of reaction variation after 800 s

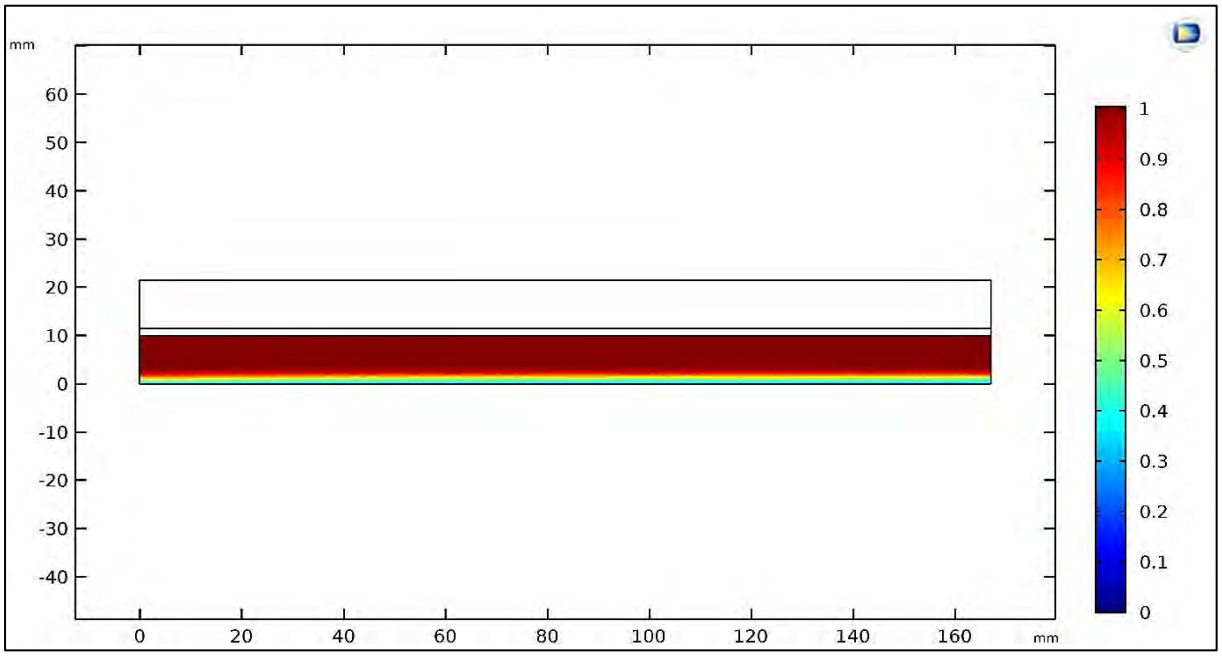

Fig. 4.21: Extent of reaction variation after 1200 s

Table 4.21. Effect of increase in hydration reaction time

Hydration reaction time (s)	Conversion from reactant to product (%)	Total energy received by HTF (kJ) (Target = 500 kJ)	Total energy for sensible heating (kJ)	Total energy output from ESB (kJ)	Efficiency of energy transfer from ESB to HTF (%)
800	60.38	254.61	86.78	341.39	74.58
1200	83.75	353.17	81.86	435.03	81.18

Along with increase in energy received by HTF, there is also improvement in efficiency of energy transfer from ESB to HTF in case of 1200 s of time, but due to operating constraints it is not possible to increase time of hydration beyond 800s. Thus, time of hydration reaction is taken as 800 s for further simulations.

4.2.2.6 Conclusions of parametric studies

Based on results of different parametric studies discussed in section 4.2.2.1 to 4.2.2.5, following conclusions are drawn.

Table 4.22. Observations from parametric studies

Operating parameter	Effect on hydration reaction
Water vapour supply pressure	Higher value of supply pressure gives higher rate of reaction. Thus, it should be as high as possible.
Initial ESB temperature	No significant impact on reaction performance
HTF mass flow rate	For higher mass flow rates, HTF receives higher amount of energy. But at the same time lesser increase in HTF average outlet temperature is observed. Hence, tradeoff is to be made for optimum value of HTF mass flow rate.
ESB permeability	Higher energy output is observed for lower ESB porosity values and larger average particle size.
Time of hydration reaction	Up to 1200 s, it is observed that increase in time of hydration reaction yields better results due to more conversion. But after 1200 s, rate of conversion is negligible.

4.2.2.7 Revised operating conditions

After analyzing results of 2-D simulations for different parametric studies, it is conveyed to Faurecia team. Based on their inputs, operating conditions are revised as follows:

Table 4.23. Comparison of operating conditions for simulation

Operating parameter	Values at the start of project	Revised values
Initial temperature of ESB	Minimum 338 K (65 ˚C)	Minimum 338 K (65 ˚C)
Water vapour supply pressure	To be decided accordingly	47.13 kPa (P_{sat} corresponding to 80 ˚C)
HTF inlet temperature	Minimum 338 K (65 ˚C)	Minimum 338 K (65 ˚C)
HTF flow rate	5 to 40 ltr min^{-1}	10 ltr min^{-1}
ESB porosity	40 to 60 %	40 %
ESB average particle diameter	30 μm and 150 μm	150 μm
Hydration reaction time	10 minutes	800 s

4.2.2.8 2-D simulations based on revised operating parameters and results

The 2-D hydration simulations are carried out again with the revised operating conditions given in Table 4.24. For current simulations, only operating conditions are revised but physical phenomena involved in solving the problem are still the same. So, it is expected that current simulation results should follow similar trend as that of results of earlier different parametric studies.

Table 4.24. Revised operating conditions for simulation

Initial temperature of ESB	338 K (65 ˚C)
Water vapour supply pressure	47.13 kPa (P_{sat} corresponding to 80 ˚C)
HTF inlet temperature	338 K (65 ˚C)
HTF flow rate	10 ltr min^{-1}
ESB porosity	40 %
ESB average particle diameter	150 µm
Hydration reaction time	800 s

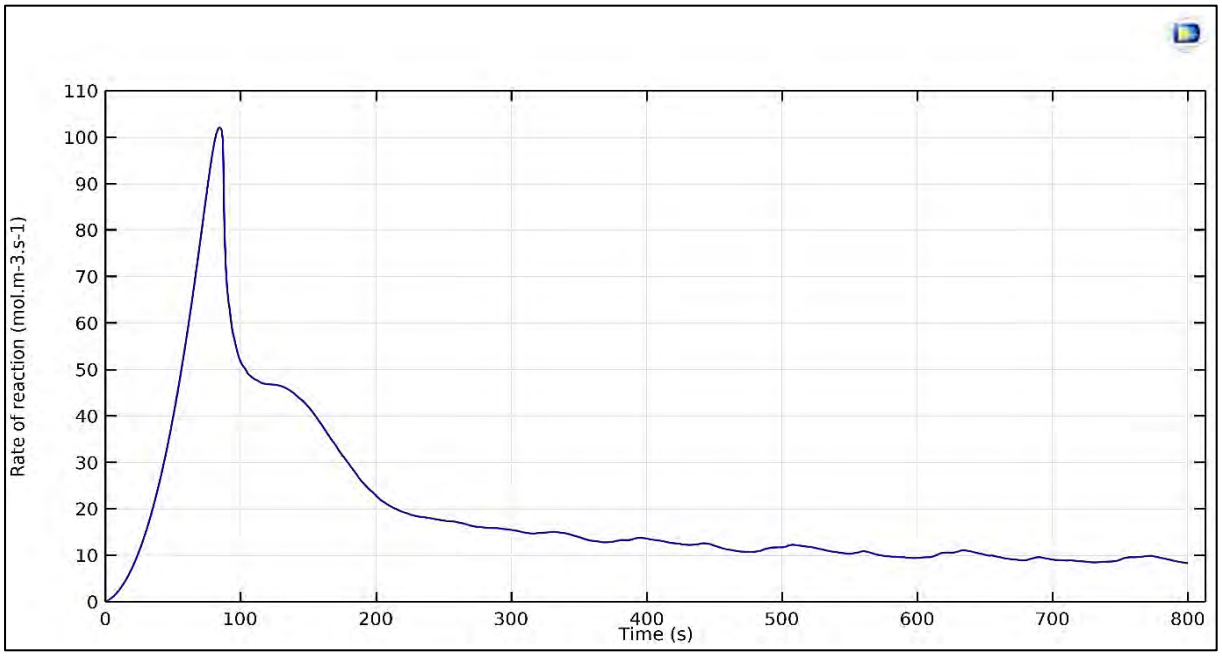

Fig. 4.22: Average rate of reaction variation

The similar trends are observed in the study carried out with revised operating conditions as shown in Figs. 4.22 to 4.27.

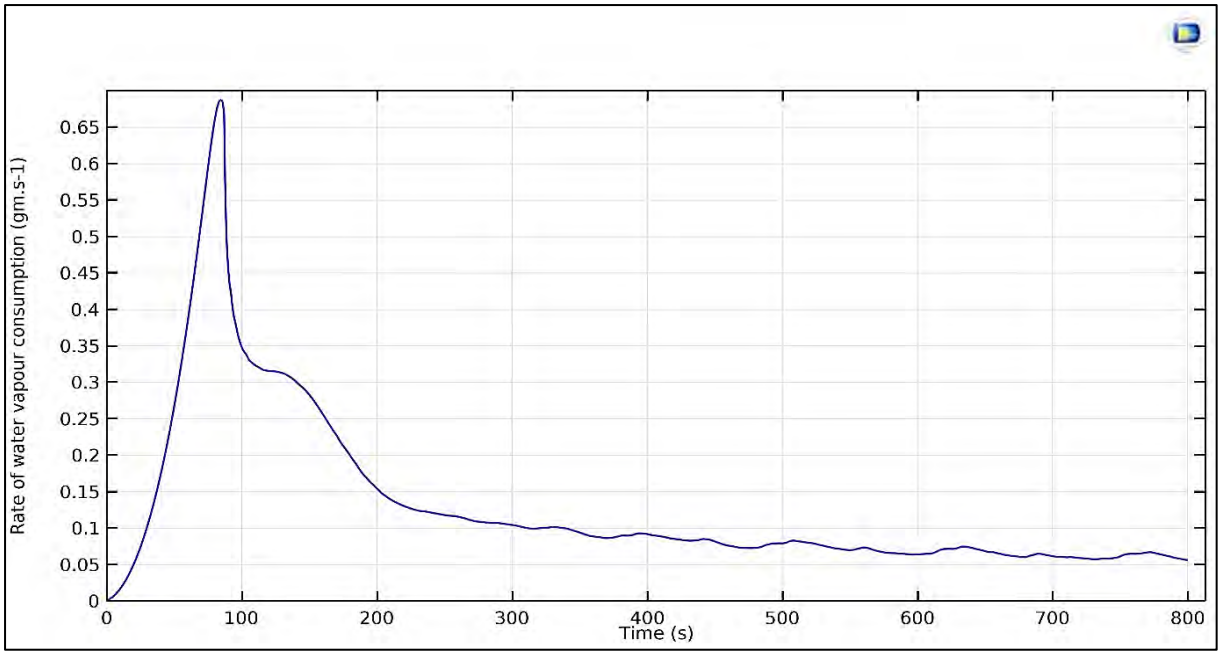

Fig. 4.23: Average rate of water vapour consumption variation

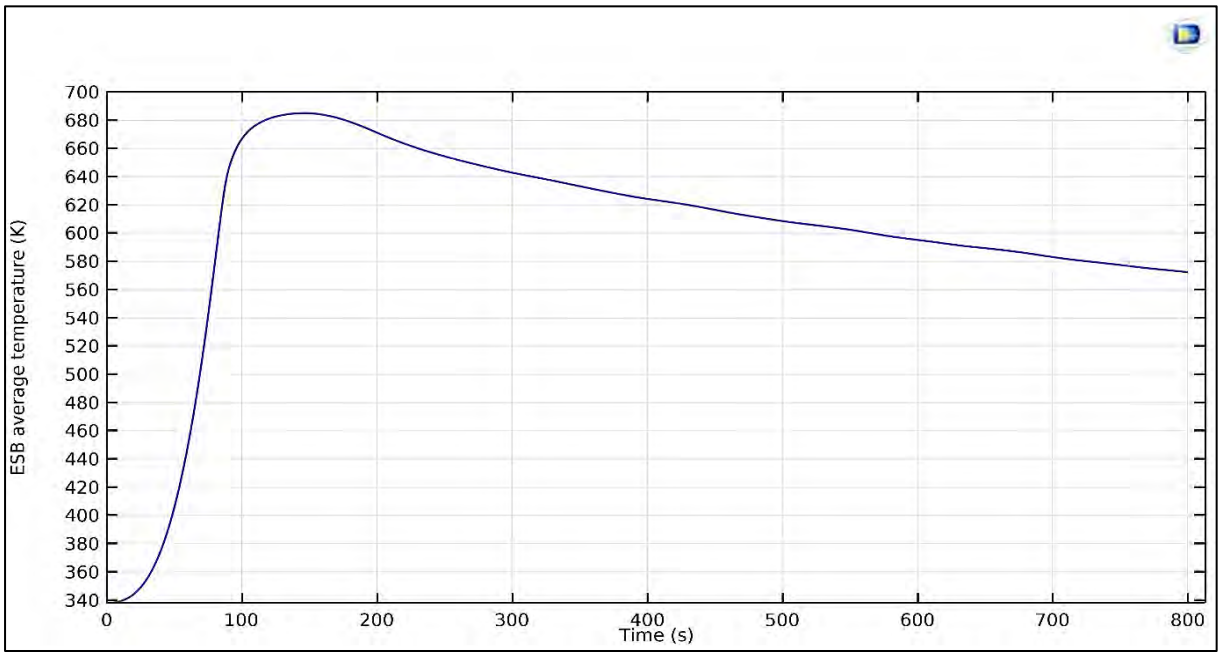

Fig. 4.24: ESB average temperature variation

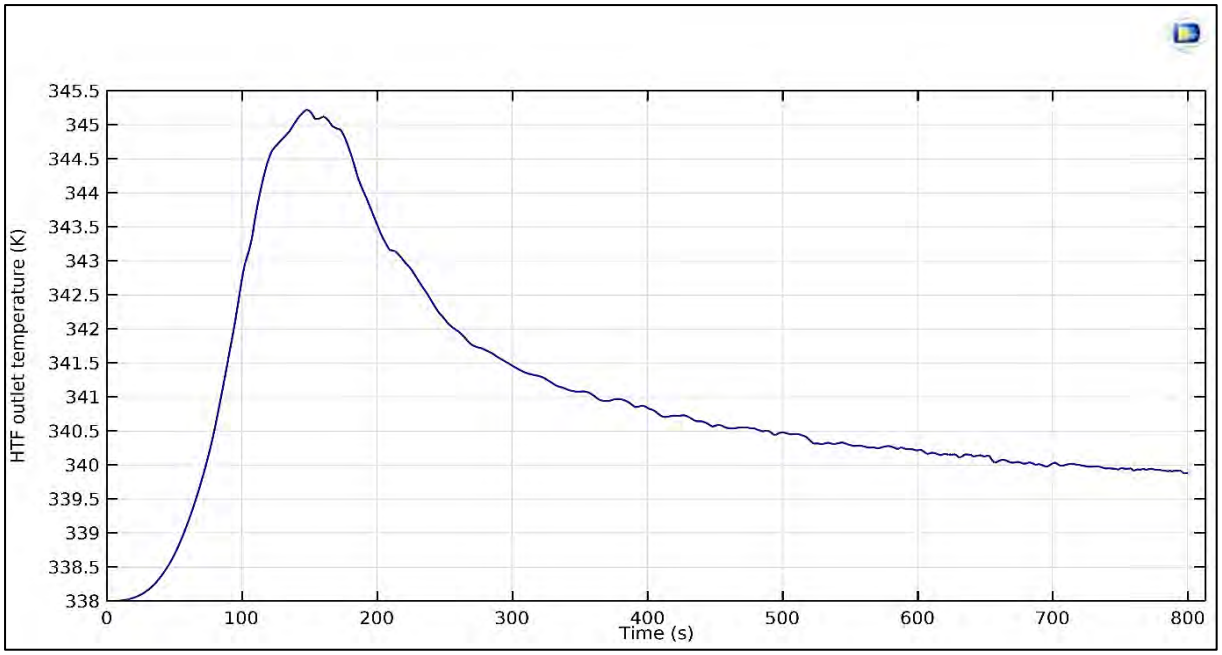

Fig. 4.25: HTF average outlet temperature variation

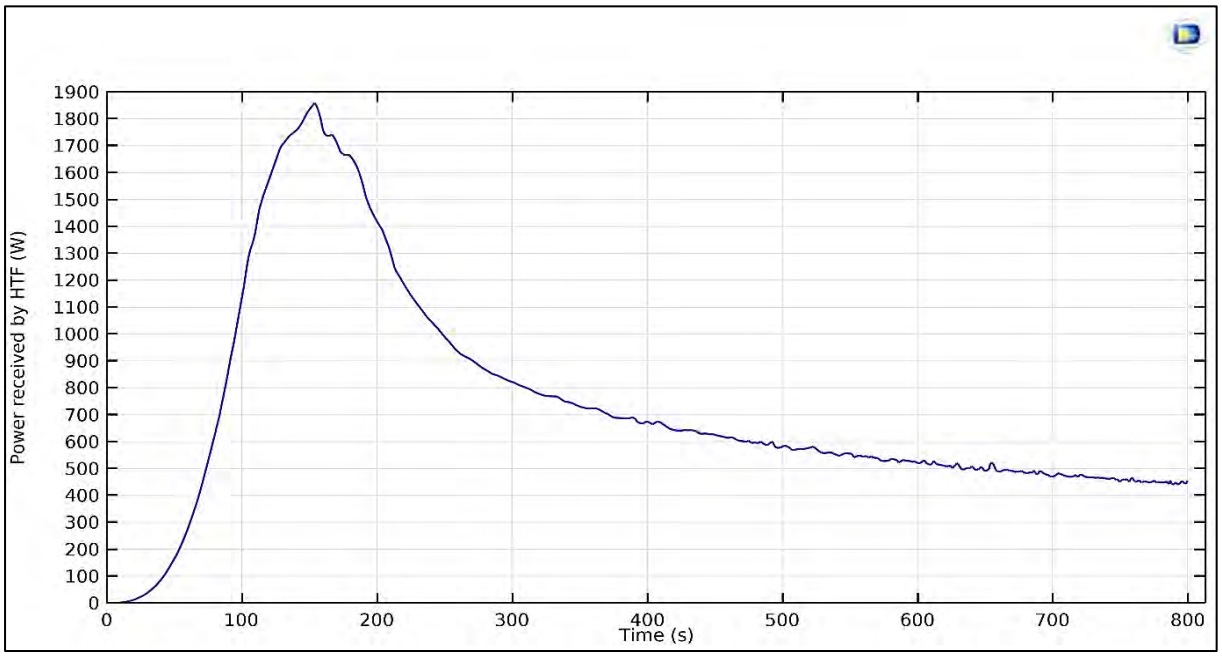

Fig. 4.26: Average power received by HTF variation

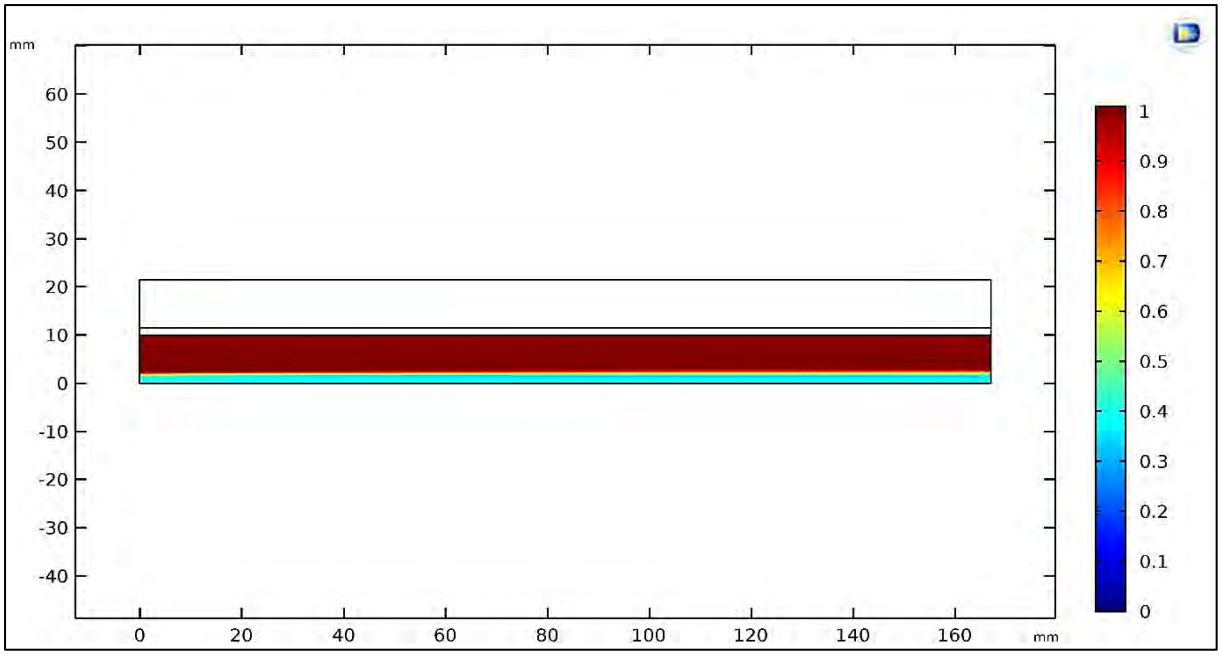

Fig. 4.27: Extent of reaction varaiation after 800 s

Table 4.25. Summary of 2-D simulation results based on revised operating conditions

Total energy output from ESB (kJ)	635.03
Total energy for sensible heating (kJ)	156.62
Total energy received by HTF (kJ) (Target = 500 kJ)	478.41
Efficiency of energy transfer from ESB to HTF (%)	75.34
Peak average power received by HTF (W)	1858.49 W at 154 s from start
Conversion from reactant to product (%)	82.05
HTF average outlet temperature (K) after 800 s	339.87
HTF average outlet temperature rise (K) after 800 s	1.87
Average HTF temperature rise (K) (Target = 3.052 K)	3.02
Average rate of reaction (mol m^{-3} s^{-1})	19.43
Total water vapour consumption (g)	104.68
Average water vapour consumption rate (g s^{-1})	0.13

From Table 4.25, it is observed that ESB can transfer 478.41 kJ of energy to HTF against the required target of 500 kJ. And respective HTF average outlet temperature rise is 3.02 K as against the requirement of 3.05 K.

4.3 3-D simulations

After performing 2-D simulations, effect of different operating parameters on hydration reaction are well understood. But there are some parameters like fins, whose effect cannot be studied with 2-D model. Thus, 3-D model is setup. Different physical phenomena involved in 3-D model are same as that of in 2-D model. Hence same COMSOL modules are used for 3-D simulations also. But these modules are modified according to 3-D geometry wherever required. For better understanding, 3-D simulations are divided into three case studies as follows:

Table 4.26. 3-D model simulation case studies

Case study I	3-D model without any fins
Case study II	3-D model with fins in ESB domain
Case study III	3-D model with fins in ESB and HTF domain

4.3.1 Case study I: 3-D model without any fins

According to design of flat reactor design, 3-D model geometry is created. To understand different domains involved in 3-D simulations, each domain along with respective dimensions are shown in Figs. 4.28 to 4.31. Figs. 4.28 and 4.29 show dimensions of HTF and ESB domain, respectively. All solid components of the system are made up of steel and hereafter called as steel frame, as shown in Figs. 4.30 and 4.31.

Objective of present study is to study changes in performance of hydration reaction for same problem setup but with 2-D and 3-D geometry.

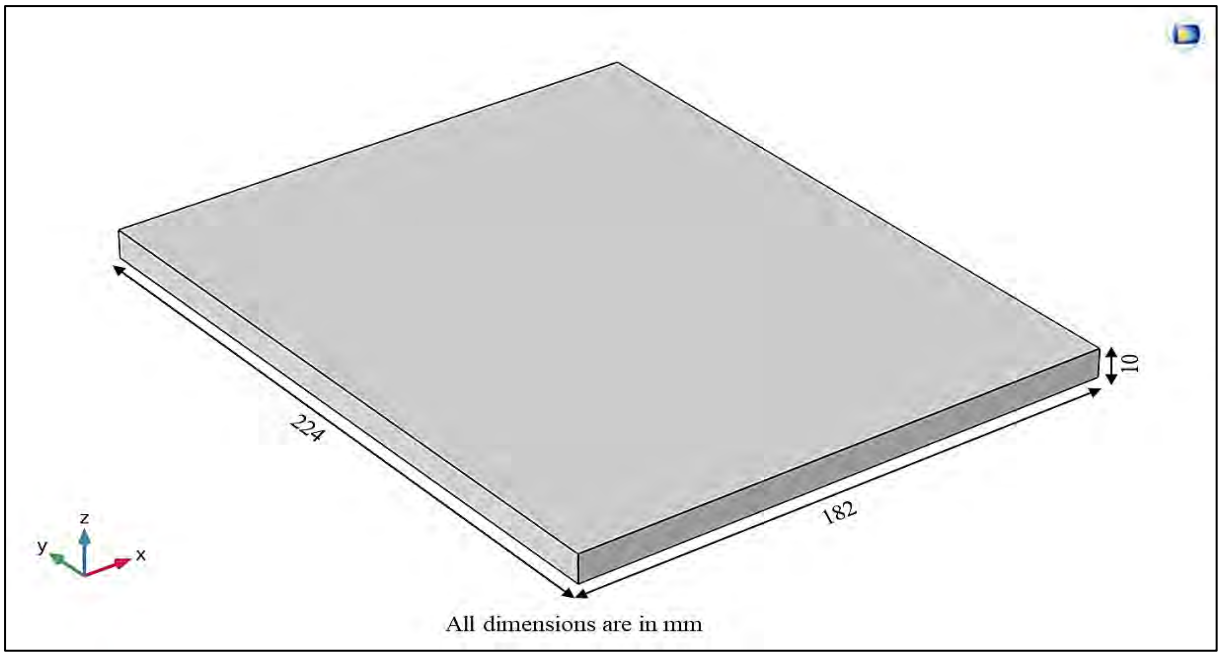

Fig. 4.28: HTF domain with dimensions

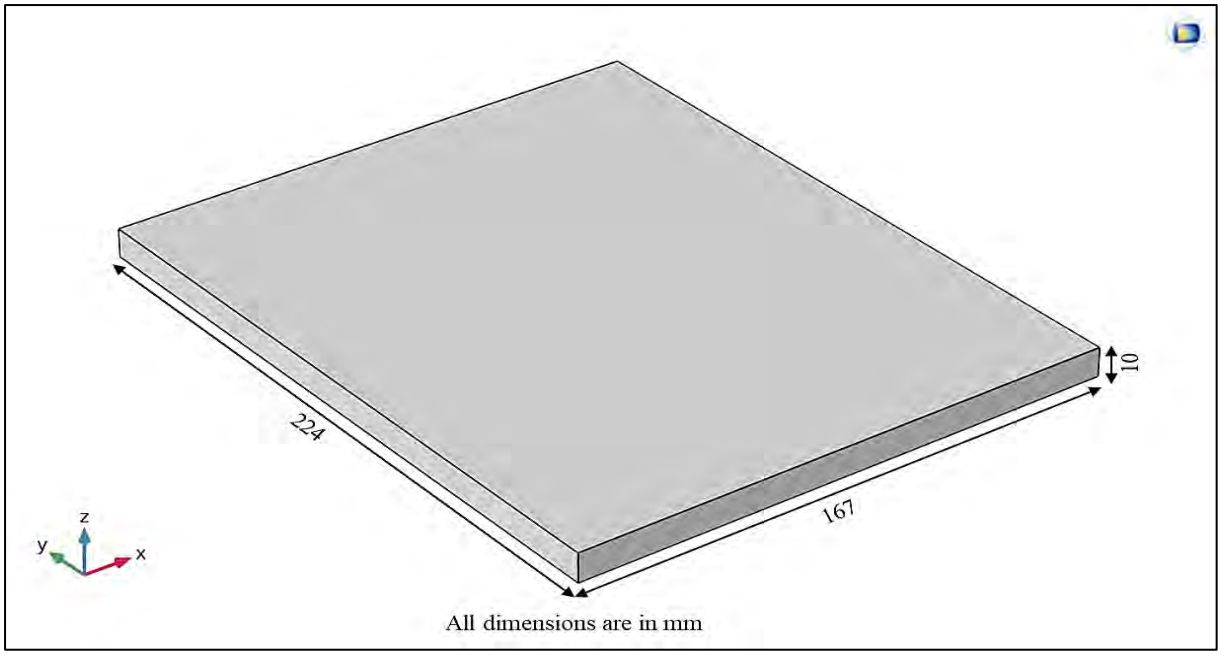

Fig. 4.29: ESB domain with dimensions

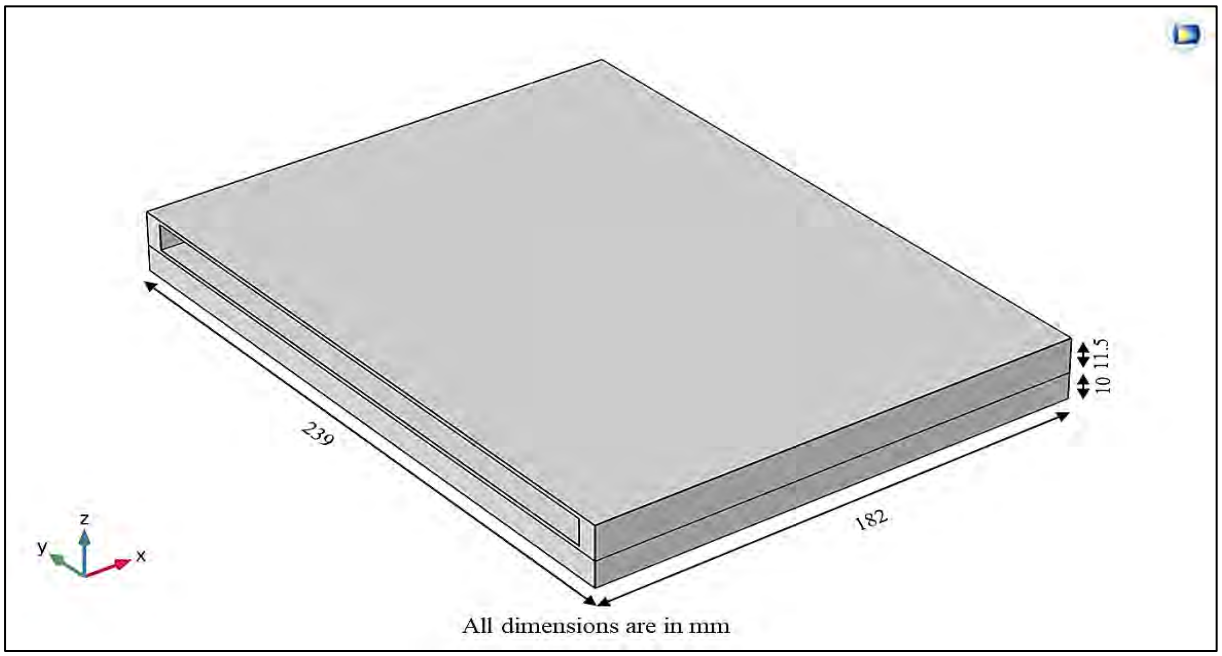

Fig. 4.30: Steel frame with dimensions

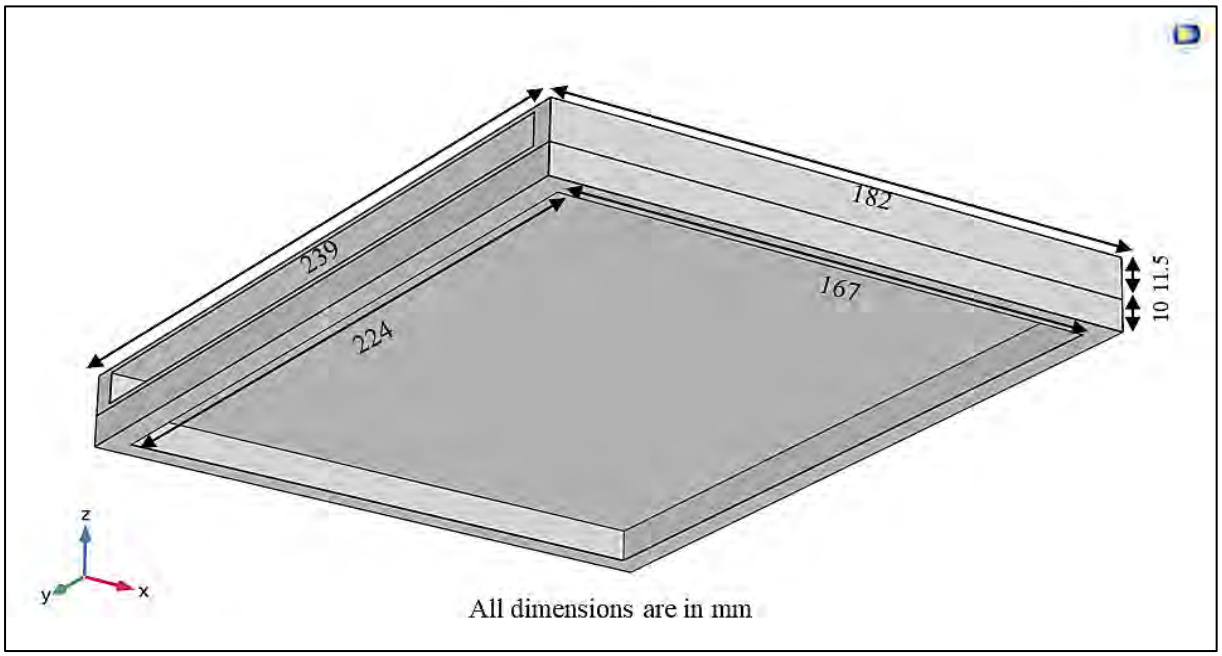

Fig. 4.31: Steel frame dimensions (bottom view)

Fig. 4.32 shows the schematic of simplified 3-D model. HTF and ESB domains are placed at appropriate positions within steel frame as shown in Fig. 4.32. The entry and exit of HTF are indicated as HTF inlet and HTF outlet, respectively. Water vapour enters ESB domain from the bottom surface as shown. During simulations, all exterior walls of steel domain are assumed to be insulated. Other assumptions for 3-D simulations are listed in section 4.1.

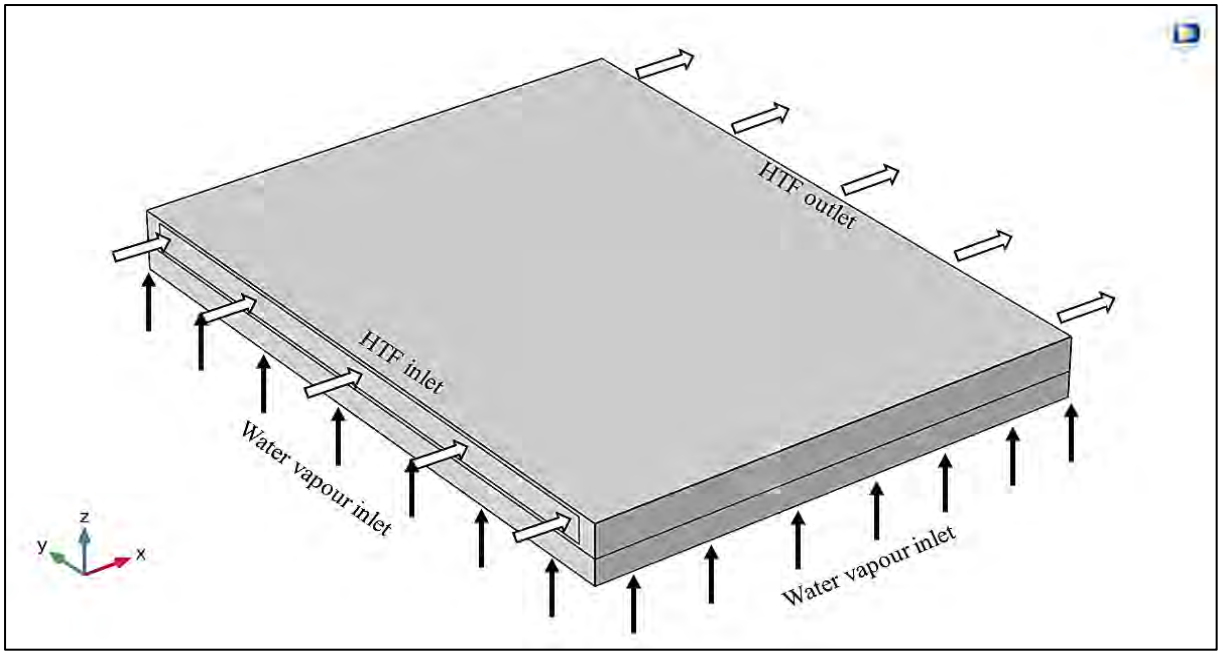

Fig. 4.32: Schematic of simplified 3-D model

The dimensions of ESB, HTF and steel frame domains are summarised in Table 4.26.

Table 4.27. Dimensions of 3-D model
(all dimensions are in mm)

Length of ESB domain	167
Width of ESB domain	224
Height of ESB domain	10
Length of HTF domain	182
Width of HTF domain	224
Height of HTF domain	10
Outer length of steel domain	182
Outer width of steel domain	239
Total height of steel domain	21.5

Operating conditions used for 3-D simulations are as shown in Table 4.28.

Table 4.28. Operating conditions for 3-D simulation

Initial temperature of ESB	338 K (65 ˚C)
Water vapour supply pressure	47.13 kPa (P_{sat} corresponding to 80 ˚C)
HTF inlet temperature	338 K (65 ˚C)
HTF flow rate	10 ltr min^{-1}
ESB porosity	40 %
ESB average particle diameter	150 µm
Hydration reaction time	800 s

Based on above operating conditions simulations are performed and following results are obtained.

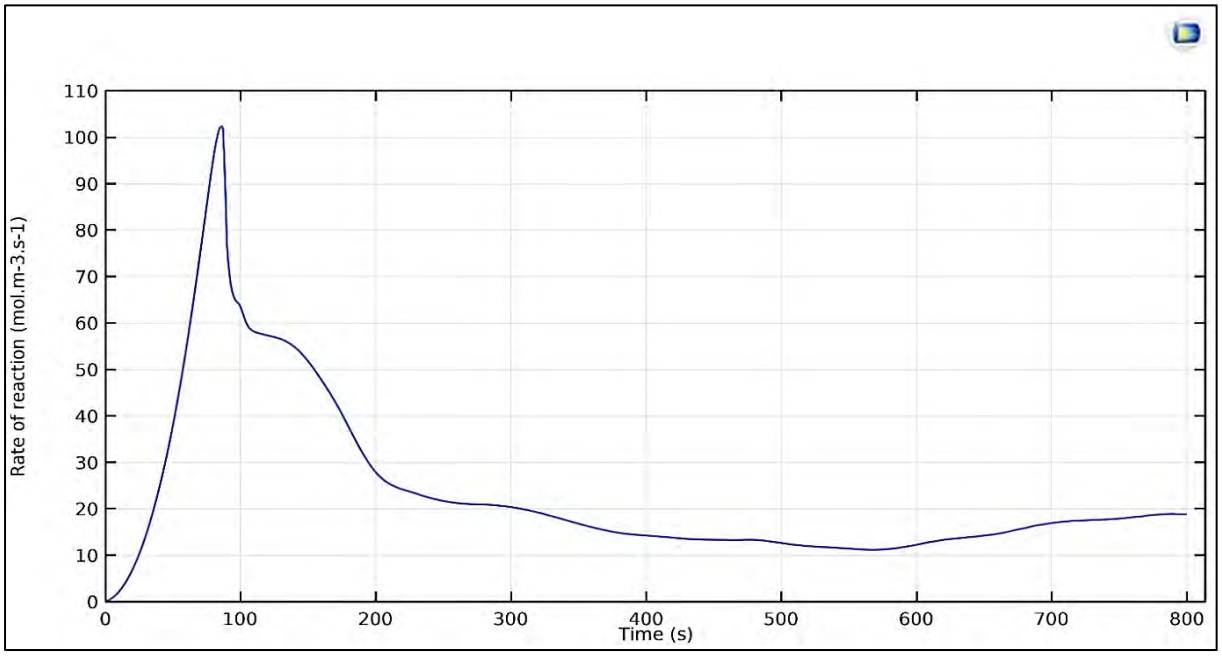

Fig. 4.33: Average rate of reaction variation

Figs. 4.33 and 4.34 show variations in average rate of reaction and average water vapour consumption, respectively. This variations are similar to that observed in 2-D model as

shown in Figs. 4.22 and 4.23 up to 550 s. But in case of 3-D model, it is observed that average rate of reaction value gradually increases after around 550 s.

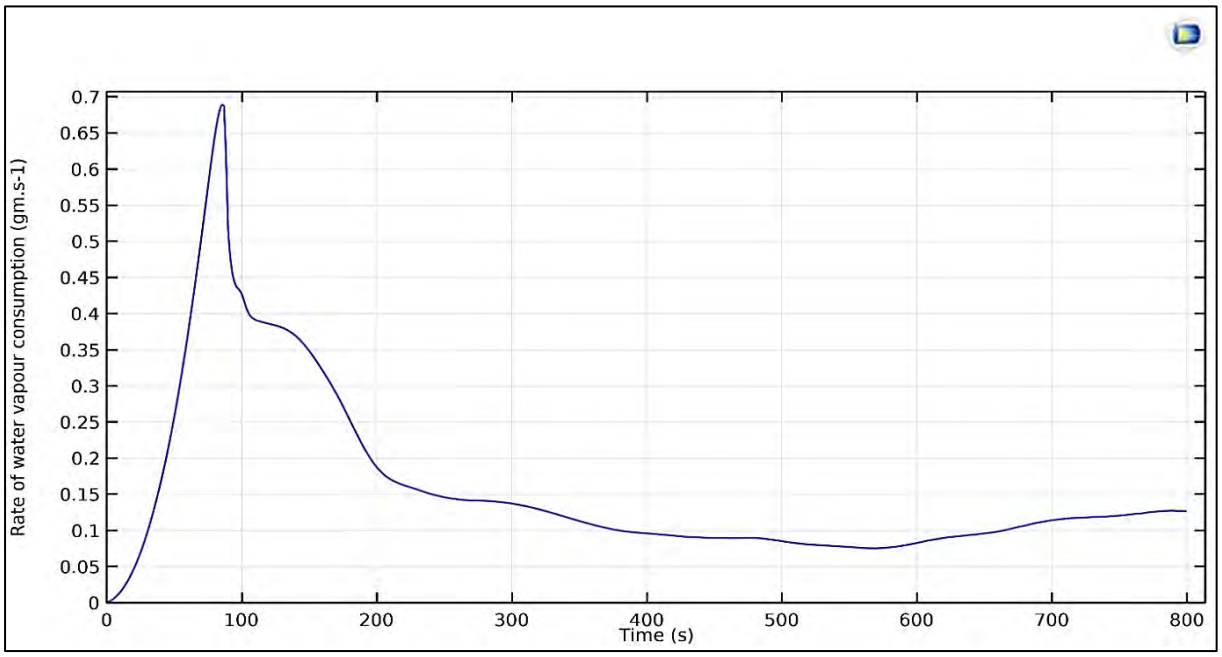

Fig. 4.34: Average rate of water vapour consumption variation

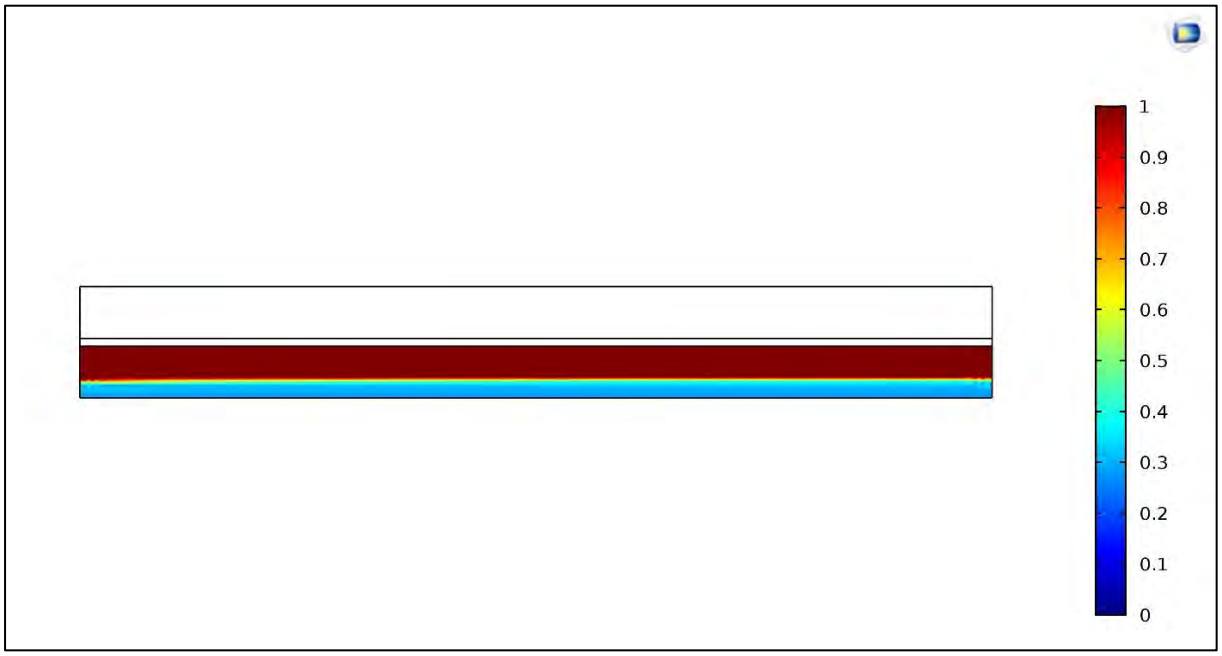

Fig. 4.35: Variation in extent of reaction after 600 s in 2-D model

The increase in average rate of reaction in 3-D model is explained with the help of Figs. 4.35 ad 4.36. Figs. 4.35 and 4.36 show extent of reaction across ESB after 600 s in 2-D and 3-D model, respectively. As the vertical side walls were assumed to be insulated in 2-D model, conversion doesnot start from vertical walls of ESB domain as shown in Fig. 4.35. But for 3-D model, heat transfer also takes place from vertical ESB walls to steel frame surrounding

them which results in the additional conversion of reactant into product near vertical walls of ESB domain. This phenomenon is called as edge effect for further analysis and is highlighted in Fig. 4.36.

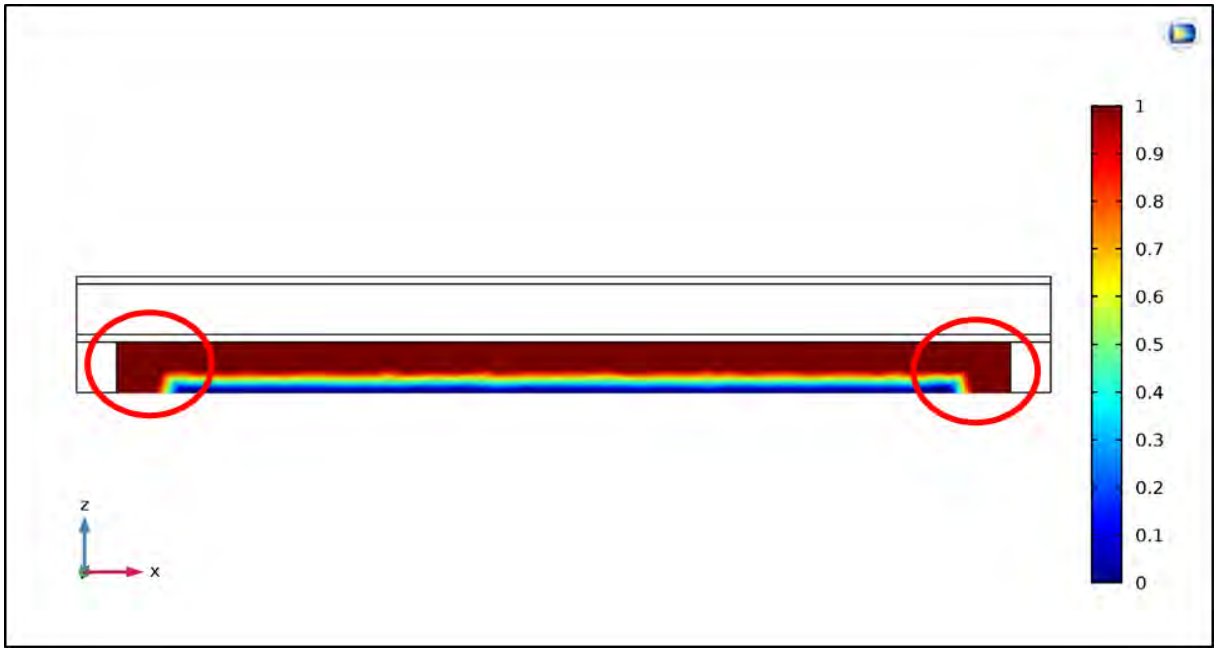

Fig. 4.36: Variation in extent of reaction after 600 s in 3-D model

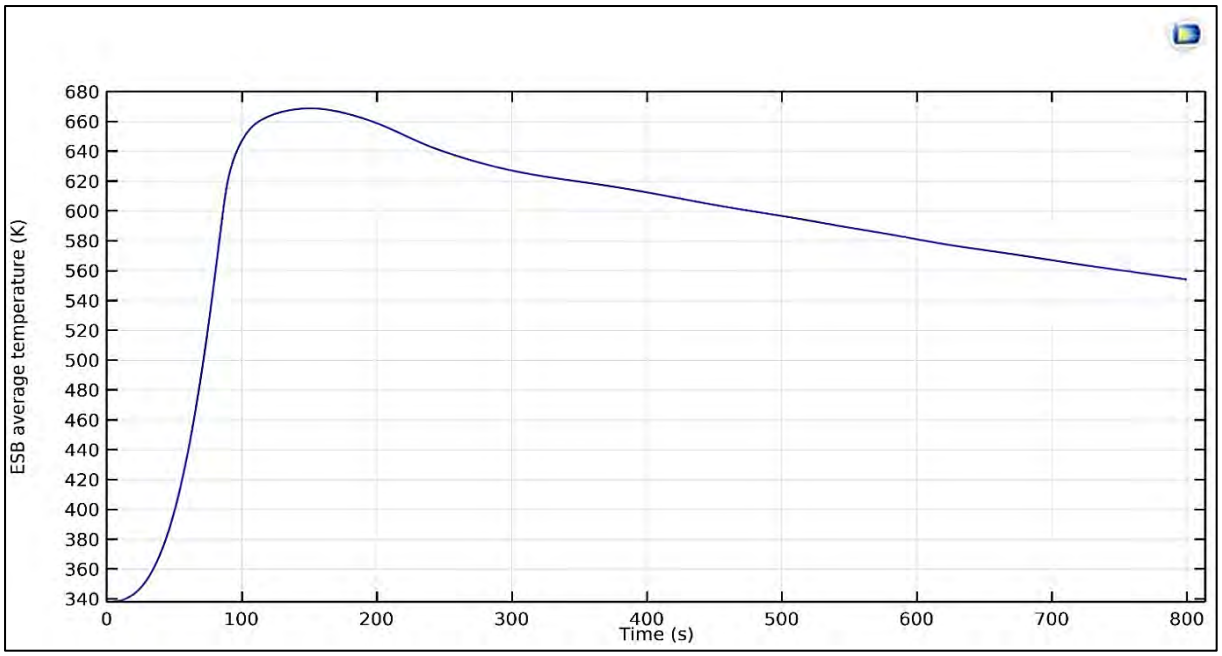

Fig. 4.37: ESB average temperature variation

Fig. 4.37 and 4.38 show variations of ESB average temperature and HTF average outlet temperature, respectively. The variations are similar to that observed in 2-D model as shown in Figs. 4.24 and 4.25.

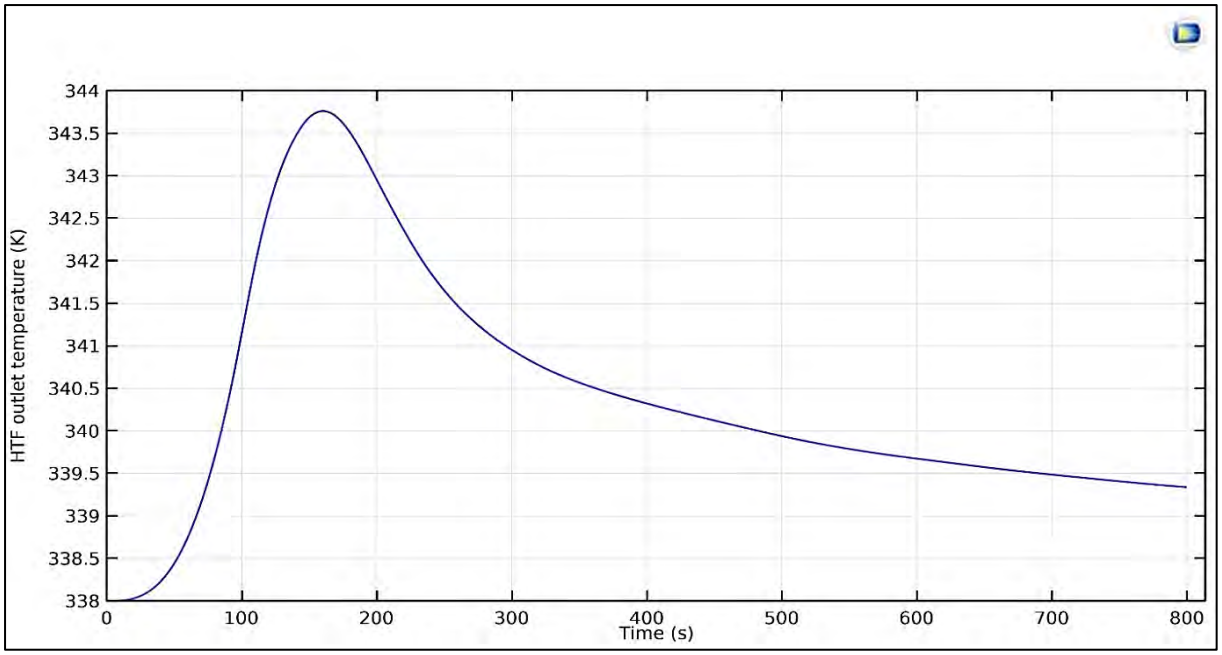

Fig. 4.38: HTF average outlet temperature variation

But in 3-D model, it is observed that values of ESB average temperature and HTF average outlet temperature are lower than that values observed in 2-D model. Table 4.29 shows the comparison between average ESB and HTF outlet temperatures obtained from simulations of 2-D and 3-D models.

Table 4.29. Comparison of different temperature values for 2-D and 3-D model (Case study I)

Parameter	2-D results	3-D Results
Maximum ESB average temperature (K)	685.04	668.89
Average ESB temperature (K)	600.45	586.64
Average ESB temperature (K) at the end of 800 s	572.35	554.24
Maximum HTF average outlet temperature (K)	345.22	343.76
Average HTF outlet temperature rise (K)	3.02	2.40
HTF average outlet temperature (K) at the end of 800 s	339.87	339.34

The reduction in average temperature values for 3-D model are explained with the help of Figs. 4.39 to 4.40. In Fig. 4.39, temperature at boundaries of ESB with the surrounding steel frame is lower than the core of ESB domain. Due to this temperature gradient, fraction of heat released by hydration reaction is spent in sensible heating of steel frame. Thus, ESB average temperature is lower than 2-D model. In 2-D model, there is no such steel frame surrounding ESB. Exact values of HTF average outlet temperatures are given in Table 4.30.

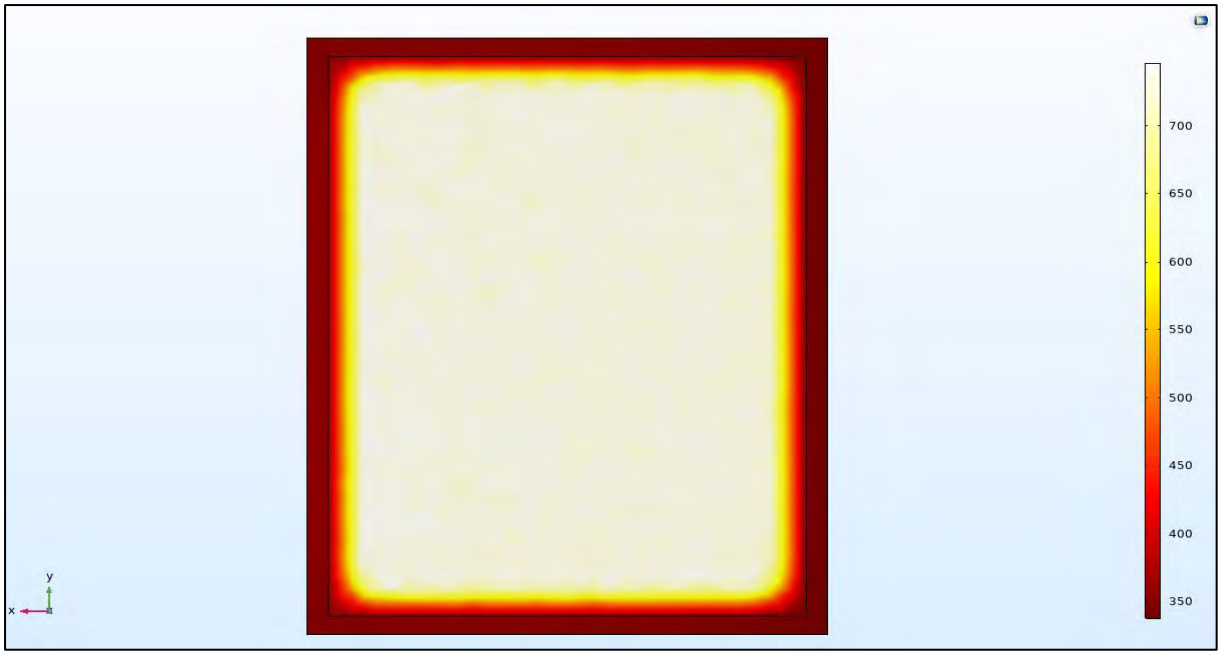

Fig. 4.39: Temperature variation at the bottom surface of ESB, after 800 s

HTF domain is also surrounded by steel frame as shown in Fig. 4.40. Fraction of energy received by HTF is spent in sensible heating of steel frame surrounding the HTF domain. Also, there is additional thermal boundary layer formation along vertical walls of HTF domain as shown in Fig. 4.41. Thus, HTF average outlet temperature is lower than 2-D model. In 2-D model, there is no such steel frame surrounding HTF doamin and also vertical thermal boundary layers are absent.

Fig. 4.40: HTF outlet temperature variation, at the end of 800 s

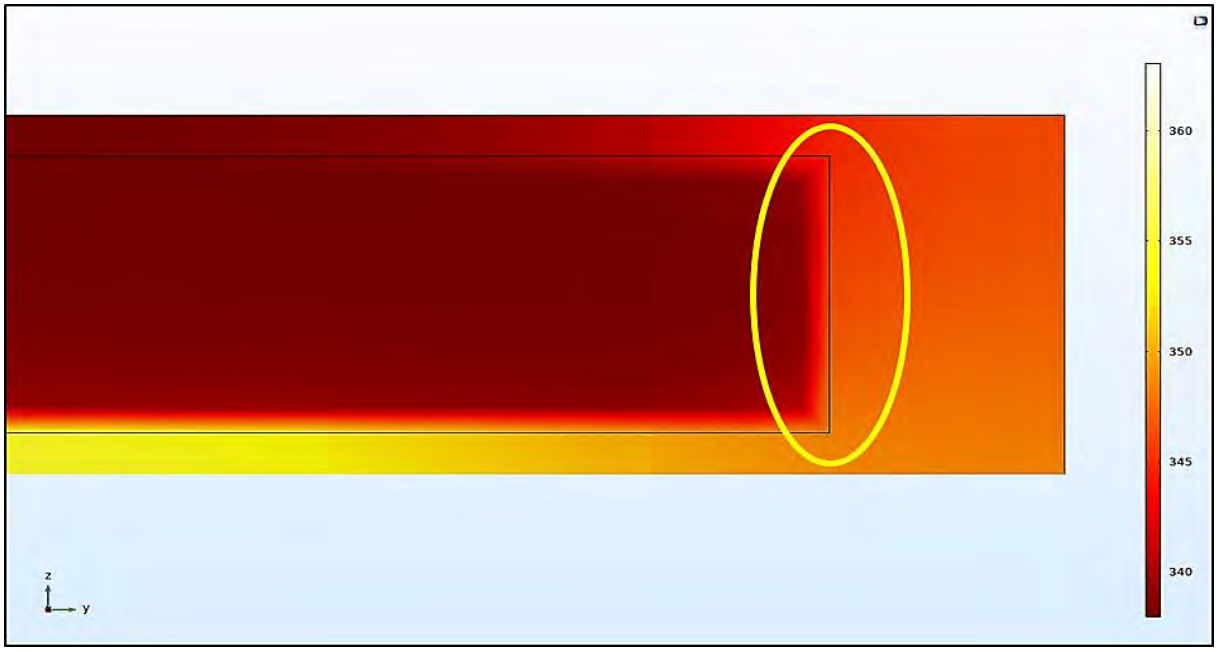

Fig. 4.41: HTF outlet temperature variation, at the end of 800 s (Close-up view)

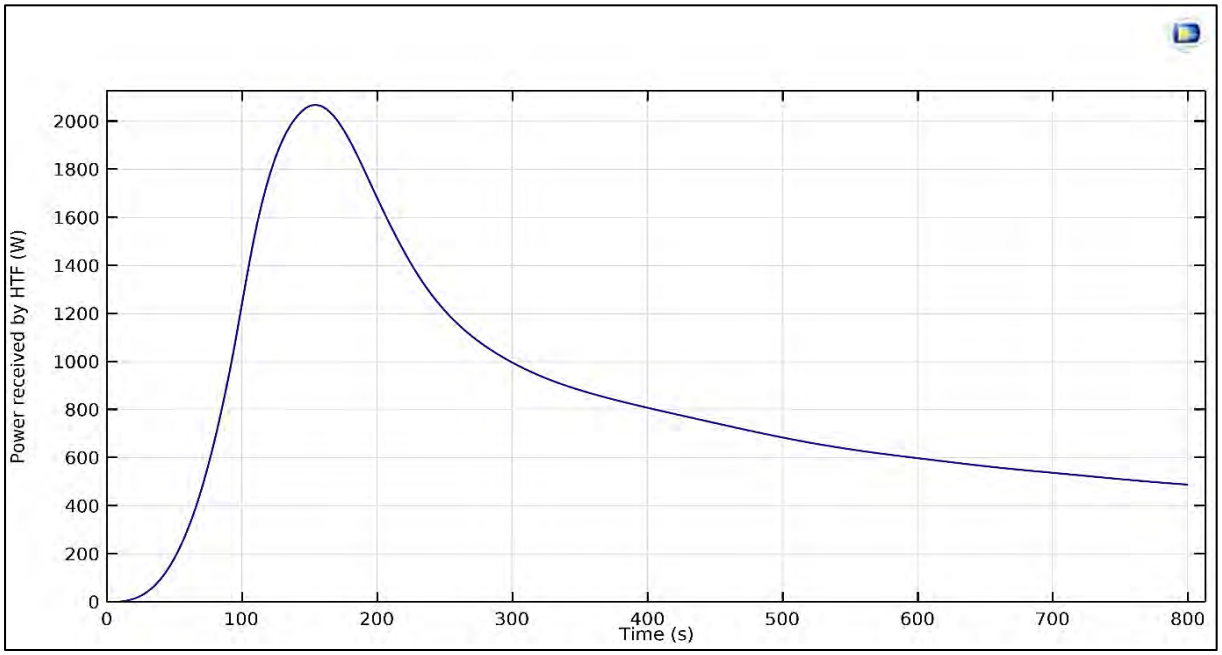

Fig. 4.42: Average power received by HTF variation

Fig. 4.42 shows average power received by HTF variation. The variation is similar to that observed in 2-D model as shown in Fig. 4.26. But peak average power achieved in 3-D model is higher than 2-D model due to edge effect. Exact values are shown in Table 4.30.

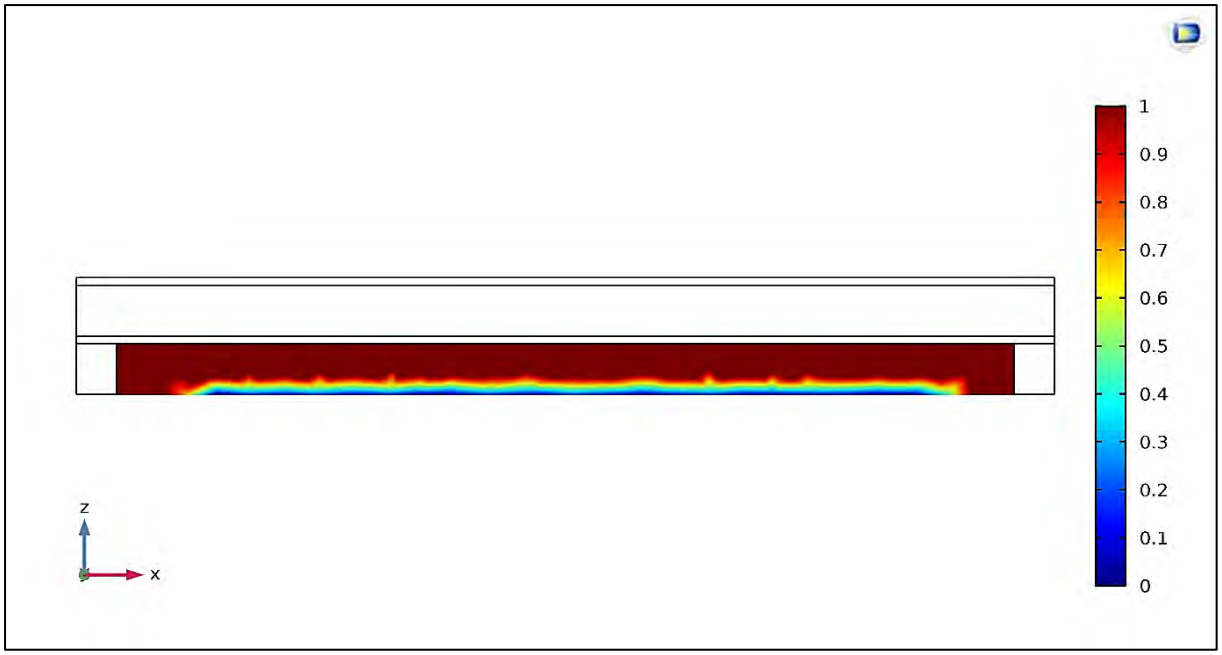

Fig. 4.43: Extent of reaction variation after 800 s

Fig. 4.43 show extent of reaction variation across ESB after 800 s in 3-D model Case study I. Comparison between the results obtained from the simulations of 2-D and 3-D model is given in Table 4.30 as follows:

Table 4.30. Comparison of 2-D and 3-D model (Case study I) results

Parameter	2-D model	3-D model
Conversion from reactant to product (%)	82.05	99.38
Total energy output from ESB (kJ)	635.03	770.41
Energy spent for sensible heating of ESB (kJ)	156.62	156.14
Energy spent for sensible heating of steel frame (kJ)	N/A	8.23
Total energy received by HTF (kJ) (Target = 500 kJ)	478.41	606.04
Efficiency of energy transfer from ESB to HTF (%)	75.34	78.66
Average peak power received by HTF (W)	1858.49 W at 154 s from start	2068.45 W at 154 s from start
HTF average outlet temperature (K) after 800 s	339.87	339.34
HTF average outlet temperature rise (K) after 800 s	1.87	1.34
Average HTF temperature rise (K) (Target = 3.052 K)	3.02	2.40
Average rate of reaction (mol m^{-3} s^{-1})	19.43	23.57
Total water vapour consumption (g)	104.68	126.99
Average water vapour consumption rate (g s^{-1})	0.13	0.16

Due to edge effect observed in extent of reaction variation as mentioned in Fig. 4.35 and 4.36, higher conversion is observed in 3-D model as shown in Table 4.30. The increase in

conversion results in higher value of total energy output from ESB in 3-D model. Energy spent for sensible heating of ESB is almost similar in both the models. In 3-D model, fraction of energy released by ESB is spent for sensible heating of steel domain. This part of energy loss is absent in 2-D model. Due to higher conversion, total energy received by HTF and efficiency of energy transfer from ESB to HTF are higher in 3-D model. Because of higher conversion, average peak power received by HTF, average rate of reaction and average water vapour consumption rate are also higher in 3-D model. Also, total water vapour consumption is higher as conversion is higher in 3-D model. But, due to energy loss from HTF to steel frame, HTF average outlet temperature rise is lower in 3-D model.

4.3.2 Case study II: 3-D model fins in ESB domain

For present study, same problem setup is used as that of case study I. Only difference between case study I and II is of 3-D geometry.

Objective of present study is to study the effect of providing fins in ESB domain on performance of hydration reaction. 3-D geometry with fins in ESB domain as shown in Fig. 4.44. The dimensions of fins are taken from flat ESB design and mentioned in Table. 4.31.

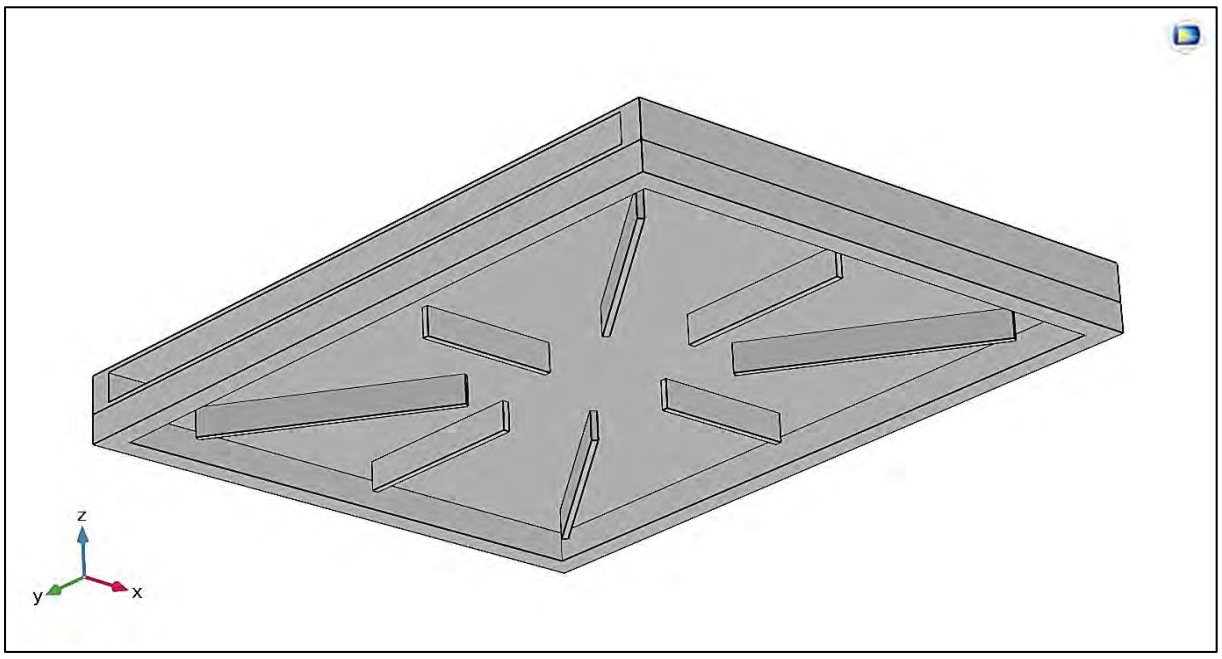

Fig. 4.44: Fins in ESB domain

Table 4.31. Dimension of fins in ESB domain
(all dimensions are in mm)

Height of fins	10
Width of fins	2
Length of fins parallel to X - axis	45
Length of fins parallel to Y - axis	60
Length of oblique fins	81.12
Inclination of oblique fins from X - axis	+/- 55˚
Length of ESB domain	167
Width of ESB domaim	224
Height of ESB domain	10

Table 4.32. Effect of fin volume on ESB volume

Volume occupied by fins	3724 mm^3
Volume of ESB	374080 mm^3
Volume occupied by fins as % of ESB volume	0.996 %

From Table 4.32 it is observed that proposed fins occupy nearly 1 % of total ESB volume.

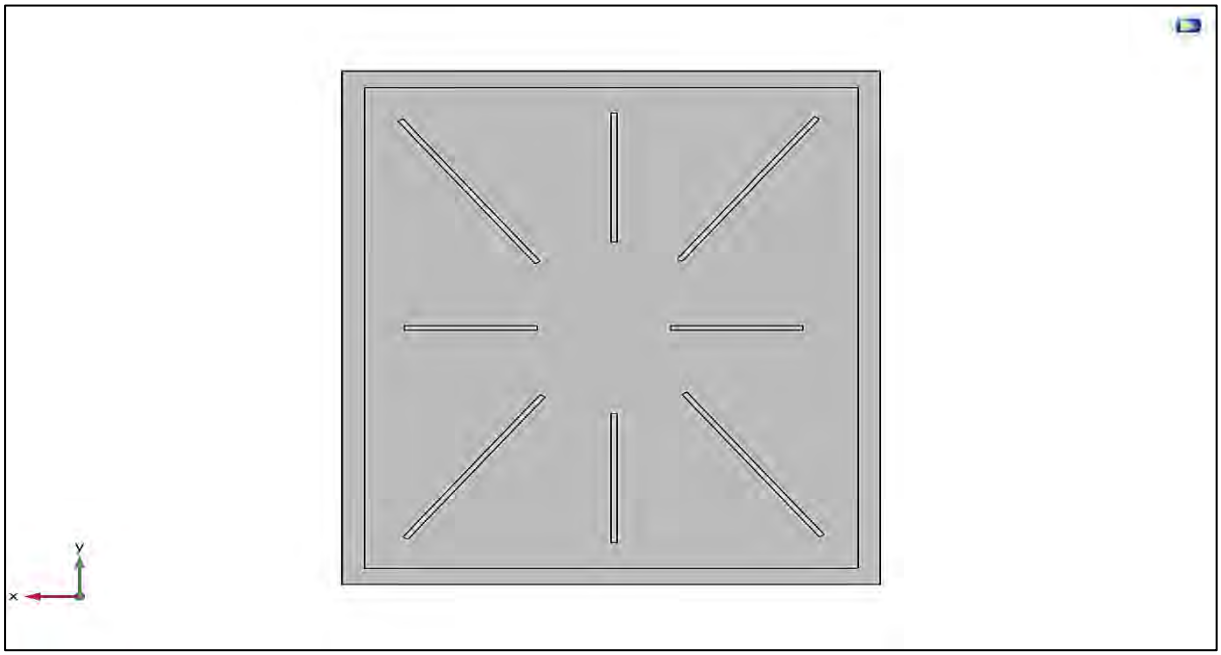

Fig. 4.45: ESB domain with fins – bottom view

Table 4.33. Operating conditions for 3-D simulation

Initial temperature of ESB	338 K (65 ˚C)
Water vapour supply pressure	47.13 kPa (P_{sat} corresponding to 80 ˚C)
HTF inlet temperature	338 K (65 ˚C)
HTF flow rate	10 ltr min^{-1}
ESB porosity	40 %
ESB average particle diameter	150 µm
Hydration reaction time	800 s

Based on above operating conditions simulations are performed and following results are obtained.

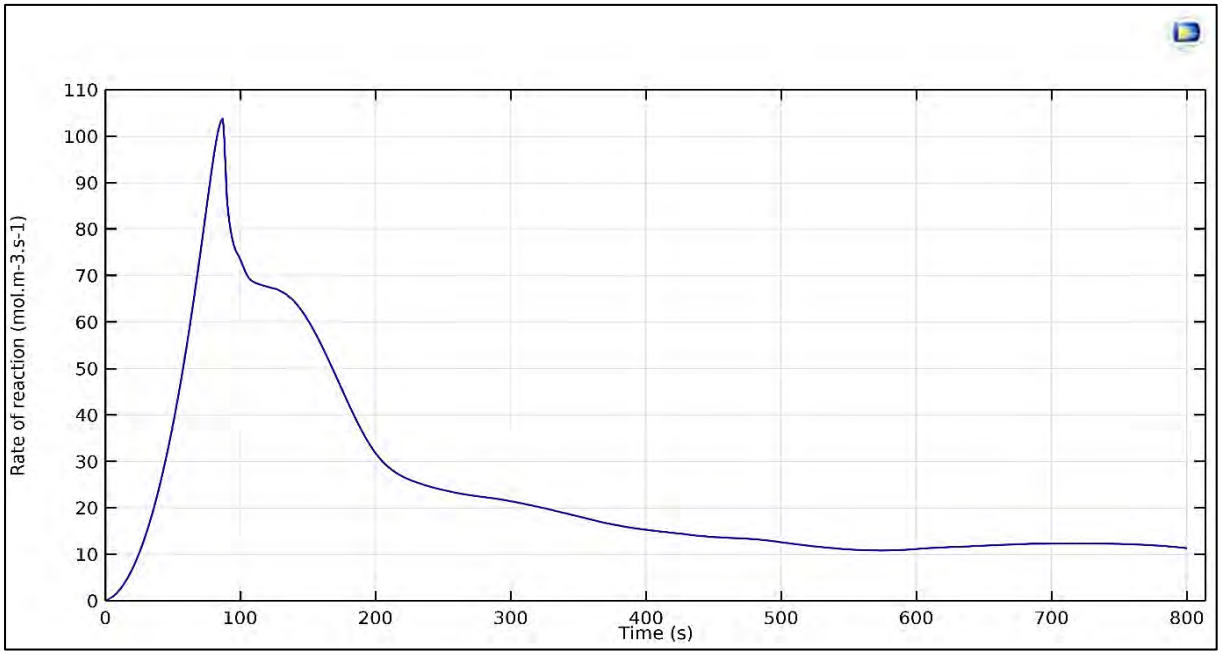

Fig. 4.46: Average rate of reaction variation

Figs. 4.46 and 4.47 show variation of average rate of reaction and average water vapour consumption, respectively. The variation up to 550 s is similar to that observed in 3-D model in case study I as shown in Figs. 4.33 and 4.34. But as compared to 3-D model case study I, average rate of reaction remains almost constant after around 550 s in case study II. In case study I, edge effect has significant impact after 550 s. But in present study, due to addition of fins, the vertical walls from where conversion starts are increased by significant amount, thus edge effect doesn't have much significant impact. From Table 4.35, it is observed that average rate of reaction (for 800 s time) is slightly higher in case study II. Thus, it is concluded that fins in ESB domain help in regulating average rate of reaction.

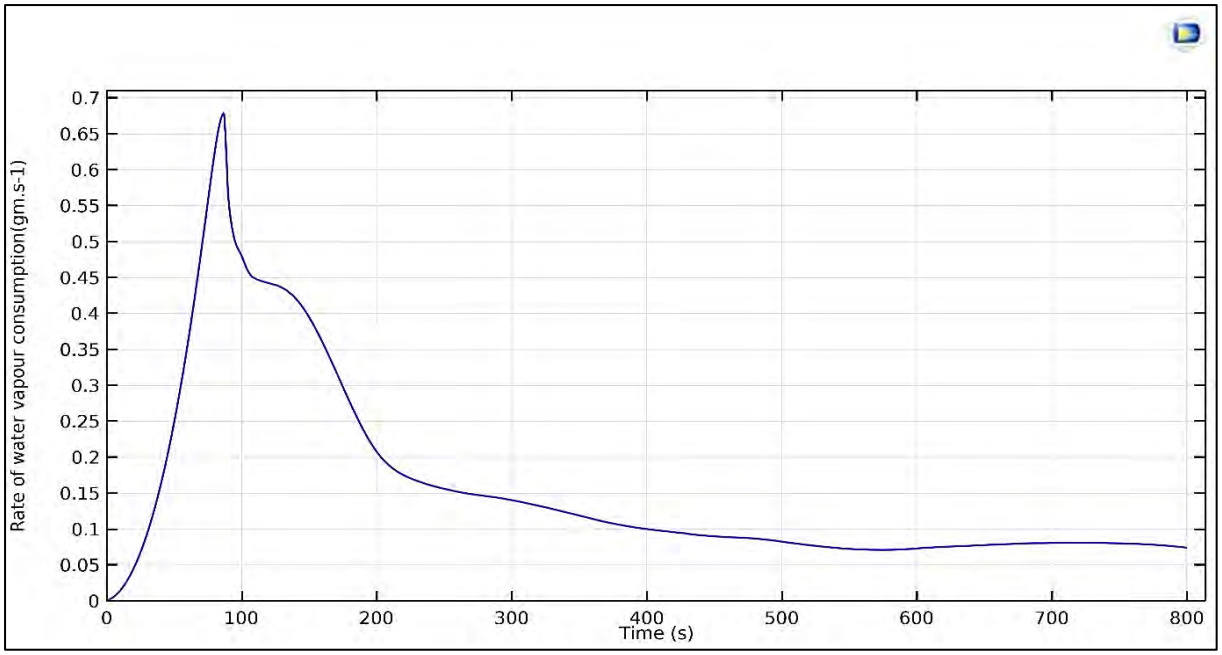

Fig. 4.47: Average rate of water vapour consumption variation

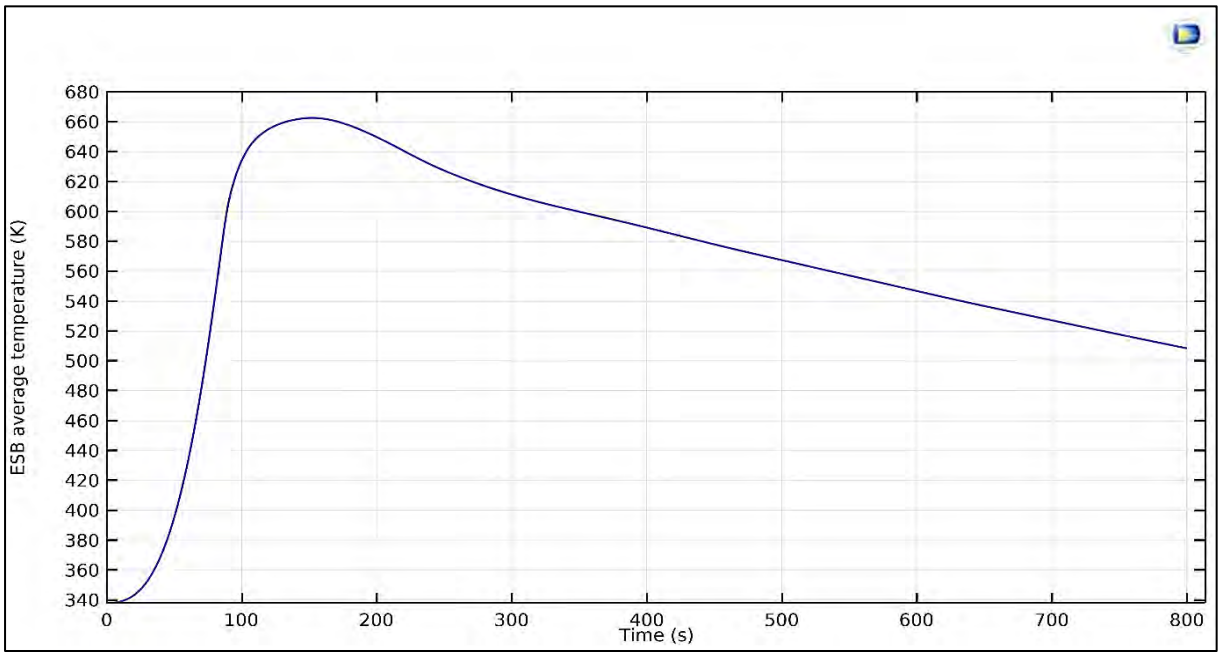

Fig. 4.48: ESB average temperature variation

Figs. 4.48 and 4.49 show variations of ESB average temperature and HTF average outlet temperature, respectively. The variations are similar to that observed in case study I. For case study II, average temperature values are lower for ESB as compared to case study I. But for case study II, average temperature values are higher for HTF as compared to case study I, as shown in Table 4.34.

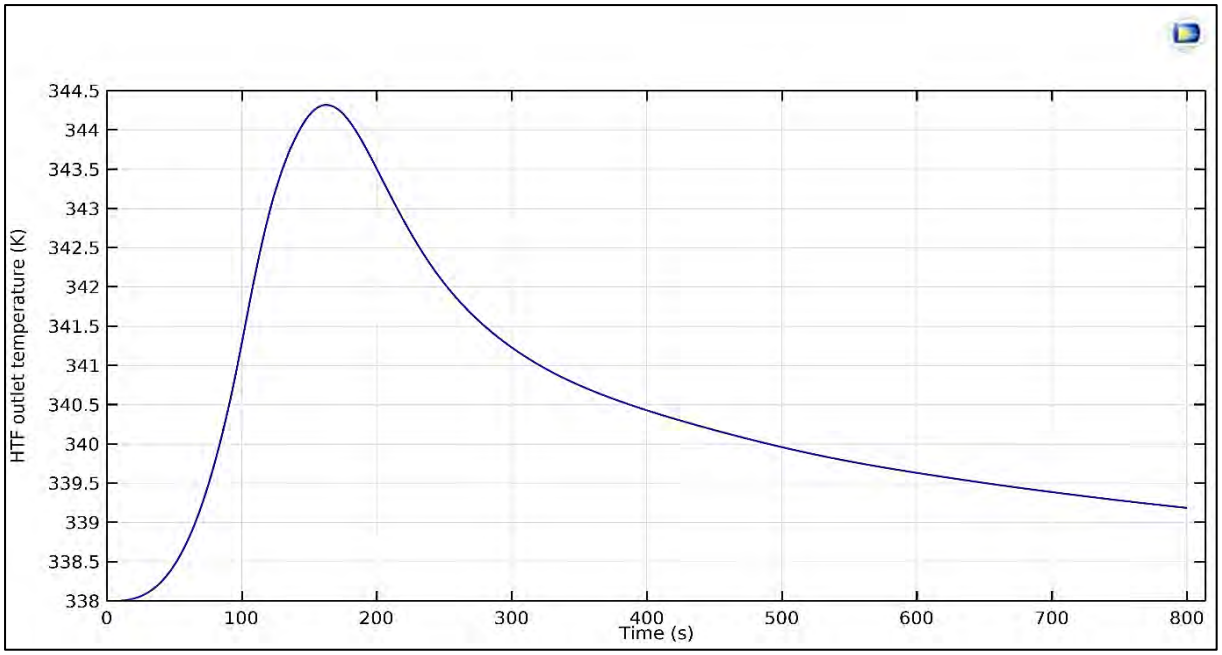

Fig. 4.49: HTF average outlet temperature variation

Table 4.34. Comparison of different temperature values for 3-D model case study I and II

Parameter	Case study I	Case study II
Maximum ESB average temperature (K)	668.89	662.62
Average ESB temperature (K)	586.64	563.62
Average ESB temperature (K) at the end of 800 s	554.24	508.45
Maximum HTF average outlet temperature (K)	343.76	344.02
Average HTF outlet temperature rise (K)	2.40	2.52
HTF average outlet temperature (K) at the end of 800 s	339.34	339.19

From Table 4.34, it is observed that peak, average and final ESB temperatures are lower in case study II. But, average HTF outlet temperature is higher in case II. This is due to increase in heat transfer between ESB and HTF because of fin addition to ESB domain. Fins addition also results in decrease in energy spent for sensible heating of ESB as shown in Table 4.35.

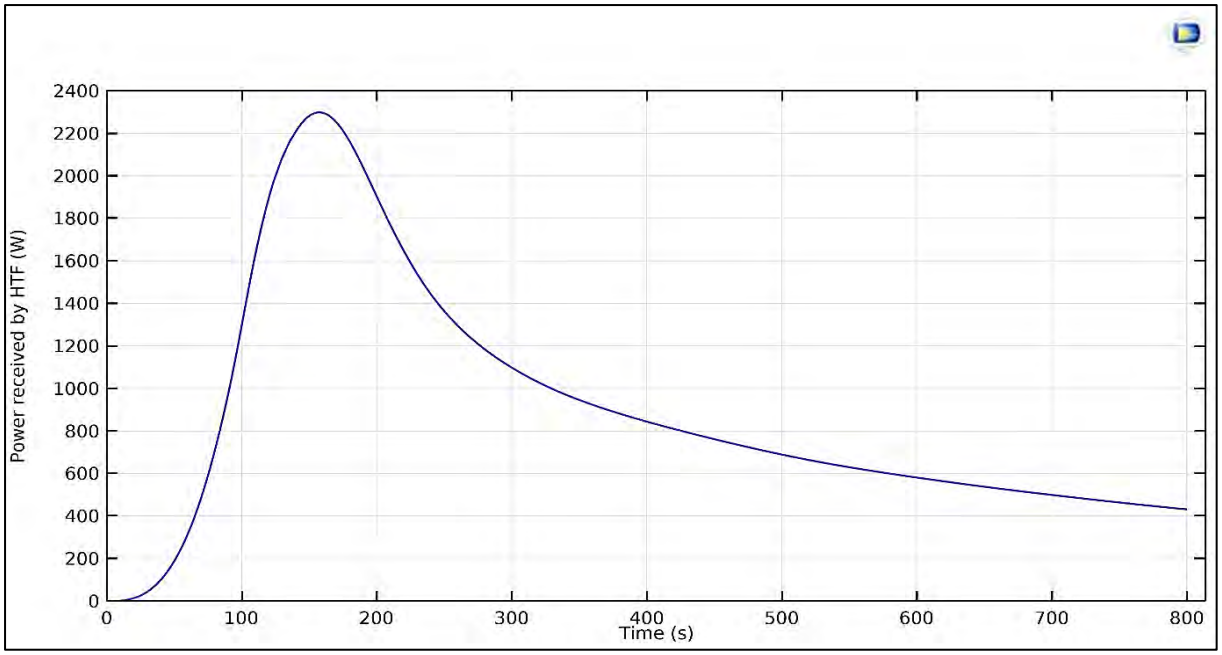

Fig. 4.50: Average power received by HTF variation

Fig. 4.50 shows average power received by HTF variation. The variation is similar to that observed in 3-D model case study I as shown in Fig. 4.42. But peak average power achieved in case study II is higher than case study I due to fins. Exact values are shown in Table 4.35.

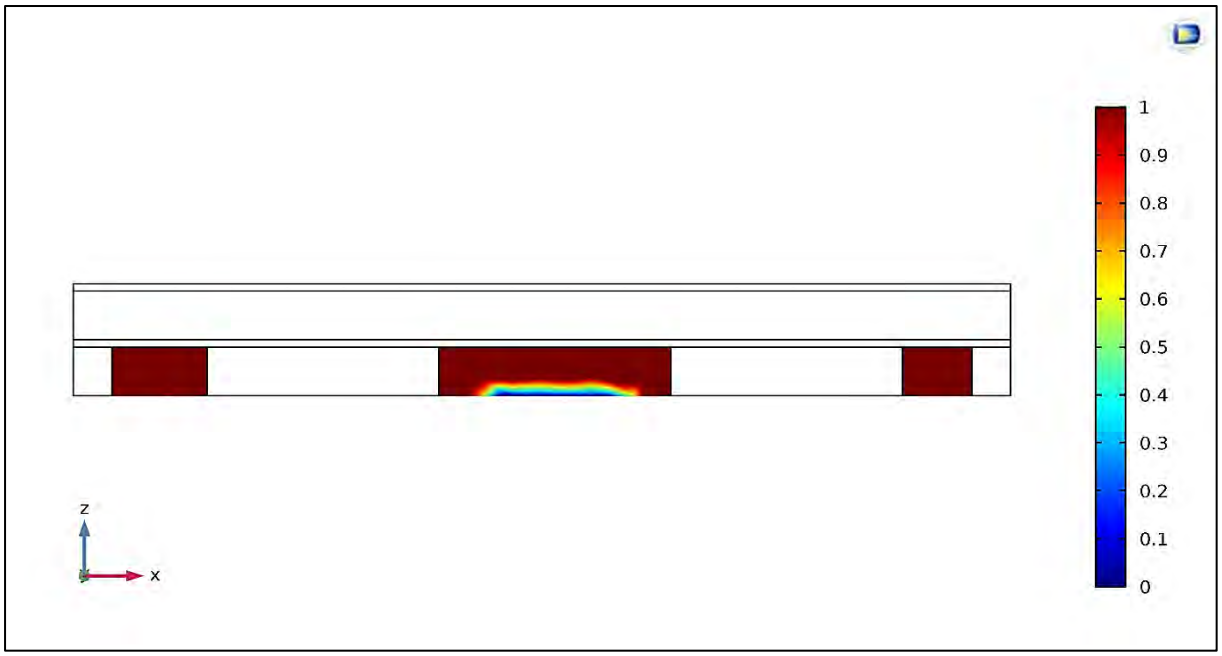

Fig. 4.51: Extent of reaction variation after 800 s

Fig. 4.51 shows extent of reaction variation across ESB after 800 s in 3-D model case study II. Comparison of 3-D model case study I and II is given in Table 4.35.

Table 4.35. Comparison between results of 3-D model case study I and II

Parameter	Case study I	Case study II
Conversion from reactant to product (%)	99.38	99.88
Total energy output from ESB (kJ)	770.41	762.87
Energy spent for sensible heating of ESB (kJ)	156.14	123.70
Energy spent for sensible heating of steel frame (kJ)	8.23	8.67
Total energy received by HTF (kJ) (Target = 500 kJ)	606.04	630.50
Efficiency of energy transfer from ESB to HTF (%)	78.66	82.65
Average peak power received by HTF (W)	2068.45 W at 154 s from start	2298.66 W at 157 s from start
HTF average outlet temperature (K) after 800 s	339.34	339.19
HTF average outlet temperature rise (K) after 800 s	1.34	1.19
Average HTF temperature rise (K) (Target = 3.052 K)	2.40	2.52
Average rate of reaction (mol m^{-3} s^{-1})	23.57	24.03
Total water vapour consumption (g)	126.99	125.75
Average water vapour consumption rate (g s^{-1})	0.16	0.16

It is observed from Table 4.35 that due to volume occupied by fins in ESB, total energy output from ESB slightly decreases from 770.41 kJ in case study I to 762.87 kJ in study II. Energy spent in sensible heating of ESB is considerably decreased in case study II. Due to addition of fins, steel frame thermal mass increased and hence the energy spent for sensible heating of steel frame is increased in case study II. Because of the above reasons, total energy received by HTF and efficiency of energy transfer from ESB to HTF are higher in case study II. Due to addition of fins, peak power received by HTF and average HTF outlet temperature rise are higher in case study II. As conversion in both the cases are almost same, average rate of reaction, average water vapour consumption rate and total water vapour consumption are almost same.

4.3.3 Case study III: 3-D model fins in ESB and HTF domain

For present study, same problem setup is used as that of case study II. Only difference between case study II and III is of 3-D geometry. Dimensions of fins in HTF domain are not yet finalised. Thus, for present study, assumed fin dimensions are given in Table 4.36. Dimensions of fins in ESB domain are same as case study II.

Objective of present study is to study the effect of providing fins in ESB and HTF domain on performance of hydration reaction. 3-D geometry with fins in ESB and HTF domain is shown in Fig. 4.52 and 4.53.

Table 4.36. Dimension of fins in HTF domain
(all dimensions are in mm)

Length of fins	182
Width of fins	3
Height of fins	5
Total number of fins	17
Centre to centre distance between consecutive fins	10
Length of HTF domain	182
Width of HTF domaim	224
Height of HTF domain	10

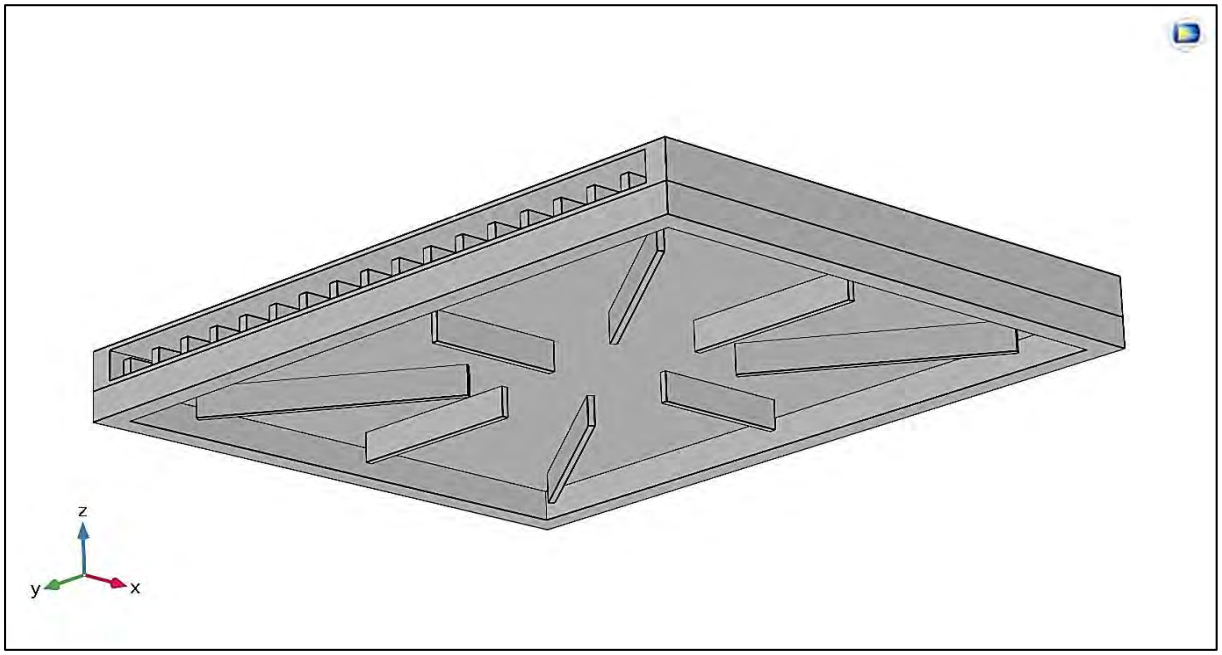

Fig. 4.52: Fins in HTF and ESB domain

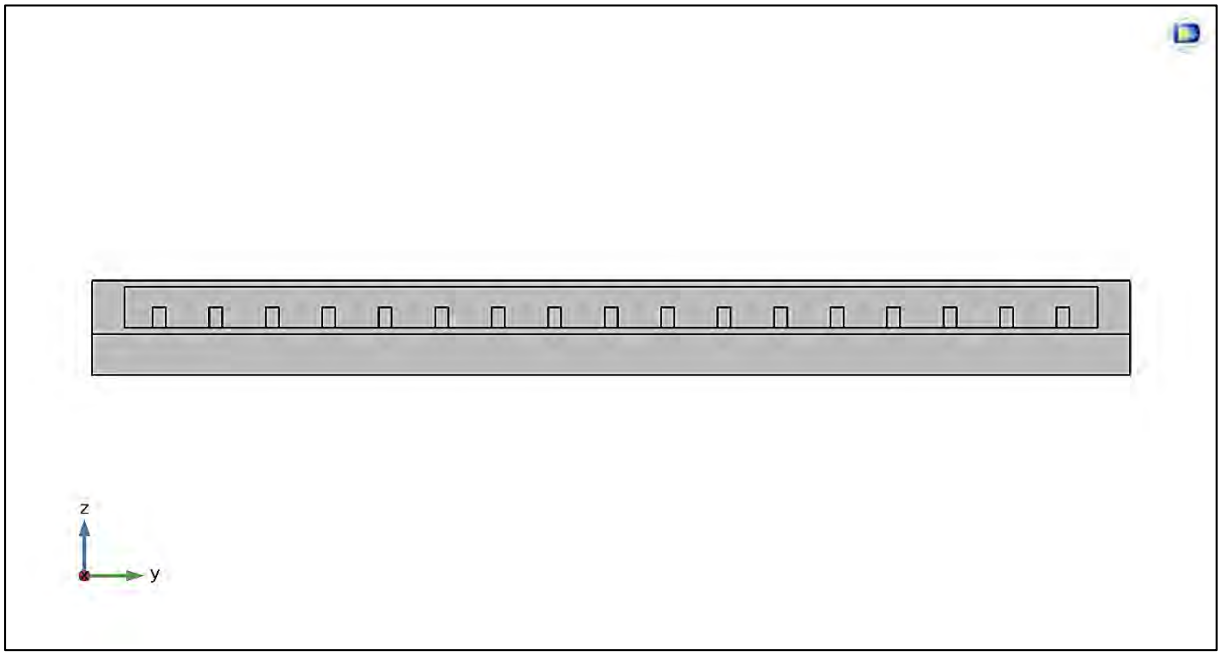

Fig. 4.53: Arrangement of fins in HTF domain

Table 4.37. Operating conditions for 3-D simulation

Initial temperature of ESB	338 K (65 ˚C)
Water vapour supply pressure	47.13 kPa (P_{sat} corresponding to 80 ˚C)
HTF inlet temperature	338 K (65 ˚C)
HTF flow rate	10 ltr min^{-1}
ESB porosity	40 %
ESB average particle diameter	150 µm
Hydration reaction time	400 s

Based on operating conditions shown in Table 4.37, simulation is done and following results are obtained.

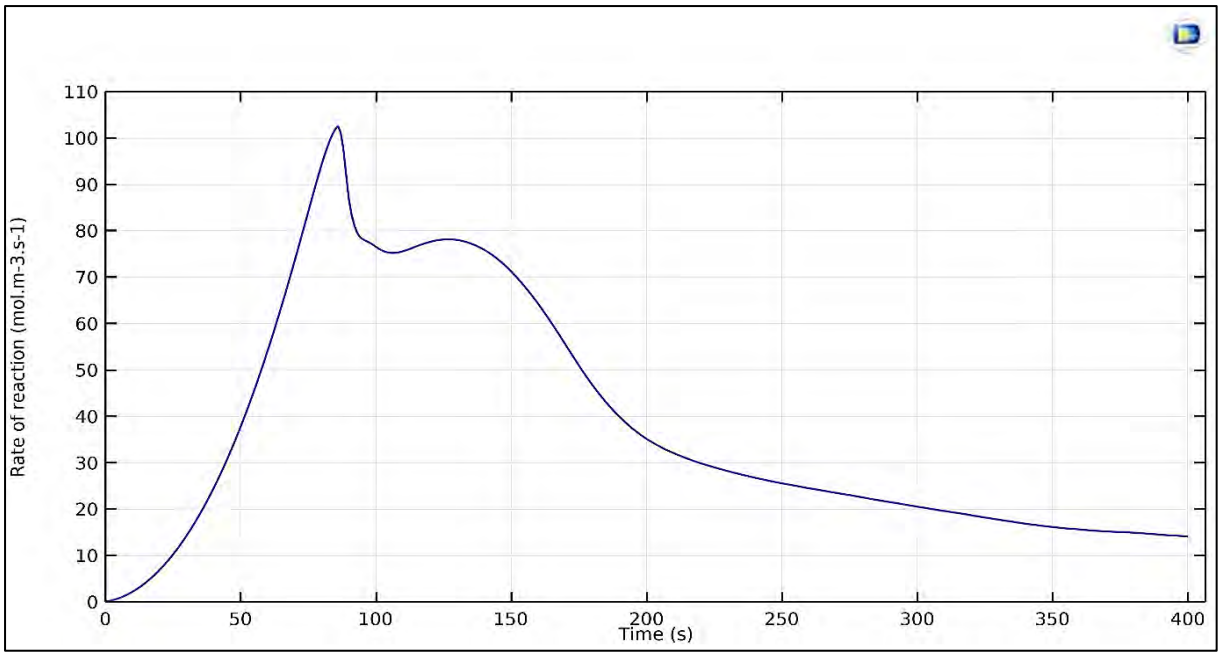

Fig. 4.54: Average rate of reaction variation

Figs. 4.54 and 4.55 show variations in average rate of reaction and average water vapour consumption, respectively. The variations are similar to that observed in 3-D model in case study II as shown in Figs. 4.49 and 4.50. But as compared to 3-D model case study II, average rate of reaction is higher in case study III which is shown in Table 4.39. The increase in average rate of reaction can be attributed to increase in surface area of heat transfer between HTF and ESB via steel frame separating the two domains.

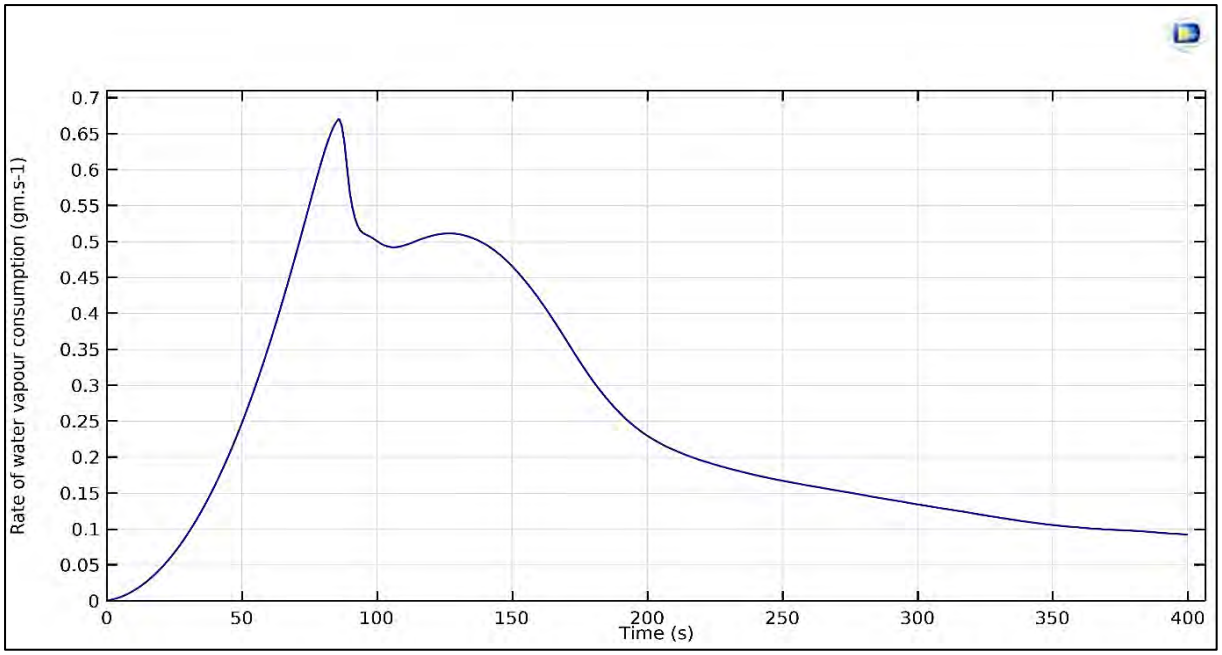

Fig. 4.55: Average rate of water vapour consumption variation

As average rate of reaction increases, average rate of water vapour consumption also increases. And since average rate of water vapour consumption is higher in case study III, more amount of water vapour is consumed as shown in Table 4.39.

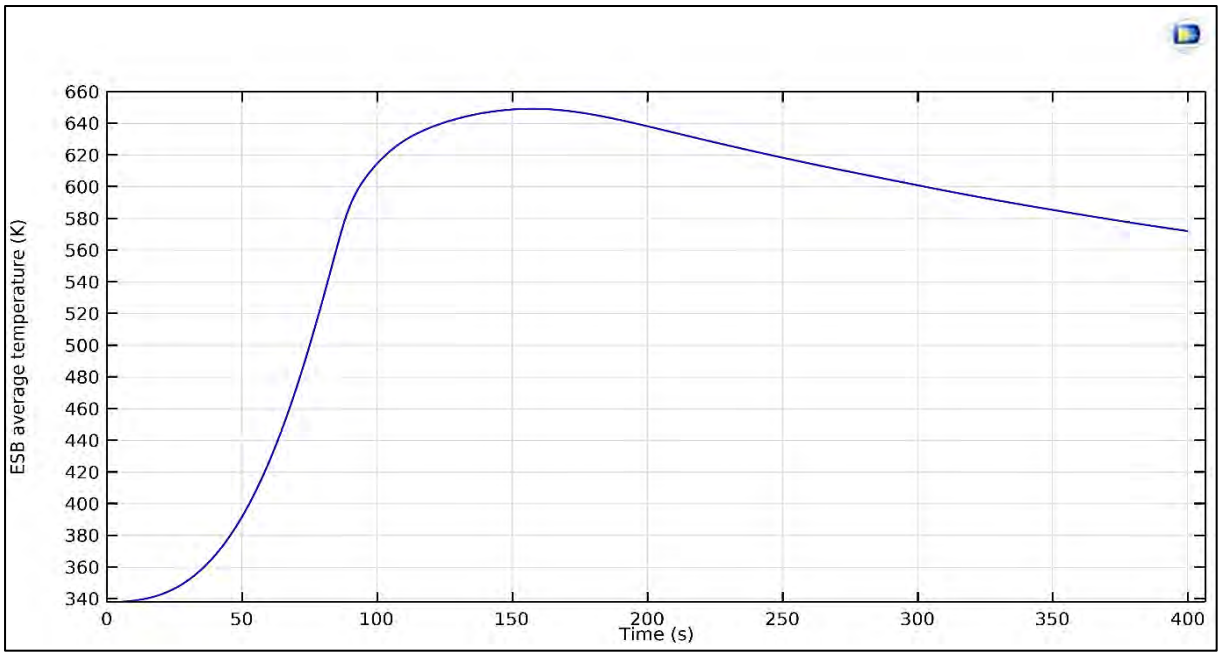

Fig. 4.56: ESB average temperature variation

Fig. 4.56 shows trend of ESB average temperature variation in present study. This variation is similar to that of Fig. 4.51 of case study II. But different average temperature values observed in case study III are lower than that of case study II which are shown in Table 4.38.

Table 4.38. Comparison between different temperature values of 3-D model in case study II and III

Parameter	Case study II	Case study III
Maximum ESB average temperature (K)	662.62	649.30
Average ESB temperature (K)	563.62	568.68
Average ESB temperature (K) at the end of simulation	508.45 (at the end of 800 s)	572.14 (at the end of 400 s)
Maximum HTF average outlet temperature (K)	344.02	344.66
Average HTF outlet temperature rise (K)	2.52	3.23
HTF average outlet temperature (K) at the end of simulation	339.19 (at the end of 800 s)	339.98 (at the end of 400 s)

It is observed from Table 4.38 that even though maximum ESB average temperature is lower in case study III, average ESB temperature is higher. Also, final ESB temperature in case study III is significantly higher than that in case study II. This is due to increase in average rate of reaction in case study III as shown in Table. 4.39. This results in increase in energy spent for sensible heating of ESB. Average and final HTF outlet temperatures are also higher in case study III.

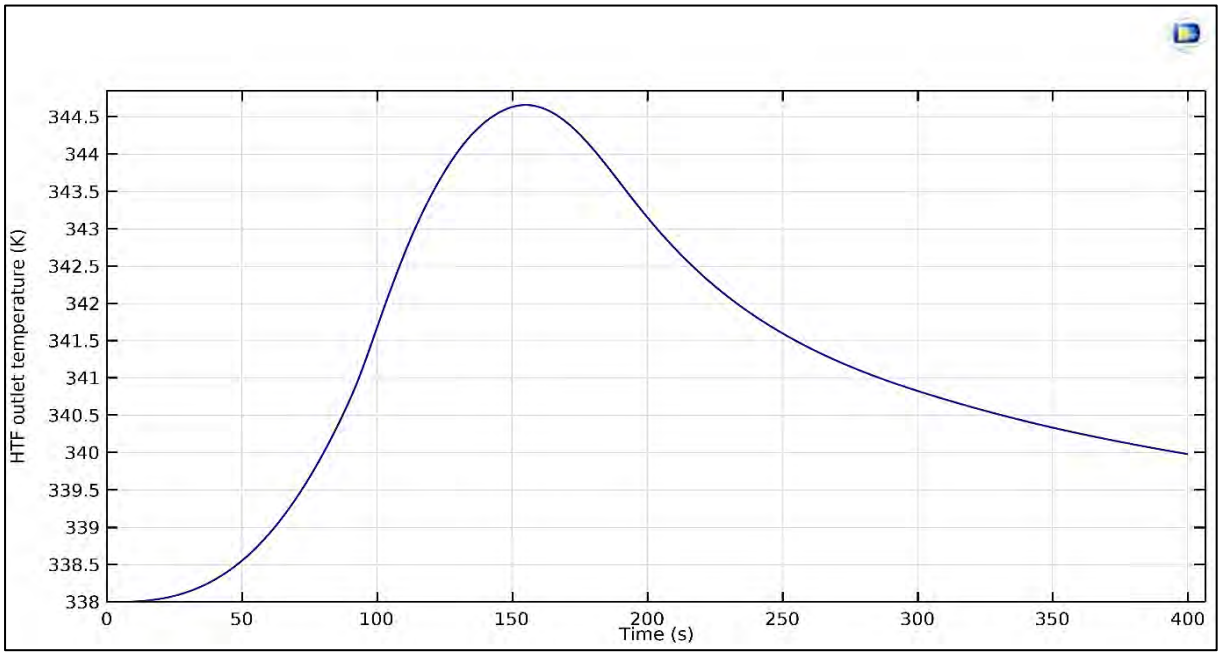

Fig. 4.57: HTF average outlet temperature variation

Fig. 4.57 shows trend of HTF average outlet temperature variation in present study. This variation is similar to that of Fig. 4.48 of case study II. But different average temperature values observed in case study III are higher than that of case study II which are shown in Table 4.38.

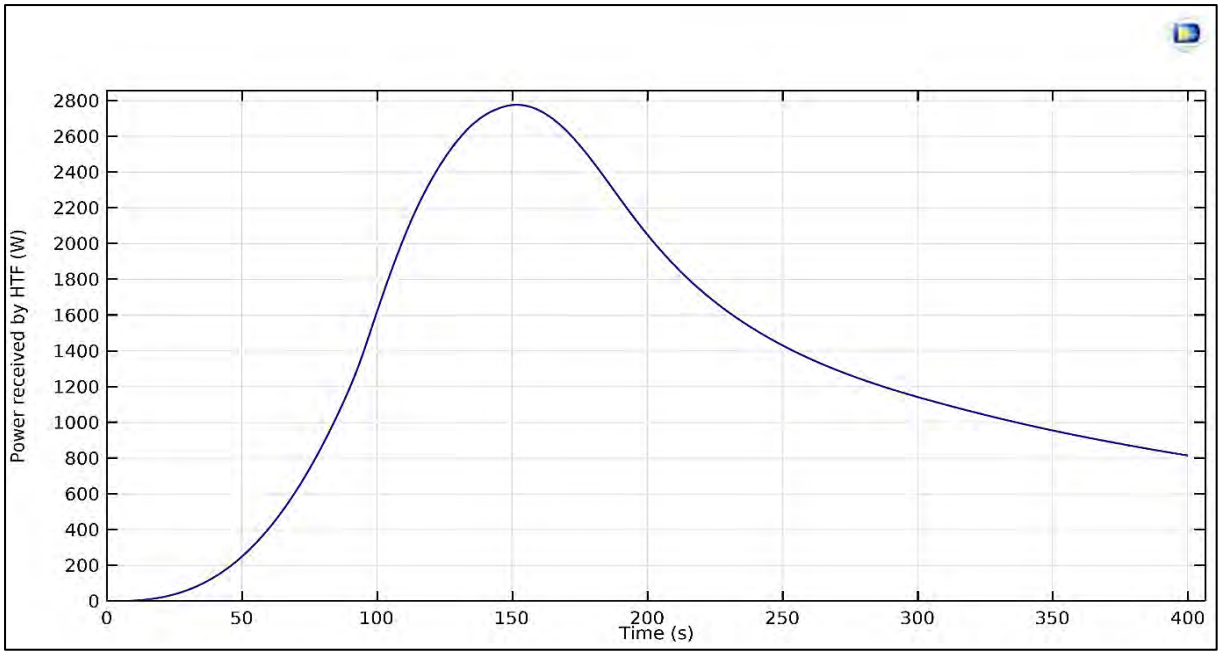

Fig. 4.58: Average power received by HTF variation

Fig. 4.58 shows average power received by HTF variation. This variation trend is similar to variation observed in 3-D model case study II as shown in Fig. 4.50. Peak average power received by HTF variation is higher in case study III as shown in Table 4.39 due to higher average rate of reaction.

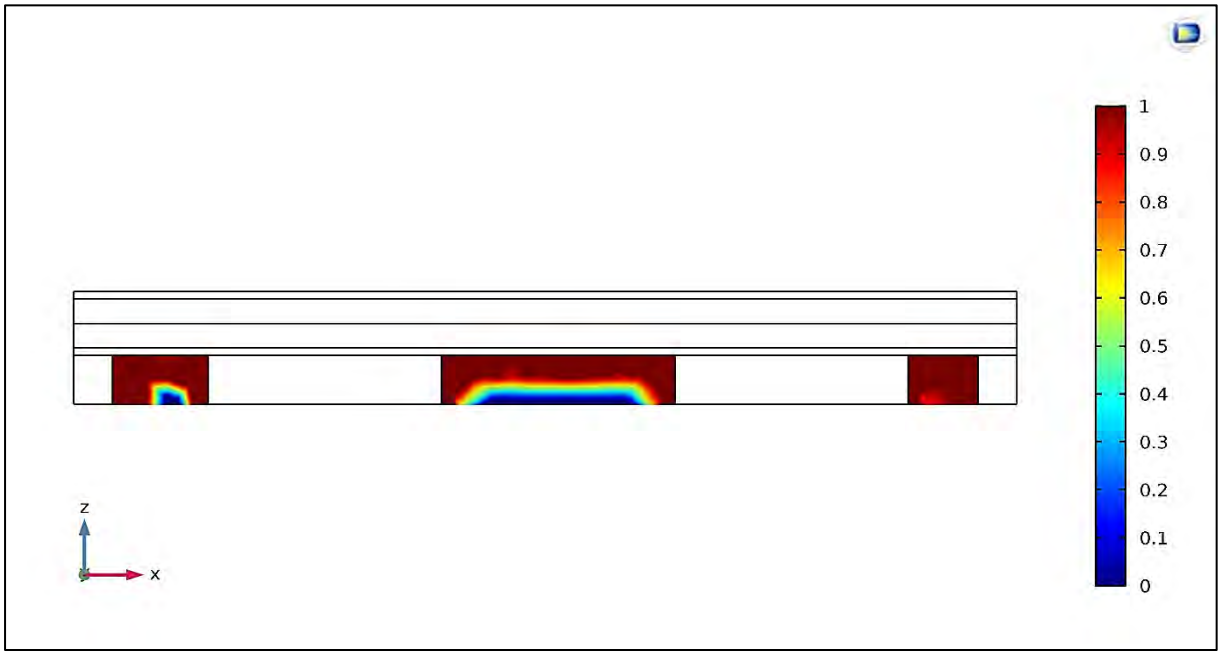

Fig. 4.59: Extent of reaction varaiation after 400 s

Fig. 4.59 shows extent of reaction across ESB after 400 s in 3-D model case study III. Comparison of 3-D model case study I and II is given in Table 4.39.

Table 4.39. Comparison of 3-D model case study II and III results

Parameter	Case study II	Case study III
Time required for 100% conversion (s)	~800	~487
Time of hydration reaction for present study (s)	800	400
Conversion from reactant to product (%)	99.9	85.49
Total energy output from ESB (kJ)	762.87	598.31
Energy spent for sensible heating of ESB (kJ)	123.70	144.41
Energy spent for sensible heating of steel frame (kJ)	8.67	14.32
Total energy received by HTF (kJ) (Target = 500 kJ)	630.50	439.58
Efficiency of energy transfer from ESB to HTF (%)	82.65	73.47
Average peak power received by HTF (W)	2298.66 W at 157 s from start	2776.92 W at 152 s from start
HTF average outlet temperature (K) after 400 s	339.19	339.98
HTF average outlet temperature rise (K) after 400 s	1.19	1.98
Average HTF temperature rise (K) (Target = 3.052 K)	2.52	3.23
Average rate of reaction (mol m^{-3} s^{-1})	24.03	37.68
Total water vapour consumption (g)	125.75	98.58
Average water vapour consumption rate (g s^{-1})	0.16	0.25

In case study II, the time taken for 100 % conversion of reactant into product is around 800 s. But in case study III, full conversion takes place in 487 s. It proves the effectiveness of fin addition in HTF domain. Reaction time for hydration is taken as 400 s in case study III after observing the reaction completion time as 487 s. So, Table 4.39 shows comparison between different reaction parameters for case study II (with fins only in ESB domain and hydration reaction time of 800s) and case study III (with fins in both ESB and HTF domain and hydration reaction time of 400s).

For case study III, 85.49 % conversion is observed in 400 s as opposed to 99.9 % conversion in case study II at the end of 800 s, as shown in Table 4.38. Hence even though average reaction rate is higher, total energy output from ESB is lower in case study III. ESB average temperature is higher in case study III as shown in Table 4.39 which results in higher energy requirement for sensible heating of ESB. Due to increase in thermal mass of system because of fins in HTF domain, energy required for sensible heating of steel frame is also higher in case study III. Thus, total energy received by HTF and efficiency of energy transfer from ESB to HTF are lower in case study III.

But due to higher reaction rates, peak power received by HTF is significantly higher in case study III. Average rise in HTF temperature is also higher in case study III. Due to increase in reaction rates, average rate of reaction and average water vapour consumption is also higher in case study III. Since only 85.49 % conversion has occurred in case study III, total water vapour consumption is lower as compared to case study II.

Dimensions of fins in HTF domain are not finalized yet. But, as the 3-D model is ready it can be used with slight modifications in future for finalized dimensions of fins. Same model can also be used to study the effect of changing fin dimensions on performance of hydration reaction.

CHAPTER 5

DEHYDRATION REACTION SIMULATIONS

After detailed study of dehydration reaction as shown in chapter 4, dehydration reaction is also studied on similar lines in present chapter. To start the simulations, first simplified 2-D model is setup. Effect of variation of different operating parameters on dehydration reaction performance is studied by performing different parametric studies on the 2-D model. Based on discussions of 2-D parametric studies' results, operating parameters are revised which are given in subsequent sections. As per revised operating conditions, 3-D model simulations are to be performed.

5.1 Assumptions for simulations of dehydration reaction

1. ESB is modelled as porous medium with uniform distribution of material.
2. As dehydration reaction proceeds with time, $Ca(OH)_2$ gets converted into CaO. Hence solid phase of ESB is combination of $Ca(OH)_2$ and CaO depending on extent of reaction. Thus, all the required thermophysical properties of solid phase of ESB are assumed as a linear function of extent of reaction.
   For example,
   density of solid phase of ESB = (1-X)*density of $Ca(OH)_2$ + X*density of CaO
   where X is extent of reaction.
3. Average particle diameter of ESB particles and ESB porosity remains constant throughout the reaction.
4. At the start of simulation, it is assumed that only $Ca(OH)_2$ is present in ESB.
5. Water vapour released is assumed to be uniformly distributed throughout the ESB domain for whole reaction time.
6. At the start, ESB pressure is assumed to be equal to water vapour outlet pressure. Time required for ESB pressure (which will be equal to equilibrium pressure for corresponding ESB temperature) to reach water vapour outlet pressure is neglected.
7. At the start, ESB is considered to be at uniform temperature. Also, local thermal equilibrium is assumed between solid and vapour phase of ESB.
8. Water vapour outlet pressure remains constant throughout the reaction.
9. The inlet temperature of EG is constant throughout the reaction.
10. Except for water vapour outlet boundary/surface and EG inlet and outlet boundaries/surfaces (depending on 2-D/3-D case), all other exterior boundaries are insulated.
11. For dehydration reaction, initial temperature of ESB and EG is assumed to be same. In case of cold start of HEV, it is assumed that ESB will be preheated for sufficient time so that it attains the temperature of EG.
12. Different parameters shown in plots are calculated as average values by taking integrals at appropriate locations.

For example, in 2-D simulations, ESB average tempreture is calculated by taking surface integral of entire ESB domain. EG average outlet temperature is calculated by taking line integral at the EG outlet.

13. ESB particle agglomeration and degradation in material properties are not taken into account in the present study.

5.2 2-D simulations

To understand effect of different operating parameters on dehydration reaction, simplified 2-D model is created and different parametric studies are performed.

5.2.1 2-D model: Geometry and operating conditions

Based on the prototype of design model of flat ESB, a simplified 2-D model is created as shown in Fig. 5.1. Energy Storage Bed (ESB) domain is modelled as porous medium. Water vapour leaves ESB through boundary at the bottom. ESB domain is separated from EG domain by steel plate. Dimensions of 2-D model are taken from design of flat ESB and are given in Table 5.1.

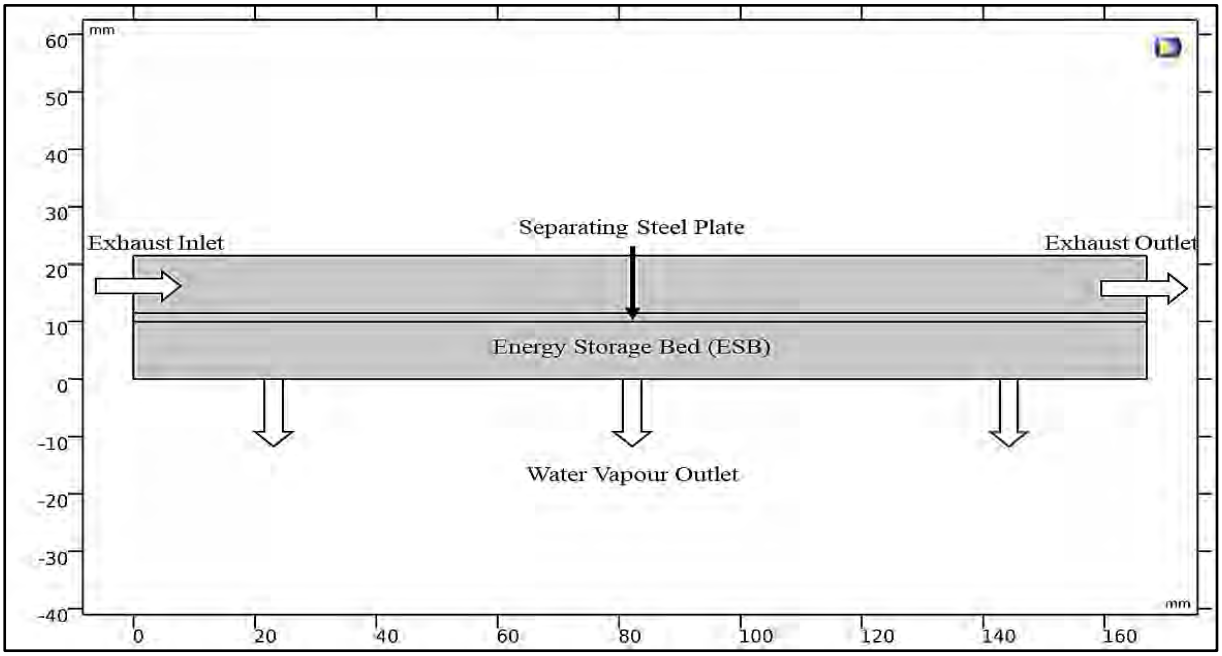

Fig. 5.1: Simplified 2-D model of ESB

Table 5.1. Dimension of 2-D model of ESB

Length of ESB domain	167 mm
Height of ESB domain	10 mm
Height of Steel Plate	1.5 mm
Height of EG domain	10 mm

Table 5.2 gives different operating conditions for 2-D simulations provided by Faurecia team.

Table 5.2. Operating conditions for simulation

Initial temperature of ESB	623 to 1073 K (350 to 800˚C)
Water vapour outlet pressure	To be decided accordingly
EG (EG) inlet temperature	623 to 1073 K (350 to 800˚C)
EG mass flow rate	100 to 350 kg hr^{-1}
ESB porosity	40 to 60 %
ESB average particle diameter	30 μm and 150 μm
Dehydration reaction time	To be decided accordingly

5.2.2 Results and discussions

To understand the effect of each of the parameter given in Table 5.2 on overall dehydration reaction performance, parametric study of each parameter is carried out. Other operating conditions are kept constant while studying the effect of varying a parameter. Results of these parametric studies are presented in subsequent sections.

5.2.2.1 Variation in water vapour outlet pressure

In dehydration reaction, the water vapor is generated by heating the liquid water stored in GSB and is supplied to ESB. Water vapour outlet pressure is equal to the saturation pressure corresponding to temperature of water in GSB. Temperature values as shown in Table 5.3 are selected for simulation.

Table 5.3. Water vapour outlet pressure values for simulation

Temperature of water vapour in GSB (˚C)	Temperature of water vapour in GSB (K)	Corresponding saturation pressure (kPa)
10	283	1.22
20	293	2.32
30	303	4.21
40	313	7.33

The other operating conditions are considered constant and shown in Table 5.4.

Table 5.4. Other operating conditions for simulation

Initial temperature of ESB	823 K (550 ˚C)
EG (EG) inlet temperature	823 K (550 ˚C)
EG mass flow rate	200 kg hr^{-1}
ESB porosity	60 %
ESB average particle diameter	30 μm
Dehydration reaction time	400 s

Based on above operating conditions simulations are performed and following results are obtained.

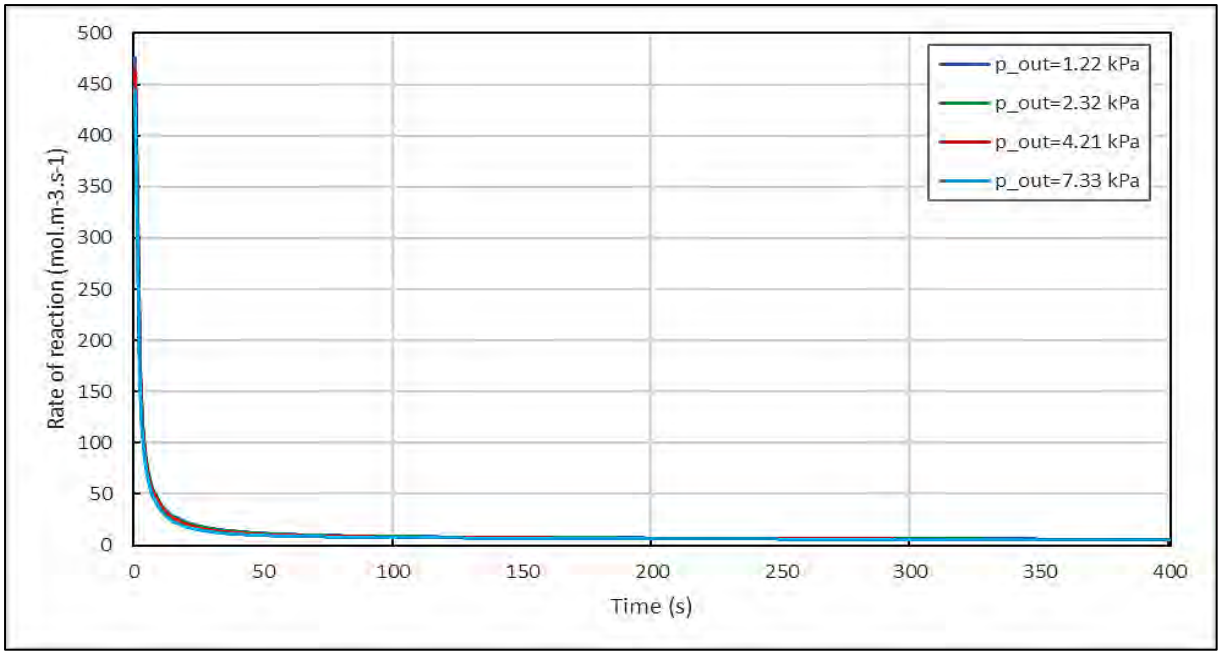

Fig. 5.2: Average rate of reaction variation

As water vapour outlet pressure (p_out) is reduced, pressure difference between ESB and GSB is increased which results in higher reaction rates as shown in Figs. 5.2 and 5.3.

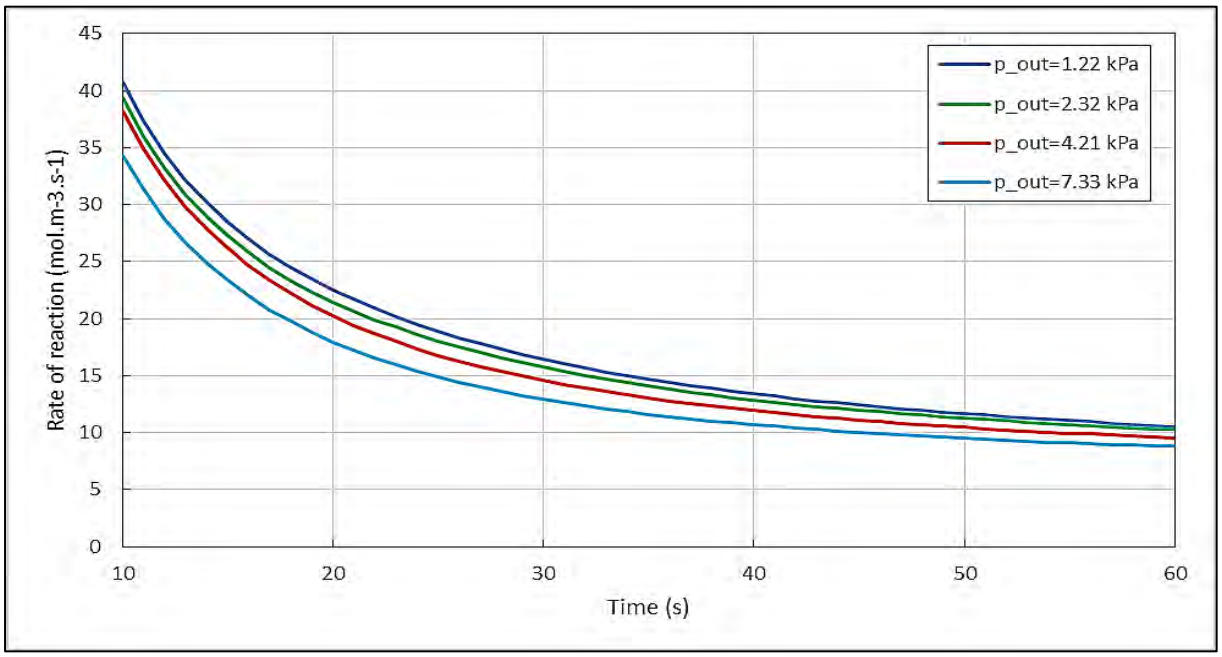

Fig. 5.3: Average rate of reaction variation (close-up view)

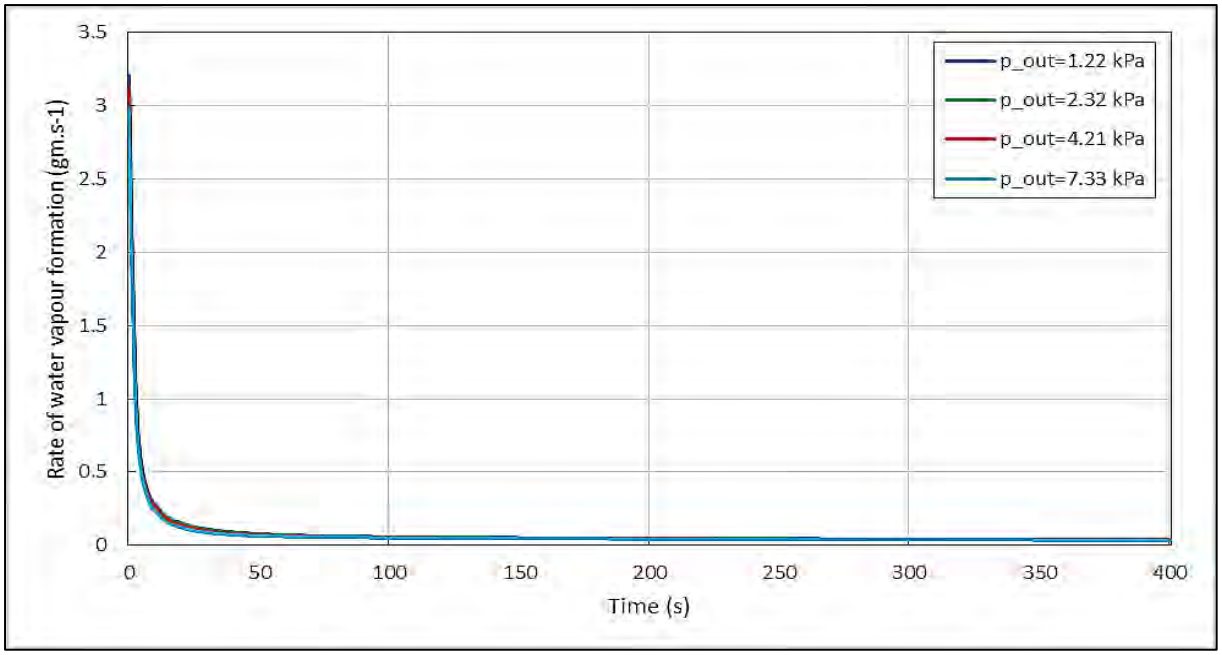

Fig. 5.4: Average rate of water vapour formation variation

At higher reaction rates, more amount of water vapour is formed in ESB which is in accordance with Figs. 5.4 and 5.5.

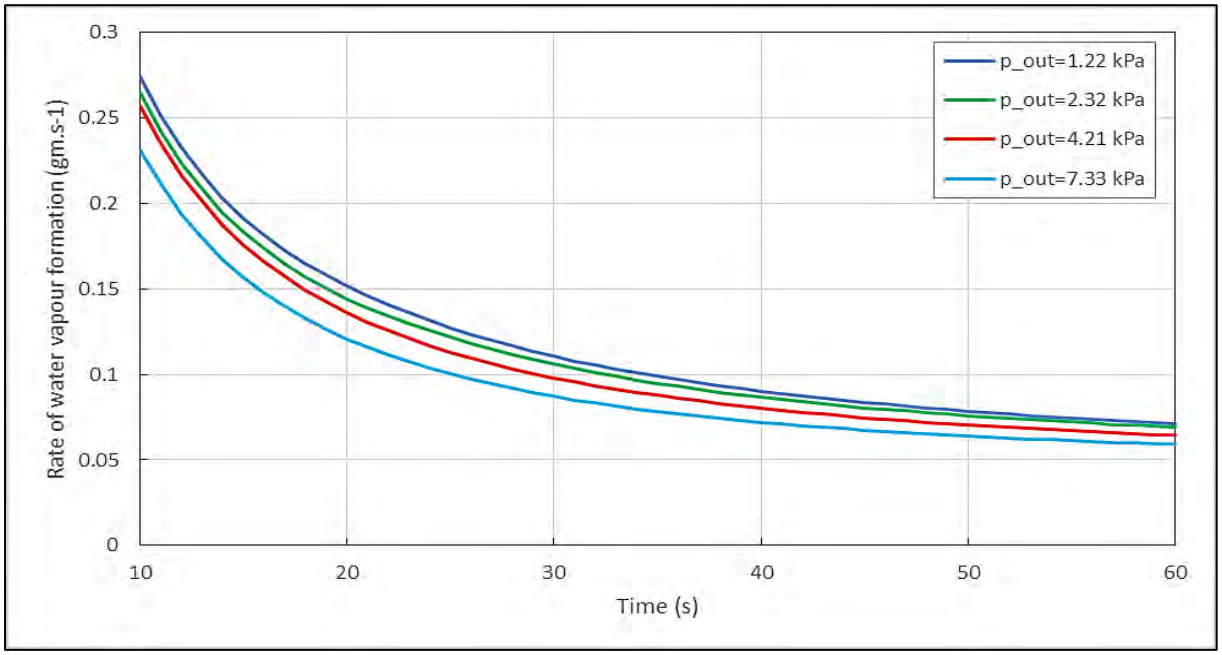

Fig. 5.5: Average rate of water vapour formation variation (close-up view)

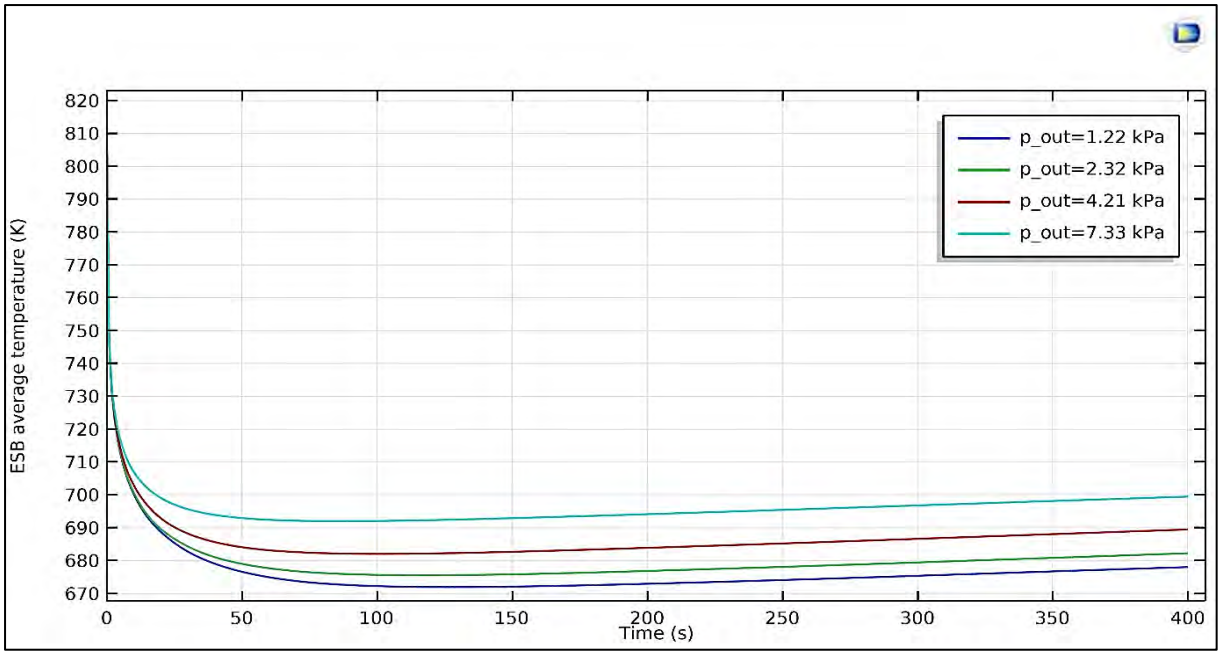

Fig. 5.6: ESB average temperature variation

At the start of dehydration reaction, rate of reaction is higher. Hence higher drop in ESB average temperature as well as EG average outlet temperature are observed as shown in Figs. 5.6 and 5.7. After around 60 s from the start of dehydration, reaction rate becomes almost constant for the rest of reaction time. In this period, ESB average temperature slightly increases as rate of temperature rise due to forced convection between EG and ESB is higher than the rate of temperature drop due to dehydration reaction. After around 60 s from start, EG average outlet temperature increases due to lower reaction rate, whereas inlet temperature of EG is kept constant at 823 K.

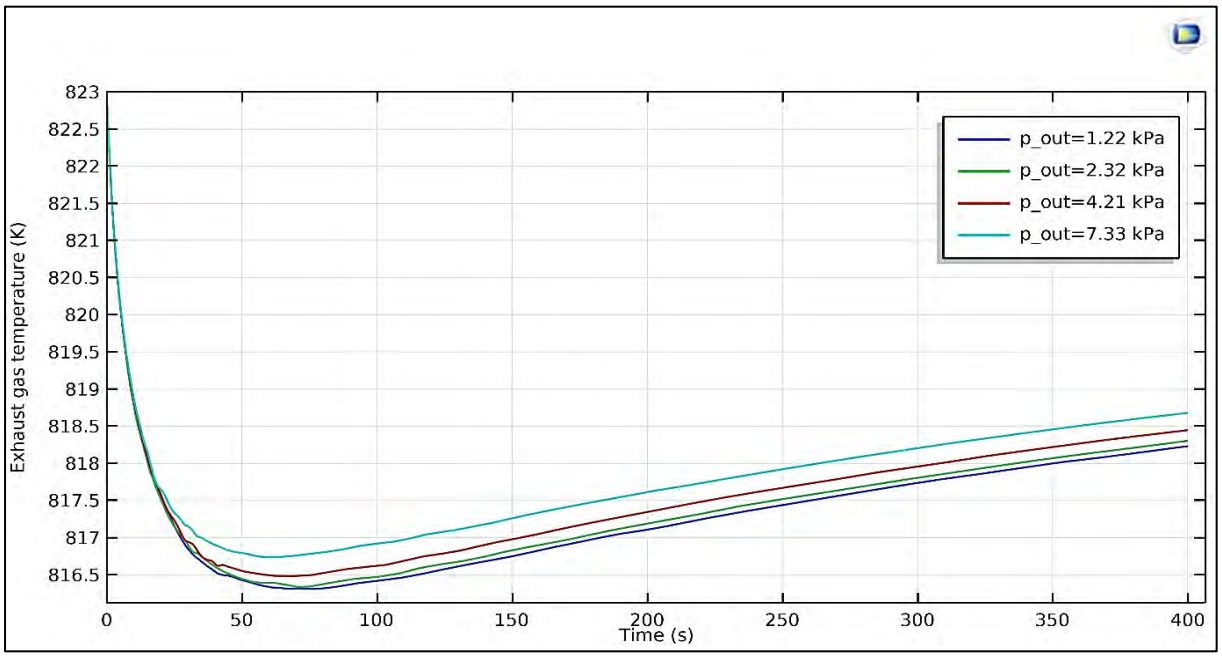

Fig. 5.7: EG average outlet temperature variation

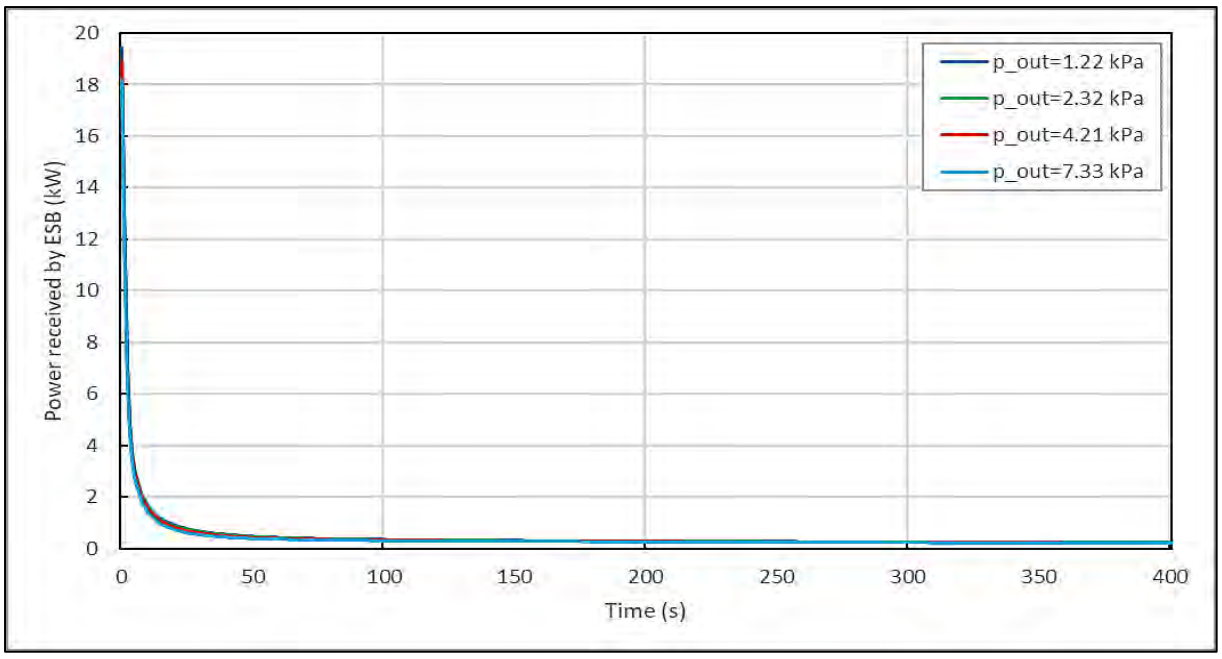

Fig. 5.8: Average power received by ESB variation

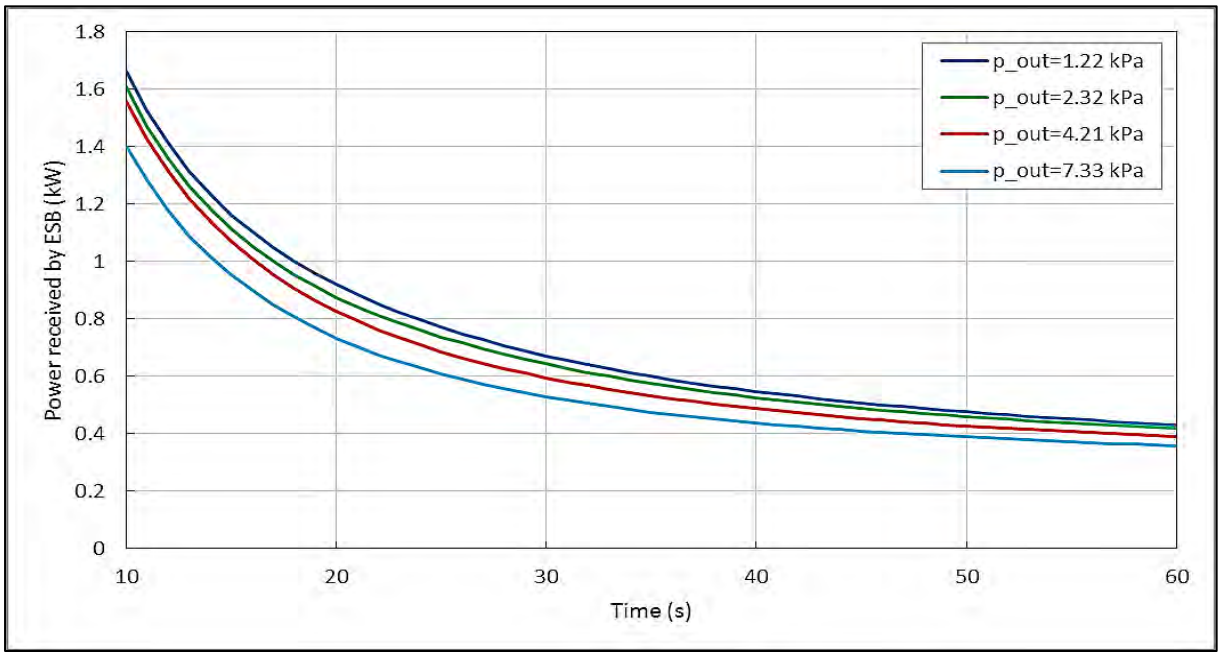

Fig. 5.9: Average power received by ESB variation (close-up view)

Reaction rate is higher for lower water vapour outlet pressure (p_out). Thus, average power received by ESB is also higher for lower water vapour outlet pressure as shown in Figs. 5.8 and 5.9. This results in higher amount of energy stored in ESB as shown in Table 5.5.

Table 5.5. Effect of variation of water vapour outlet pressure

Temperature of water vapour in GSB (˚C)	Respective Saturation Pressure (kPa)	Final ESB average temperature (K) ($T_{initial}$ = 823 K)	Total energy lost by EG to ESB (kJ)	Total energy for sensible cooling of ESB (kJ)	Total energy stored in ESB (kJ) (Target = 500 kJ)
10	1.22	678.04	127.60	57.71	185.31
20	2.32	682.25	124.57	56.32	180.88
30	4.21	689.49	120.67	53.94	174.61
40	7.33	699.49	112.57	50.61	163.18

But it is noted that due to vicinity of GSB to flowing EG in vehicle, it is difficult to maintain very low temperatures on GSB side. So, the condensation temperature of water is considered as 40 ˚C corresponding to which the water vapour outlet pressure is 7.33 kPa for further simulations.

5.2.2.2 Variation in EG inlet temperature

Based on operating conditions provided in Table 3, EG supply temperature is considered in the range of 350-800 ˚C. The chosen values are given in Table 5.6. For present simulation, it is assumed that ESB is preheated with the help of EG so that ESB temperature increases from ambient temperature to EG inlet temperature. So, EG inlet temperature is equal to initial ESB temperature.

Table 5.6. Initial EG temperature values for simulation

Initial EG temperature (˚C)	Initial EG temperature (K)
350	623
450	723
550	823
650	923

Other operating conditions for simulation are given in Table 5.7.

Table 5.7. Other operating conditions for simulation

Initial temperature of ESB	Equal to EG supply temperature
Water vapour outlet pressure	1.22 kPa (P_{sat} corresponding to 10 ˚C)
EG mass flow rate	200 kg hr^{-1}
ESB porosity	60 %
ESB average particle diameter	30 μm
Dehydration reaction time	400 s

Based on above operating conditions simulations are performed and following results are obtained.

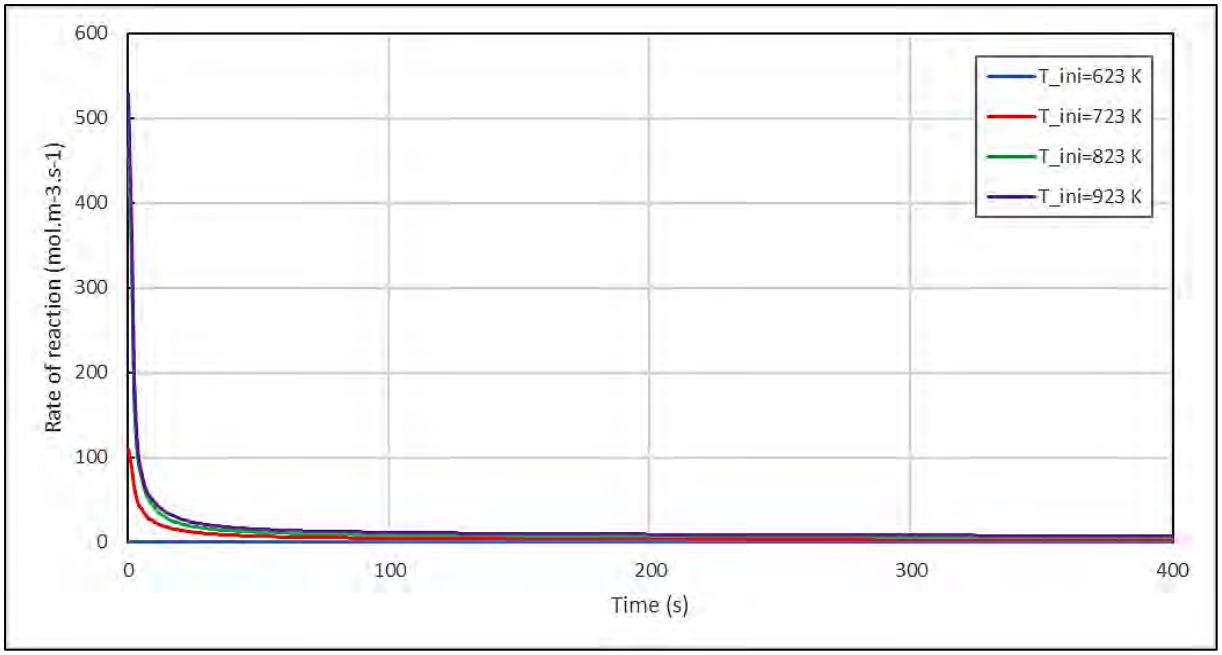

Fig. 5.10: Average rate of reaction variation

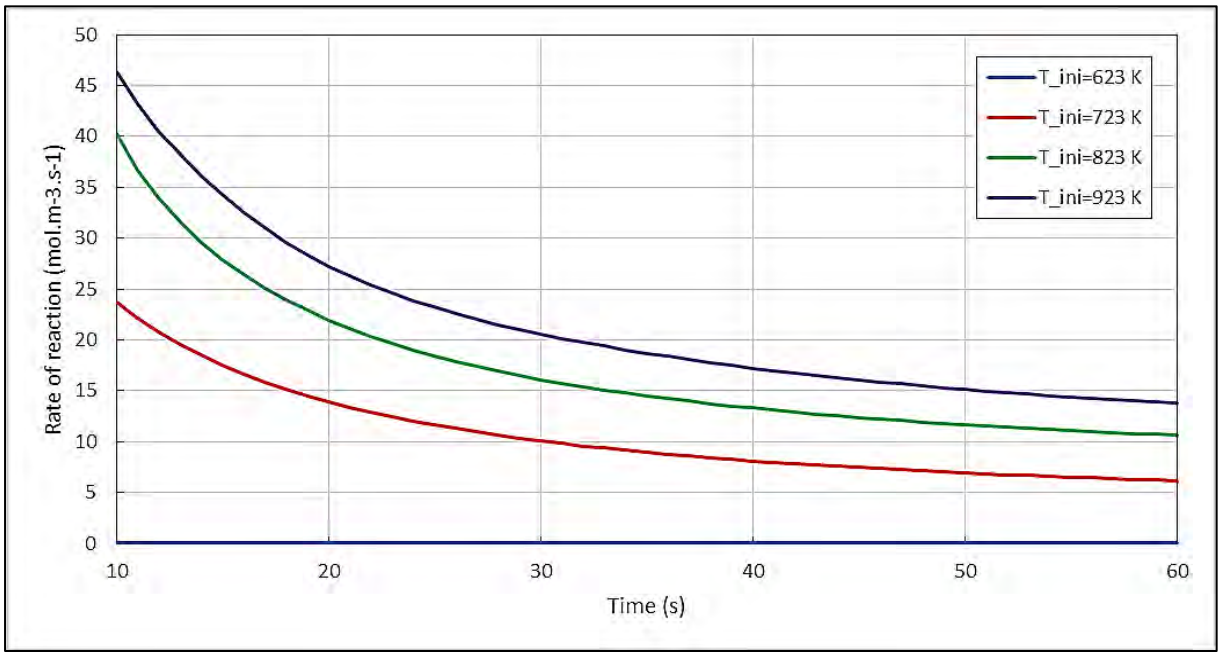

Fig. 5.11: Average rate of reaction variation (close-up view)

From Figs. 5.10 and 5.11, it is observed in case of initial ESB temprature value (T_ini) of 623 K that average rate of reaction is very low. But as T_ini values are increased to 723 K and above, significant change in average rate of reaction is noticed as shown in Figs. 5.10 and 5.11. But, it is not favourable to work at high temperatures which adds to the cost of system design. Hence, optimum value of T_ini is to be chosen.

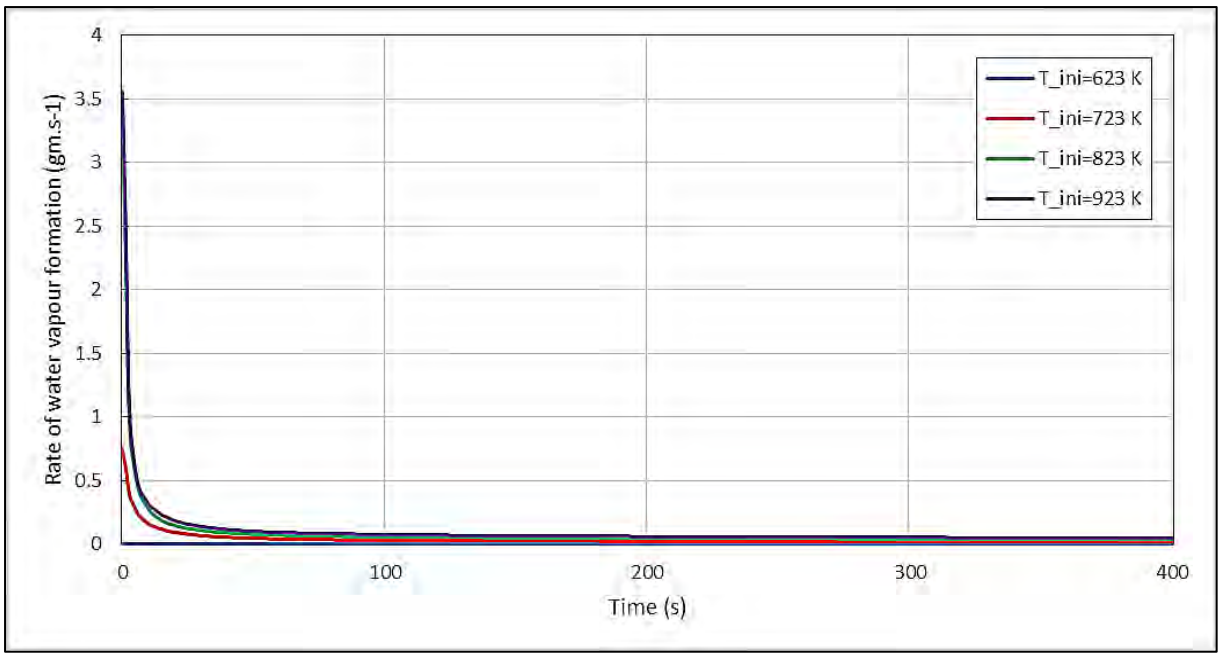

Fig. 5.12: Average rate of water vapour formation variation

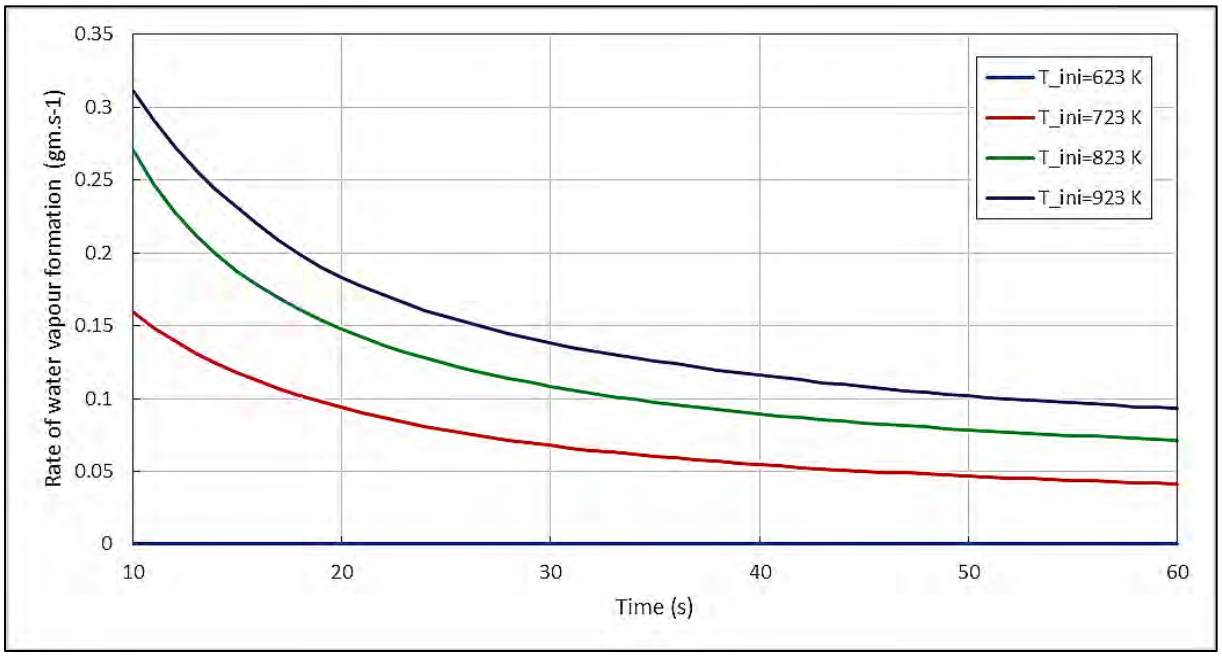

Fig. 5.13: Average rate of water vapour formation variation (close-up view)

Figs. 5.12 and 5.13 show variation average rate of water vapour formation, which follows the same trend as that of average rate of reaction.

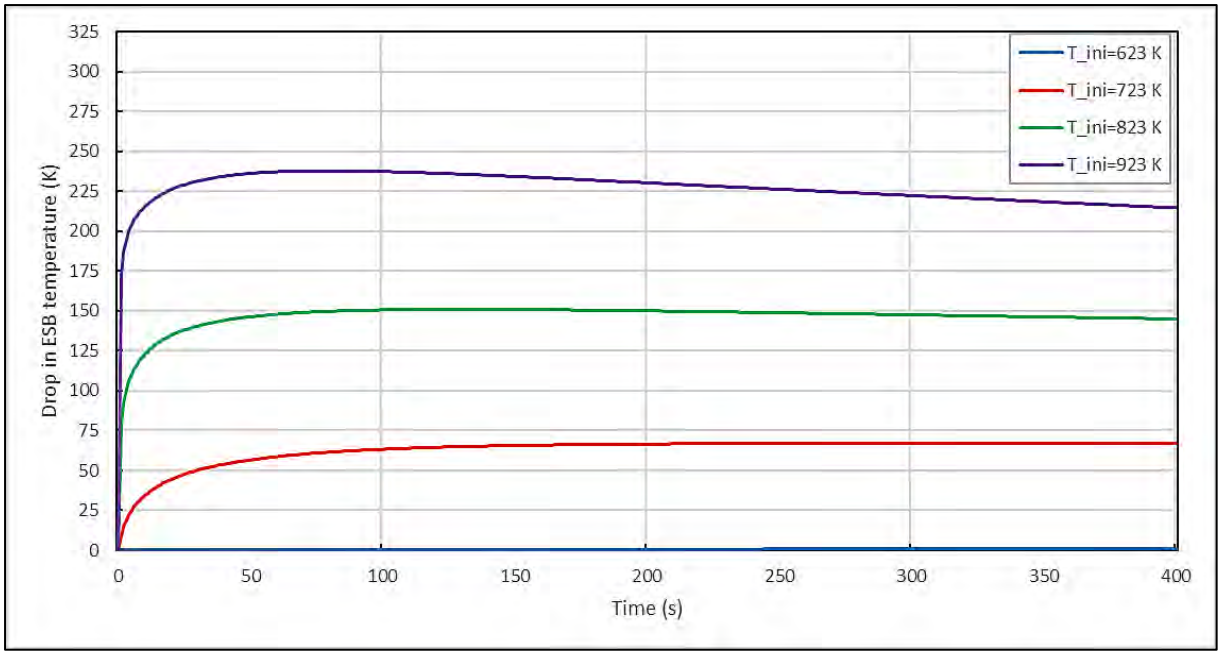

Fig. 5.14: Drop in ESB average temperature variation

From Fig. 5.14, it is noticed that for higher T_ini, higher drop in ESB average temperature is achieved. Fig. 5.15 shows corresponding drop in average outlet temperature of EG. From Table 34, it is observed that energy stored in ESB significantly increases as T_ini is increased above 723 K.

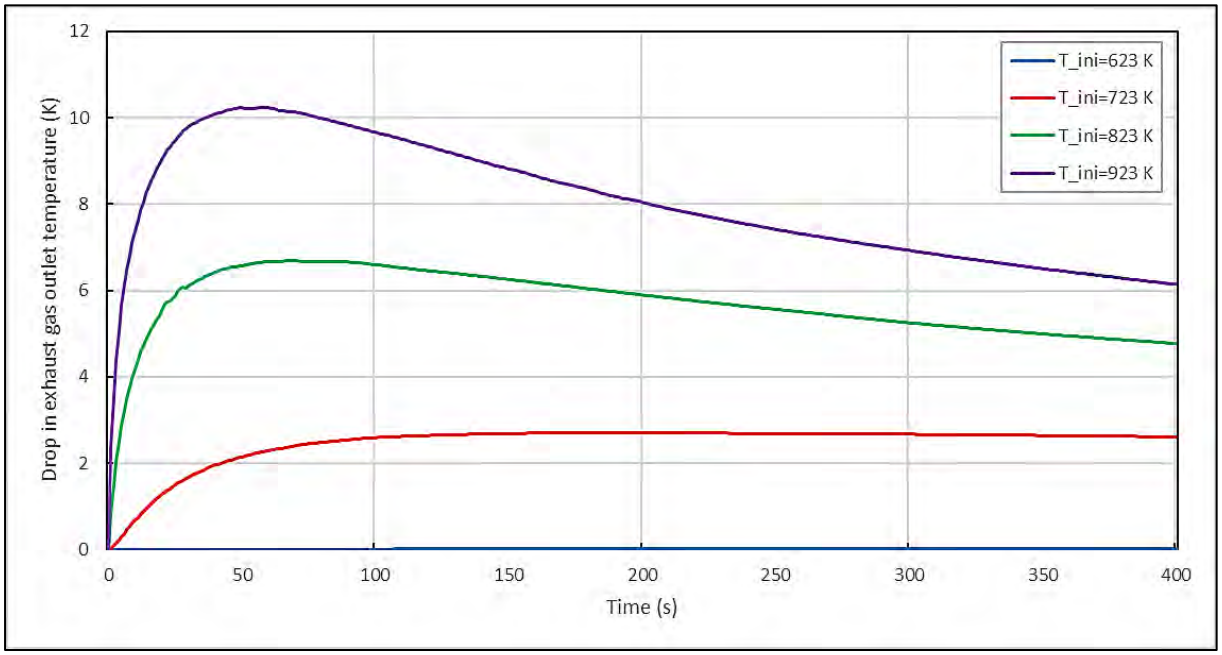

Fig. 5.15: Drop in EG average outlet temperature variation

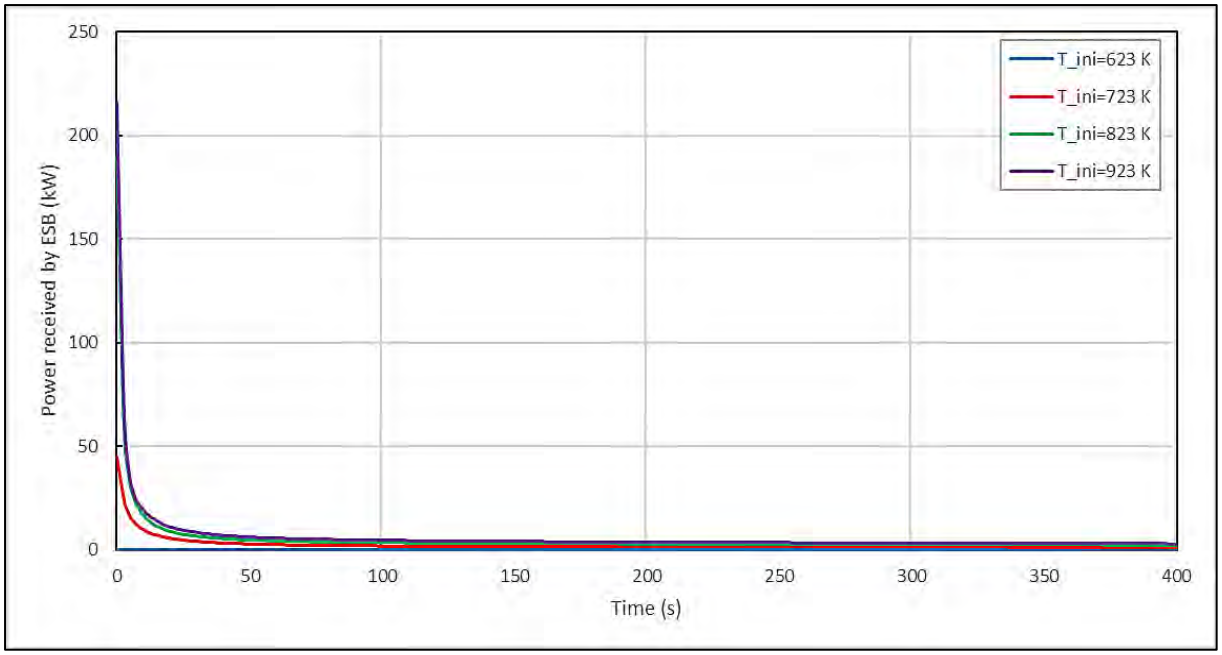

Fig. 5.16: Average power received by ESB variation

As reaction rate is higher at high values of T_ini, higher is the amount of average power received by ESB as shown in Figs. 5.16 and 5.17. And consequently, higher energy is stored in ESB as shown in Table 5.8

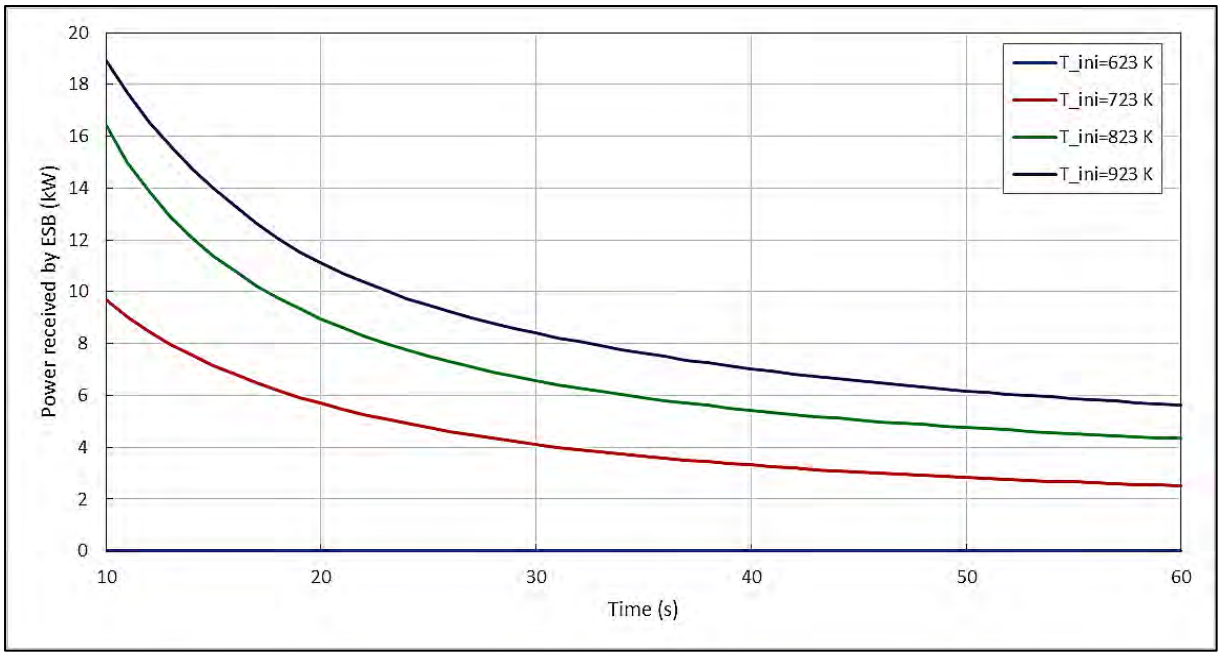

Fig. 5.17: Average power received by ESB variation (close-up view)

Table 5.8. Effect of variation of EG inlet temperature

Initial EG temperature (K)	Final ESB average temperature (K)	Conversion of reactant into product (%)	Total energy lost by EG to ESB (kJ)	Total energy for sensible cooling of ESB (kJ)	Total energy stored in ESB (kJ) (Target = 500 kJ)
623	622.14	0.11	0.37	0.43	0.81
723	655.99	12.81	64.45	30.40	94.85
823	678.03	28.29	126.49	57.70	184.20
923	708.38	40.54	151.81	75.52	227.33

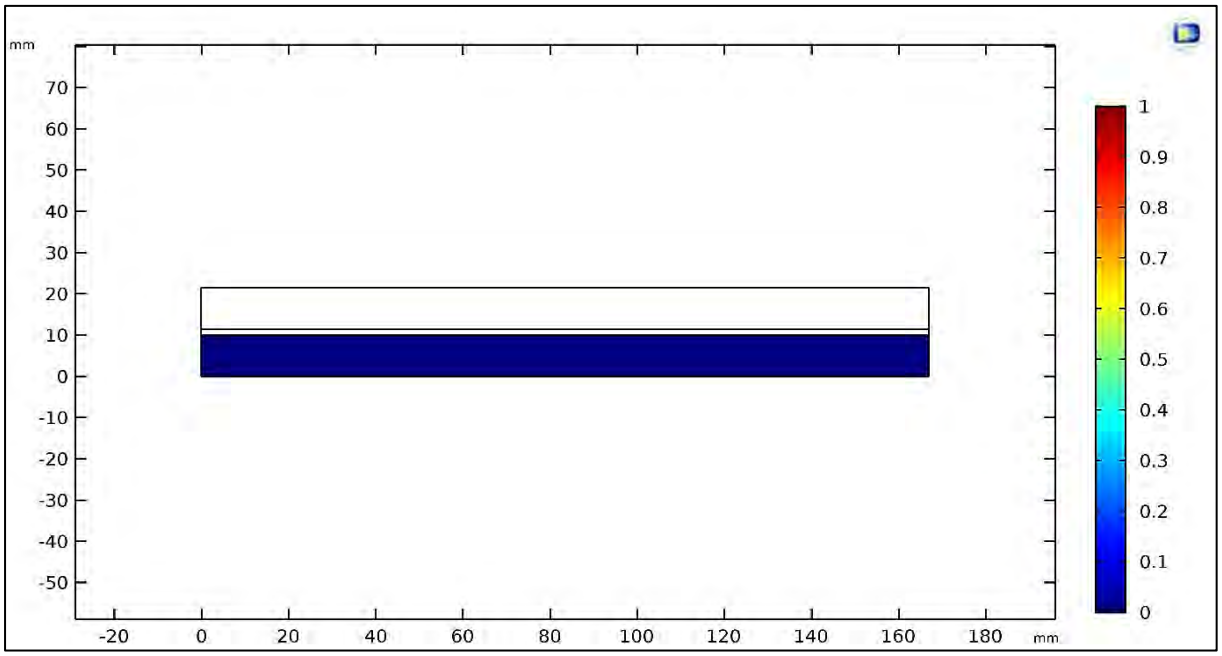

Fig. 5.18: Extent of reaction variation at the end of 400s with initial EG temperature of 623 K

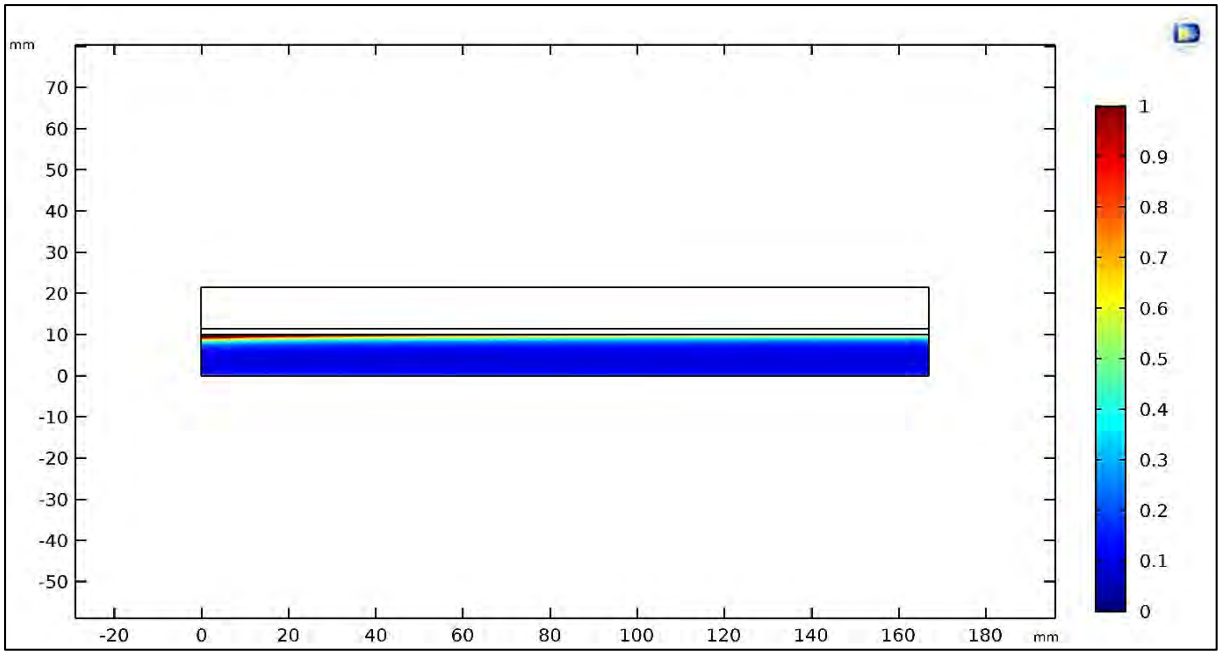

Fig. 5.19: Extent of reaction variation at the end of 400s with initial EG temperature of 723 K

The extent of reaction variation across ESB domain is shown in Figs. 5.18 to 5.21. Since there is negligible rate of reaction at T_ini values of 623 K and below, no significant conversion is observed. But as T_ini value is increased above 623 K, higher reaction rate is observed. With increase in the initial temperature of ESB (above 623 K), rise in extent of reaction (conversion) is observed.

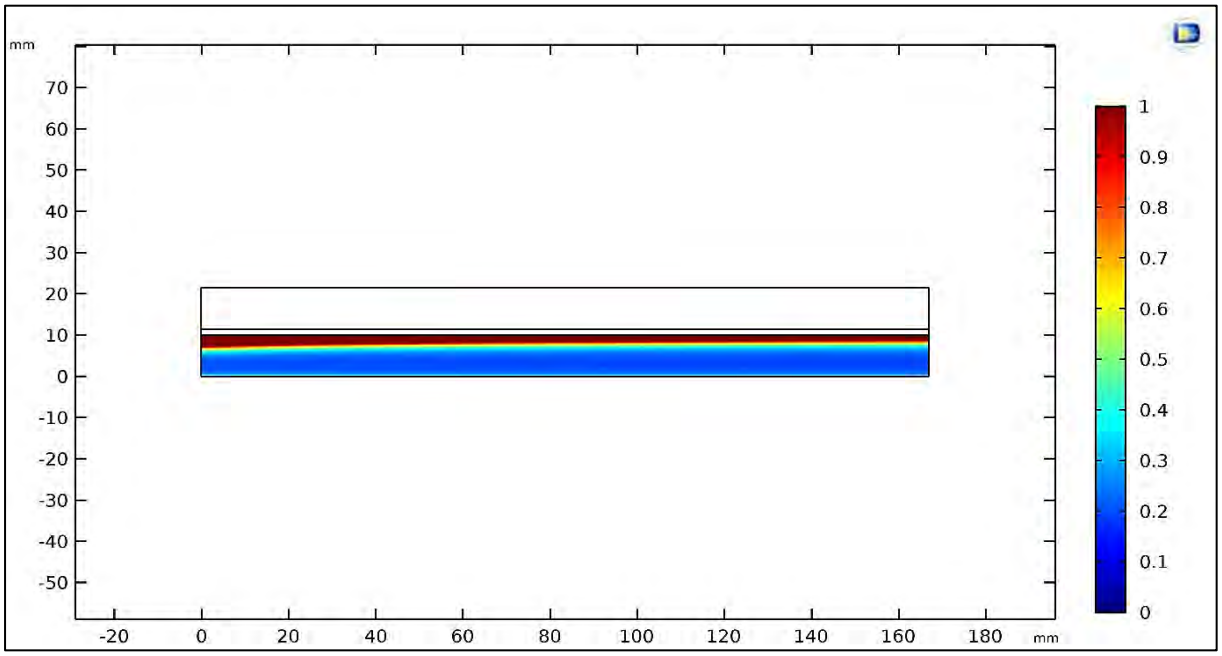

Fig. 5.20: Extent of reaction variation at the end of 400s with initial EG temperature of 823 K

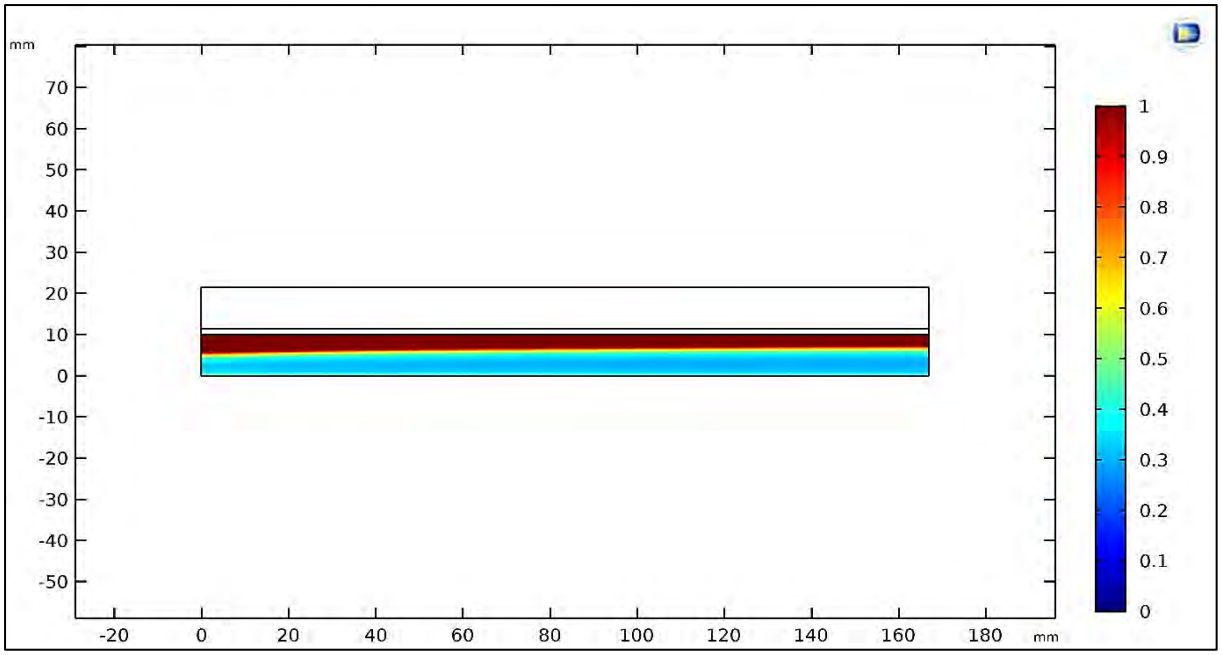

Fig. 5.21: Extent of reaction variation at the end of 400s with initial EG temperature of 923 K

Based on these observations, it is decided to fix the EG inlet temperature as 550 ˚C (823 K) for further simulations.

5.2.2.3 Variation in EG mass flow rate

Based on operating conditions provided in Table 5.2, EG mass flow rate range is 100 – 350 kg hr^{-1}. To study the effect of EG mass flow rate following values are selected as shown in Table 5.9.

Table 5.9. EG mass flow rate values for simulation

EG mass flow rate (kg hr^{-1})	EG mass flow rate (kg s^{-1})	Reynold's number ($Re_{critical}$ = 2300)	Mac Number (for incompressible flow, Ma < 0.3)
100	2.778 x 10^{-2}	6176	0.054
200	5.555 x 10^{-2}	12352	0.109
300	8.333 x 10^{-2}	18528	0.163

Other operating conditions for simulation are mentioned in Table 5.10 as shown below

Table 5.10. Other operating conditions for simulation

Initial temperature of ESB	823 K (550 ˚C)
Water vapour outlet pressure	1.22 kPa (P_{sat} corresponding to 10 ˚C)
EG inlet temperature	823 K (550 ˚C)
ESB porosity	60 %
ESB average particle diameter	30 µm
Dehydration reaction time	400 s

For different values of Reynold's number given in Table 5.9, it is observed that flow of EG through the channel is turbulent. As Mac number values are lower than 0.3, flow is assumed

to be incompressible. Based on discussion with Faurecia team, k-ε model is used to solve turbulent flow field, where k is turbulence kinetic energy and ε is dissipation rate. Following relations are used for solving turbulent flow field using k-ε model,

Hydraulic diameter (in m), $D_h = \frac{2*w*h}{(w+h)}$, where w and h are width and height of the EG flow channel, respectively.

Reynold's number, $Re = \frac{V*D_h}{\nu}$, where V is mean flow velocity and ν is kinematic viscosity of EG.

Turbulence length scale (in m), $L = 0.07 * D_h$

Turbulence intensity, $I = 0.16 * (Re_{Dh})^{\frac{-1}{8}}$

Turbulence kinetic energy (in m^{-2} s^{-2}), $k' = \frac{3}{2} * (V * I)^2$

Dissipation rate (in m^{-2} s^{-3}), $\varepsilon = \frac{C_\mu^{\frac{3}{4}} * k^{\frac{3}{2}}}{L}$, where $C_\mu = 0.09$.

Based on above operating conditions and relations, simulations are performed and following results are obtained.

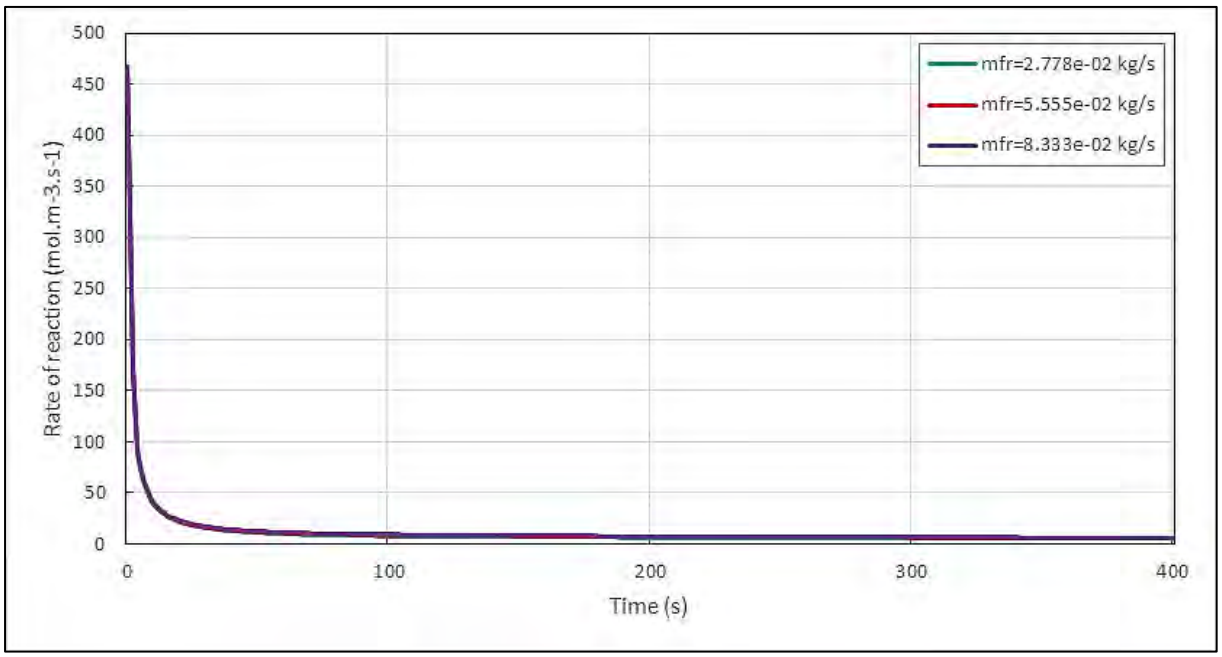

Fig. 5.22: Average rate of reaction variation

From Figs. 5.22 and 5.23, it is seen that increase in EG mass flow rate (mfr) results in increase in average rate of reaction. With increase in the EG mass flow rate (and since flow is assumed to be incompressible), mean flow velocity increases. This gives higher value of heat transfer coefficients between ESB and EG. Thus, total energy stored by ESB increases as shown in Table 5.11.

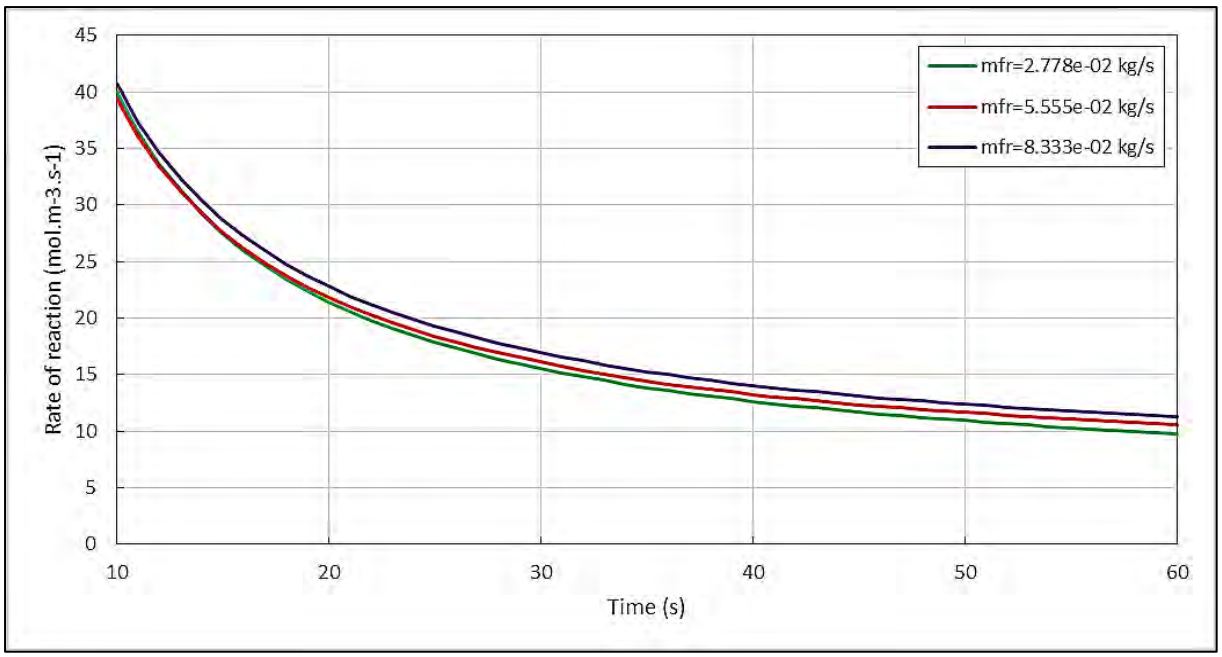

Fig. 5.23: Average rate of reaction variation (close-up view)

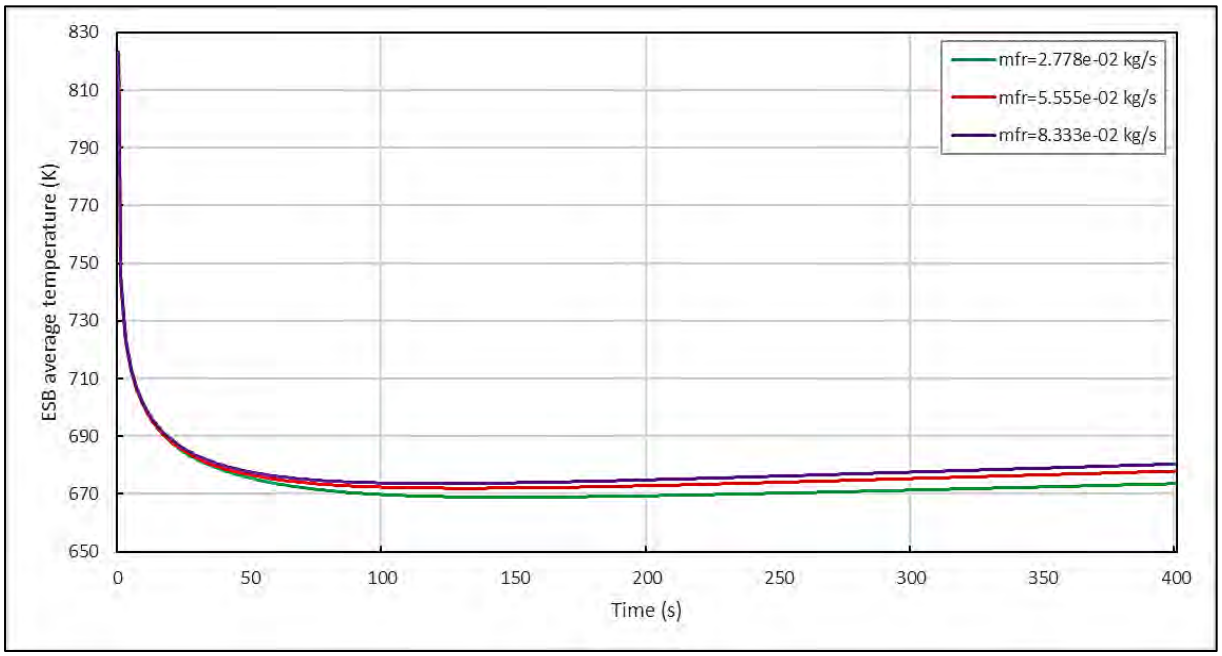

Fig. 5.24: ESB average temperature variation

But as mean flow velocity increases, available contact time between ESB and EG decreases. Hence, the change in ESB average temperature and EG average outlet temperature decreases as shown in Figs. 5.24 and 5.25.

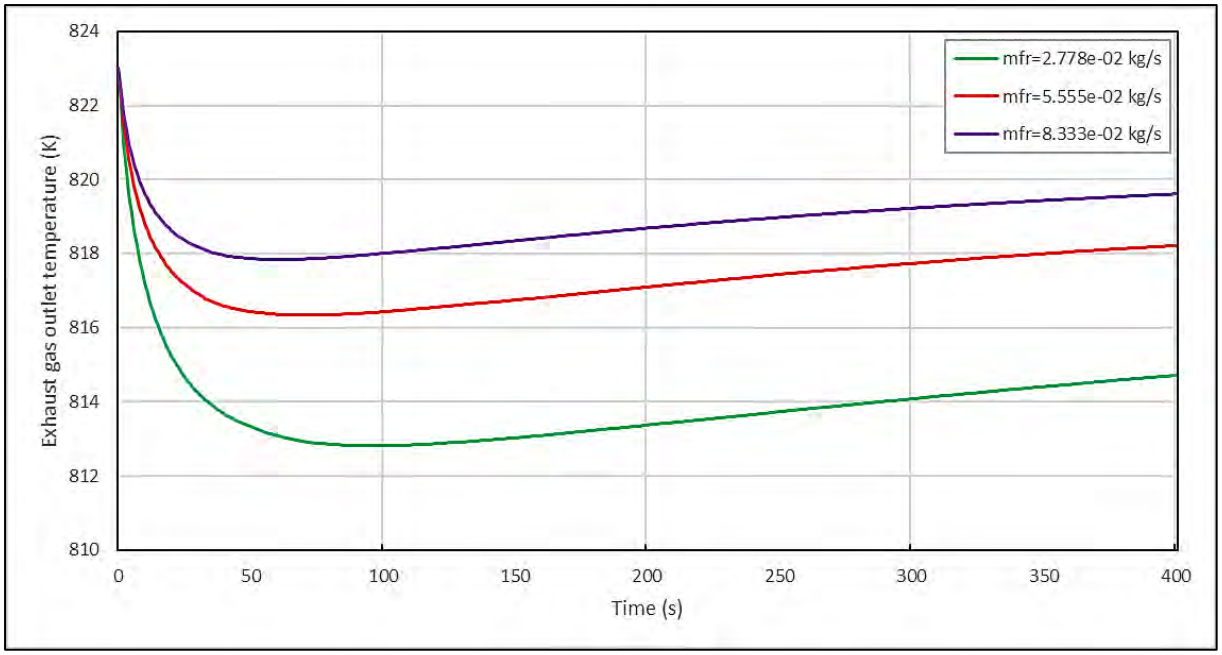

Fig. 5.25: EG average outlet temperature variation

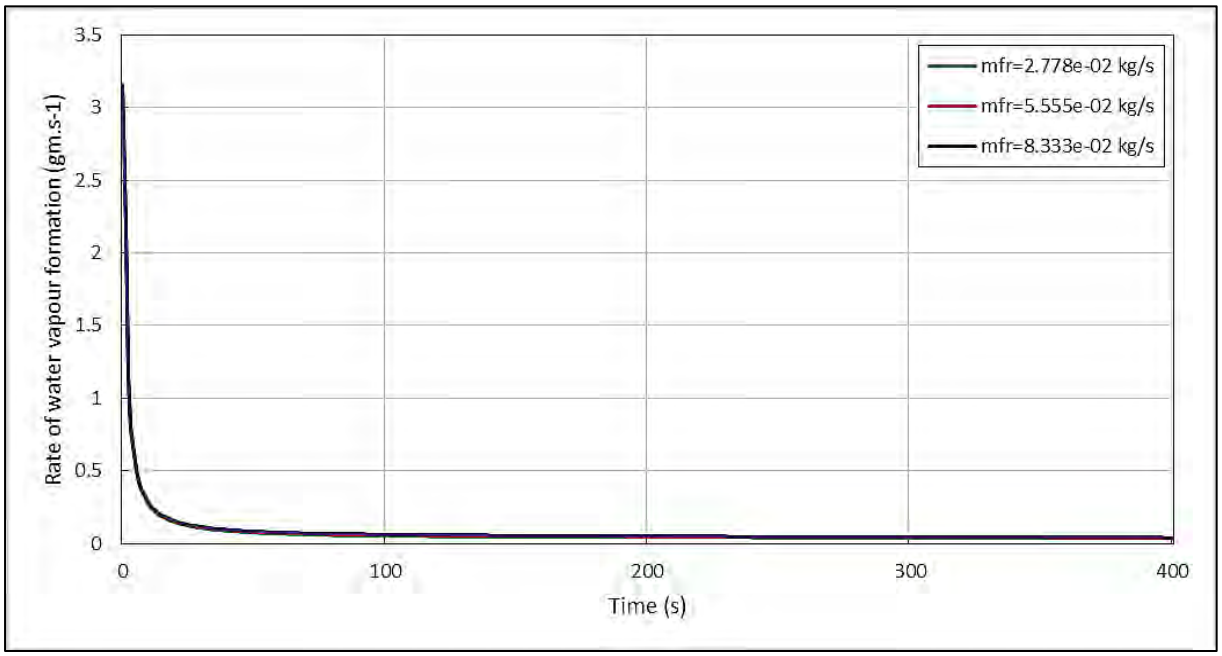

Fig. 5.26: Average rate of water vapour formation variation

Figs. 5.26 and 5.27 show variation average rate of water vapour formation, which follows the same trend as that of average rate of reaction.

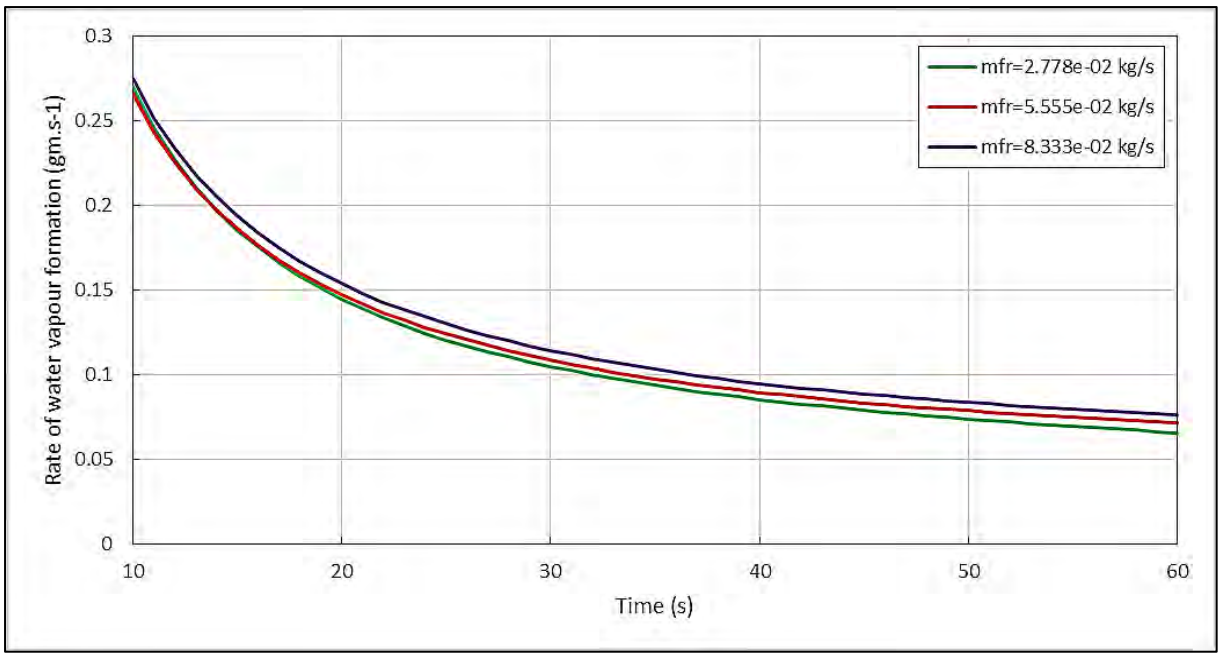

Fig. 5.27: Average rate of water vapour formation variation (close-up view)

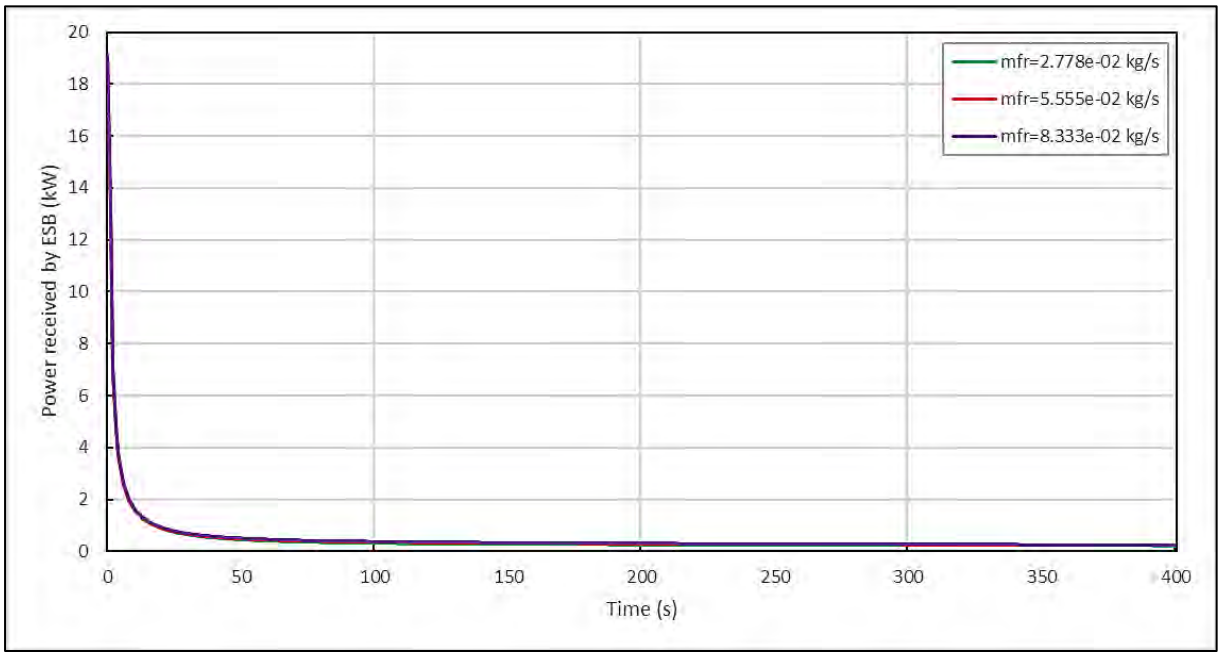

Fig. 5.28: Average power received by ESB variation

As heat transfer coefficient value is higher for higher EG mass flow rate, more amount of energy is stored in ESB as shown Figs. 5.28 and 5.29.

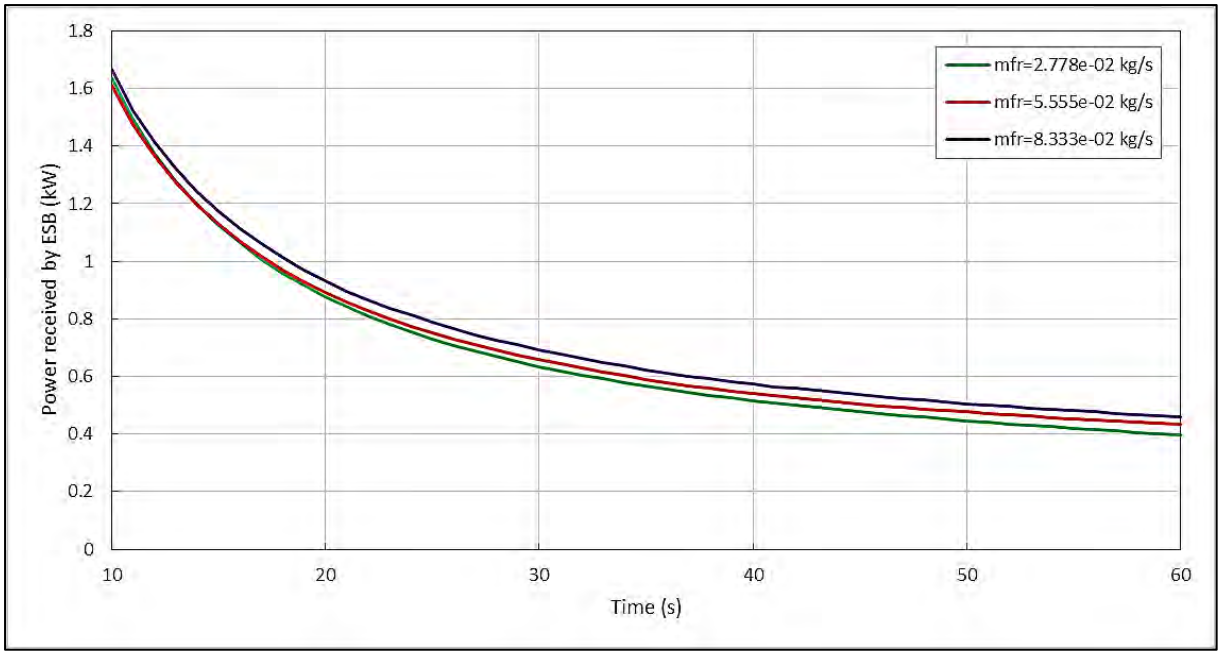

Fig. 5.29: Average power received by ESB variation (close-up view)

Table 5.11. Effect of variation of EG mass flow rate

Mass flow rate (kg/s)	Final ESB average temperature (K) ($T_{initial}$ = 823 K)	Total energy lost by EG to ESB (kJ)	Total energy in sensible cooling of ESB (kJ)	Total energy stored in ESB (kJ) (Target = 500 kJ)
2.778×10^{-2}	673.57	112.73	59.96	172.70
5.555×10^{-2}	677.92	125.91	57.77	183.68
8.333×10^{-2}	680.36	135.32	56.57	191.89

Due to design constraints of a model of vehicle engine suggested by Faurecia team, EG mass flow rate is fixed at 815 kg hr^{-1} for further simulations.

5.2.2.4 Variation in ESB permeability

Based on the operating conditions provided in Table 5.2, the particle size of ESB material is selected as 30 and 150 µm. The porosity values of ESB are chosen as 40% and 60% . Based on these parameters, ESB permeability values are calculated using Eqn 8 as shown in Table 38.

Table 5.12. ESB permeability values for simulation

ESB porosity	ESB average particle diameter (µm)	ESB permeability (m^2)
0.4	30	1.07×10^{-12}
0.4	150	2.67×10^{-11}
0.6	30	8.1×10^{-12}
0.6	150	2.02×10^{-10}

Other operating conditions for simulation are mentioned in Table 5.13 as shown below:

Table 5.13. Other operating conditions for simulation

Initial temperature of ESB	823 K (550 ˚C)
Water vapour outlet pressure	1.22 kPa (P_{sat} corresponding to 10 ˚C)
EG inlet temperature	823 K (550 ˚C)
EG mass flow rate	200 kg hr^{-1}
Dehydration reaction time	400 s

Based on above operating conditions simulations are performed and following results are obtained.

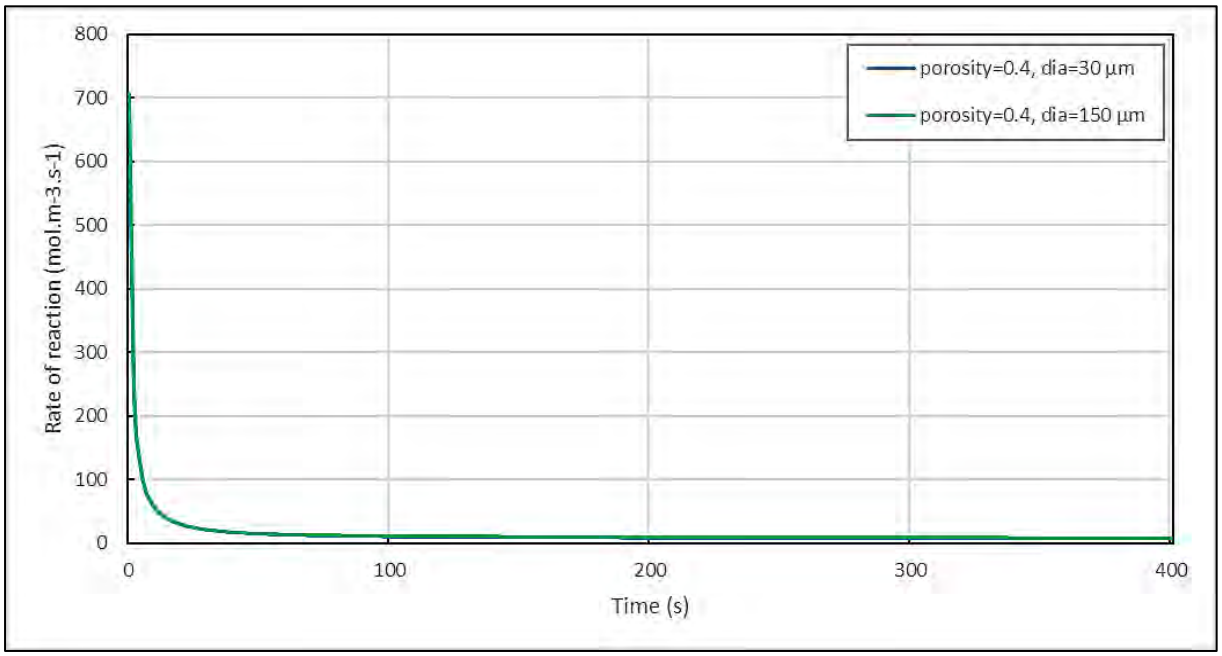

Fig. 5.30: Average rate of reaction variation for different particle sizes with porosity of 0.4

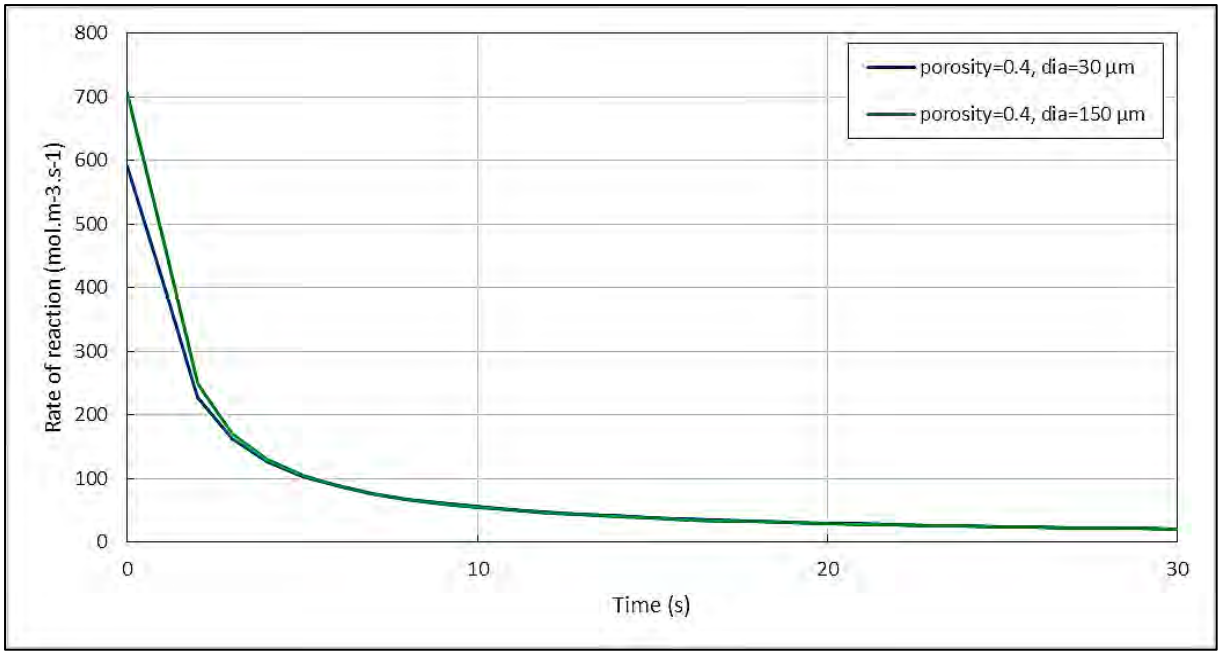

Fig. 5.31: Average rate of reaction variation (close-up view) for different particle sizes with porosity of 0.4

As ESB permeability increases, resistance to water vapour flow through ESB domain would decrease which should result in higher reaction rate and consequently higher temperature drop. For 40% porosity of ESB, significant variation in average rate of reaction for different particle sizes are observed at start of dehydration as shown in Figs. 5.30 and 5.31.

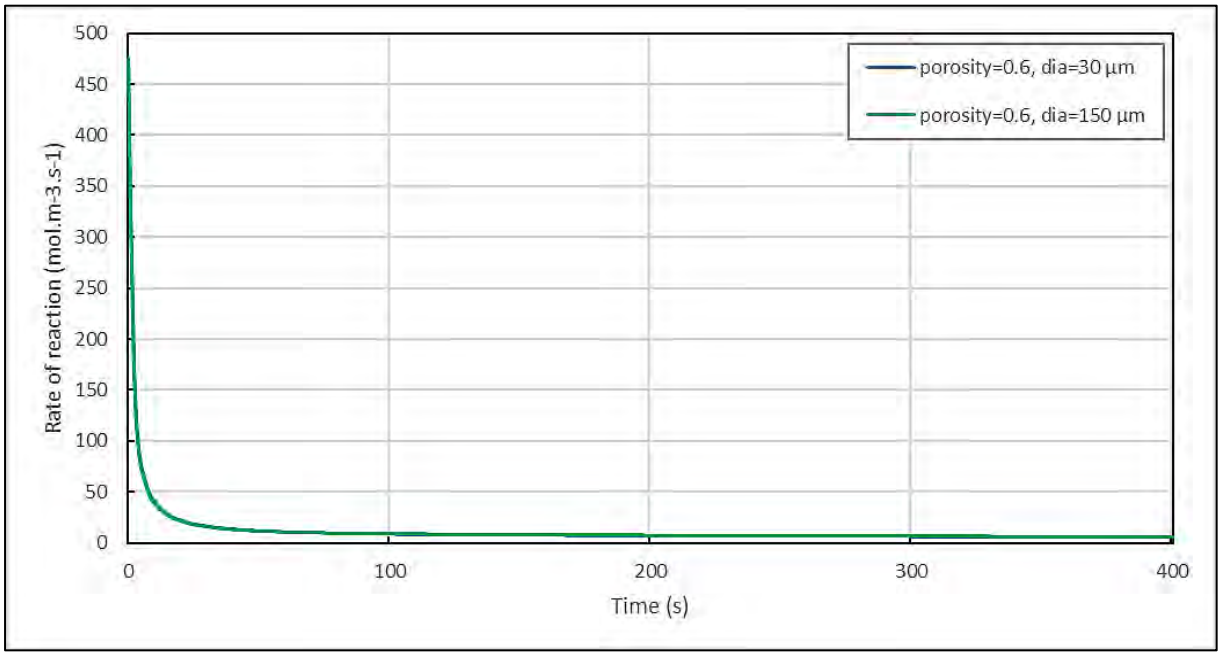

Fig. 5.32: Average rate of reaction variation for different particle sizes with porosity of 0.6

But for 60% porosity of ESB, the variation in average rate of reaction for different particle size is low as observed in Figs. 5.32 and 5.33.

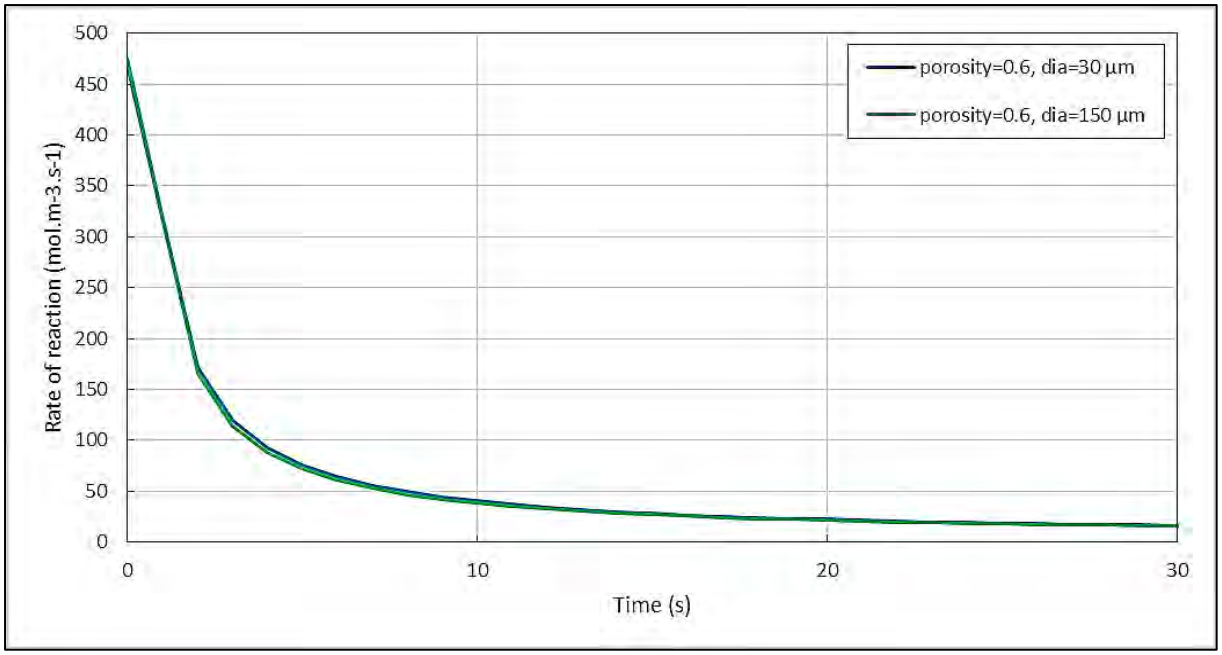

Fig. 5.33: Average rate of reaction variation (close-up view) for different particle sizes with porosity of 0.6

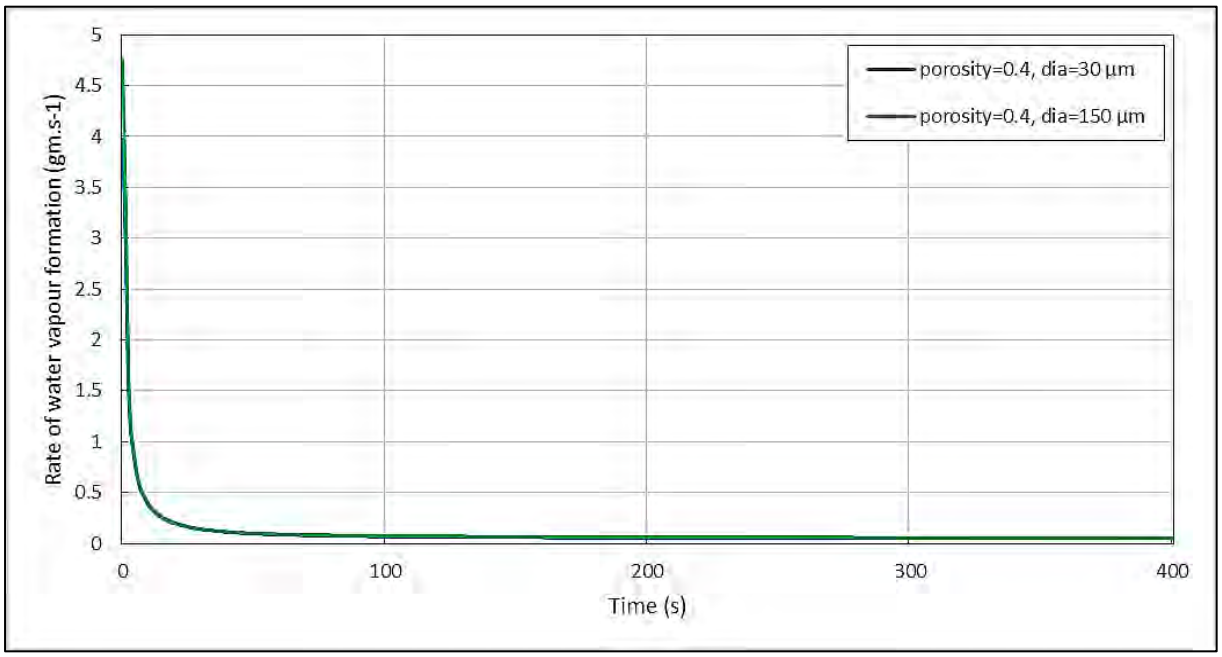

Fig. 5.34: Average rate of water vapour formation variation for different particle sizes with porosity of 0.4

Figs. 5.34 to 5.37 show variation average rate of water vapour formation which follows the same trend as that of average rate of reaction for respective porosity of ESB.

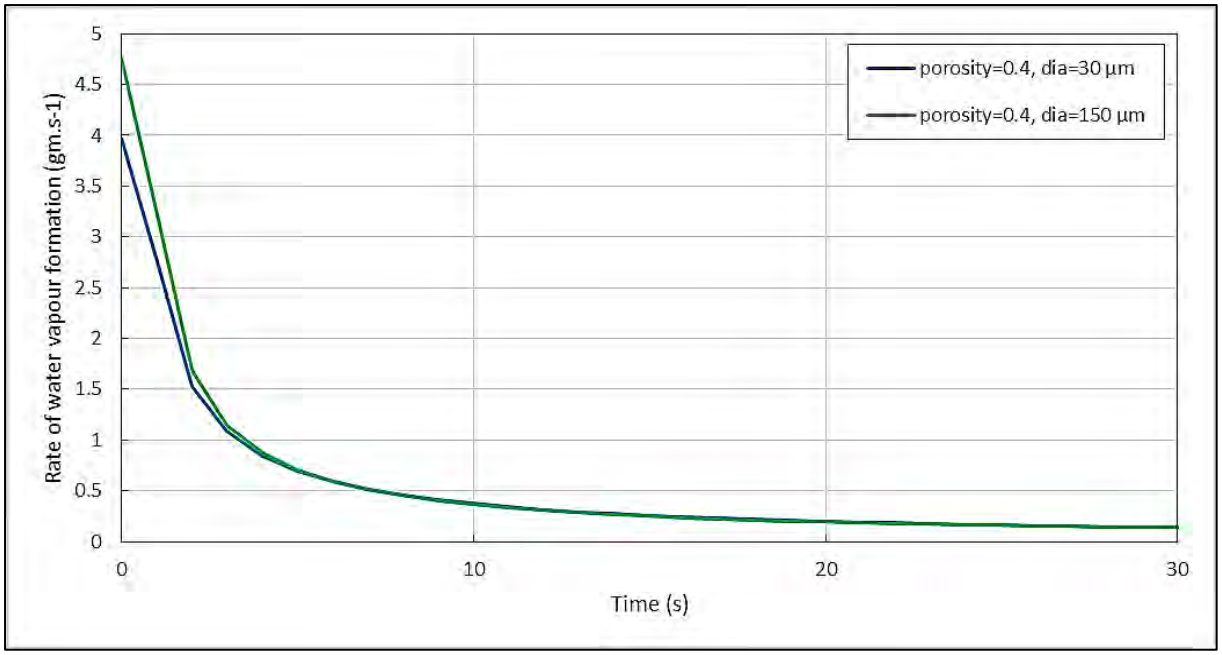

Fig. 5.35: Average rate of water vapour formation variation (close-up view) for different particle sizes with porosity of 0.4

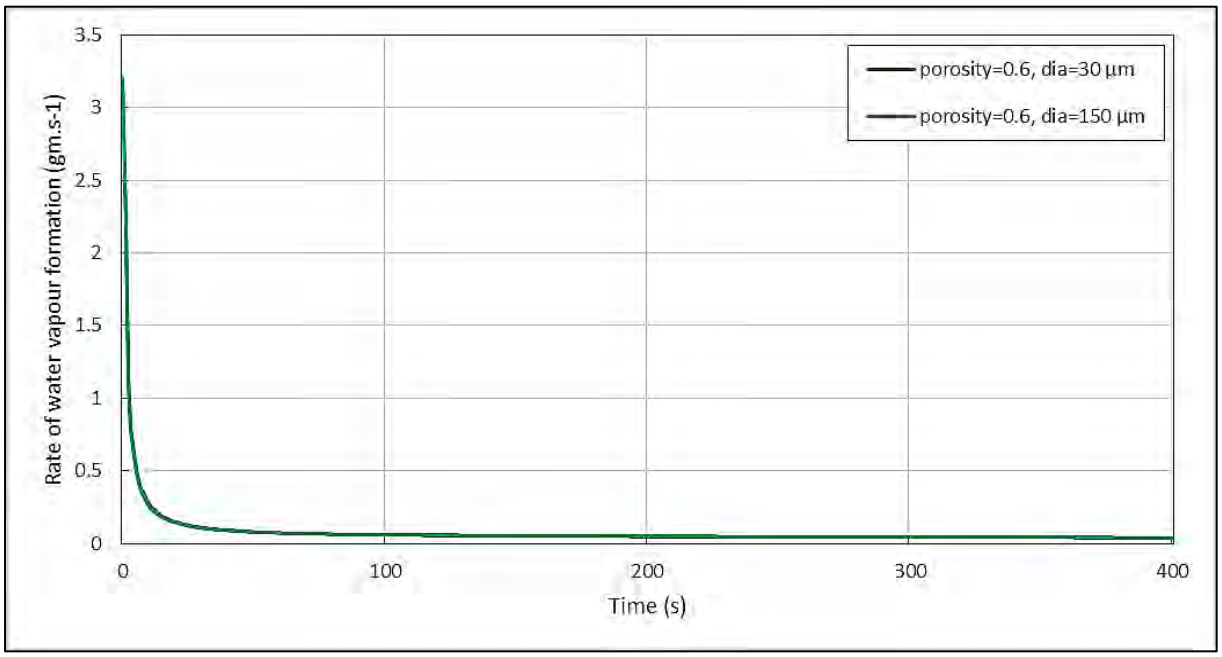

Fig. 5.36: Average rate of water vapour formation variation for different particle sizes with porosity of 0.6

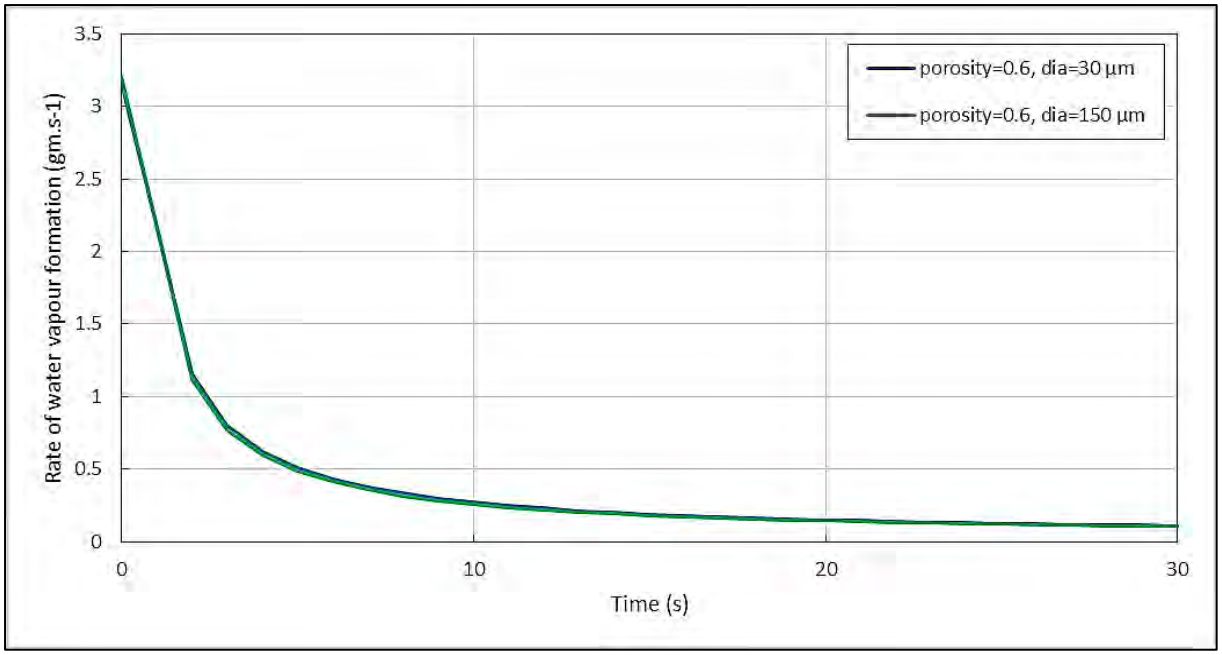

Fig. 5.37: Average rate of water vapour formation variation (close-up view) for different particle sizes with porosity of 0.6

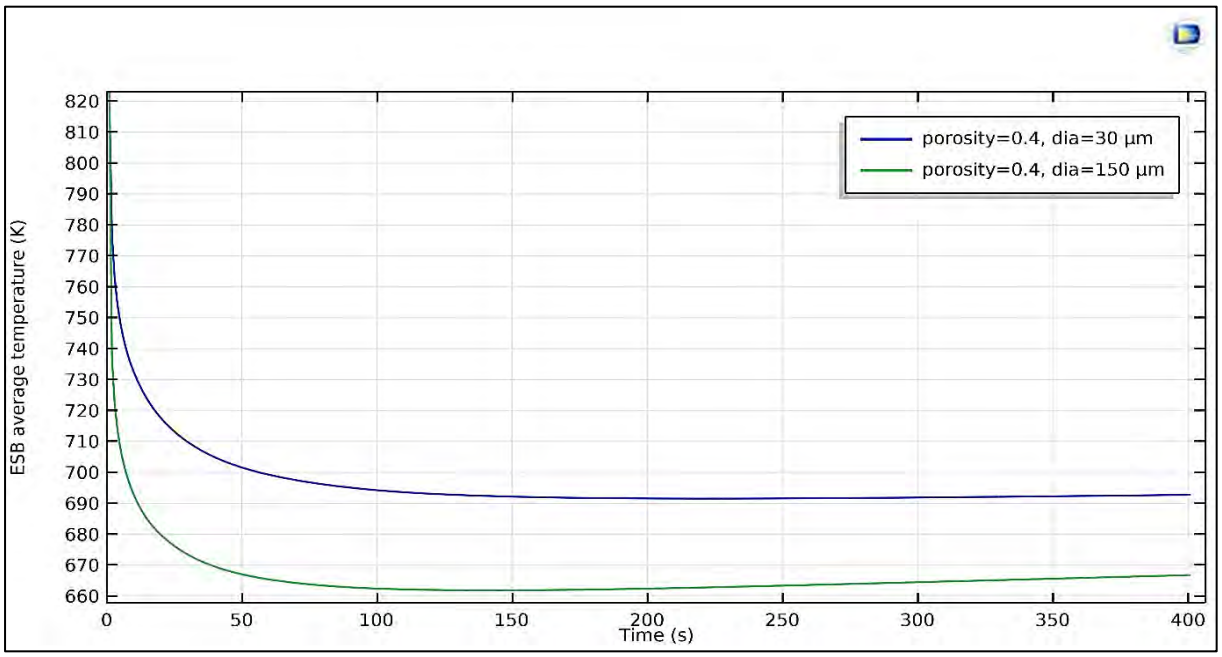

Fig. 5.38: ESB average temperature variation for different particle sizes with porosity of 0.4

For 40% porosity of ESB, there is significant variation in ESB average temperature for different particle sizes as observed in Fig. 5.38. But for 60% porosity of ESB, the variation in ESB average temperature is low as shown in Fig. 5.39. Similar variation is observed in case of EG average outlet temperature as shown in Figs. 5.40 and 5.41. From obtained results, it is concluded that larger particle size gives higher temperature rise for the same value of porosity.

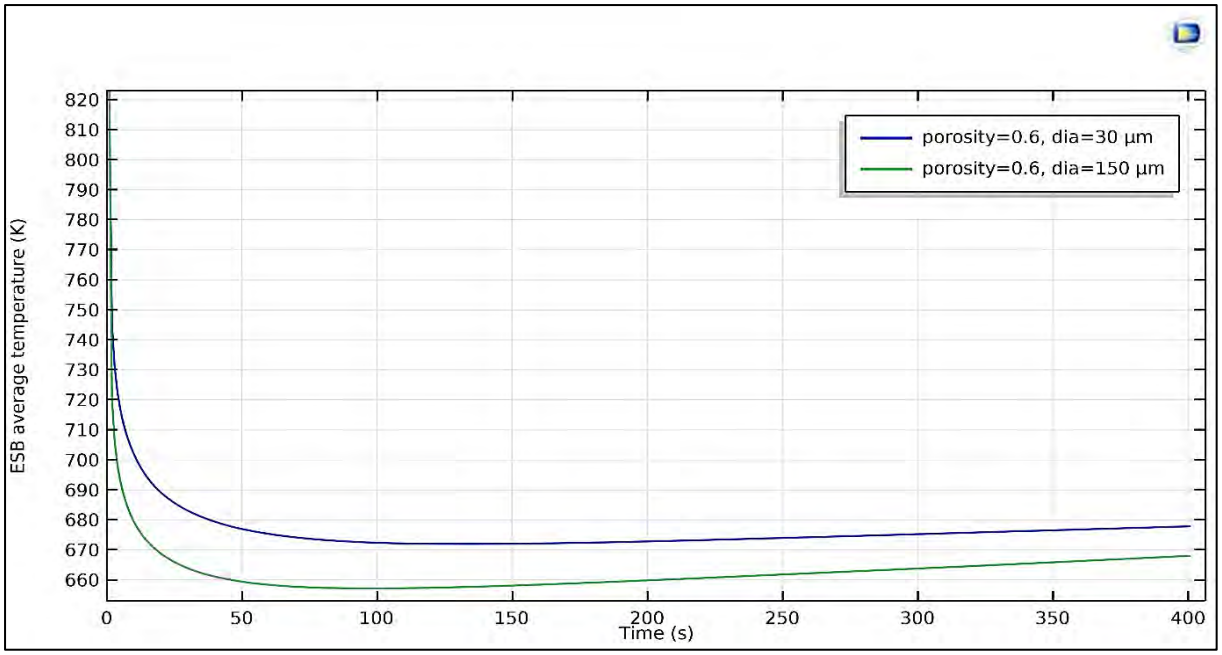

Fig. 5.39: ESB average temperature variation for different particle sizes with porosity of 0.6

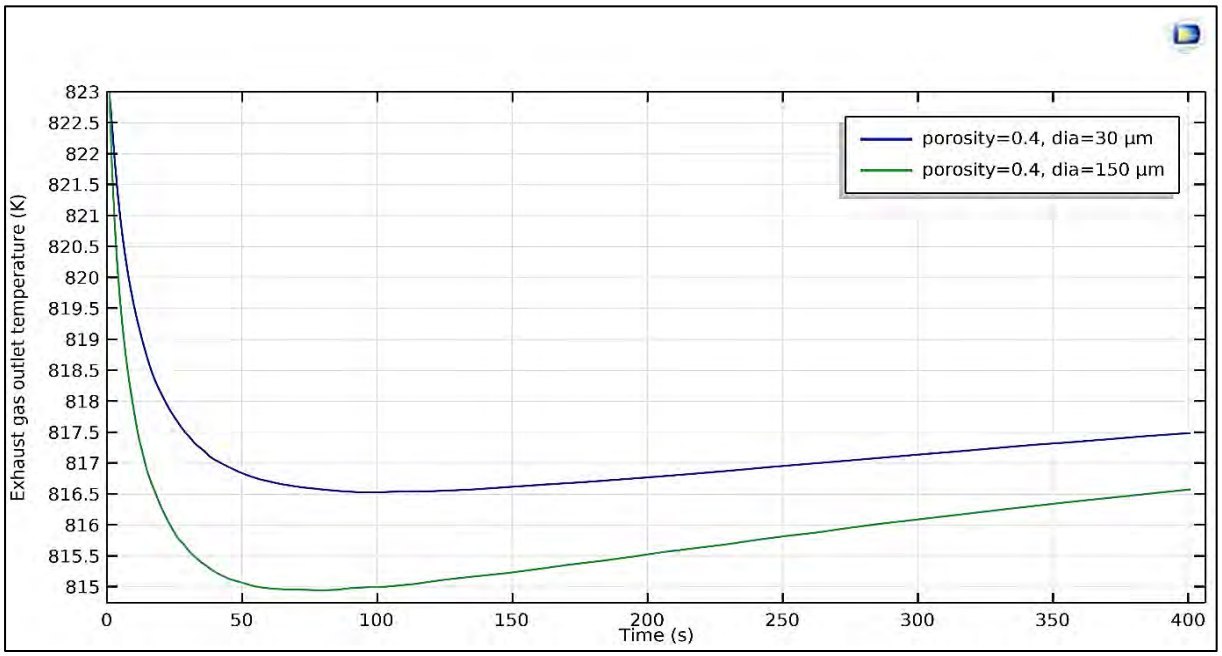

Fig.5.40: HTF average outlet temperature variation for different particle sizes with porosity of 0.4

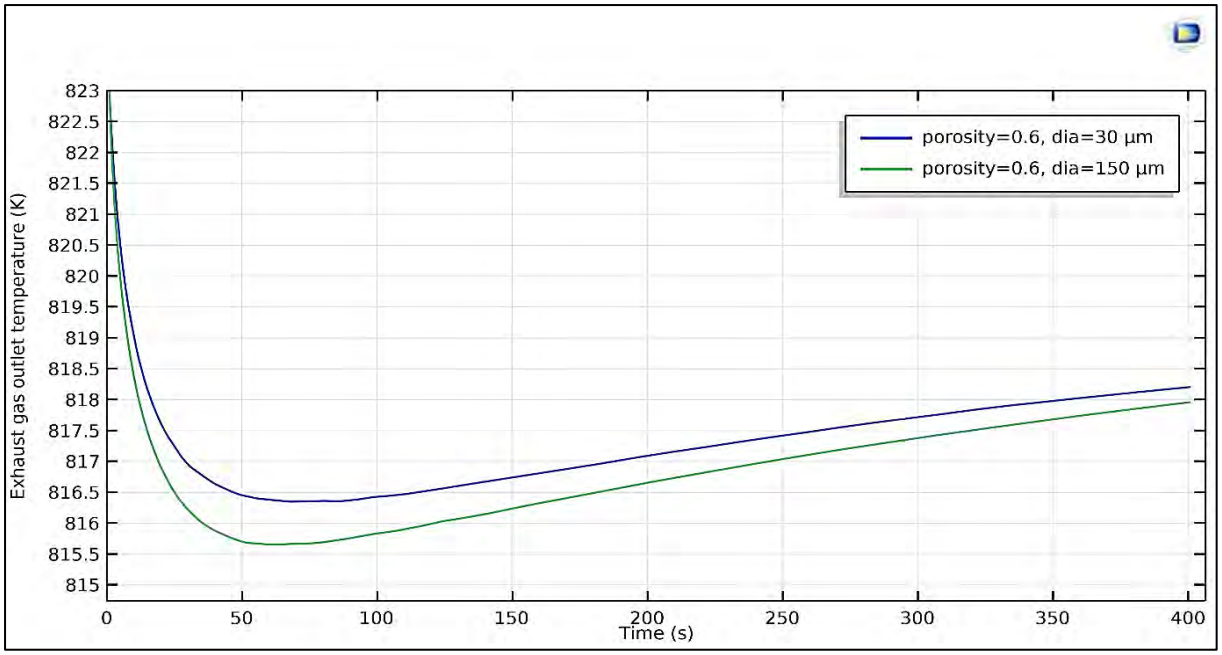

Fig. 5.41: HTF average outlet temperature variation for different particle sizes with porosity of 0.6

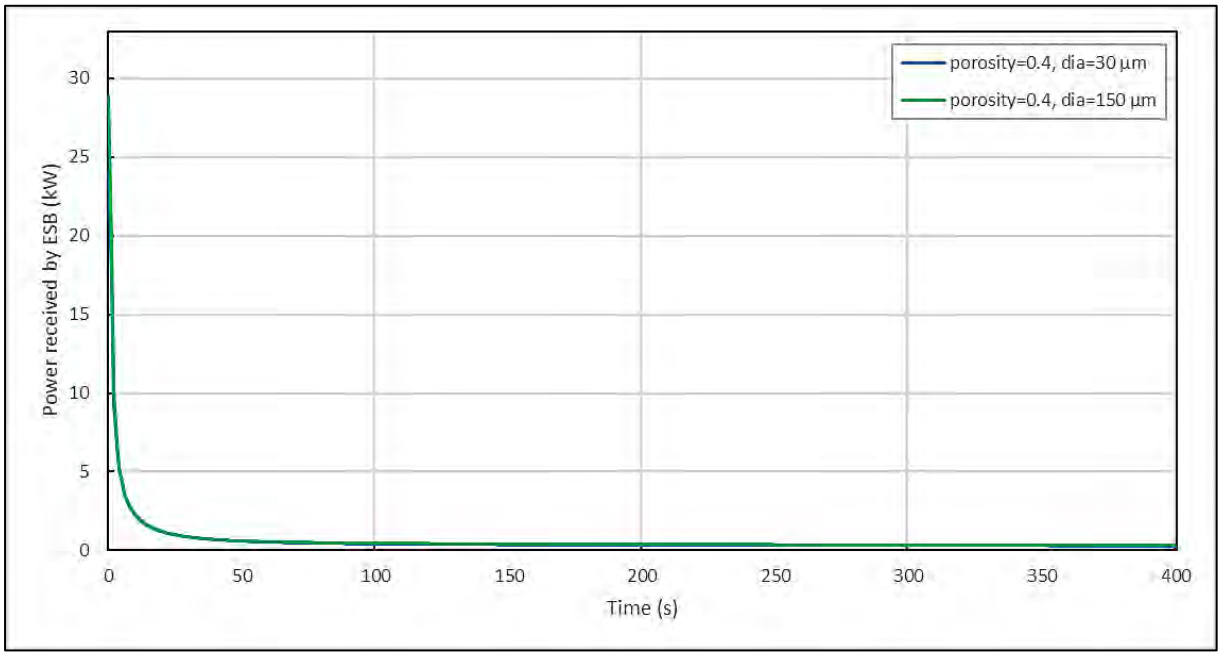

Fig.5.42: Average power received by ESB variation for different particle sizes with porosity of 0.4

Figs. 5.42 to 5.43 show the variation in average power received by ESB. Trends observed are in accordance with the respective trend of average rate of reaction which are explained earlier in Figs. 5.30 and 5.31.

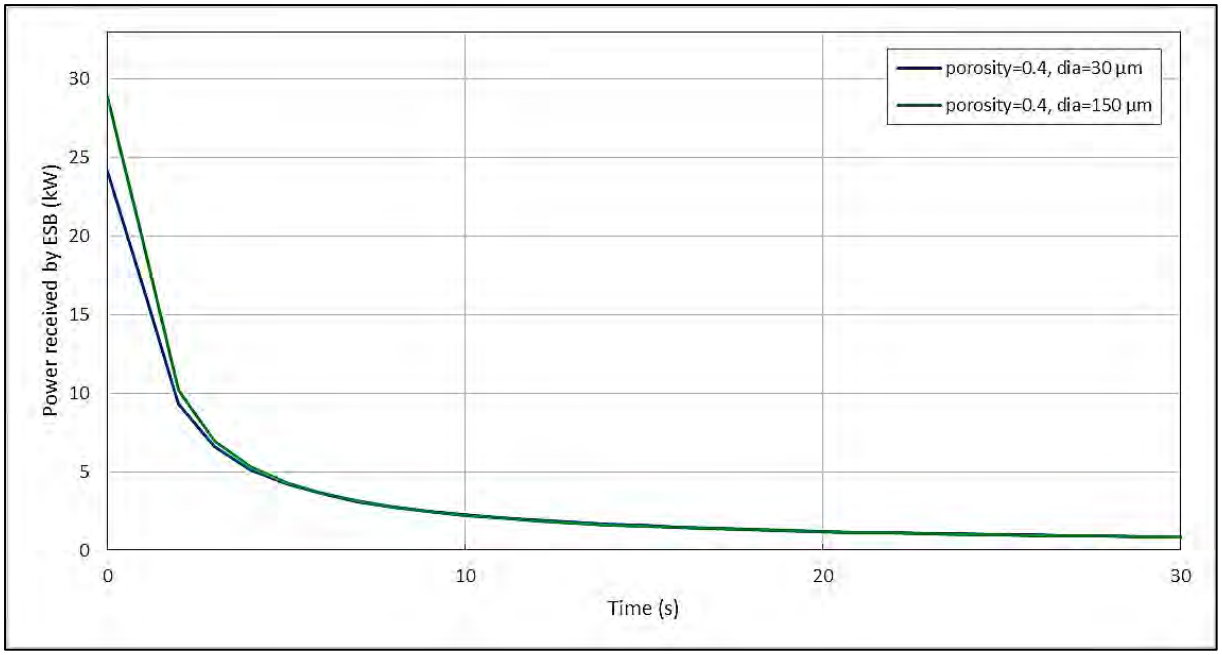

Fig.5.43: Average power received by ESB variation (close-up view) for different particle sizes with porosity of 0.4

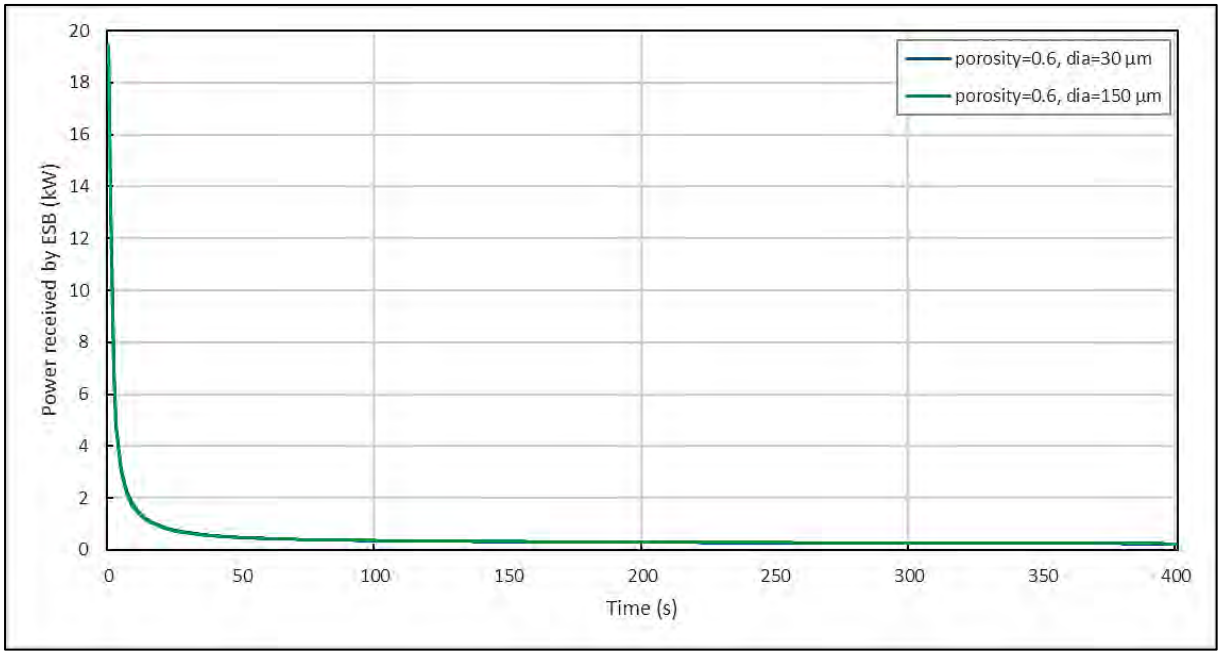

Fig.5.44: Average power received by ESB variation for different particle sizes with porosity of 0.6

Figs. 5.44 to 5.45 show the variation in average power received by ESB. Trends observed are in accordance with the respective trend of average rate of reaction which are explained earlier in Figs. 5.32 and 5.33.

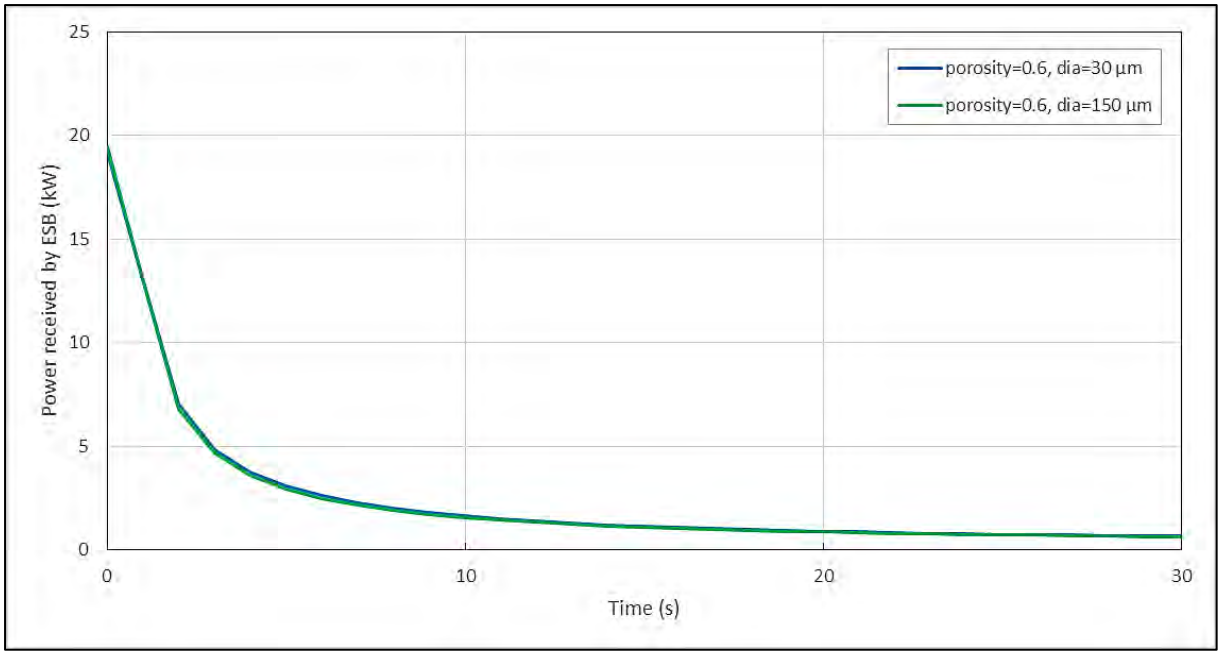

Fig.5.45: Average power received by ESB variation (close-up view) for different particle sizes with porosity of 0.6

Table 5.14. Effect of variation of ESB permeability

ESB Porosity	Average particle diameter (µm)	Initial mass of $Ca(OH)_2$ in ESB (kg)	Final ESB average temperature (K) ($T_{initial}$ = 823 K)	Total energy lost by EG to ESB (kJ)	Total energy in sensible cooling of ESB (kJ)	Total energy stored in ESB (kJ) (Target = 500 kJ)
0.4	30	0.507	692.77	145.43	81.85	227.29
0.4	150	0.507	666.82	154.28	94.20	248.49
0.6	30	0.338	677.87	127.65	57.78	185.43
0.6	150	0.338	668.05	125.68	60.53	186.20

From Table 5.14, it is observed that energy stored in ESB is higher with large particle size at constant porosity value. But with higher porosity value, the variation in energy stored in ESB with particle size is marginal. Thus, porosity and particle size of ESB are chosen as 40% and 150 µm, respectively, for further simulations.

For the various values of particle size, only the change in permeability value is considered. The effect of particle size variation in the rate expressions for dehydration is not accounted. But in actual practice, as the porosity and resistance to vapour flow through ESB change with particle size, a separate study is to be carried out to examine the effect of particle size variation on performance of ESB.

5.2.2.5 Variation in time of dehydration reaction

Based on operating conditions provided in Table 5.2, the time for dehydration reaction is to be decided accordingly. The simulations are carried out to study the effect of increase in time of dehydration reaction up to 1200 s.

Table 5.15. Operating conditions for variation of time of dehydration reaction simulation

Initial temperature of ESB	823 K (550 ˚C)
Water vapour outlet pressure	1.22 kPa (P_{sat} corresponding to 10 ˚C)
EG inlet temperature	823 K (550 ˚C)
EG mass flow rate	200 kg hr^{-1}
ESB porosity	60 %
ESB average particle diameter	30 µm
Dehydration reaction time	1200 s

Based on above operating conditions simulations are performed and following results are obtained.

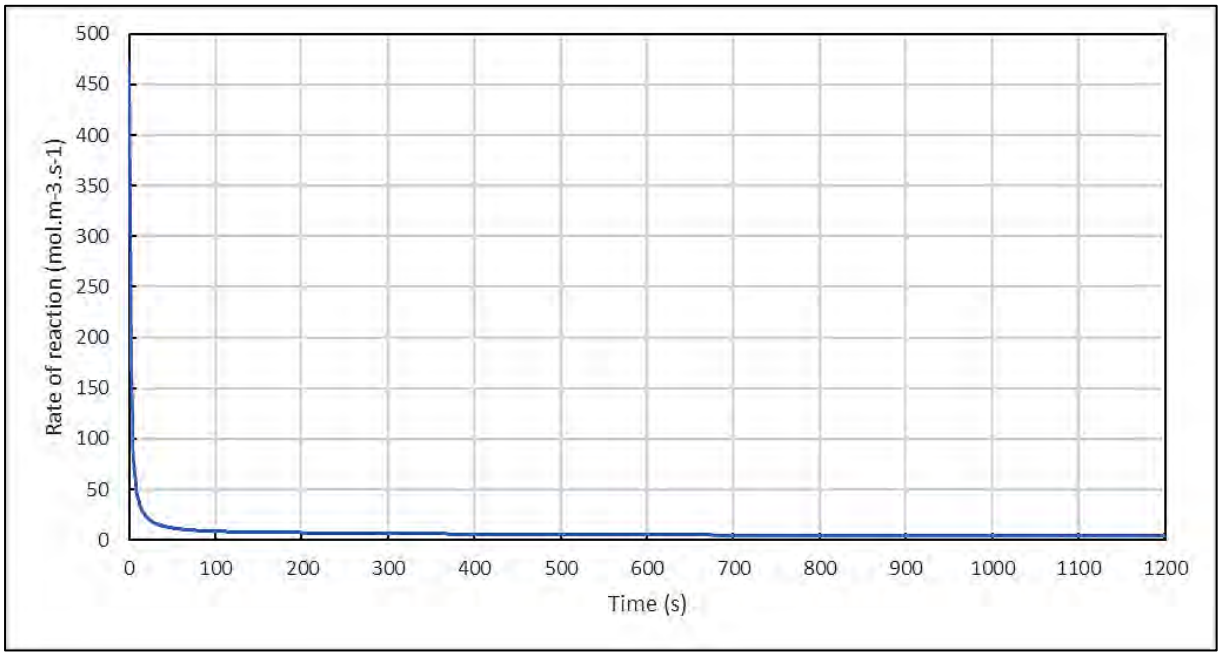

Fig. 5.46: Average rate of reaction variation

For present study, reaction time is increased by keeping other reaction operating conditions constant. Thus, variation in different output parameters, as shown in Figs. 5.46 to 5.50, follow similar trend as explained earlier in different parametric studies in sections 5.2.2.1 - 5.2.2.4.

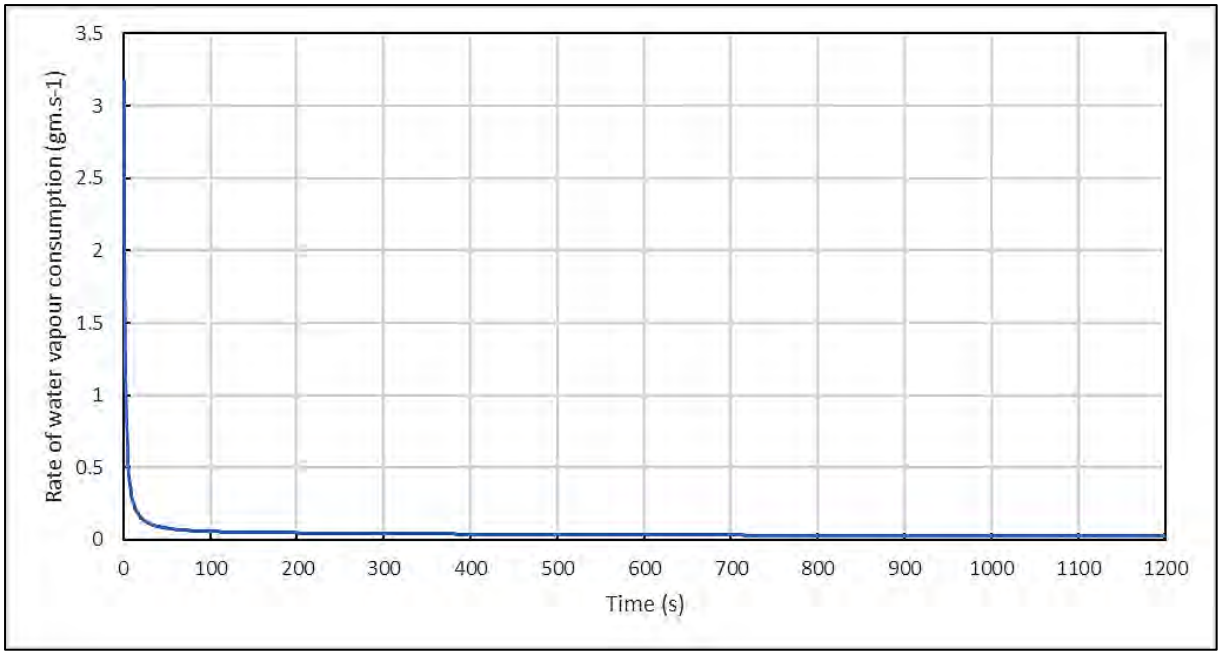

Fig. 5.47: Average rate of water vapour formation variation

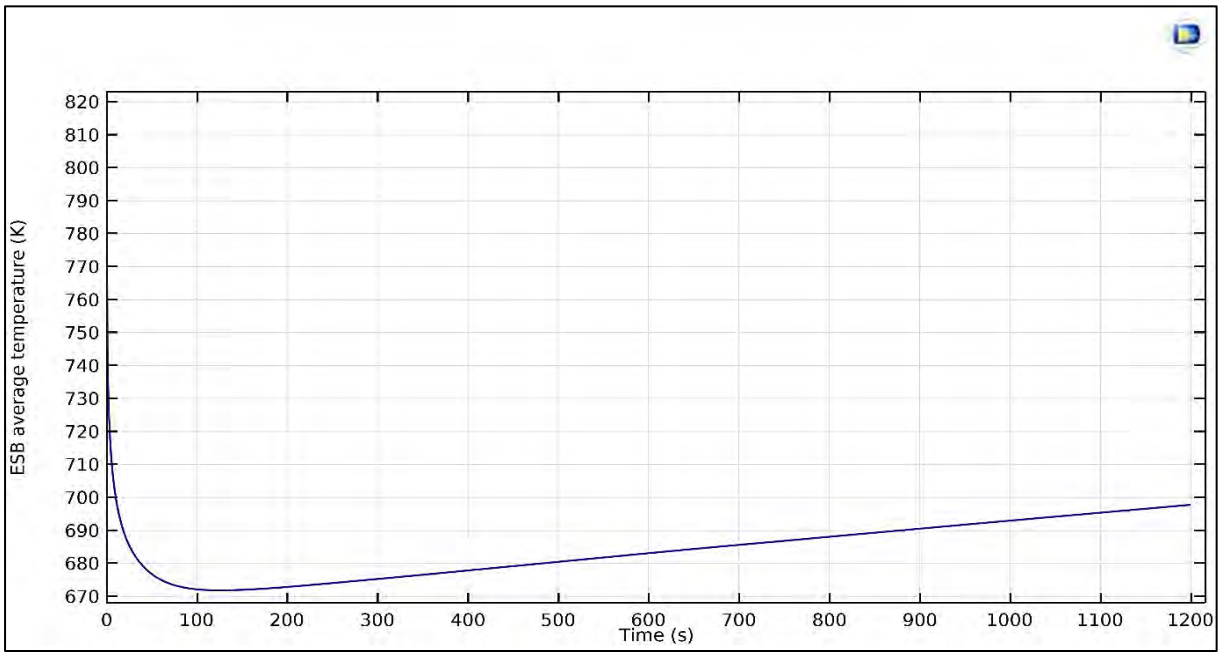

Fig. 5.48. ESB average temperature variation

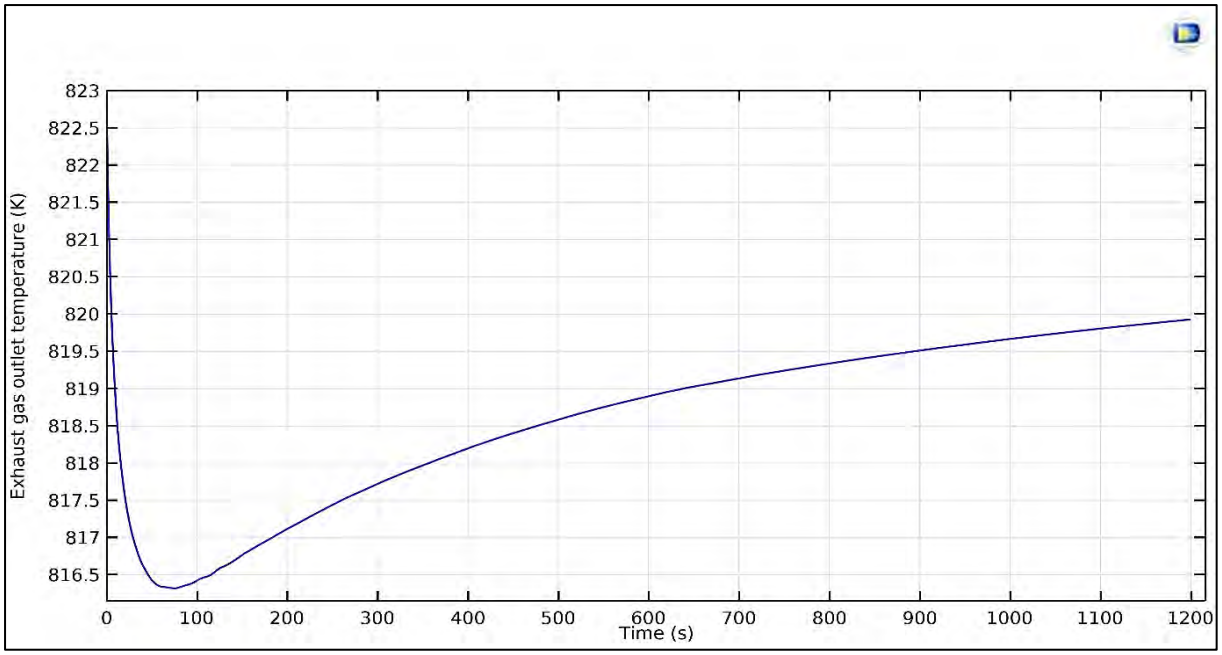

Fig. 5.49. EG outlet temperature variation

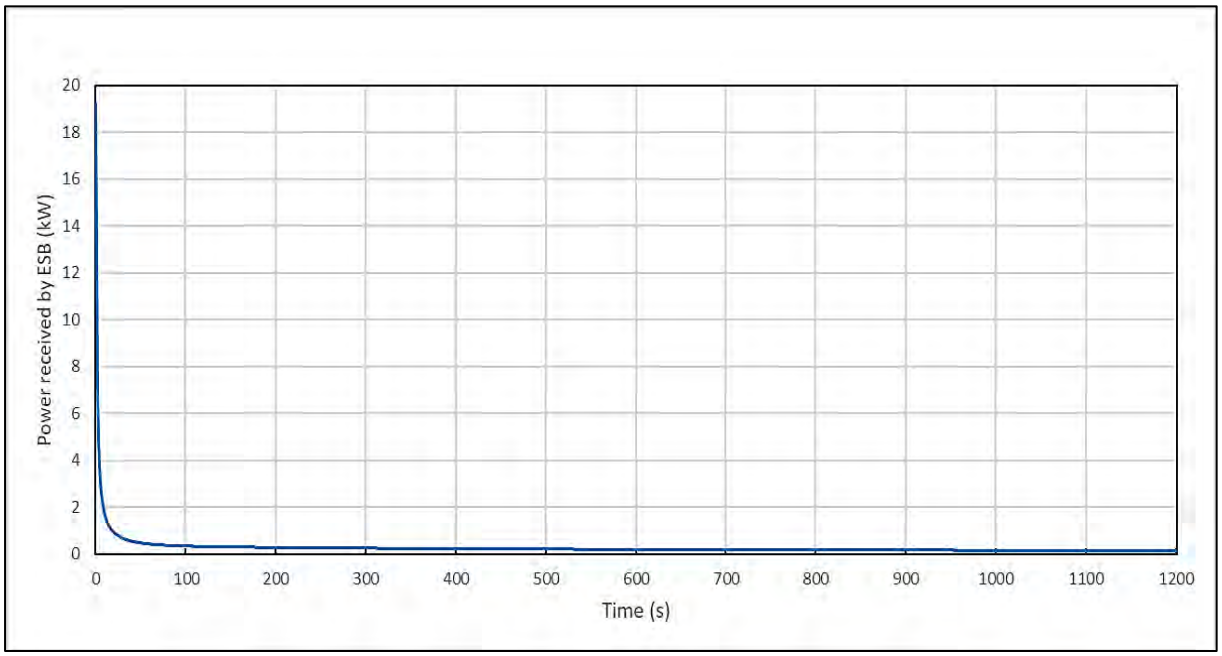

Fig. 5.50. Average power received by ESB variation

Figs. 5.51 and 5.52 show the variation in extent of reaction after 400 and 1200 s, respectively. From Table 5.16, it is observed that at the end of 400s, 28.29 % of reactant ($Ca(OH)_2$) is converted to product (CaO). This value increases to 48.39 % by the end of 1200 s. Thus, with increase in time of dehydration, more amount of reactant is getting converted into product and consequently more energy is stored in ESB.

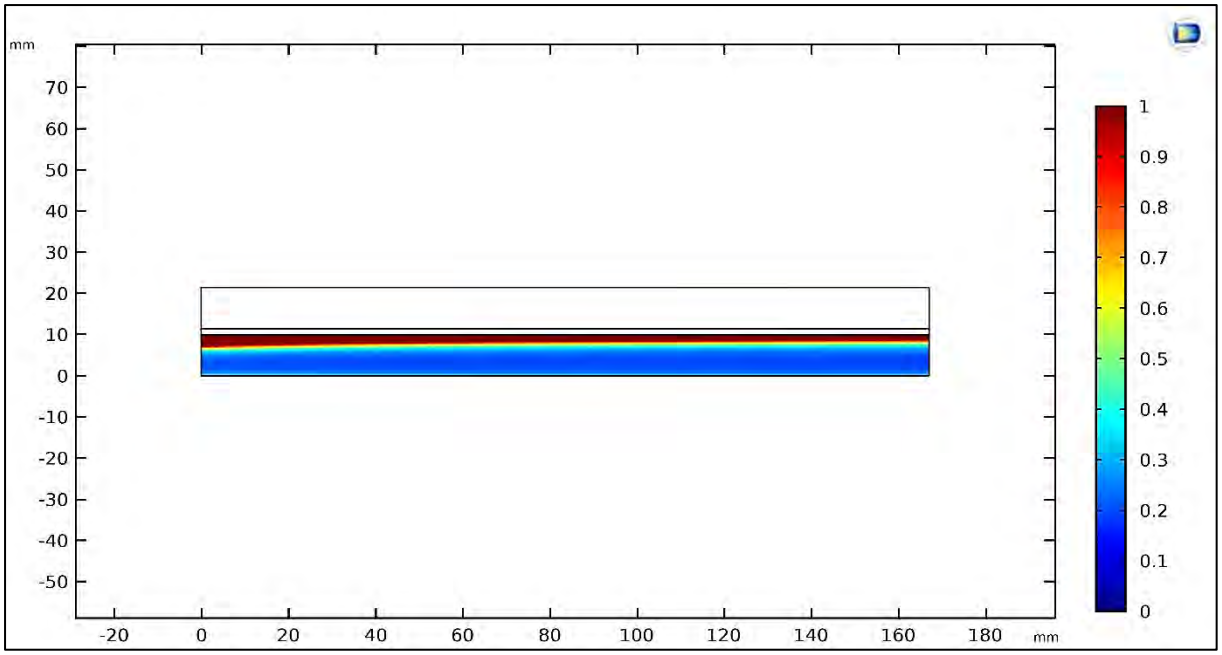

Fig. 5.51: Extent of reaction variation, at the end of 400 s

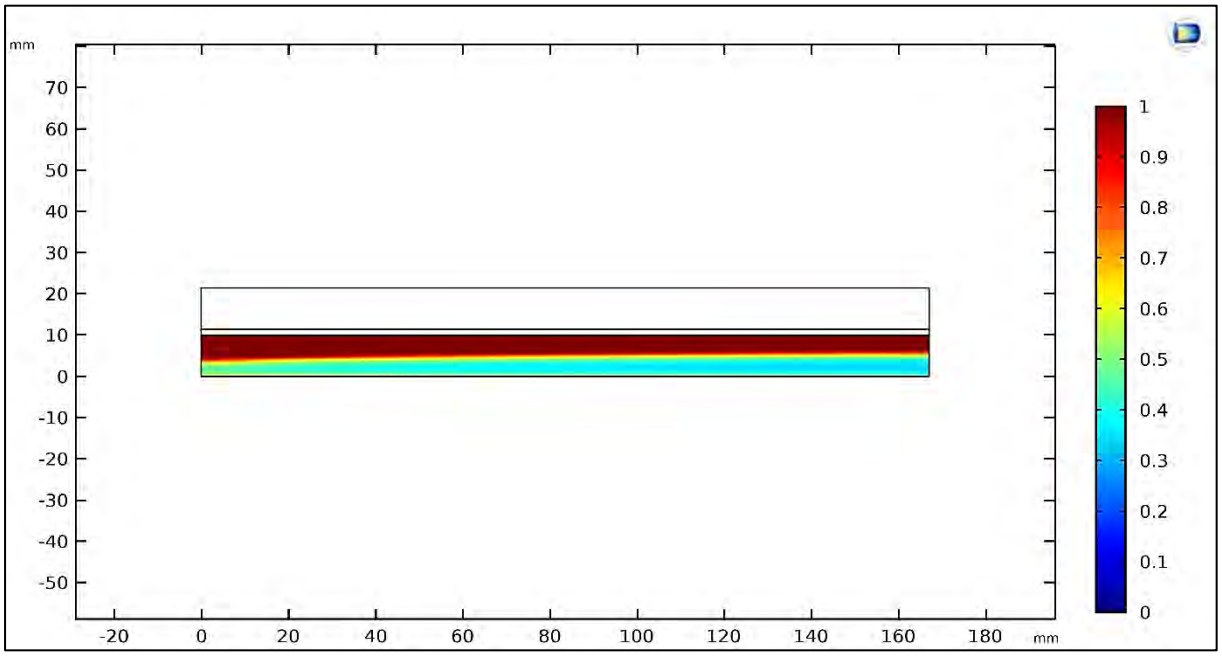

Fig. 5.52: Extent of reaction variation, at the end of 1200 s

Table 5.16. Effect of variation of time of dehydration reaction

Time for dehydration reaction (s)	Final ESB average temperature (K) (T initial = 823 K)	Conversion of reactant to product (%)	Total energy form EG to ESB (kJ)	Total energy in sensible cooling of ESB (kJ)	Total energy stored in ESB (kJ) (Target = 500 kJ)
400	678.04	28.29	127.60	57.71	185.31
1200	697.77	48.39	294.06	40.19	334.25

But due to design constraints suggested by Faurecia team, it is decided to take 800 s as the time available for dehydration reaction for further simulations.

5.2.2.6 Conclusions of parametric studies

Based on results of different parametric studies discussed in section 5.2.2.1 to 5.2.2.5, following conclusions are drawn.

Table 5.17. Observations from parametric studies

Operating parameter	Effect on dehydration reaction
Water vapour outlet pressure	Lower value of outlet pressure gives higher rate of reaction. Thus, it should be as low as possible.
EG inlet temperature	No significant reaction rate is observed below 623 K. So, it should be above 623 K. For higher conversion higher EG inlet temperature is desirable. But very high inlet temperature can cause other operational problems. Hence tradeoff is to be made for optimum value of EG inlet temperature.
EG mass flow rate	No significant impact on reaction performance in present study. But in 3-D case, due to increase in heat transfer area it may show significant impact.
ESB permeability	Higher energy storage is observed for lower ESB porosity values and larger average particle size.
Time of dehydration reaction	Up to 1200 s, it is observed that increase in time of dehydration reaction yields better results due to more conversion. But after 1200 s, rate of conversion is negligible.

5.2.2.7 Revised operating conditions

After analyzing results of 2-D simulations for different parametric studies, it is conveyed to Faurecia team. Based on their inputs, operating conditions are revised as follows:

Table 5.18. Comparison of operating conditions for simulation

Operating parameter	Values at the start of project	Revised values
Initial temperature of ESB	623 to 1073 K (350 to 800˚C)	Minimum 823 K (550 ˚C)
Water vapour outlet pressure	To be decided accordingly	7.33 kPa (P_{sat} corresponding to 40 ˚C)
EG inlet temperature	623 to 1073 K (350 to 800˚C)	Minimum 823 K (550 ˚C)
EG mass flow rate	100 to 350 kg hr^{-1}	815 kg hr^{-1}
ESB porosity	40 to 60 %	40 %
ESB average particle diameter	30 µm and 150 µm	150 µm
Dehydration reaction time	To be decided accordingly	800 s

5.2.2.8 2-D simulations based on revised operating parameters and results

The 2-D dehydration simulations are carried out again with the revised operating conditions given in Table 5.19. For current simulations, only operating conditions are revised but

physical phenomena involved in solving the problem are still the same. So, it is expected that current simulation results should follow similar trend as that of results of earlier different parametric studies.

Table 5.19. Revised operating conditions for simulation

Initial temperature of ESB	823 K (550 ˚C)
Water vapour outlet pressure	7.33 kPa (P_{sat} corresponding to 40 ˚C)
EG (EG) inlet temperature	823 K (550 ˚C)
EG mass flow rate	815 kg hr^{-1}
ESB porosity	40 %
ESB average particle diameter	150 µm
Dehydration reaction time	800 s

Based on above operating conditions simulations are performed and following results are obtained.

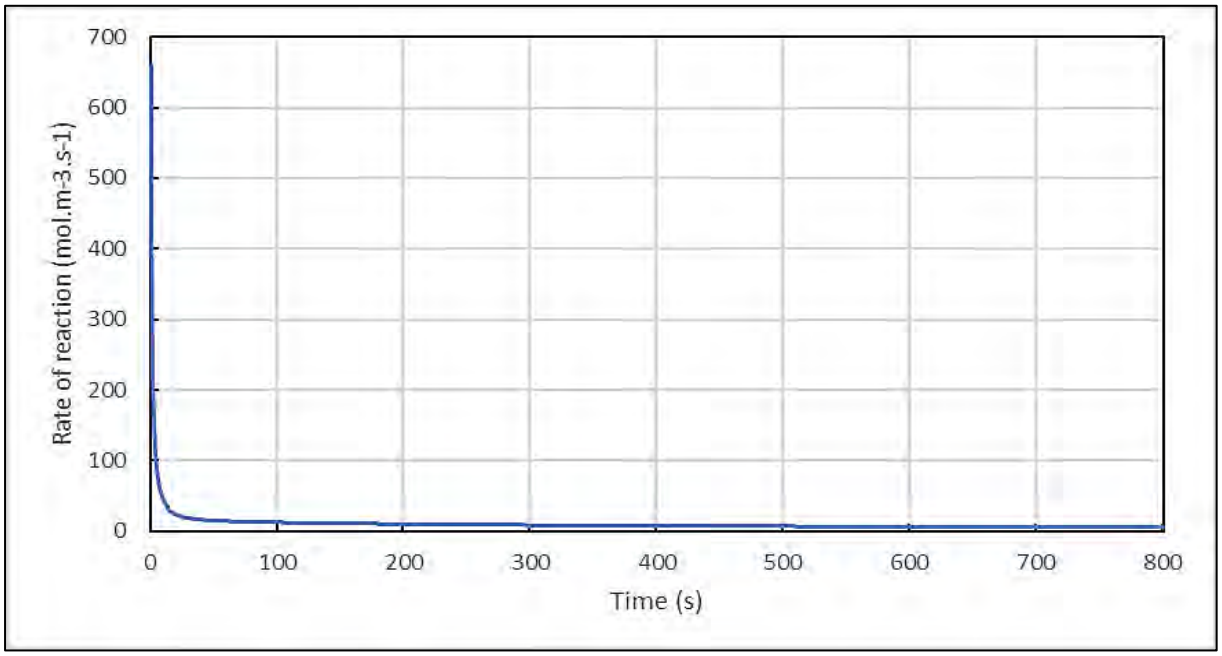

Fig. 5.53: Average rate of reaction variation

The similar trends are observed in the study carried out with revised operating conditions as shown in Figs. 5.53 to 91.

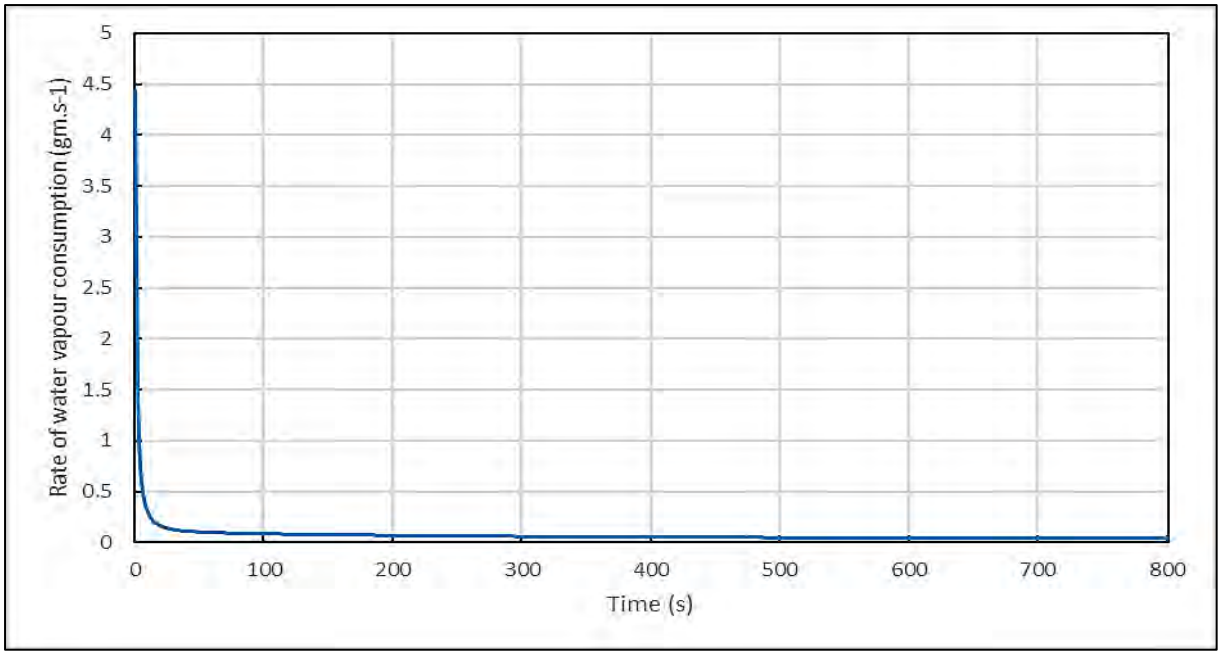

Fig. 5.54: Average rate of water vapour formation variation

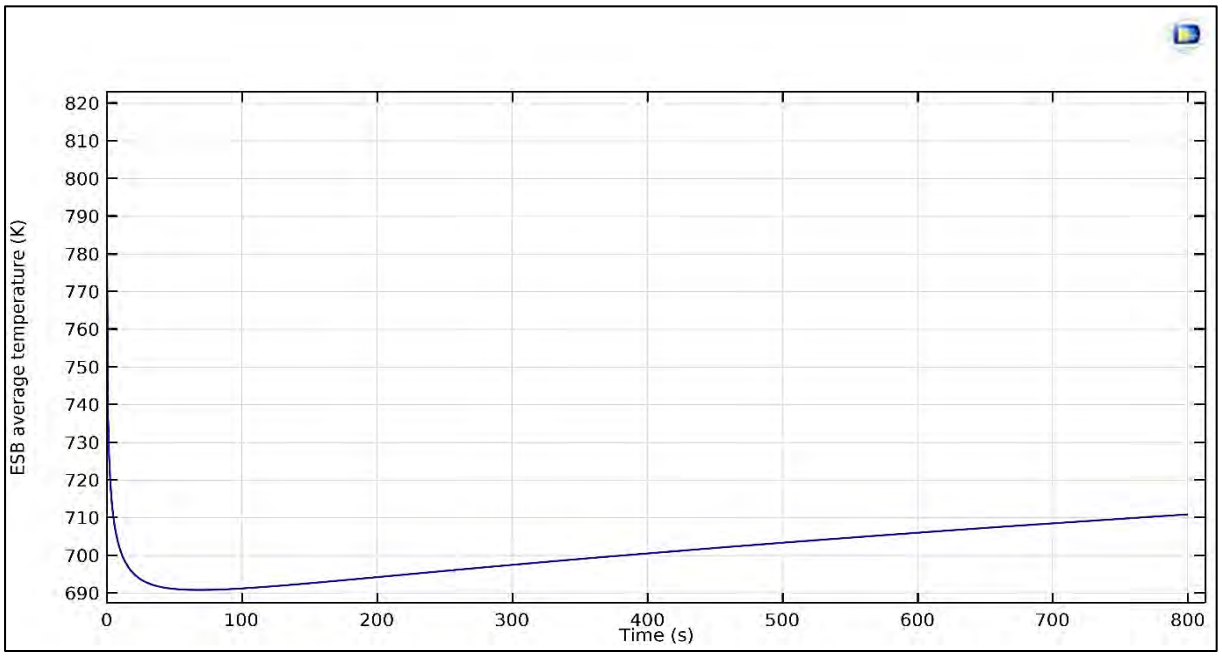

Fig. 5.55: ESB average temperature variation

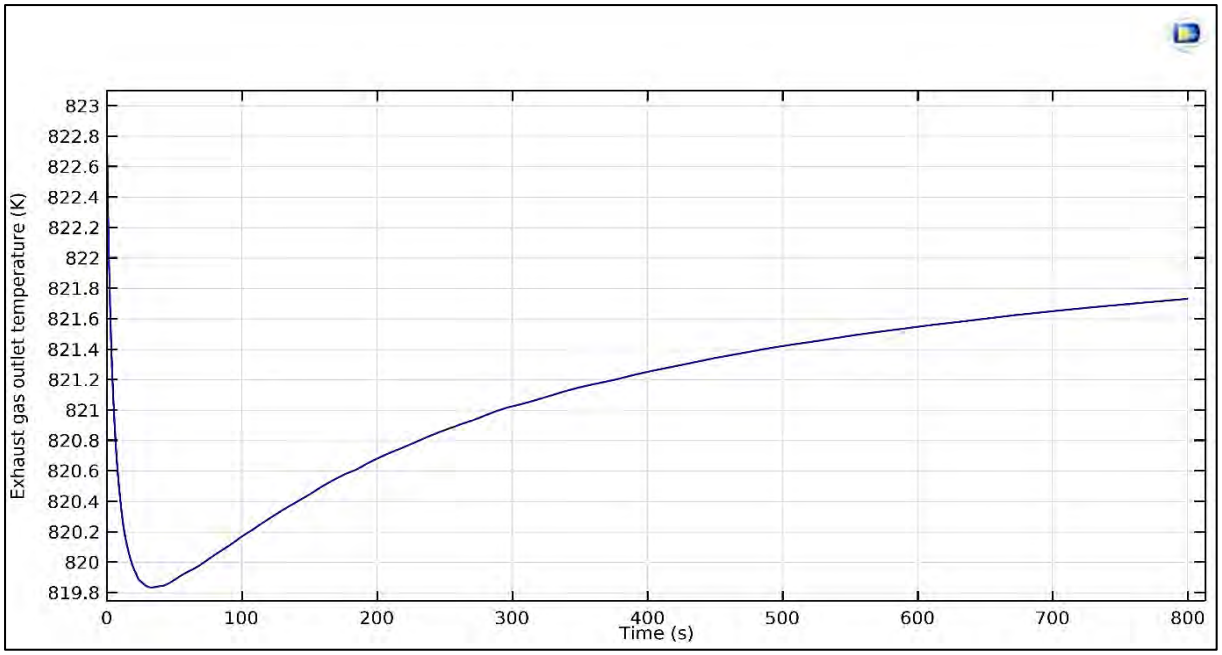

Fig. 5.56. EG average outlet temperature variation

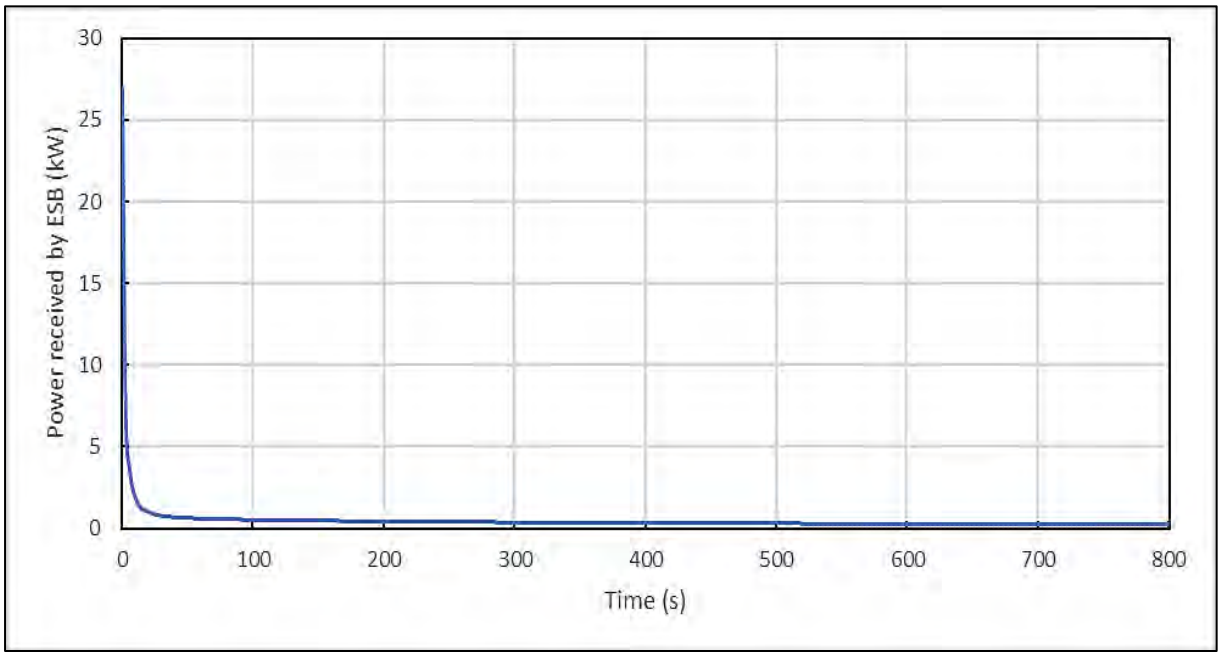

Fig. 5.57: Average power received by ESB variation

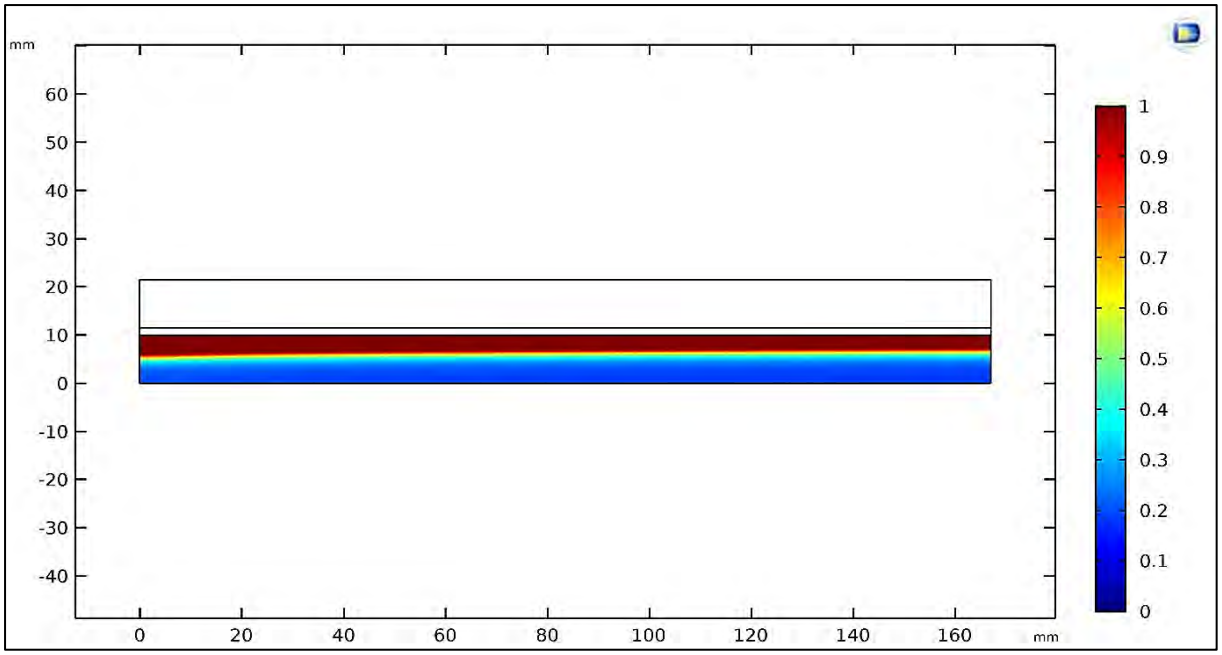

Fig. 5.58: Extent of reaction variation

Table 5.20. Summary of 2-D simulation results based on revised operating conditions

Total energy stored in ESB (kJ) (Target = 500 kJ)	353.59
Total energy from sensible cooling of ESB (kJ)	63.49
Total energy form EG to ESB (kJ)	290.10
Conversion from reactant to product (%)	35.81
Final ESB average temperature (K) after 800 s	710.89
Average rate of reaction (mol m^{-3} s^{-1})	10.82
Total water vapour formation (g)	58.28
Average water vapour formation rate (g s^{-1})	0.07

From Table 5.20, it is observed that with revised operating conditions, only 35.81 % of reactant is converted into product. Thus, ESB can store 353.59 kJ of energy against the required target of 500 kJ. So, for further 3-D simulations primary target is to increase the conversion by using fins, etc. Work is in progress for 3-D dehydration simulations on the similar lines of 3-D hydration simulations.

CHAPTER 6

COMPLETE DEHYDRATION-HYDRATION CYCLE SIMULATIONS

6.1 Introduction

In chapters 4 and 5, hydration and dehydration reactions are studied separately. But in actual practice, hydration dehydration reactions occur in cycle. So, in present study, 2-D simulations are performed for a complete dehydration-hydration cycle.

Objective of the dehydration-hydration cycle is to maximize the energy storage in ESB during dehydration reaction and to maximize the utilization of this stored energy by HTF during hydration reaction.

6.2 Processes involved in complete dehydration-hydration cycle

To carry out the dehydration and hydration in a cyclic process, the processes are to be carried out in following sequence:

1. Preheating of ESB
2. Dehydration reaction
3. Sensible cooling of ESB
4. Hydration reaction

Each of the above mentioned process is discussed in detail in following sections.

6.2.1 Preheating of ESB

One of the assumptions in 2-D dehydration simulations was that initial temperatures of ESB and EG are same. But in case of cold start of HEV, initial ESB temperature will be equal to the ambient temperature. Dehydration reaction requires minimum temperature of 450 ˚C to show significant conversion as observed in section 5.2.2.2. Thus, dehydration reaction doesn't occur at ambient temperature. So, ESB is required to be preheated.

The revised operating conditions (as mentioned in section 5.2.2.7) are used for present study and are shown in Table 6.1.

Table 6.1. Operating conditions for preheating of ESB simulation

Initial temperature of ESB	283 K (10 ˚C)
EG inlet temperature	823 K (550 ˚C)
EG mass flow rate	200 kg hr^{-1}
ESB porosity	40 %
ESB average particle diameter	150 μm
Preheating time	1200 s

For the simulation of preheating process, 2-D dehydration reaction model is used. The only difference made is that there is no outlet passage for water vapour. With no outlet, the model is reduced to sensible heating of ESB with the help of EG. Based on above operating conditions simulations are performed and following results are obtained.

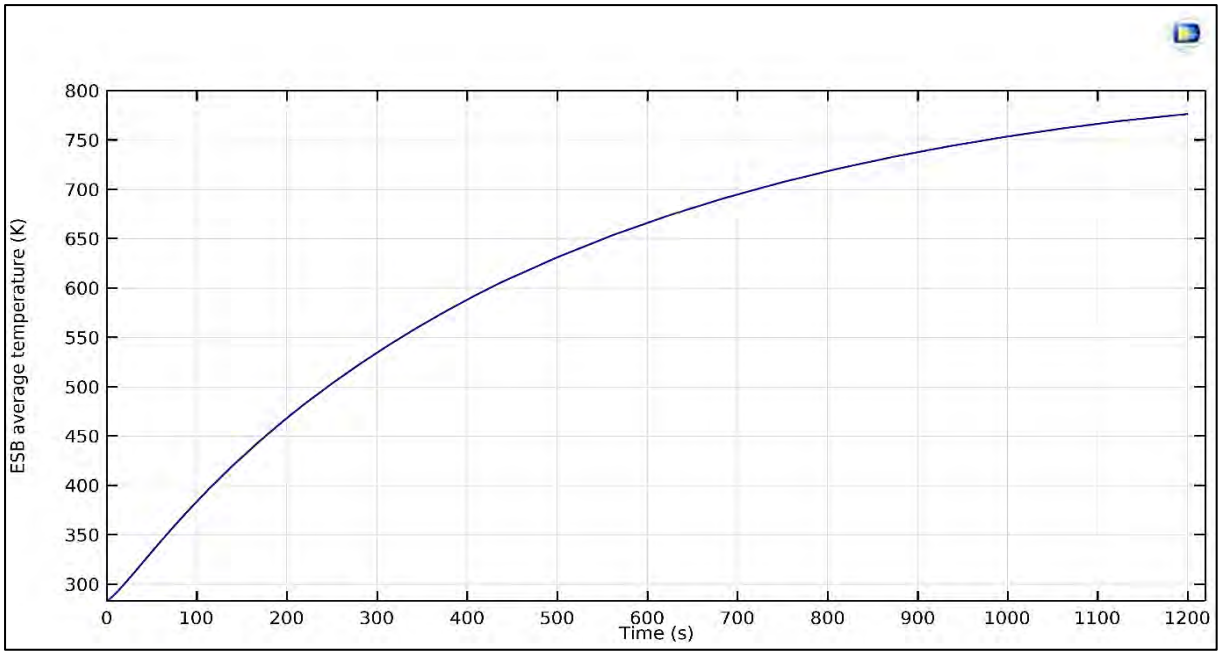

Fig. 6.1: ESB average temperature variation during preheating

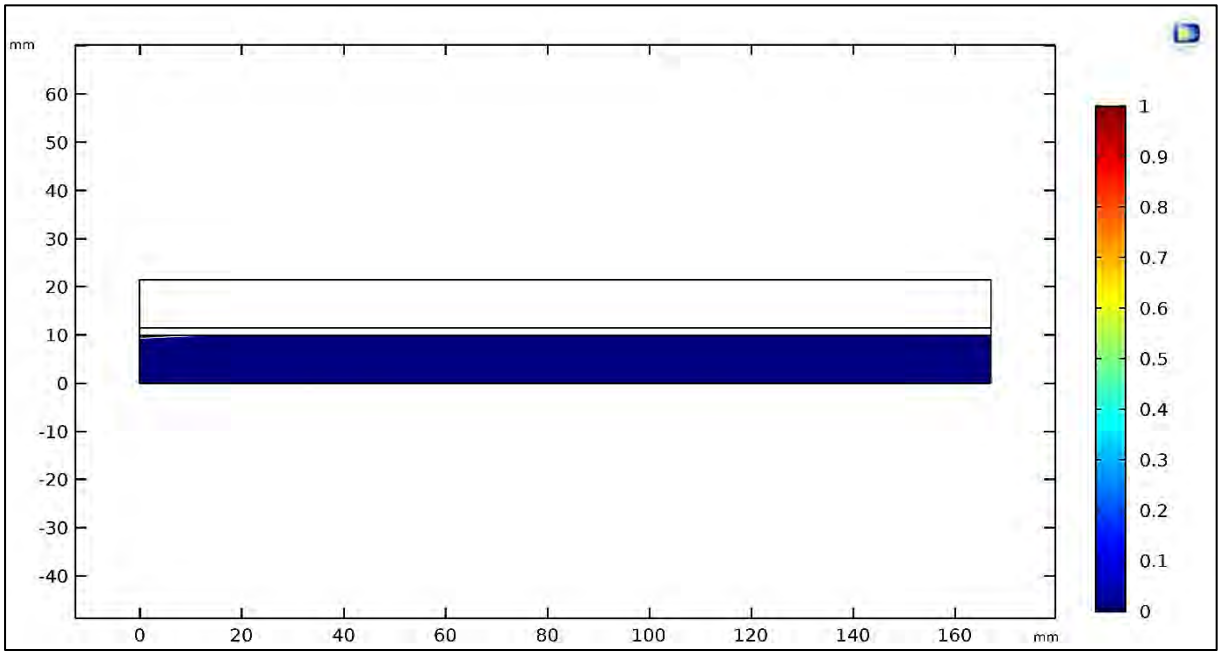

Fig. 6.2: Extent of reaction variation at the end of preheating

Fig. 6.1 shows ESB average temperature variation during preheating. As it is the case of sensible heating of ESB, average temperature of ESB gradually increases from ambient temperature of 283 K to 776.56 K. Due to poor thermal conductivity of ESB, the time taken by ESB to reach average temperature of 776.56 K is 1200 s even though the EG is supplied at constant inlet temperature of 823 K. Fig. 6.2 shows variation in extent of reaction across ESB

at the end of preheating process. As there is no chemical reaction, no significant change is observed in extent of reaction. As shown in Table 6.2, energy supplied by EG for preheating ESB is 372.29 kJ.

Table 6.2. Effect of preheating of ESB

Final ESB average temperature	776.56 K
Energy supplied by EG for preheating ESB	372.29 kJ

6.2.2 Dehydration reaction

The initial operating conditions to carry out dehydration simulation study are taken from the final operating conditions obtained from the preheating process simulation study. In the present study, 2- D dehydration reaction model is used as discussed in section 5.2. The initial operating conditions for the dehydration reaction simulation study are taken from the final operating conditions obtained from the preheating of ESB study. The operating conditions for dehydration simulation are shown in Table 6.3.

Table 6.3. Operating conditions for dehydration reaction simulation

Initial temperature of ESB	776.56 K (503.56 ˚C)
Water vapour outlet pressure	7.33 kPa (P_{sat} corresponding to 40 ˚C)
EG inlet temperature	823 K (550 ˚C)
EG mass flow rate	200 kg hr^{-1}
ESB porosity	40 %
ESB average particle diameter	150 μm
Dehydration reaction time	800 s

Based on above operating conditions simulations are performed and following results are obtained.

As shown in Fig. 6.3, ESB average temperature initially drops rapidly from 776.56 K to around 690 K due to dehydration. After then, it gradually increases to 701.72 K. Similar variation is observed in section 5.2.2.1. At the start of dehydration reaction, rate of reaction is higher. Hence higher drop in ESB average temperature is observed. After around 60 s from the start of dehydration, reaction rate becomes almost constant for the rest of reaction time. In this period, ESB average temperature slightly increases as rate of temperature rise due to forced convection between EG and ESB is higher than the rate of temperature drop due to dehydration reaction as shown in Fig. 6.3.

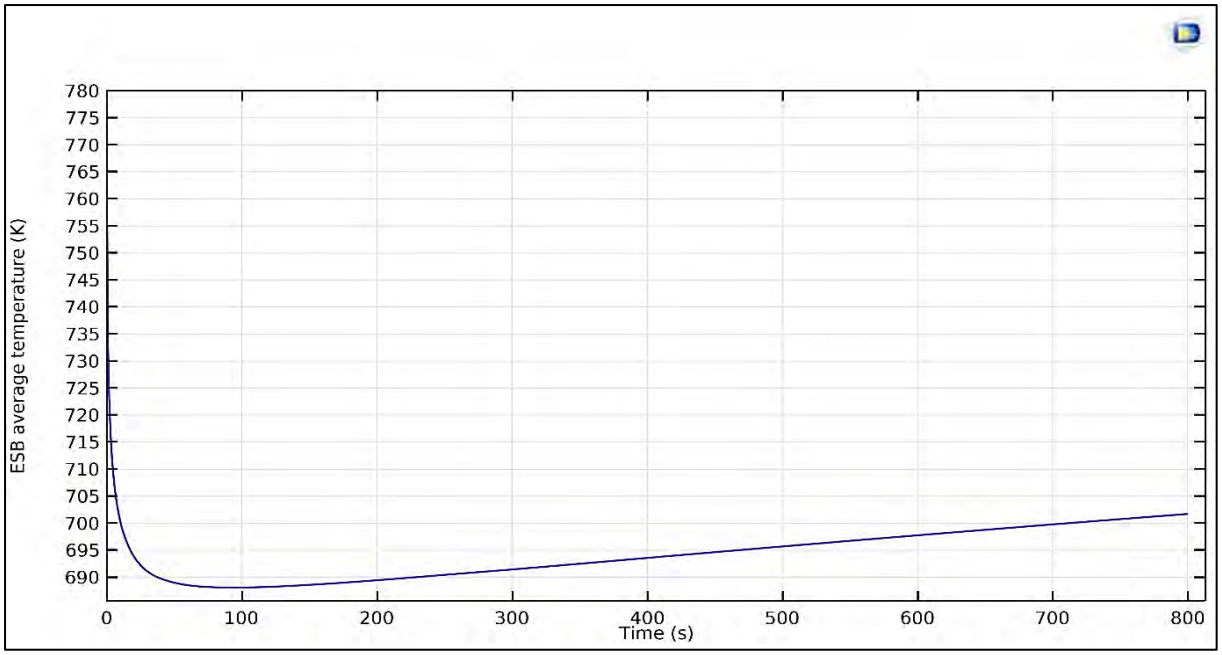

Fig. 6.3: ESB average temperature variation during dehydration

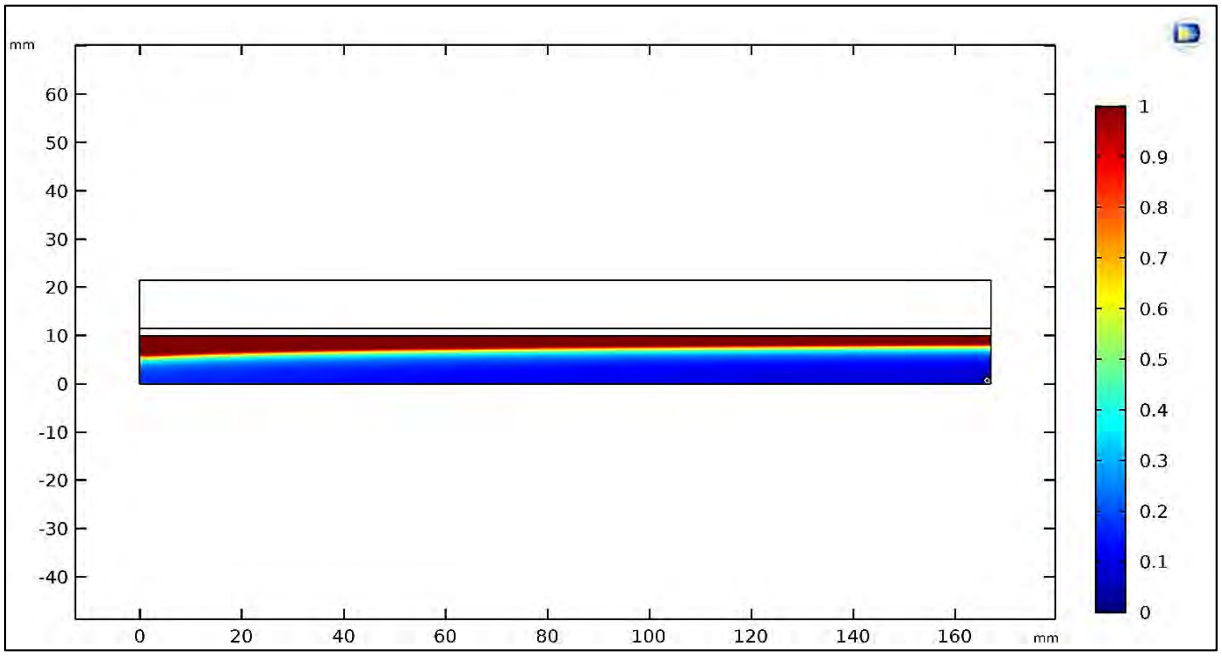

Fig. 6.4: Extent of reaction variation at the end of dehydration

Fig. 6.4 shows extent of reaction variation across ESB at the end of dehydration reaction. By the end of dehydration reaction, 28.91 % of reactant got converted into product. During this conversion process, 293. 72 kJ of energy is stored in ESB as shown in Table 6.4.

Table 6.4. Effect of dehydration reaction

Final ESB average temperature	701.72 K
Conversion from $Ca(OH)_2$ to CaO	28.91 %
Total energy supplied by exhaust gas to ESB	247.58 kJ
Total energy from sensible cooling of ESB	46.14 kJ
Total energy stored in ESB	293.72 kJ

6.2.3 Sensible cooling of ESB

After dehydration reaction, it is observed that ESB average temperature is 701.72 K. There are two options after dehydration reaction

1. Start hydration reaction by supplying water vapour to ESB – But, hydration reaction is exothermic in nature. So, it will result into further increase in ESB average temperature. Equilibrium pressure corresponding to 750 K is 53.87 kPa. This means if hydration reaction is to occur at temperatures of 750 K or above, minimum supply pressure of water vapour must be above 53.87 kPa. But, the maximum value of water vapour supply pressure for hydration is selected as 47.13 kPa as discussed in section 4.2.2.1. Hence, it is not feasible to start the hydration reaction immediately after dehydration.
2. Perform sensible cooling of ESB – The decrease in ESB temperature results in the decrease of corresponding equilibrium pressure. So, it would be feasible to perform hydration reaction within given operating conditions. At the same time, HTF continuously receives energy from ESB. This received energy can be utilised for cabin heating. In subsequent calculations, it is found that ESB sensible cooling also increases overall cycle efficiency.

Thus, sensible cooling of ESB is performed after dehydration process. For the simulation of sensible cooling process, 2-D hydration reaction simulation model is used. The only difference made is that there is no inlet passage for water vapour. As there is no inlet passage, the model is reduced to sensible cooling of ESB. The initial operating conditions for sensible cooling process simulation study are taken from the final operating conditions obtained from the dehydration reaction. The operating conditions for the hydration simulation are shown in Table 6.5.

Table 6.5. Operating conditions for sensible cooling of ESB simulation

Initial temperature of ESB	701.72 K
HTF inlet temperature	338 K
HTF flow rate	10 ltr min^{-1}
ESB porosity	40 %
ESB average particle diameter	150 μm
ESB cooling time	1200 s

Based on above operating conditions simulations are performed and following results are obtained.

As shown in Fig. 6.5, ESB average temperature decreases during sensible cooling process. ESB average temperature gradually decreases from 701.72 K to 343.47 K. In the meantime, 204.04 kJ of energy is transferred to HTF from ESB as shown in Table 6.6.

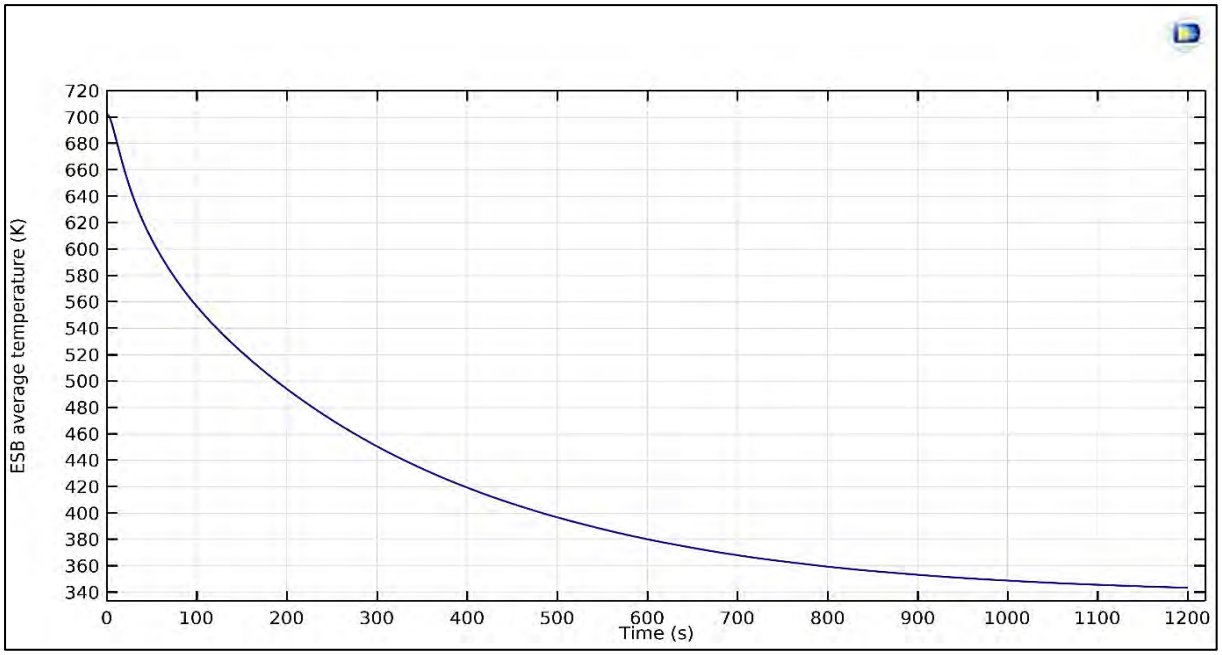

Fig. 6.5: ESB average temperature variation during ESB cooling

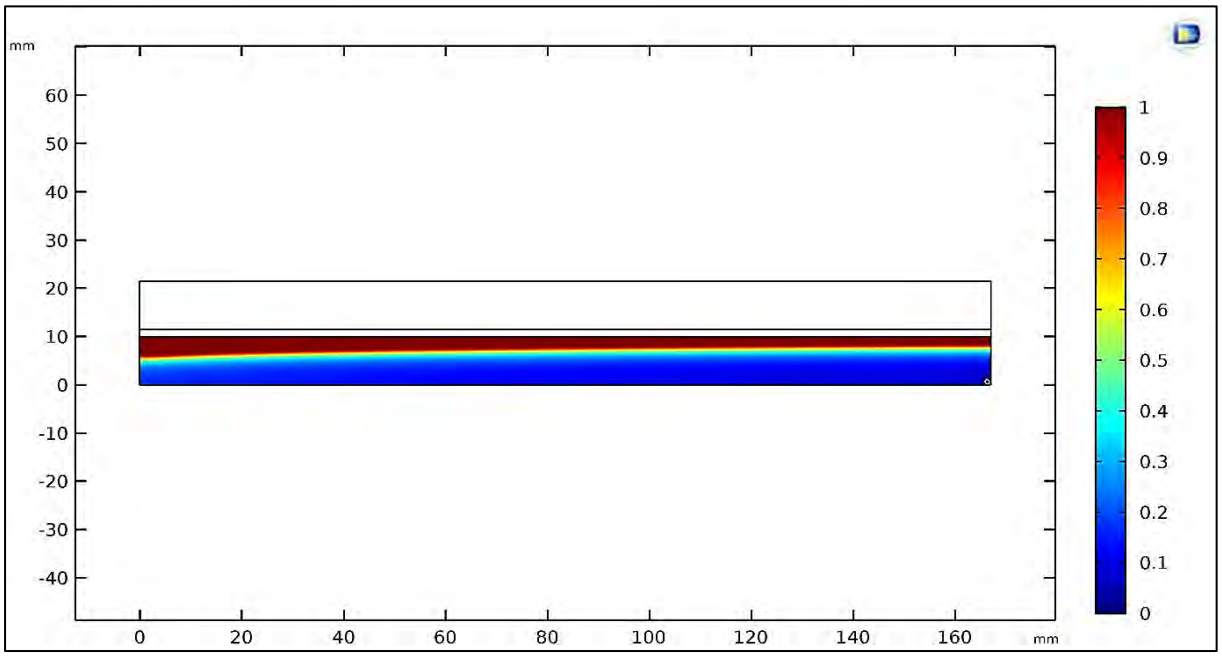

Fig. 6.6: Extent of reaction variation at the end of sensible cooling of ESB

Since hydration reaction is not started yet, there is no change in extent of reaction variation across ESB during sensible cooling process as shown in Fig.6.5.

Table 6.6. Effect of sensible cooling of ESB

Final ESB average temperature	343.47 K
Energy lost by ESB to HTF	204.04 kJ

6.2.4 Hydration reaction

The hydration reaction is started after sensible cooling of ESB. 2-D hydration reaction simulation model is used for simulation as discussed earlier in section 4.2. The initial operating conditions for hydration simulation study are taken from the final operating conditions obtained from the sensible cooling process simulation study of ESB. The operating conditions for the hydration simulation are shown in Table 6.7.

Table 6.7. Operating conditions for hydration reaction simulation

Initial temperature of ESB	343.47 K
Water vapour supply pressure	47.13 kPa (P_{sat} corresponding to 80 ˚C)
HTF inlet temperature	338 K
HTF flow rate	10 ltr min^{-1}
ESB porosity	40 %
ESB average particle diameter	150 µm
Hydration reaction time	800 s

Based on above operating conditions simulations are performed and following results are obtained.

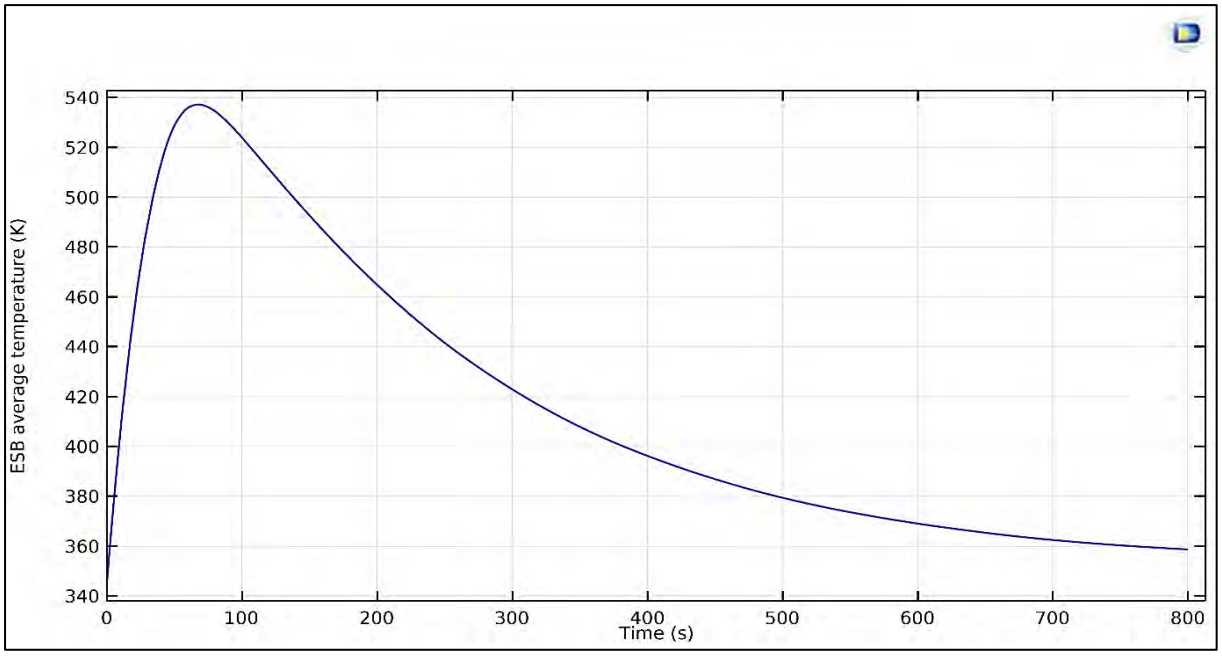

Fig. 6.7: ESB average temperature variation during hydration

Fig.6.7 shows that ESB average temperature increases from 358.73 K to a maximum value of around 538 K and then gradually decreases to 358.73 K by the end of hydration reaction. From Fig.6.8 and Table 6.8, it is observed that out of 28.29 % of CaO formed after

dehydration process, 16.26 % CaO got converted back to $Ca(OH)_2$. But, 12.03 % of CaO is still present in ESB at the end of hydration.

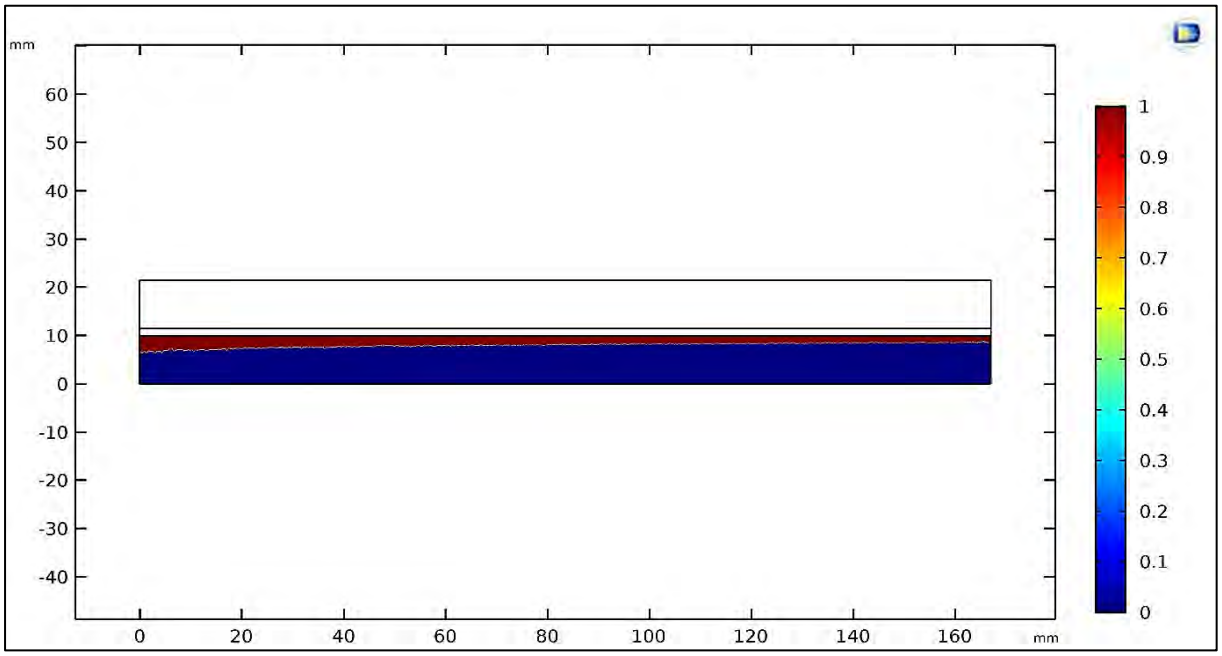

Fig. 6.8: Extent of reaction variation at the end of hydration

Table 6.8. Effect of hydration reaction

Final ESB average temperature	358.73 K
Amount of CaO still present in ESB	12.03 %
Conversion of CaO back to $Ca(OH)_2$	16.26 %
Total energy received by HTF	164.30 kJ
Total energy for sensible heating of ESB	30.10 kJ
Total energy output from ESB	194.40 kJ

The average temperature of ESB during complete dehydration-hydration cycle is shown in Fig. 6.9.

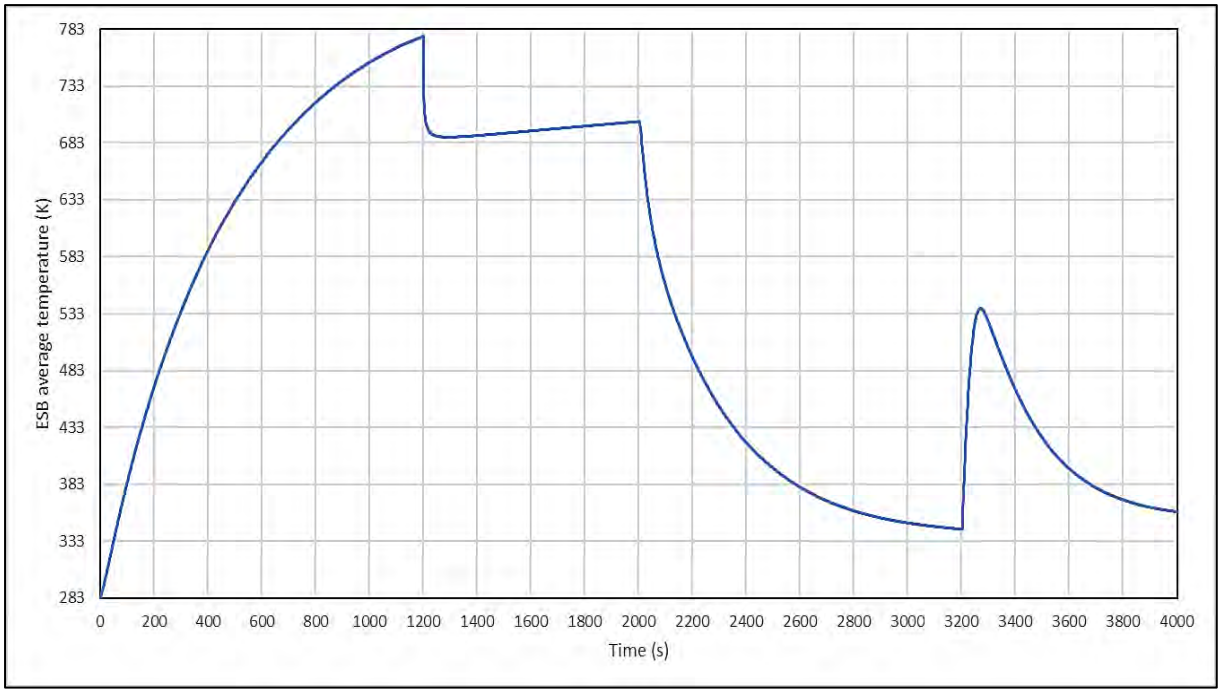

Fig. 6.9: ESB average temperature during the cyclic process

6.3. Efficiency calculations

Based on above results, different efficiencies are calculated as shown below:

6.3.1 Chemical reaction efficiency

Chemical reaction efficiency is defined as the ratio of energy transferred to HTF from ESB during hydration reaction to the energy stored in ESB during dehydration reaction.

From Table 6.4 and 6.8, out of 293.72 kJ of energy stored in ESB during dehydration reaction 164.30 kJ is transferred to HTF at the end of hydration reaction.

So, chemical reaction efficiency = 164.30/293.72 = 55.94 %.

6.3.2 Overall cycle efficiency

It is defined as the ratio of total energy released by ESB to the total energy received by ESB, taking ESB domain as control volume.

Total energy received by ESB = Energy taken from EG for preheating of ESB + Energy taken from EG by ESB during dehydration

So, total energy received by ESB = 372.29 + 247.58 = 619.87 kJ,

Total energy released by ESB = Energy given by ESB to HTF during sensible cooling of ESB + Energy released from ESB during hydration

Total energy released by ESB = 204.04 + 194.40 = 398.44 kJ,

Thus, overall cycle efficiency = 398.44/619.87 = 0.6428 = 64.28 %.

For overall system efficiency, GSB performance and minimization of other losses are required to be considered. For present study, degradation in thermo-physical properties of ESB materials and respective variation in rate of reaction expressions are not considered. This model strictly follows assumptions as mentioned in sections 4.1 and 5.1. But in due course of time, if relation between material properties, rate expressions and number of cycles is established, then this model can be modified accordingly.

CHAPTER 7

CONCLUSIONS

7.1 Conclusions of the present study

The thermochemical energy storage system based on gas-solid chemical reaction is chosen to store thermal energy of exhaust gas (EG) in hybrid electric vehicle (HEV). The stored energy is later utilized for cabin heating. The thermal energy storage (TES) system is developed by the addition of energy storage bed (ESB) and gas storage bed (GSB) in the existing setup of HEV. The analysis of ESB had been started with the gas-solid pair involving hydration/dehydration of K_2CO_3. But due to lack of literature study and kinetic expressions on hydration/dehydration of K_2CO_3, it is not perceived further. Then after thorough literature study, hydration/dehydration of $CaO/Ca(OH)_2$ is selected as the suitable gas-solid pair for proposed TES. To carry out the initial study of energy storage bed, simulations are performed in 2-D model of geometry. Extent of influence of different operating parameters is studied by performing 2-D parametric simulations. The important conclusions of 2-D model parametric studies are

- On increasing the water vapour supply pressure during hydration, the rate of reaction increases which results in the increase in water vapour consumption, temperatures of ESB and HTF. Consequently, the thermal power received by Heat Transfer Fluid (HTF) is also increased at high water vapour supply pressure.

- The effect of raising ESB temperature is insignificant on hydration reaction.

- No effect of varying the mass flow rate of HTF on the hydration reaction performance. But with increase in mass flow rate, total energy received by HTF increases with lower rise in outlet temperature. Thus, optimum value of mass flow rate of HTF is to be selected.

- Higher energy output is observed for lower ESB porosity values and larger average particle size.

- The extent of conversion is 83.75 % at the end of 1200 s after which the conversion rate ceases to very low value.

Based on these observations, initial operating conditions are revised and 2-D hydration reaction simulations are performed with revised operating conditions. Conclusions of the revised operating conditions based simulation are

- The total energy released by ESB during hydration is 635.03 kJ out of which the energy received by HTF is 478.41 kJ against the target of 500 kJ.
- Average HTF temperature rise is observed to be 3.02 K against the requirement of 3.05 K.
- The maximum power of 1858.49 is observed at 154 s from the start of hydration. It is required to achieve maximum power of 3000 W in 60 s from start of hydration reaction.

- Out of initial concentration of reactant (CaO), 82.05 % is converted into product ($Ca(OH)_2$) by the end of hydration reaction.

After studying the effect of various parameters on the performance of hydration reaction, the simulations are further extended to 3-D model. The simulations of 3-D model are done three different case study as 3-D model without any fins, 3-D model with fins in ESB domain, and 3-D model with fins in ESB and HTF domain. The important conclusions obtained from the simulation of 3-D model for hydration reaction are

- Due to edge effect of steel frame in 3-D model, higher conversion is observed (Case study I) which results in high average rate of reaction and average water vapour consumption. Consequently, the increase in total energy output from ESB, total energy received by HTF, average peak power received by HTF and efficiency of energy transfer from ESB to HTF are observed.
- But, HTF average outlet temperature rise is lower in 3-D model due to energy loss from HTF to steel frame.
- In 3-D model, fraction of energy released by ESB is consumed by surrounding steel frame which was not observed in 2-D model.
- With addition of fins in ESB domain, there is no significant change in energy output from ESB. But, addition of fins in ESB domain significantly increases the efficiency of heat transfer from ESB to HTF from 78.66 % (without fins) to 82.65 % (with fins in ESB domain). Thus, it is observed that higher amount of energy is received by HTF. Peak power received by HTF is significantly increased from 2068.45 W (with no fins) to 2298.66 W (with fins in ESB domain). Average HTF temperature rise is also higher in case of fins in ESB domain.
- With fins addition in both ESB and HTF domain, it is observed that for reaction completion, it takes 487 s as compared to 800 s in case of fins in ESB domain. Thus, reduction of 39.13 % is observed in reaction completion time with fins in ESB and HTF domain as compared to fins in ESB domain only. Peak power received by HTF is also significantly improved from 2298.66 W (with fins in ESB domain) to 2776.92 W (with fins in both ESB and HTF domain).

After detailed study of hydration reaction, dehydration reaction is also studied on similar lines. First 2-D model is setup and different parametric studies are performed. The important conclusions of 2-D model parametric studies are

- It is observed that lower value of water vapour outlet pressure gives higher rate of reaction which results in more conversion of reactant into product and higher amount of energy is stored in ESB.
- No significant reaction rate is observed below 623 K. So, it should be kept above 623 K. For higher conversion it is observed that higher EG inlet temperature is desirable. But very high inlet temperature can cause other operational problems. Hence trade-off is to be made for optimum value of EG inlet temperature.
- No significant impact of EG mass flow rate variation is observed on dehydration reaction performance in present study.

- Higher energy storage is observed for lower ESB porosity values and larger average particle size.
- For dehydration reaction, it is observed that increase in time of dehydration reaction up to 1200 s yields more conversion of reactant into product, but rate of conversion becomes negligible after 1200 s.

Based on the findings of parametric studies, initial operating conditions are revised and 2-D dehydration reaction simulations are performed with revised operating conditions. Conclusions of the revised operating conditions based simulation are

- Energy stored in ESB is 353.59 kJ. Required amount of energy to be stored in ESB is 500 kJ.
- 35.81 % of initial reactant concentration ($Ca(OH)_2$) is converted into product (CaO) by the end of dehydration reaction.

2-D simulations for a complete dehydration-hydration cycle has been performed. Complete dehydration-hydration cycle involves four processes i.e. preheating of ESB, dehydration reaction, sensible cooling of ESB and hydration reaction respectively. Conclusions of the study are

- 293.72 kJ of energy is stored in ESB during dehydration reaction and out of the stored in ESB, 164.30 kJ is transferred to HTF at the end of hydration reaction. So, chemical reaction efficiency is observed to be 55.94 %.
- But for overall cycle, total energy received by ESB (619.87 kJ) is sum of energy taken from EG for preheating of ESB (372.29 kJ) and energy taken from EG by ESB during dehydration reaction (247.58 kJ). And total energy released by ESB (398.44 kJ) is sum of energy given by ESB to HTF during sensible cooling of ESB (204.04 kJ) and energy released from ESB during hydration reaction (194.40 kJ). Thus, overall cycle efficiency is observed to be 64.28 %.

7.2 Scope for future work

2-D simulations of hydration and dehydration reaction are completed. But, due to time constraints, following studies are yet to be performed

- The dehydration simulations of 3-D model are to be performed with and without fins.
- The structure of ESB is to be optimized to improve the performance.
- The designing of GSB is to be performed.
- A system level analysis of TES system consisting of ESB and GSB with various additional components is to be done.

References

[1] Devrim Aydin, Sean P.Casey, Saffa Riffat, The latest advancements on thermochemical heat storage systems, Renewable and Sustainable Energy Reviews 41, 356-367, 2015.

[2] L.C. Sogutoglu, P.A.J. Donkers, H.R. Fischer, H.P. Huinink, O.C.G. Adan, In-depth investigation of thermochemical performance in a heat battery: Cyclic analysis of K_2CO_3, $MgCl_2$ and Na_2S, Journal of Applied Energy 215, 159–173, 2018.

[3] M. A. Stanish and D. D. Perlmutter, Kinetics and Transport Effects in the Dehydration of Crystalline Potassium Carbonate Hydrate, AlChE Journal 29, 806-812, 1983.

[4] M. A. Stanish and D. D. Perlmutter, Kinetics of Hydration- Dehydration Reactions Considered as Solid Transformations, AlChE Journal 30, 557-563, 1984.

[5] L.C. Sogutoglu, P.A.J. Donkers, H.R. Fischer, H.P. Huinink, O.C.G. Adan, In-depth investigation of thermochemical performance in a heat battery: Cyclic analysis of K_2CO_3, $MgCl_2$ and Na_2S, Journal of Applied Energy 215, 159–173, 2018.

[6] Rate Processes in Cycling a Reversible Gas-Solid Reaction by M. A. Stanish and D. D. Perlmutter, AlChE Journal 30, 56-62, 1984.

[7] Thermochemical energy storage and conversion: A state of the art review of the experimental research under practical conditions by Jaume Cot-Gores, Albert Castell, Luisa F. Cabeza, published in Renewable and Sustainable Energy Reviews 16, 5207–5224.

[8] Garg HP, Mullick SC, Bhargava AK. Chemical Energy Storage, In Solar Thermal Energy Storage, D. Reidel Publishing Company Holland 1985, 292–427.

[9] Ervin G. Solar heat storage using chemical reactions. J Solid State Chem 1977, 22, 51–61.

[10] Felderhoff M., Urbanczyk R. Peil S. Thermochemical Heat Storage for High Temperature Applications – A Review. Green 2013, 3(2), 113 – 123.

[11] Hartman M, Trnka O, Svoboda K, Kocurek J. Decomposition kinetics of alkaline-earth hydroxides and surface area of their calcines. Chem Eng Sci. 1994, 49, 1209–16.

[12] F. Schaube, L. Koch, A. Wörner∗, H. Müller-Steinhagen, A thermodynamic and kinetic study of the de- and rehydration of $Ca(OH)_2$ at high H_2O partial pressures for thermo-chemical heat storage, Thermochimica Acta 538 (2012) 9– 20.

[13] Y.A. Criado, M. Alonso, J.C. Abanades, Kinetics of the $CaO/Ca(OH)_2$ Hydration/Dehydration Reaction for Thermochemical Energy Storage Applications, Industrial & Engineering Chemistry Research 53 (2014) 12594−12601.

[14] H. Shao, T. Nagel, C. Robkopf, M. Linder, A. Wörner, O. Kolditz, Non-equilibrium thermo-chemical heat storage in porous media: Part 2-A 1D computational model for a calcium hydroxide reaction system, Energy 60 (2013) 271-282.